Chemical Controls on the Uptake of Ozone to the Ocean

Lucy Brown

Doctor of Philosophy

University of York

Chemistry

June 2024

Abstract

Ozone deposition to the ocean represents one of the largest sinks of ozone from the troposphere, but is highly uncertain. Chemical reactions with the sea surface drive deposition to the ocean, however the identity and contribution of different reactive compounds remains unclear. Iodide is considered one of the main drivers of ozone uptake to the ocean, however there is also an expected contribution from organic matter, the nature of which is not well characterised.

This work aimed to investigate these chemical drivers , including re-measuring the kinetics and temperature dependence of the reaction between ozone and iodide. With the ozone-iodide reaction as a baseline, ozone uptake to seawater was analysed, and the "missing" reactivity quantified.

A method was developed, which facilitated ozone uptake measurements to iodide solutions and seawater. The rate of reaction between ozone and iodide was measured, yielding Arrhenius parameters of A = 5.4 ± 23.0 $\times 10^{10}$ M^{-1} s^{-1} and E_a = 7.0 ± 10.5 kJ mol^{-1}. This weak temperature dependence has implications for the spatial and temporal variation in ozone dry deposition to the ocean, and subsequent emissions of iodine-containing compounds.

Ozone uptake was measured to remote and coastal seawater samples. Ozone uptake to remote samples ranged from 2.97 to 6.32 $\times 10^{-6}$, with 25.0 to 66.3 $\%$ of uptake attributed to iodide, while for the coastal samples ozone uptake ranged 0.87 to 4.00 $\times 10^{-6}$, with 36.0 to 148.2 $\%$ predicted by iodide. Unsaturated fatty acids were identified as a potential source of reactivity in the remote samples.

This dataset of ozone uptake measurements to authentic seawater samples, with complementary biogeochemical measurements, furthers our understanding of ozone loss from the troposphere by improved knowledge of the drivers of dry deposition to the ocean.

Contents

List of Tables

List of Figures

List of Acronyms

BATS Bermuda Atlantic Time Series

BLEACH Bermuda Boundary Layer Experiment on the Atmospheric Chemistry of Halogens

BPR back pressure regulator

CTD conductivity, temperature, density sensor

CONNECT Pan Atlantic Connectivity of Marine Biogeochemical Processes / Impact of Anthropogenic Pressures

CVAO Cape Verde Atmospheric Observatory

DMS dimethyl sulfide

DOC dissolved organic carbon

DOI dissolved organic iodine

DOM dissolved organic matter

EC eddy covariance

EF enrichment factor

FA fatty acid

GC-MS gas chromatography - mass spectrometry

GFF glass fiber filter

HPLC high performance liquid chromatorgaphy

IC ion chromatography

IQR inter-quartile range

MILAN Sea Surface Microlayer at Night

MRC mass flow controller

NOM natural organic matter

OVOC oxidised volatile organic carbon

PAH polyaromatic hydrocarbon

PFA perfluoroalkoxy alkane plastic

PML Plymouth Marine Laboratories

POC particulate organic carbon

RV research vessel

SML sea surface microlayer

SCCM standard cubic centimetres per minute

SAS surface active substances

SA surface area

SLPM standard litres per minute

SPE solid phase extraction

SST sea surface temperature

TOC total organic carbon

ULW underlying water

VOC volatile organic carbon

YLL years of life lost

WCO Western Channel Observatory

WHO World Health Organisation

Acknowledgements

This project was funded by the European Research Council, Horizon Europe European Research Council (grant no. 833290). My trip to Bermuda was funded by a UK Associates of BIOS internship, courtesy of AXA XL.

I would like to first thank my supervisor, Professor Lucy Carpenter, who it has been a pleasure to work with, and who has provided consistent support and feedback, as well as countless exciting opportunities during the last 3.5 years.

The whole Carpenter group has provided feedback and friendship. I would like to thank Matthew Jones and Rosie Chance for valuable input throughout the project, and Ryan Pound and David Loades, who have offered good humoured advice and encouragement. Special thanks also go to everyone who I have shared and enjoyed field work with; David and Katherine who were wonderful people to complete the CONNECT cruise with, and on the BLEACH campaign, Will, Wes, Lewis, and everyone else in Bermuda with me who made the campaign possible.

My thanks also extend to all the scientists and crew involved in the CONNECT and BLEACH campaigns, as well as all staff and technicians at PML for collecting extraordinary volumes of SML. My thanks to Birgit Quack (GEOMAR), PI of the CONNECT cruise, for allowing reproduction of nutrient data measured on the cruise, Christa Marandino (GEOMAR) for allowing reproduction of DMS data, and Anja Engel (GEOMAR) for the sensor-based cruise data. Furthermore to the team at Arditi, Alexandra Rosa and Claudio Cardoso for being responsible for CTD operations, measurements and data processing. Finally, to Andrew Peters for organising the BLEACH campaign and supporting lab set up and sampling trips in Bermuda.

Lastly to my support network, who this would not have been possible without. I am grateful to my parents for their unwavering support in everything I have done, and to my Luke, who I cannot thank enough.

Authors Declaration

I declare that this thesis is a presentation of original work and I am the sole author. This work has not previously been presented for a degree or other qualification at this University or elsewhere. All sources are acknowledged as references.
Chapter 3 of this work was accepted for publication in Atmospheric Chemistry and Physics. I was the first author on this piece of work.

Brown, L. V., Pound, R. J., Ives, L. S., Jones, M. R., Andrews, S. J., Carpenter, L. J., (2024), Negligible temperature dependence of the ozone-iodide reaction and implications for oceanic emissions of iodine, *Atmospheric Chemistry and Physics*, 24(7), pp. 3905 - 3923. doi:10.5194/acp-24-3905-2024

1 Introduction

1.1 The Sea Surface Microlayer

The sea surface microlayer (SML) is the interfacial layer at the surface of the ocean, which acts as the site of mass and energy transfer between the ocean and the atmosphere, with a depth of between 1 and 1000 μm (Liss and Duce, 1997). The SML has biological and physiological properties which are measurably distinct from the underlying water (ULW) (Cunliffe et al., 2013; Zhang et al., 2003). The SML depth is often operationally defined, depending on the sampling method used. Popular sampling methods include using a membrane filter, the glass screen method and the Garrett screen, in order of increasing sampling depth (Cunliffe and Wurl, 2014). This work utilised the Garrett screen method of collection, as it allowed efficient collection of large sampling volumes. All of these collection methods are labour intensive and time consuming, therefore it would be desirable to parameterise the SML based on properties of the ULW; the sampling of which is more practical.

The SML has been demonstrated to be enriched in several species compared to the ULW, including dissolved organic carbon (DOC) (Reinthaler et al., 2008; Sieburth et al., 1976; Pinxteren et al., 2017; Engel and Galgani, 2016; Zäncker et al., 2017; Stolle et al., 2020; Wurl et al., 2009; Gašparović et al., 2007), amino acids (Zäncker et al., 2017; Engel and Galgani, 2016) , lipids (Frka et al., 2009), and gels (Wurl et al., 2009). These compounds can either be produced *in-situ* by bacteria and phytoplankton, or in the ULW and transported upwards (Gašparović et al., 2007).

The SML is notably enriched in surface active substances (SAS) (Wurl et al., 2009; Gašparović et al., 2007; Frka et al., 2009). These compounds have a hydrophilic and a hydrophobic component, therefore accumulate at phase boundaries, including the SML, and on the surface of bubbles rising through the water column, augmenting accumulation in the SML (Wurl et al., 2009). Examples of SAS in the ocean include proteins, carbohydrates, polysaccharides, hydrocar-

bons, humic substances, fatty acids and lipids (Schmidt and Schneider, 2011).

A schematic of the SML is displayed in Fig. 1. This conceptual image demonstrates the scale of the SML as well as physical processes acting on it, including turbulence, wind and rising bubbles, and some relevant chemical interactions.

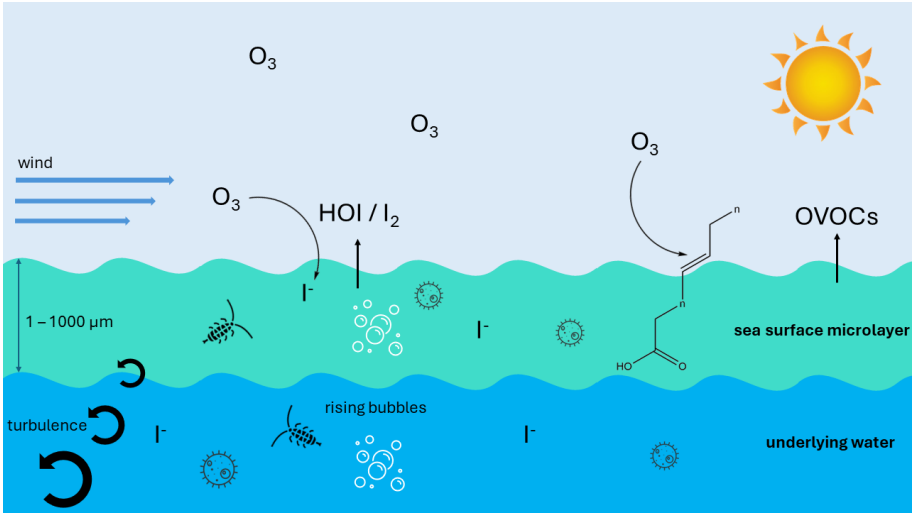

Figure 1: Schematic of the SML.

Studies have demonstrated that the SML persists at high wind speeds, *i.e.* is quite resistant to the effects of turbulence. Enrichment of surface active material in the SML has been measured up to around 10 m s^{-1}) (Wurl et al., 2011; Zäncker et al., 2017; Engel and Galgani, 2016; Pinxteren et al., 2017). For context, the global average wind speed over the ocean is 6.64 m s^{-1} (Archer and Jacobson, 2005).

This persistent, distinct environment facilitates exchange of all gases to and from the ocean. This work is focused on ozone uptake to the ocean, therefore consideration of the SML is vital to ensure findings are applicable to the environment. In this work, ozone uptake was considered to both SML and ULW samples. The differences between the two environments were investigated, and this information was used to gain understanding of the process of ozone deposition to the ocean.

1.2 Ozone in the Atmosphere

Ozone (O_3) is a trace gas, found throughout the atmosphere. It is most concentrated in the stratosphere (Fig. 2), where the ”ozone layer” absorbs UV-C and

UV-B rays. In the stratosphere, ozone protects animal and plant life from damaging ultraviolet radiation, however in the troposphere, ozone exerts a damaging effect.

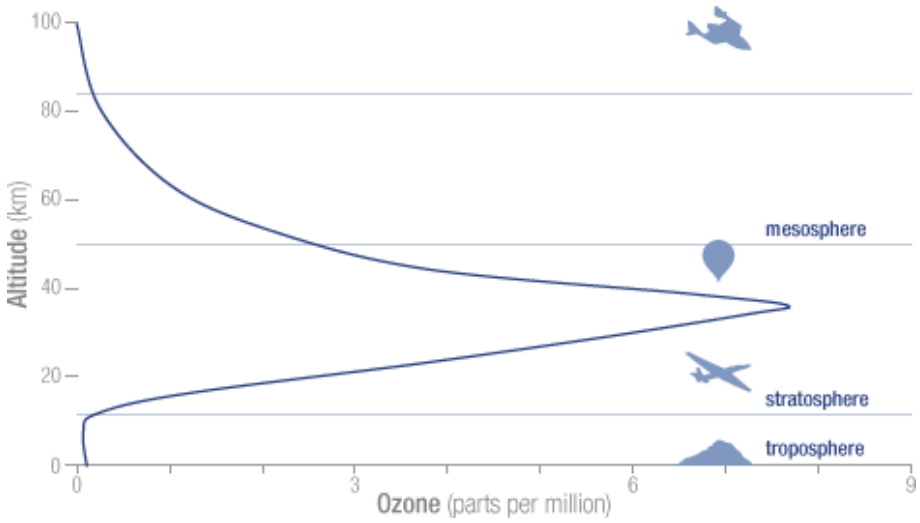

Figure 2: Schematic of the concentration of ozone across the vertical profile of the atmosphere (https://ozonewatch.gsfc.nasa.gov/facts/ last accessed 06/06/2024).

Climate Impacts Ozone is an important tropospheric pollutant and greenhouse gas, with estimated radiative forcing of 0.40 W m^{-2} (reported ranges span 0.20 - 0.65 W m^{-2}) (Watson et al., 1995; Ramaswamy et al., 2001; Forster et al., 2007; Myhre et al., 2013). The warming effect of ozone in the troposphere derives from its absorption of infrared radiation from the Earths surface, which reduces radiative cooling.

Health Impacts Accurate monitoring and prediction of ozone concentrations is also important due to its impact on human health. Acute effects of ozone exposure have been extensively studied, and include gradual decrease in lung function (Kinney et al., 1996), an increase in out-of-hospital cardiac arrests (Zhao et al., 2017a), and increased new-onset asthma in children (Nuvolone et al., 2018). A review of several studies concluded an excess mortality risk of 0.26 % associated with an increase of 5 ppb in the 1-hour daily maximum ozone concentration (Nuvolone et al., 2018). Acute exposure to ozone concentrations in excess of 35 ppb caused 24,000 premature deaths in the 27 EU member states in 2020.

The impacts of long term exposure on human health has been shown to increase risk of respiratory mortality (Jerrett et al., 2009), and pulmonary mortality (Atkin-

son et al., 2016). The European Environment Agency reported years of life lost (YLL), which are years of potential life lost due to premature death. Combined YLLs due to ozone exposure in the 27 countries in the European Union totalled 249,000.

Evidence for health impacts due to ozone exposure mean the World Health Organisation (WHO) recommend exposure to ozone be limited to 60 μg m^{-3}, approximately 30 ppb (as the daily maximum 8-hour mean ozone concentrations). As this is not currently achievable in many parts of the world, interim targets of 100 μg m^{-3} (50 ppb), then 70 μg m^{-3} (35 ppb) are set (WHO, 2021).

Agricultural Impacts Ozone, upon entering the stomata of plants generates further reactive oxygen species which exert oxidative stress on the plant. This reduces photosynthesis, growth and biomass accumulation (Rai and Agrawal, 2012; Ainsworth et al., 2012). The impact of ozone on crops including maize, soybeans, rice and wheat was estimated to correspond to present day global economic losses of $\$14 - \$26$ billion (Dingenen et al., 2009), the impacts of which are mostly felt in countries with little or no ozone mitigation strategies, and which rely heavily on agriculture (i.e. China and India).

The Tropospheric Ozone Burden The tropospheric ozone burden ($\sim$340 Tg) is controlled by a balance of influx from the stratosphere ($\sim$550 Tg (O_3) year^{-1}), chemical production ($\sim$5100 Tg (O_3) year^{-1}), chemical destruction ($\sim$4650 Tg (O_3) year^{-1}), and dry deposition ($\sim$1000 Tg (O_3) year^{-1}) to the Earth's surface (Stevenson et al., 2006). These processed are outlined in Figure 3.

Sources of ozone in the troposphere are influxes from the stratosphere and photochemical production. Ozone is produced in the troposphere as a secondary product following photolysis of NO_2. This involves peroxy radicals, which drive the conversion of NO to NO_2 in the radical propagation cycle. RO_2 are organic peroxy radicals (R = alkyl, aryl or alkenyl group) and HO_2 is the hydroperoxy radical. Peroxy radicals are formed from the oxidation of organic compounds, and typically have an atmospheric lifetime on the order of 1-100 s. Peroxy radicals react with NO, primarily by R1, whereby the alkoxy radical (RO), and and NO_2

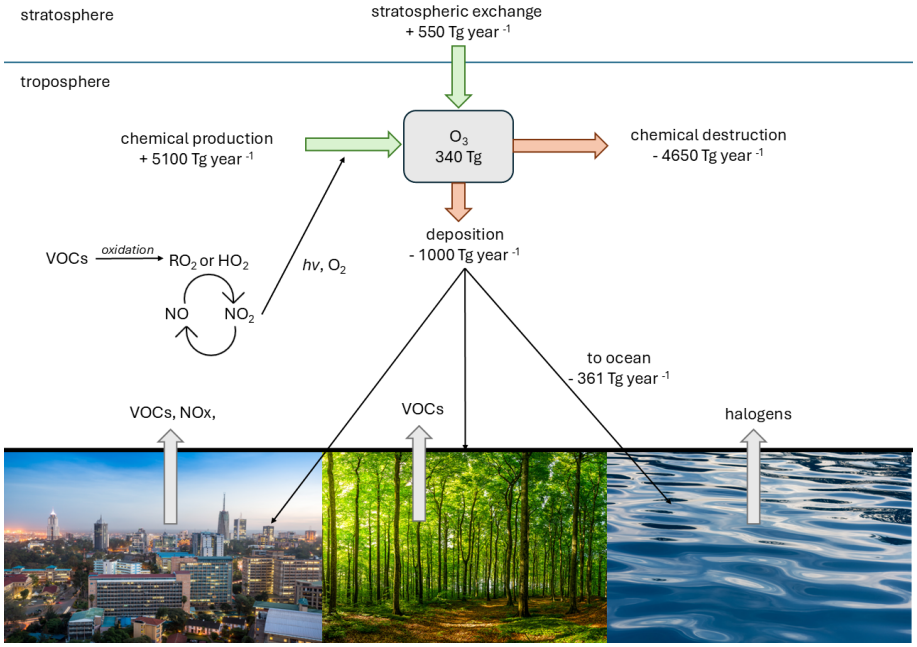

Figure 3: Simplified schematic of the major processes controlling the tropospheric ozone burden. Magnitudes of sources and sinks from Stevenson et al. (2006).

are formed. This route leads to radical propagation, and promotes ozone formation via a chain reaction. A minor reaction pathway, including collision with third-body M, forms the alkyl nitrate ($RONO_2$), and hinders ozone formation (R2). Ozone production by chain reaction occurs via reactions R3 and R4. In this process, NO_2 is photolysed back to NO, with release of triplet oxygen atoms ($O(^3P)$), which reacts with molecular oxygen to form ozone. The chain reaction is NOx catalysed, and converts O_2 to O_3.

$$RO_2 \text{ or } HO_2 + NO \rightarrow NO_2 + RO \text{ or } OH \quad \text{(R1)}$$

$$RO_2 + NO + M \rightarrow RONO_2 + M \quad \text{(R2)}$$

$$NO_2 + h\nu \rightarrow NO + O(^3P) \, (\lambda \leq 400\,nm) \quad \text{(R3)}$$

$$O_2 + O(^3P) + M \rightarrow O_3 + M \quad \text{(R4)}$$

Ozone can be photolysed to the hydroxyl radical, OH.

$$O_3 + h\nu \rightarrow O(^1D) + O_2 \, (\lambda \leq 315\,nm) \quad \text{(R5)}$$

$$O(^1D) + H_2O \rightarrow 2\,OH \quad \text{(R6)}$$

Chain termination in high NO_x conditions leads to nitric acid, $HONO_2$.

$$OH + NO_2 + M \rightarrow HONO_2 + M \quad \text{(R7)}$$

Chain termination in low NO_x environments is driven by H_2O_2 and ROOH formation.

$$HO_2 + O_3 \rightarrow OH + 2\,O_2 \quad \text{(R8)}$$

$$OH + O_3 \rightarrow HO_2 + O_2 \quad \text{(R9)}$$

$$HO_2 + HO_2 \rightarrow H_2O_2 + O_2 \quad \text{(R10)}$$

$$HO_2 + RO_2 \rightarrow ROOH + O_2 \quad \text{(R11)}$$

Ozone is lost from the troposphere primarily via chemical destruction, as described by the above reactions, acting as an oxidant. Photo-cycling of halogen-containing species, released from biological sources in the ocean, and by reaction of ozone with seawater iodide (Carpenter et al., 2013) also leads to efficient ozone destruction over the ocean (Read et al., 2008; Vogt et al., 1999), and in polar regions (Benavent et al., 2022). In this cycle, photochemical transformation of organic halogens and molecular halogens (X_2) produce halogen atoms (X), which react with ozone to form XO (R12). XO can be rapidly photolysed back to X and O atoms, regenerating ozone (R13), or can react with HO_2 or other XO molecules (R14), leading to catalytic ozone loss (Vogt et al., 1999; Simpson et al., 2007).

$$X + O_3 \rightarrow XO + O_2 \quad \text{(R12)}$$

$$XO + h\nu \rightarrow X + O \quad \text{(R13)}$$

$$XO + XO \rightarrow 2\,X + O_2, X_2 + O_2 \quad \text{(R14)}$$

Another significant source of loss of ozone from the troposphere is deposition to surfaces. Deposition to crops and soil occurs with a velocity on the order of

0.1 to 1 cm s^{-1} (Wesely and Hicks, 2000). While ozone deposition to the ocean is considerably slower than deposition to crops and soil, the extensive coverage of Earth's surface by ocean makes it a significant sink of ozone from the troposphere. Dry deposition of ozone to the ocean surface is estimated to contribute approximately a quarter of the total loss of ozone from the atmosphere (Figure 3) and represents the single largest deposition flux of ozone (mean of 361 Tg (O_3) $year^{-1}$, calculated from 15 different models), the second and third largest depositional sinks were grasslands and deciduous trees, respectively (Hardacre et al., 2015).

Despite the importance of oceanic dry deposition for tropospheric ozone concentrations, the process and its drivers are not well understood. Dry deposition to the ocean has the largest uncertainty, compared to deposition to other surfaces. Ozone models typically apply a single global deposition velocity of 0.05 cm s^{-1} to the ocean, despite large variances in measured values, shown in Table 1 (Ganzeveld et al., 2009). The current state-of-the-art in ozone deposition modelling over the ocean included a term for chemical reactivity due to bulk-phase iodide reactions, which improved estimations of deposition velocity compared to measurements (Luhar et al., 2018).

The dry deposition velocity (v_d) of ozone to the ocean has been reported by several authors with highly variable results, but typically of the order of 0.01 - 0.10 cm s^{-1}, as outlined in Table 1. Techniques used to measure deposition velocity have evolved over time, however recently the preference has been for eddy covariance (EC) methods (Gusten and Heinrich, 1996; Burba, 2013), either on a fixed tower (Fig. 4a), or a moving platform such as a ship or aircraft (Table 1). Tower EC measurements typically depict coastal sites, while ship or aircraft based measurements are able to measure more remote sites. EC is a direct micro-meteorological technique which measures the total vertical flux of a gas in the surface boundary layer. Three orthogonal wind velocities are measured with high frequency (e.g. 10 Hz) to model local eddies, and this is combined with simultaneous ozone concentrations to obtain a vertical flux of ozone, where

a positive flux indicates deposition. The benefit of EC measurements are that it allows in-situ observation of the authentic sea surface, therefore does not rely on replication of the sea state in a laboratory.

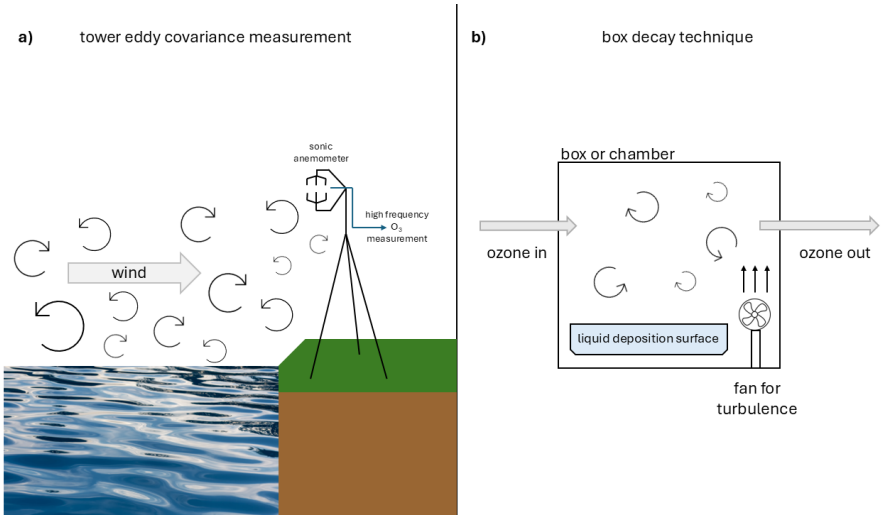

Figure 4: Schematic of a) eddy covariance measurements performed over the ocean from a tower and b) the box decay technique.

More historical measurements were performed in a laboratory, via box decay (Fig. 4b), as described in Garland et al. (1980). Using this technique, the surface in question is held within a box or chamber, and after correcting for background losses to inert surfaces, the rate of loss of ozone within the box is modelled as the destruction rate of ozone by the reactive surface. In these types of techniques, air-side resistances must be accounted for, as they differ from those found in the environment.

Table 1: Previously reported measurements of the dry deposition velocity of ozone over seawater.

v_d (cm s^{-1})		Method	Location	Reference
0.02 - 0.1		Box decay	Southern English Coast	Garland et al. (1980)
0.02 - 0.15		Box decay	South Australia	Galbally and Roy (1980)
0.007 - 0.04		Tower EC	Lake Michigan	Wesely et al. (1981)
0.052, 0.050		Aircraft EC	Gulf of Mexico	Lenschow et al. (1982)
0.057		Aircraft EC	North Pacific	Lenschow et al. (1982)
0.015 - 0.037		Aircraft EC	Eastern North Pacific	Kawa and Jr. (1989)
0.028		Box decay	Southern English Coast	McKay et al. (1992)
0.088		Tower EC	Coastal North Sea	Gallagher et al. (2001)
0.128 (low tide)		Tower EC	Coastal north-west France	Whitehead et al. (2009)
0.0302 (high tide)		Tower EC	Coastal north-west France	Whitehead et al. (2009)
0.025		Tower EC	Mace Head, Ireland	McVeigh et al. (2010)
0.028 - 0.16		Tower EC	Barrow, Alaska	Helmig et al. (2012)
0.017 - 0.065	IQR	Tower EC	Southern English Coast	Loades et al. (2020)
0.007 - 0.058	IQR	Tower EC	Bermuda	Drysdale et al. (2023)
0.012 - 0.034	IQR	Ship EC	North Atlantic	Stapleton et al. (2023)

Studies investigating the drivers of ozone deposition to the ocean have identified iodide to be one of the main drivers (Garland et al., 1980; Chang et al., 2004), however an additional, missing reactive component is often cited, commonly attributed to organic matter (Garland et al., 1980; Shaw and Carpenter, 2013; Martino et al., 2012; Saint, 2019). The contribution of iodide to ozone deposition is not currently well quantified, nor is the identity or significance of the missing reactivity. This is the key motivation for this work.

1.3 The Mechanism of Deposition

Research into the heterogeneous deposition of gas to a liquid surface has been motivated by several key findings in atmospheric chemistry, including the oxidation of SO_2 to form acid rain (Gorham, 1998) and the formation of the Antarctic ozone hole (Jones and Shanklin, 1995). Several terms are used to quantify the uptake of a molecule from the gas phase to the liquid phase.

Deposition velocity is commonly used to quantify the rate of deposition. v_d is defined as the net flux of a molecule to a surface divided by its gaseous concentration, $[X]_{(g)}$ (Eq. 1). In units of cm s^{-1}, this a commonly used quantification of the speed of deposition to a surface.

Another way of quantifying deposition to a surface is the uptake coefficient, γ. This dimensionless coefficient describes the probability of uptake of a gas molecule to the liquid phase, and is normalised to the number of gas-surface collisions (Eq. 2). The number of gas-surface collisions depends on the thermal velocity of the molecule, ω (calculated by Eq. 3), which depends on the Boltzmann constant, k_b in J K^{-1}, the temperature, T, in Kelvin and the mass of the gaseous molecule, m in kg.

$$v_d = \frac{flux}{[X]_{(g)}} = \frac{\omega}{4}\gamma = \frac{1}{r_{tot}} \tag{1}$$

$$number\ of\ gas-surface\ collisions = \frac{[X]_{(g)}\omega}{4} \tag{2}$$

$$\omega = \sqrt{\frac{3k_bT}{m}} \tag{3}$$

To describe all of the processes involved in the deposition of a molecule, a method of analysis has been developed based on resistances to deposition. This simplifies the complex series of processes into individual resistances, analogous to electrical resistors. The total resistance to deposition, r_{tot}, is the combined effect of all processes involved in deposition, and is the inverse of v_d (Eq. 1).

In the simplest depiction of this model, there are three component resistances; r_a, r_b and r_c (Eq. 4). r_a and r_b are air-side resistances which occur in series, where r_a is influenced by factors such as wind speed and aerodynamic roughness (Chang et al., 2004), and r_b is influenced by diffusion across the quasilaminar sub-layer directly above the surface. In this work, r_a and r_b were never considered separately, therefore their combined impact is termed r_{diff} herein (Eq. 5).

r_c is often termed the surface resistance, and encapsulates all processes involved in the transfer of a molecule from the gas phase to the liquid phase. It is controlled by many physical and chemical processes, which were investigated in this work. In this framework, r_c is of the greatest significance when considering chemical controls on deposition of ozone, accounting for $>$90 % of the total observed resistance over marine waters (Lenschow et al., 1982; Kawa and Jr., 1989).

$$r_{tot} = r_a + r_b + r_c \tag{4}$$

$$r_{diff} = r_a + r_b \tag{5}$$

In the resistor model each process resistance (r_x), has a reciprocal conductance (Γ_x), related by Eq. 6. Conductances are normalised to the rate of gas-surface collisions by Eq. 2, therefore are dimensionless. Both terms will be used in this work.

$$r_x = \frac{4}{\omega}\frac{1}{\Gamma_x} \tag{6}$$

In the simplest case, a non-reactive trace gas is transferred to the liquid according to Fig. 5a where uptake is controlled by diffusion through the gas phase, mass

accommodation to the liquid and resistance due to saturation, which all occur in series. This scheme is described in Eq. 7.

$$\frac{1}{\gamma} = \frac{1}{\Gamma_{diff}} + \frac{1}{\alpha_{aq}} + \frac{1}{\Gamma_{sat}} \tag{7}$$

α_{aq} is the mass accommodation coefficient, the probability that a molecule that strikes the liquid surface will enter the bulk liquid phase. $1/\Gamma_{sat}$ is the resistance due to solubility limitation, and accounts for the case where the liquid is saturated with the trace gas, at which point net uptake would become zero. In the case of ozone, solubility is low but reactivity is high, therefore $1/\Gamma_{sat}$ is negligible, and can be removed for simplicity.

Reaction greatly increases ozone uptake to seawater, therefore conductance terms are added to account for reaction both in the bulk and on the surface of liquid surfaces. In the heterogeneous process of gaseous ozone depositing to a liquid there are two possible locations for chemical reaction; the liquid surface, following adsorption of ozone, or in the bulk aqueous phase, following absorption of ozone. This work includes instances where there are only bulk reactions happening, and when there are simultaneous bulk and surface reactions. Each of these scenarios are treated differently.

1.3.1 Bulk Only Reactions

In the case where there is reaction occurring only in the bulk liquid phase, there is a conductance in parallel to α_{aq}, the conductance associated with bulk phase reaction, Γ_{aq}, (Fig. 5b). The resistor model for ozone uptake with a simple bulk phase-only reaction is shown in Eq. 8.

$$\frac{1}{\gamma_{aq}} = \frac{1}{\alpha_{aq}} + \frac{1}{\Gamma_{aq}} \tag{8}$$

Resistance due to bulk aqueous phase reaction with species *i*, r_{aq}, is described in Eq. 9. It is dependent on the second order rate constant for the reaction between ozone and any bulk phase ozone reactive species, i (k_i), as well as the

dimensionless Henry's law coefficient, H, the concentration of species i, [i], and the aqueous diffusivity of ozone, D_{aq}.

$$r_{aq} = \frac{H}{\sqrt{D_{aq} \sum k_i [i]}} \tag{9}$$

1.3.2 Surface Only Reactions

If uptake were occurring only due to surface reactions, the resistor model would occur via Eq. 10 (Fig. 5c). This includes the conductance associated with surface phase reaction, Γ_{surf}, and the surface accommodation coefficient, α_{surf}, the probability that a molecule that strikes the liquid surface will adsorb to the surface. Eq. 11, describes how α_{aq} is related to α_{surf} by the ratio of the rate of desolvation from the surface, k_d to the rate of solvation into the bulk phase, k_{sol} (Davidovits et al., 2006; Ammann et al., 2013). α_{aq} is inherently lower than α_{surf}, due to the possibility of desolvation.

$$\frac{1}{\gamma_{surf}} = \frac{1}{\alpha_{surf}} + \frac{1}{\Gamma_{surf}} \tag{10}$$

$$\frac{1}{\alpha_{aq}} = \frac{1}{\alpha_{surf}} + \frac{1}{\alpha_{surf}} \frac{k_d}{k_{sol}} \tag{11}$$

The concentration of ozone available for reaction with surface active substances is determined by the Langmuir isotherm (Eq. 12), which depends on the near-surface gaseous ozone concentration, $[O_3]_{gs}$, as well as the number of surface sites per area, or $1/\sigma$, where σ is the the cross sectional area of an adsorbed ozone molecule. It also depends on the tendency of an ozone molecule to adsorb on the water surface, which is quantified as the adsorption equilibrium coefficient of ozone, K_{O_3}. Resistance due to surface reactions (with surface species *s*) is calculated by Eq. 13, which includes the second order rate constant for ozone with *s* (k_{O_3-s}), and the concentration of *s* at the surface ($[s]_{int}$), and the concentration of surface-adsorbed ozone, calculated by the Langmuir isotherm.

$$[O_3]_{(surf)} = \frac{K_{O_3}[O_3]_{(gs)}}{\sigma(1 + K_{O_3}[O_3]_{(gs)})} \tag{12}$$

$$\frac{1}{\Gamma_{surf}} = \frac{\omega}{4}\frac{\sigma(1+K_{O_3}[O_3]_{gs})}{k_{O_3-s}[s]_{int}K_{O_3}} \tag{13}$$

1.3.3 Simultaneous Surface and Bulk Reactions

For ozone uptake to seawater, a framework for ozone deposition was used which considered the simultaneous impacts of bulk reaction and surface reaction. This framework was described in detail in Davidovits et al. (2006), Ammann et al. (2013) and Moreno et al. (2018). In the case of simultaneous surface and bulk reactions, Eqs. 8 and 10 combine to give Eq. 14 (fig. 5d).

$$\frac{1}{\gamma} = \frac{1}{\Gamma_{diff}} + \frac{1}{\alpha_{surf}} + \frac{1}{\frac{1}{\frac{k_d}{\alpha_{surf}k_{sol}}+\frac{1}{\Gamma_{aq}}}+\Gamma_{surf}} \tag{14}$$

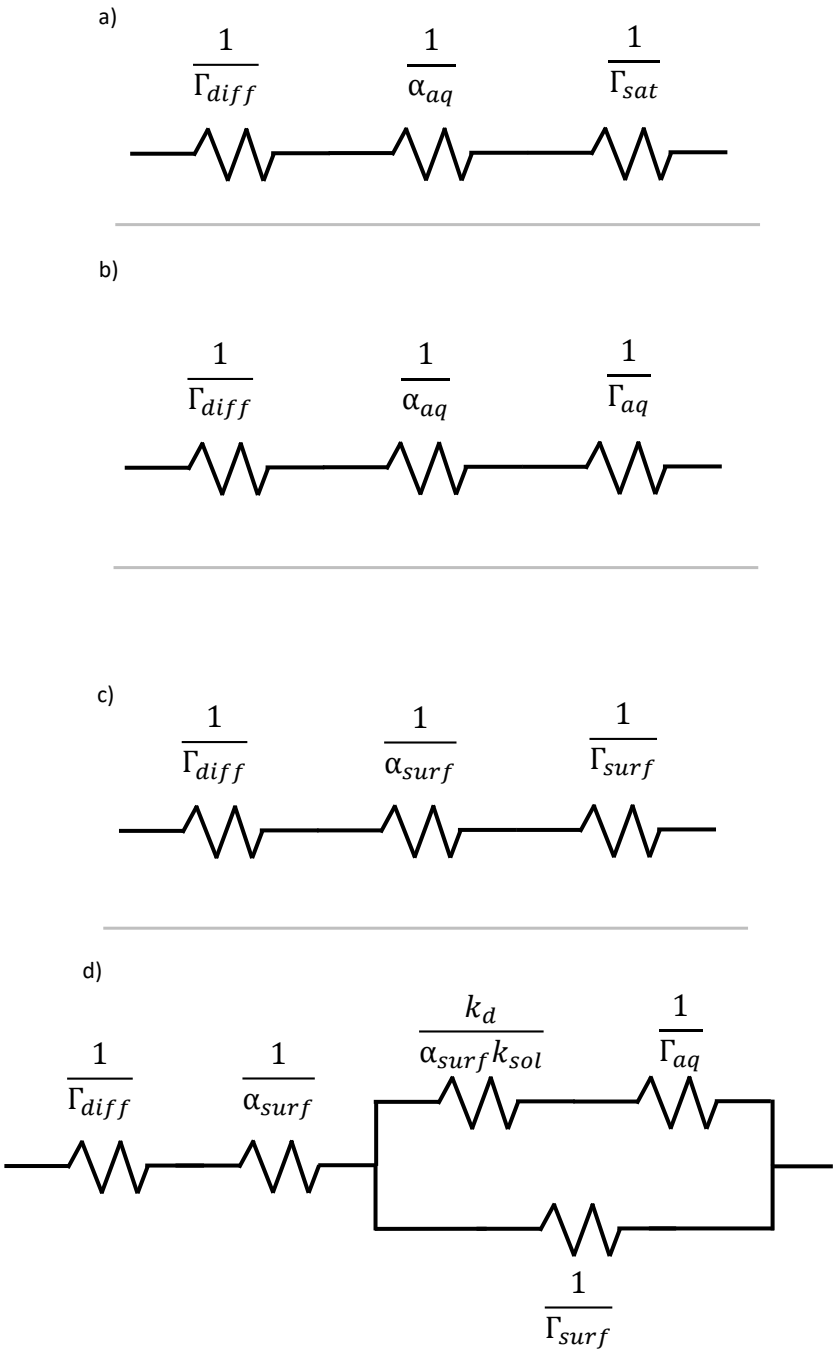

Figure 5: Resistor models for a) deposition of a non-reactive molecule. b) deposition of a molecule which reacts in the bulk phase. c) deposition of a molecule which reacts on the surface of the liquid. d) deposition of a molecule which reacts simultaneously on the surface and in the bulk phase. Zig-zag symbols represent instances of resistance.

1.3.4 Limitations of the Resistor Model

Resistor models provide simple expressions for understanding gas uptake to liquids, however there are some limitations arising from their simplicity. For application of the resistor model, assumptions must be made, including that of steady state conditions, and regarding the location of the model, i.e. whether it is on the surface or in the bulk of the solution, however in reality, heterogeneous reactivity is often far more complex than a binary surface vs bulk scenario. Resistor models are also not well equipped to handle different mixing scenarios; homogeneous mixing is assumed, therefore this must be sought experimentally.

For more detailed analysis of complex reactive scenarios, models have been developed. Multi-layer models numerically solve coupled equations taking into account mass transfer and chemical reactions. These models require detailed knowledge of physical parameters for each species under analysis, and are computationally complex. Additionally, many of the required physical parameters are not well quantified, therefore large uncertainties can arise. An example of one of these models is the KM-SUB model which explicitly calculates all stages of gas uptake from mass accommodation, and resolving concentration gradients within the liquid (Shiraiwa et al., 2010).

In this work the resistor model was deemed sufficient for analysis, as for the reactions in question, it is well established whether they occur in the bulk or the surface of the liquid. Considerations were also made in the experimental design to achieve homogeneous mixing of the solution. Use of multi-layer models would allow further research into combined surface and bulk reactions, and would be especially useful for research into product formation and emissions.

1.4 Aims of This Work

Detailed understanding of the drivers of ozone deposition to the ocean would improve our mechanistic understanding of ozone deposition to the ocean, and in turn the sinks of global tropospheric ozone concentrations; important for air qual-

ity and human health, climate and agriculture.

Introductions to the specific chemical reactions under investigation are given in chapter-specific introductions.

In this thesis, Chapter 2 describes the adaptation of an existing flow reactor method for measurement of ozone uptake, to improve usability and adaptation to field studies.

Chapter 3 describes measurement of the rate of reaction of ozone with iodide, with particular attention to its temperature dependence. The implications of this reaction, in terms of emissions of halogens to the atmosphere, are considered.

Chapter 4 describes measurements of ozone uptake to well-characterised, authentic seawater solutions. The contribution of iodide to uptake is considered, as well as a potential source of ”missing” organic reactivity; unsaturated fatty acids.

A conclusions chapter draws this work together, with consideration of recommended future work.

2 Flow Reactor Method Development

2.1 Abstract

A method was sought to measure ozone uptake to iodide solutions and seawater samples. An existing flow reactor, with a movable injector, was adapted to an improved variable flows method. In this method, the flow rate of ozone-containing gas was varied, giving different reaction times between the gas and the liquid phase. This set up accommodated temperature control, replenishment of the liquid phase, and automated experimental control and logging. Two different sized flow reactors were used, and after characterisation of the diffusive resistance, were utilised in study of ozone uptake to iodide solutions and seawater.

2.2 Introduction

Methods to measure ozone uptake to solution include the box decay technique (Garland et al., 1980), the droplet train technique (Magi et al., 1997), coated wall reactors (Pöschl et al., 1998) and heterogeneous flow reactors (Shaw and Carpenter, 2013).

The droplet train technique generates droplets of the liquid phase using a vibrating orifice generator. The droplets travel through a chamber at a set speed, interacting with the gas in question. Changes in the gas phase are monitored, or the collected droplets are measured. From known factors including droplet surface area and reaction time with the gas phase, uptake can me measured.

Coated wall reactors and heterogeneous flow reactors operate on a similar principal. The area of the liquid surface, either as a trough of liquid, or a coating on a surface, is known and acts as a sink for the reactive gas in question. The reactive gas under study flows through the reactor, and the reaction time between the gas and the liquid surface is controlled, traditionally by changing the injection point of the reactive gas.

For this work, a heterogeneous flow reactor was chosen, for its comparability to

gas deposition over the sea surface. Previous studies using heterogeneous flow reactors have applied ozone over seawater solution in a round flask, however this is not optimal due to the complex gas flow patterns incurred (Fig. 6c). The gas flow is turbulent, and this does not allow accurate calculation of reaction times or gas flow speeds. For accurate kinetic analysis the reaction times between reagents must be accurately known, which is possible with a laminar flow. A laminar flow is a gas flow with a smooth, regular path (Fig. 6a), compared to an unpredictable path (Fig. 6b). It is described by the Reynolds number, Re, calculated by Eq. 15. ρ is the fluid density (of air), Q is the gaseous flow speed, L is the radius of the reactor and μ is the dynamic viscosity of the gas. A low Reynolds number describes a more laminar flow, with Re $<$ 2000 considered laminar. Narrow flow reactors were used in this project to ensure a laminar flow of ozone over the liquid surface.

$$Re = \frac{\rho Q L}{\mu} \tag{15}$$

Also required from the flow reactor was the ability to replenish the liquid phase and temperature control the flow reactor and liquid reservoir. This was to allow study of the temperature dependence of the reaction between ozone and iodide, and to combat chemical depletion in the low concentration iodide solutions required for this study.

The method described in this chapter is a development of an existing set-up, which used a movable injector to alter the reaction time between ozone and a liquid surface. The movable injector method was used in the work of Saint (2019) and described therein. Alterations were made to allow automation of the experimental run, and more comprehensive logging of instrument output and diagnostics.

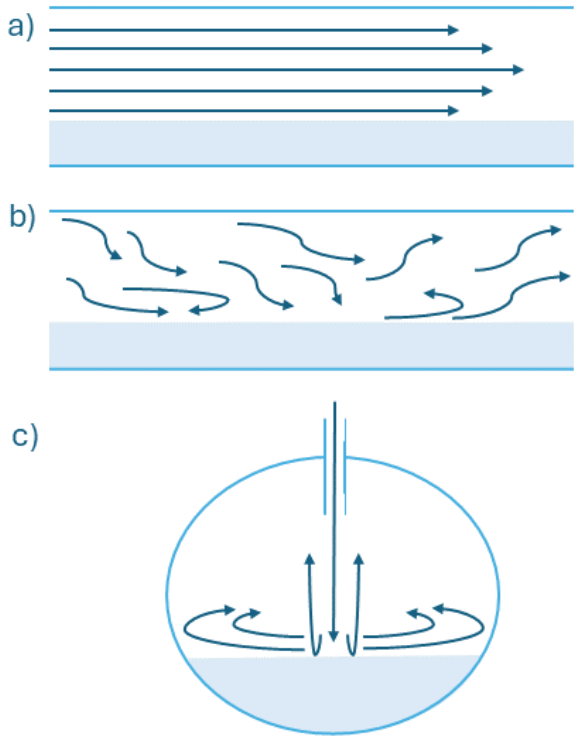

Figure 6: Schematic representations of a) laminar flow of gas in a flow reactor. b) turbulent flow of gas in a flow reactor. c) turbulent flow of gas in a round flask.

2.3 Flow Reactor Development

2.3.1 Ozone Generation and Quantification

Ozone was generated via a Pen-Ray ultra-stable ozone generator (97-0067-02, UVP). This generator applies shortwave UV radiation at 185 nm to convert O_2 to O_3 from lab-generated compressed air. This involves molecular oxygen disassociation, to form atomic oxygen (R15), which can react with molecular oxygen to form excited ozone. The excited ozone is stabilised by collision with body M (R16).

$$O_2 + uv\ (<242\,\mathrm{nm}) \longrightarrow 2\,O(^3P) \qquad \text{(R15)}$$

$$O(^3P) + O_2 + M \longrightarrow O_3* + M \longrightarrow O_3 + M \qquad \text{(R16)}$$

Ozone was quantified by a Thermo 49i UV ozone monitor (specifications provided in Table 2), with quantification via UV absorption at 254 nm. O_3 is quantified by application of the Beer-Lambert law (Eq. 16), where I is the UV light intensity of the sample with O_3, I_0 is the UV light intensity of a sample without O_3 (reference gas), K is the molecular absorption coefficient of O_3, 308 cm $^{-1}$ (at 0 °C and 1 atmosphere), L is the path length (38 cm) and C is O_3 mixing ratio in parts per million (ppm).

$$\frac{I}{I_0} = e^{-KLC} \tag{16}$$

Table 2: Thermo 49i specifications. Precision, zero noise and lower detectable limit are manufacturer provided (Scientific, 2007). Data acquisition period was user-defined.

Characteristic	Specification
sampling volume	1.4 SLPM
precision	1 ppb
zero noise	0.25 ppb
lower detectable limit	0.5 ppb
data acquisition period	4 s

2.3.2 Flow Reactor Design

The flow reactor was a custom made double walled glass tube, with length and diameter to suit the intended use. The double wall design allowed temperature control, via a Grant Optima R3/TX150 recirculating water bath. Dimensions of the two different flow reactors used are shown in Table 3, and schematics of the set-ups are displayed in later sections (Sections 2.3.3 and 2.3.4). For the work on ozone-iodide kinetics, described in chapter 3, the larger flow tube was suitable as it allowed a large range of reaction times. For field work a smaller design was required for integration into an on-ship laboratory. As a consequence, to access similar reaction times dilution of the sample flow was necessary. For all subsequent seawater measurements performed in the lab, the smaller flow reactor was used for comparability to field measurements, and to allow measurements with

smaller volumes of sample.

Table 3: Flow tube design details

	Iodide Kinetics	Seawater Studies
length (cm)	149.4 ± 0.1	78.2 ± 0.1
diameter (cm)	4.04 ± 0.04	3 ± 0.04
total volume (cm^3)	1915.2 ± 40	552.8 ± 20
flow rate range (SCCM)	1200-4500	400-1200
reaction times (s)	19.8-65.0	14.1-77.0

The smaller flow reactor was designed during this project, and work was done to ensure that an appropriate sensitivity was achieved with smaller dimensions. Based on previous work, the anticipated minimum deposition velocity anticipated for measurement was 0.02 cm s^{-1} (Saint, 2019). Different geometries were therefore investigated to ensure this deposition velocity was accessible.

Experimentally, deposition velocity was calculated by measuring ozone as a function of reaction time. Residual ozone was measured after each reaction time; and a mean ozone concentration for each reaction time was obtained ($[O_3]_t$). A plot of $\ln[O_3]$ against reaction time yielded a linear trend, the gradient of which calculated (m). v_d was calculated by Eq. 17, where V is the headspace volume in cm^3 and SA is the liquid surface area in cm^2.

$$v_d = \frac{-mV}{SA} \tag{17}$$

The ideal geometry would have a high surface area and a low headspace, thus maximising the area-to-volume ratio (SA/V). The highest surface area would be achieved with the tube exactly half filled with liquid. Some real-world samples (collected from from the Plymouth Marine Laboratories (PML) - see Chapter 4) were already collected when this design was being considered, with 3 × 0.5 L available from each weekly sampling event. The total volume available per sample was therefore 1.5 L, and this was considered as a constraint on the maximum flow reactor volume (3000 cm^3 total cylindrical volume). This would however not allow for any pumping of the sample.

SA/V is largest at smaller diameters (Fig. 7), therefore a narrow tube was preferable. Small diameters do limit reaction time however, which increases with total volume. Reaction time must be balanced; too small an exposure time limits sensitivity, while too long a reaction time is impractical due to the time taken to stabilise between flow rate steps. For this design, 240 s was chosen as the maximum practical reaction time.

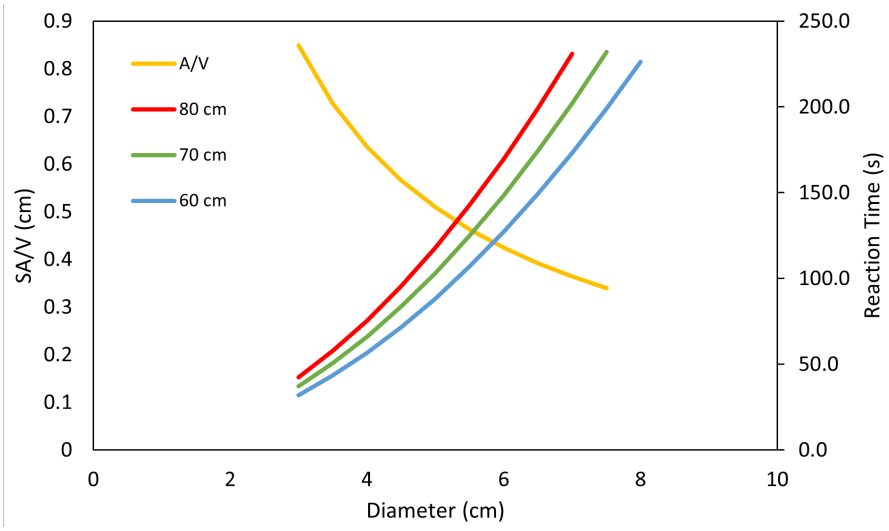

Figure 7: Variation in SA/V ratio (orange line, left y-axis) and maximum reaction time (red, green and blue lines, right y-axis) with flow reactor diameter, for lengths 60, 70 and 80 cm.

The lowest deposition velocity measurable was then estimated by assuming a lowest acceptable decrease in ozone of 2 ppb across the flow tube (in line with the instrument noise/sensitivity, Table 2), at the lowest ozone concentration likely to be used (20 ppb), for each geometry according to Eq. 17. The gradient, m, was therefore estimated using $ln[20ppb] - ln[18ppb]$, and the reaction times calculated in Fig. 7. The deposition velocity lower limits for a variety of diameters of 60, 70 and 80 cm long flow tubes are displayed in Fig. 8, and are all well below the expected minimum deposition velocities. As any of the investigated lengths and diameters would give suitable sensitivity, sample volume was then considered. The water sample was continuously flowed through the flow reactor using a peristaltic pump, to minimise chemical depletion by ozone. The residence time is lowest when the volume held in the reactor is small, therefore keeping liquid volume in the tube low was a priority.

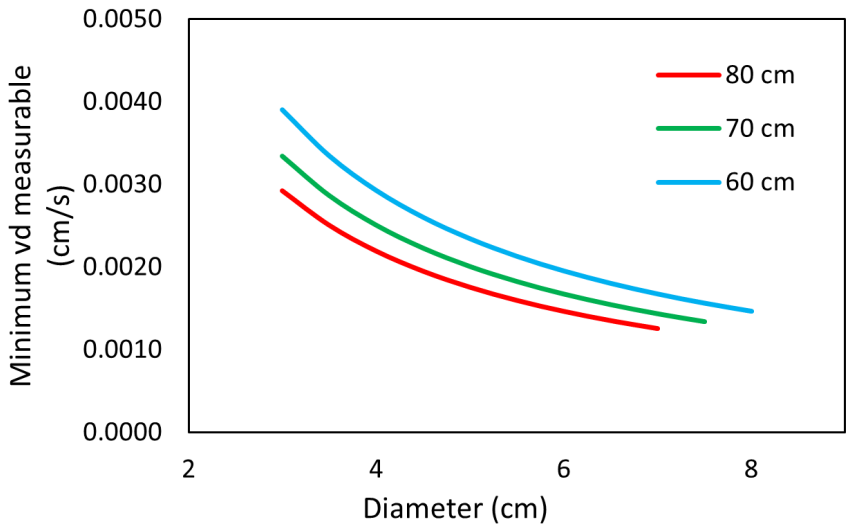

Figure 8: Variation in minimum measurable deposition velocity with flow reactor diameter, for lengths 60, 70 and 80 cm.

Considering all of these points, the optimised dimensions chosen for the main chamber of the new design were $\approx$ 80 cm length, 3 cm diameter. This design maximised the SA/V ratio, and minimised sample volume. The length gave flexibility in accessible reaction times. The minimum deposition velocity measurable was anticipated to be 0.003 cm s^{-1}, below the expected minimum of approx. 0.02 cm s^{-1} by a factor of nearly 10, and requires a maximum of 280 cm^3 of sample (assuming a half-full reactor). The final dimensions of the manufactured flow reactor are given in Table 3.

2.3.3 The Movable Injector Method

The first technique used in this project to measure ozone uptake utilised a movable injector, as described in detail in Saint (2019). This was an established method within the research group, therefore provided a starting point and baseline for method development. This method involved injecting ozone-enriched air at various distances along the flow tube (1.5 m, 4 cm I.D.). There was a constant flow of air along the length of the tube, and the movable injector (1.6 m, 6 mm O.D. glass rod) was inserted to a series of lengths, altering the reaction time between

ozone and the solution (Eq. 18).

$$reaction\ time = \frac{injector\ length}{total\ length} \times \frac{total\ volume}{gas\ flow\ rate} \tag{18}$$

The gas flow regime used for this method was 800 SCCM carrier gas (air) and 800 SCCM ozone-enriched air from the movable injector. Equal parts ozone/carrier gas was previously shown to be the optimal ratio, providing a good balance between minimising retro-diffusion and low aerodynamic resistance (Saint, 2019). Retro-diffusion refers to ozone-enriched air travelling backwards from the injection site, which would disrupt laminarity of the flow. A laminar flow was sought throughout the experiments to ensure accuracy in calculation of reaction time. For flow = 1.6 SLPM, R_e = 60, satisfying the requirement for laminar flow ($R_e <$ 2000).

A schematic of the movable injector method is provided in Fig. 9, and a picture of the set up in Fig. 10.

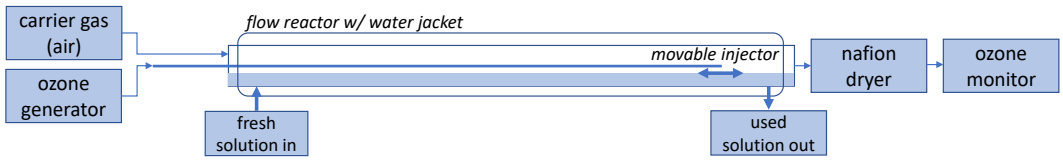

Figure 9: Schematic of movable injector method

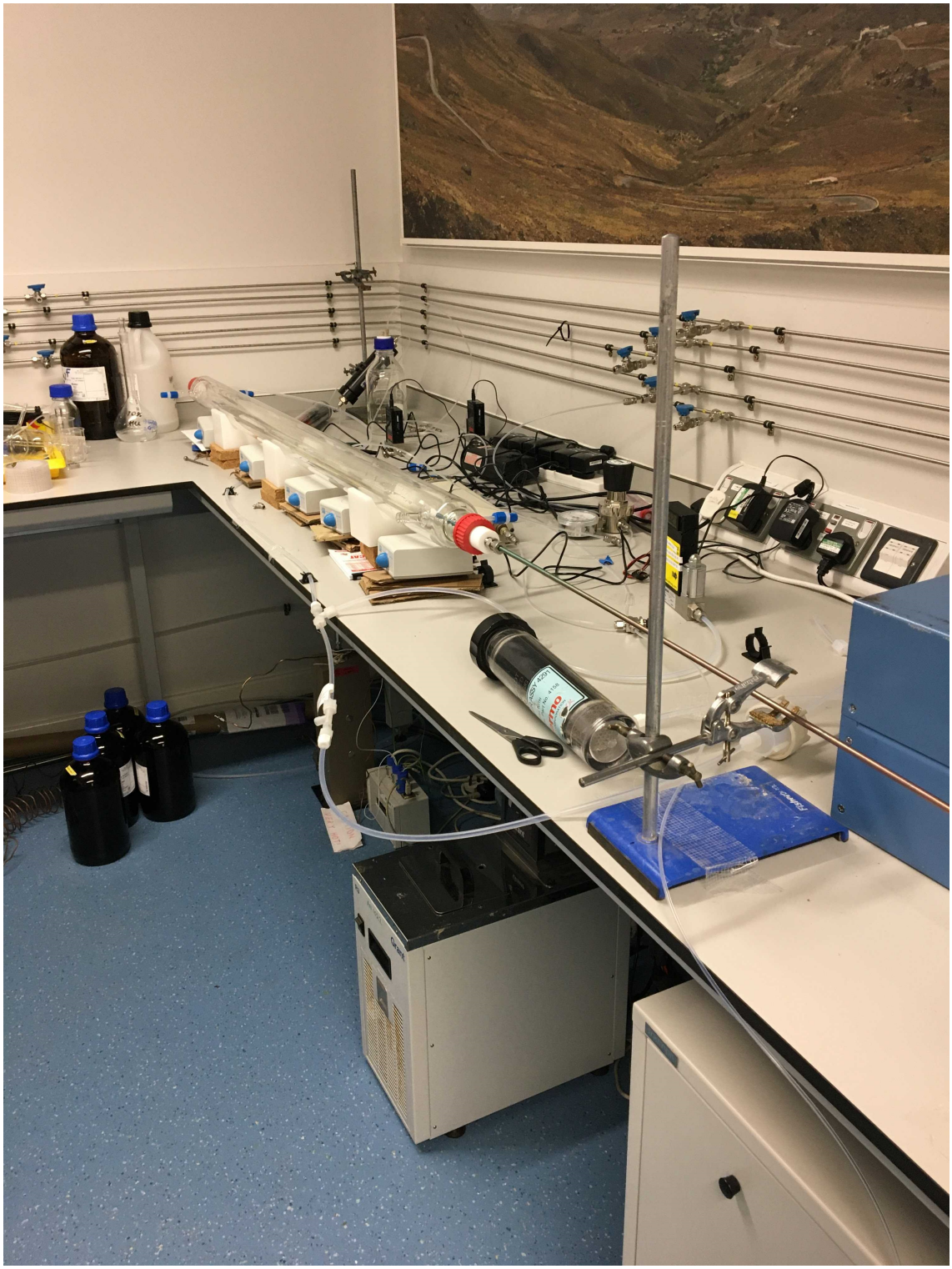

Figure 10: Picture of large flow reactor set up for the movable injector method, with the injector fully extended.

To test the consistency of the gas flow in this method, the ozone output after passing through the empty flow reactor was tested at various lengths, and the results shown in Fig. 11. The concentration obtained was consistent, except at 130 cm exposed length, where less ozone was consistently detected. This could indicate that a stable laminar flow had not developed at this point, and a possible explanation for this is that there could be a localised high pressure near the carrier gas inlet, limiting the flow of ozone into the tube. A different ratio of carrier gas/ozone was also tested (1200 SCCM air/400 SCCM ozone), however a similar trend was observed. As this effect was seen across different days, flow regimes and ozone concentrations it was decided to use 110 cm as the maximum reaction length.

Ozone was generated from compressed air, therefore there may have been some influence from any NOx present interacting with the generated ozone (through photochemical cycles discussed in Section 1.2). This could be tested for by performing future experiments with ozone generated from pure oxygen.

Figure 12 shows an example measurement made using this method. In this graph, x-axis errors are displayed, which are propagated from measurement errors in flow tube geometry, however these are likely to be an underestimation, as errors in reaction length were not quantified. Reaction length was chosen by lining up the end of the movable injector with external markings on the flow reactor, however the effects of refraction (through 2 layers of glass and 1 layer of water) mean human error in this measurement is likely.

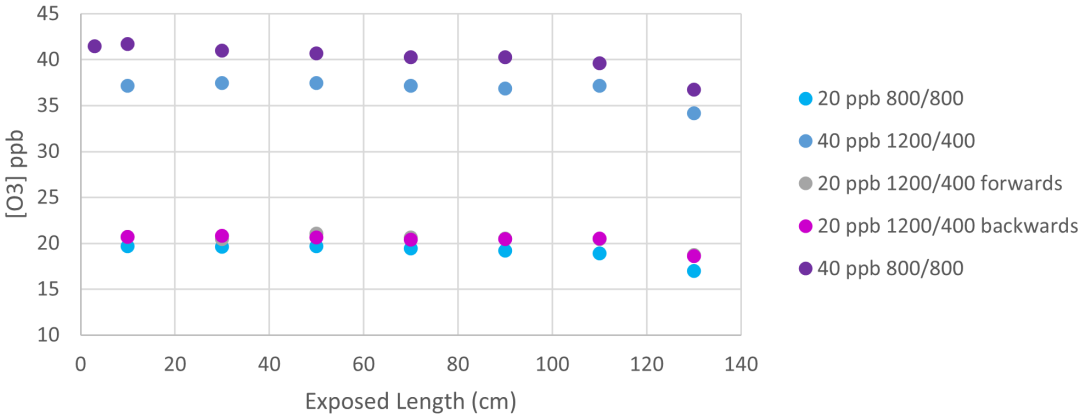

Figure 11: Residual ozone measured after passing through empty flow reactor. Exposed length is equal to the total flow tube length minus the injector length. $[O3]_0$ = 20 or 40 ppb, with different flow rates tested, where e.g. 1200/400 = air flow (SCCM)/ozone flow (SCCM). Forward/backward indicates moving the inlet from long to short exposed lengths and vice versa. Where not indicated, the direction was forwards.

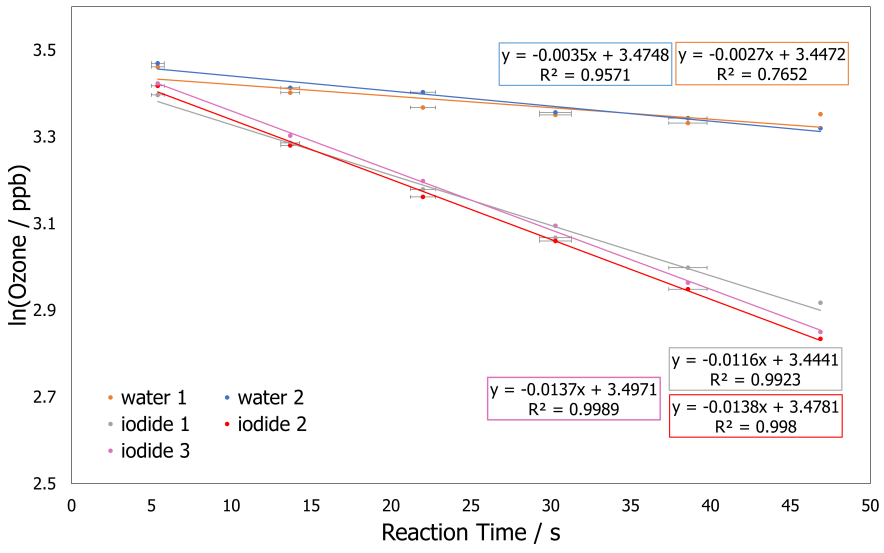

Figure 12: Example experimental output from movable injector method. Experimental conditions: 1 μM iodide in 10 mM phosphate buffer (pH = 8), 40 ppb ozone, T = 19 °C. x-axis error bars display error in reaction time propagated from flow-tube geometry. y-axis errors were calculated as the standard error of the mean of ozone concentration, however are not visible. The error in ln(ozone), propagated from the standard error of the mean, was on the order of 10^{-3}.

2.3.4 The Variable Flows Method

A new method was developed for this work, based conceptually on the movable injector method, however allowing a greater degree of automation. This method is termed the variable flows method herein.

In this method, the flow of ozone-containing air is passed over the liquid sample at varying flow rates, resulting in varying reaction times between O_3 and the liquid surface.

The benefits of this newly developed technique include:

- More compact for deployment on a ship
- The control of flow rates is automated, therefore precise and with a lower possibility of human error. This improves confidence in calculation of reaction times.
- All mass flow rates and pressures of mass flow controllers (MFCs) and back pressure regulators (BPRs) are logged alongside the ozone instrument output, allowing automated data collection and processing.
- Logged instrument parameters are available for troubleshooting.

A schematic of the new variable flow method is shown in Fig. 13. Lab-generated compressed air was passed through a hydrocarbon trap. Part of the flow was passed through an ozone generator. The concentration of ozone generated was dependent on the residence time of the gas within the generator, therefore this flow had to be constant at all times. If required, the ozone-enriched air was diluted with compressed air, to give a total mass flow greater than the fastest flow rate to be used in the experiment. An MFC was used to direct the required mass flow of ozone-enriched air through the flow reactor or bypass line. The gas inlet in the flow reactor was positioned above the liquid level, so the gas was, at all times, passing over the liquid, rather than bubbling through it.

Gas flow surplus to the experimental requirement was removed from the system by a BPR after the ozone generator, which had a vacuum pump providing the

necessary pressure differential. Downstream of the flow reactor, the analytical flow was dried using a Nafion dryer (with lab-generated compressed air providing the dry counter flow), and passed through the ozone monitor. Flow surplus to the analytical requirement was removed by a second BPR, attached to the same vacuum pump. The BPRs were necessary to avoid pressure build up within the sealed system, and the constant pressure in the flow tube meant that reaction times were accurately known. The typical pressure set point for the BPR after the ozone generator was 12 psig, and 15.0 psia for the BPR controlling the flow tube pressure.

The liquid phase was pumped into and drained out of the flowtube continuously, with stirrer bars providing additional mixing. For the larger flow tube 5 stirrer bars were used, equally spaced throughout the tube, and for the smaller flow tube, 3 stirrer bars were used.

Pictures of the experimental set-up are included in Figure 14, and a detailed experimental method is included in Appendix 6.1.1.

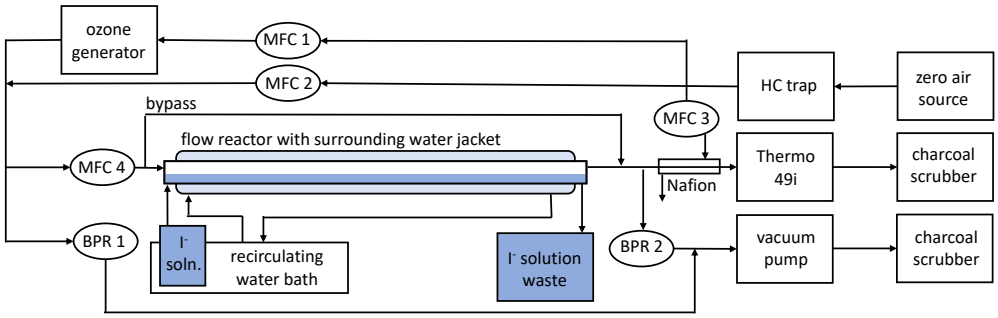

Figure 13: Schematic of the experimental set up for the variable flows method. MFC = mass flow controller, BPR = back pressure regulator.

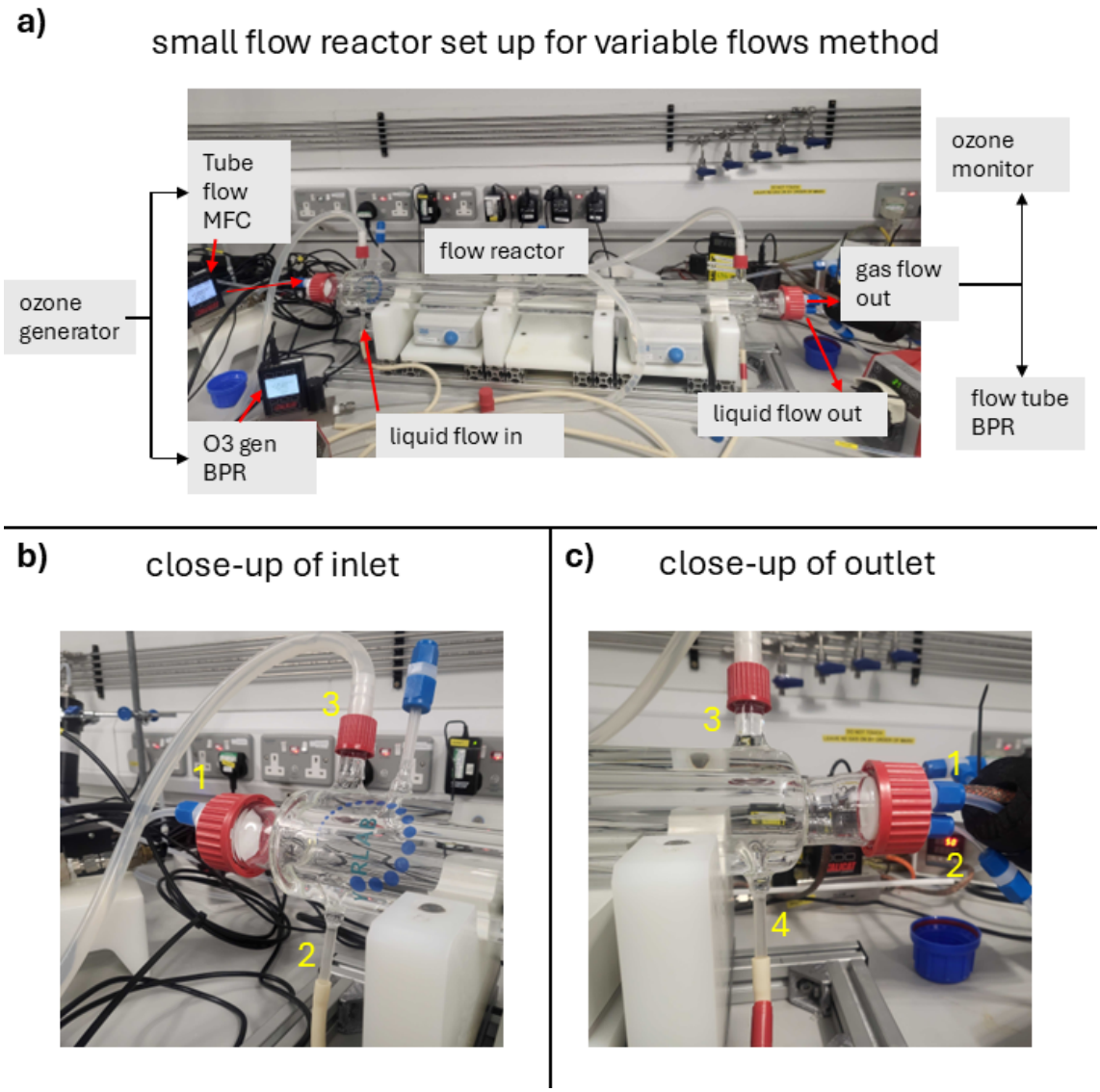

Figure 14: a) Labelled picture of the small flow reactor set up for the variable flows method. 2 stirrer plates are shown (grey boxes with blue dials); during experiments, a third stirrer plate was also present. b) Close up of inlet, with components numbered; 1. gas inlet line 2. liquid inlet line 3. water jacket connection to recirculating water bath. c) Close up of outlet with components numbered 1. gas outlet line 2. liquid outlet line 3. water jacket connection to recirculating water bath 4. additional line used for cleaning, which was not present during experiments (the glass port was capped).

To test that pressure (Fig. 15a) and ozone supply (Fig. 15b) were independent of flow rate, the ozone output after travelling through the empty tube was measured for flows from 1600 SCCM to 9500 SCCM. Despite the large difference in flow rates applied, only a small variation in ozone concentration of a few ppb was observed between the maximum and minimum flow rates, which was consistent over several hours, and could be attributed to wall losses. The small variation in ozone concentration was deemed acceptable, and was accounted for in the experimental blank performed each day. There was a small variation of pressure (approx. 0.5 psi) in the inlet line, however this was unavoidable. The outlet pressure, which was considered the pressure inside the tube, is held constant throughout the experiment. To minimise the difference between inlet and outlet pressure, it was decided to carry out the experiments at 15.0 psi, rather than 14.7 psi, as in Figure 15.

This test granted confidence that changing flow rates downstream of the ozone generator were not influencing residence time within the generator, and hence ozone concentration. It also demonstrated that the pressure in the flow tube was constant, despite changing flow rates, which grants confidence in calculation of reaction times.

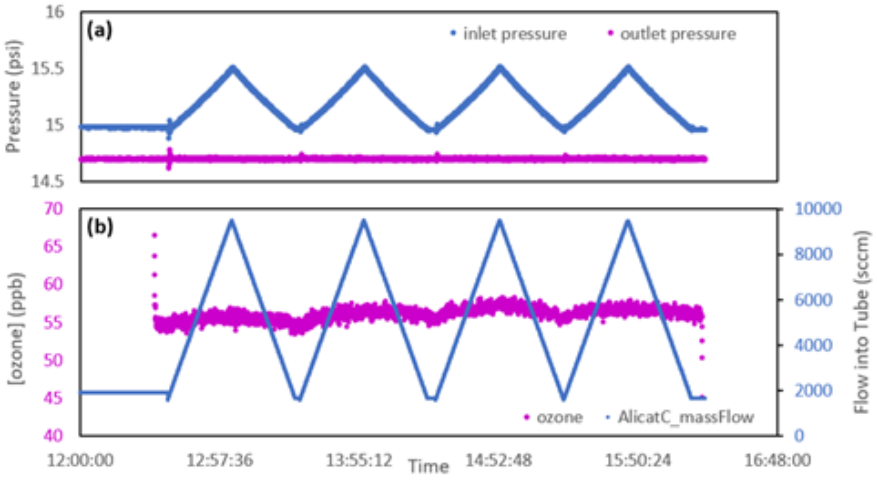

Figure 15: a) pressure in inlet (blue) and outlet (purple) of flow tube during varied flows, b) ozone concentration in ppb (purple, left axis) after variable flow rates (blue, right axis) through the empty flow tube.

The variable flows method was used throughout this work, and for all measure-

ments herein. Example experimental outputs can be seen in Chapter 3, Figures 23 and 24.

2.3.5 Comparison between Movable Injector and Variable Flows Methods

It was sought to confirm that the two methods gave comparable results when measuring ozone uptake over an iodide solution (preparation described in Section 3.4.1.1). As the concept of the measurement was the same, i.e. measurement of the residual ozone after various reaction times between ozone and the solution, it was expected that both methods should give similar results provided all gas flows were behaving as expected. Paired experiments were performed at 21 and 25 °C, over a solution of 5 μM iodide, in 10 mM phosphate (buffered to pH 8) with $[O_3]_0$ = 40 ppb. The experimental output is displayed in Fig 16 and results in Table 4. There is good agreement between results, therefore it was decided to proceed with the variable flows method. Iodide concentrations were not verified during these experiments, so there may have been variation in the iodide concentration in the liquid phase, which could cause variation in ozone uptake.

The variable flow method has a lower risk of human error, as the gas flow rates are computer controlled. In the movable injector method, there was risk of human error in the positioning of the injector. This is potentially seen in the experimental output, as there is some variation from linearity, which could be due to inaccuracies in positioning the injector. Uncertainties in reaction time are displayed in Fig. 16, For the movable injector method, these are propagated from uncertainties in headspace volume (Table 3) and injector position (10 - 130 cm, with an uncertainty applied of $\pm$ 2 cm). For the variable flows method, uncertainties in the reaction time are propagated from errors in the headspace volume (the same as for the movable injector), and from the flow rate (1000 - 3000 $\pm$ 1 SCCM). The uncertainties in reaction time for the variable flows method are approximately half that of the movable injector method.

In calculation of uncertainty of aqueous resistance, in both instances uncertainties were considered from uncertainty in surface area, headspace volume, and

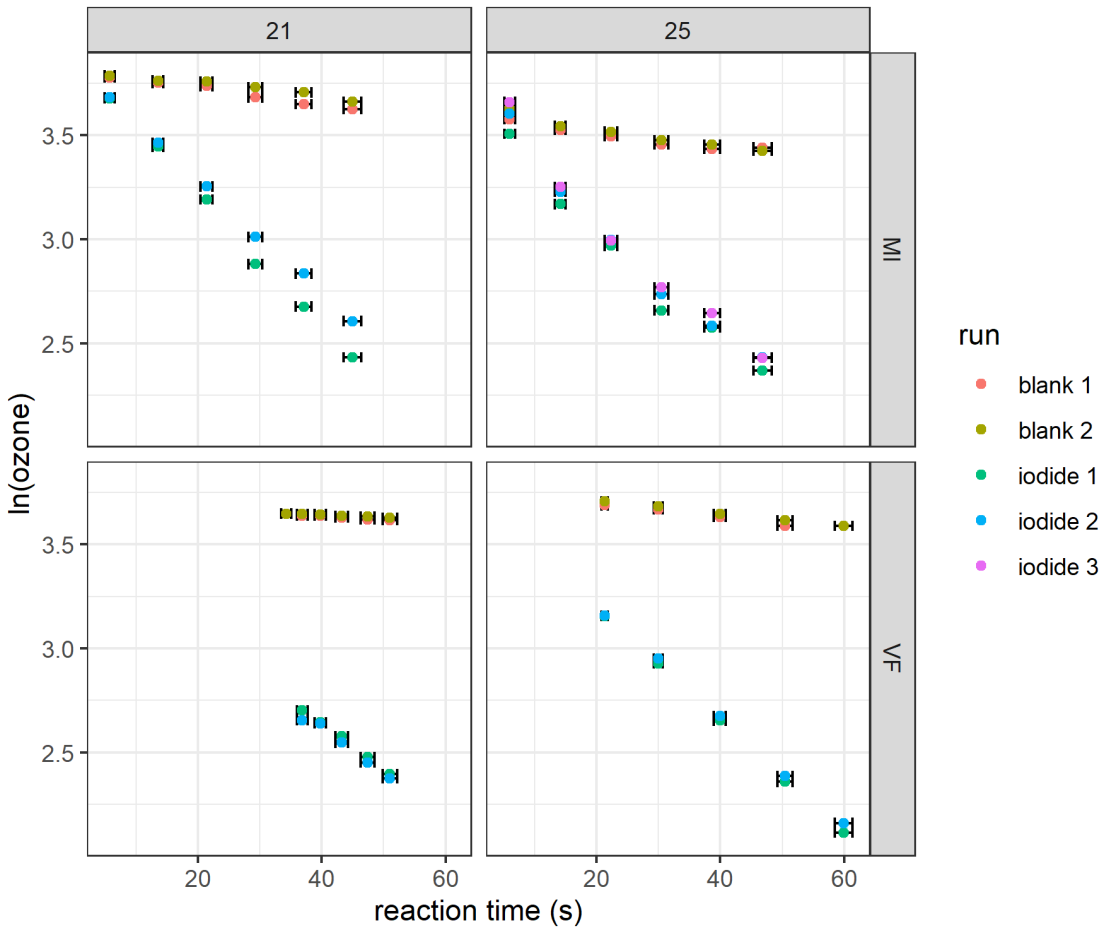

Figure 16: Experimental output for movable injector (MI) and variable flows (VF) methods. Experiments were performed at 21 (left) or 25 (right) °C, over a solution of 5 μM iodide, in 10 mM phosphate (buffered to pH 8) with $[O_3]_0$ = 40 ppb

gradient of ozone change with reaction time (the analytical method is described in detail in Chapter 3). The uncertainty in surface area and headspace volume was the same for both methods. The uncertainty in surface area could be reduced by adapting the apparatus to have a trough of known surface area. This would mean the surface area would not have to be determined by calculation from the liquid volume (Appendix 6.2.2). The main difference between the methods with regards to uncertainty was in reaction time. To test if differences in uncertainty with regards to reaction time had a large impact on slope error, the gradient of ozone change with reaction time for both methods was analysed using a York regression, with consideration of uncertainties in both the x (ln[O3]) and y (reaction time) directions; for the variable flows method, the slope uncertainty was 10.2 and 3.6 % for 21 and 25 °C, respectively, compared to 3.8 and 3.9% for the movable injector method. The variable flows experiment at 21 °C was an early test of this

method, performed over a narrow range of flow rates due to equipment availability at the time, causing a larger uncertainty, not representative of later experiments. The experiment at 25 °C was performed over a range of flows more typical of the work described in this thesis, and had a similar precision compared to the movable injector method. Propagated through to aqueous resistance values, results are displayed in Table 4. The two methods are deemed to be similar in precision, however the variable flows method is still less prone to human error.

Additionally, the data processing for the variable flows method could be more streamlined, and automated by coding in R (Team, 2021). For the movable injector method, because the position of the injector was not logged, it was difficult to automate analysis, therefore data processing had to be performed manually in Excel, and thus had a greater risk of human error.

Table 4: Comparable experiments from variable flows and movable injector methods

Method	Temperature (°C)	r_{aq} (s cm^{-1})
Movable injector	21	9.8 ± 0.8
Variable flows	21	8.7 ± 1.6
Movable injector	25	9.2 ± 0.8
Variable flows	25	8.4 ± 0.7

2.3.6 Background and Blank Measurements

2.3.6.1 Ozone Uptake to Plastic Tubing and Fittings

A first background measurement was taken to evaluate if there was ozone uptake to the tubing (perfluoroalkoxy alkane, PFA) and fittings (PFA and stainless steel), which were used extensively in the setup. To test this, ozone was flowed at the experimental flow rates through the bypass line. It was not possible to calculate the volume of the internal tubing and fittings, therefore reaction times could not be calculated. The ozone concentration as a function of flow rate is displayed in Figure 17.

It was observed that there was a variation of approximately 4 ppb between the highest and the lowest flow rates. This ambient loss will be accounted for in the

blanks performed prior to measurement, whether to the glass surface or to the phosphate buffer.

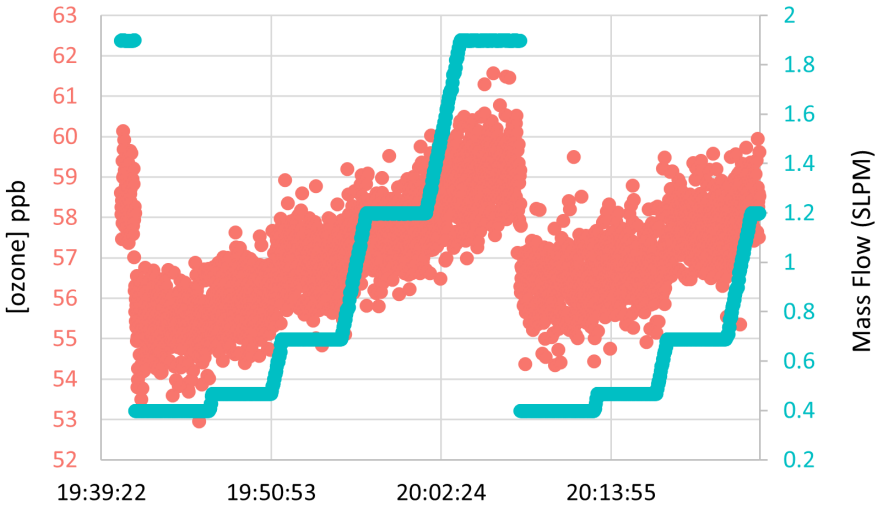

Figure 17: Ozone concentration after various flow rates through the bypass line. The x axis shows the timescale of the experiment.

2.3.6.2 Ozone Uptake to Glass Surface of Flow Reactor

For measurements of ozone uptake to seawater samples, background measurements were performed to determine any uptake to the glass flow reactor surface. The glass surfaces (as well as tubing and fittings) were pre-conditioned with a high concentration of ozone for at least an hour prior to the measurement, or until the measured ozone concentration downstream of the flow reactor was stable for $>$ 15 minutes.

The gradients of the blank measurements over the glass surface are displayed in Figure 18. The mean gradient is -0.0012 s^{-1}, with a standard deviation of 0.0013 s^{-1}. To apply this blank, the glass gradient was then subtracted from the seawater gradient.

2.3.6.3 Ozone Uptake to Phosphate Solution

The third type of blank which was considered was ozone uptake to a phosphate buffer solution (10 mM H_2PO_4, Sigma-Aldrich, with pH adjusted to 8.0 with small additions of NaOH). This blank accounts for uptake to the exposed glass surface, tubing and fittings, and was used for the kinetics work described in Chapter 3. In

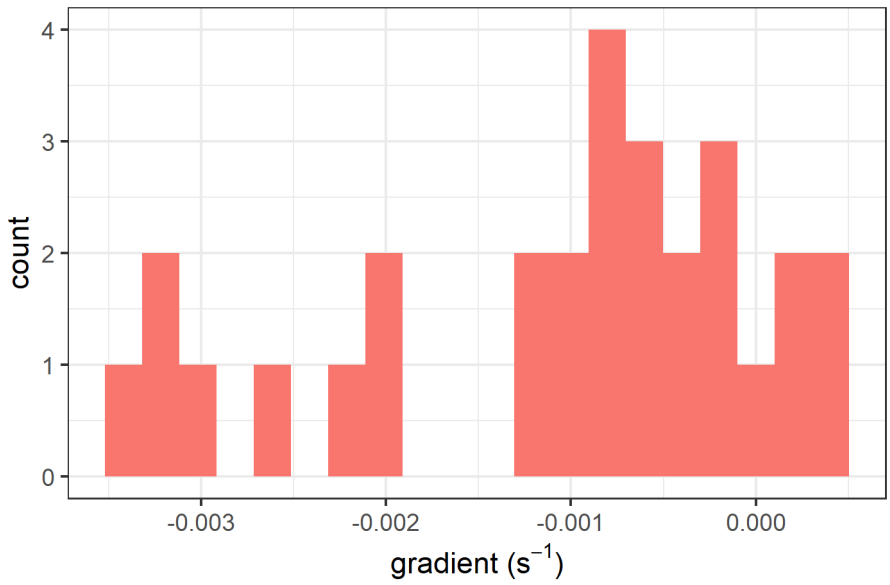

Figure 18: Histogram of gradients of ln[O_3] against reaction time for blank measurements over the glass surface, measured prior to PML samples, reported in Chapter 4.

this work, the phosphate solution was pre-conditioned with a high concentration of ozone for at least one hour to remove ozone-reactive contaminants (or until the downstream ozone measurement was stable, as above), before measurement of ozone uptake to the liquid surface. The same solution was then spiked with iodide, and the uptake re-measured. Further details on this procedure are described in Chapter 3.

Ozone uptake over the phosphate solution was measured prior to each measurement of ozone-iodide kinetics. The gradients of measurements for the blank, compared to the iodide measurements, are shown in Figure 19. The mean gradient is -0.0044 s^{-1}, with a standard deviation of 0.0016 s^{-1}.

The gradient was slightly greater over the phosphate buffer solution than to the glass surface (glass range = -0.0033 s^{-1} to 0.0005 s^{-1}, phosphate buffer range = -0.0068 s^{-1} to -0.001 s^{-1}). While ozone solubility in pure water is low, its uptake could be increased by contaminants in the phosphate or NaOH used to prepare the buffer solution. It was attempted to avoid this by extensive pre-oxidation with ozone, however some increased reactivity proved to be unavoidable. Despite this, it is observed that the blank measurements are distinct from the iodide-containing measurements in all cases.

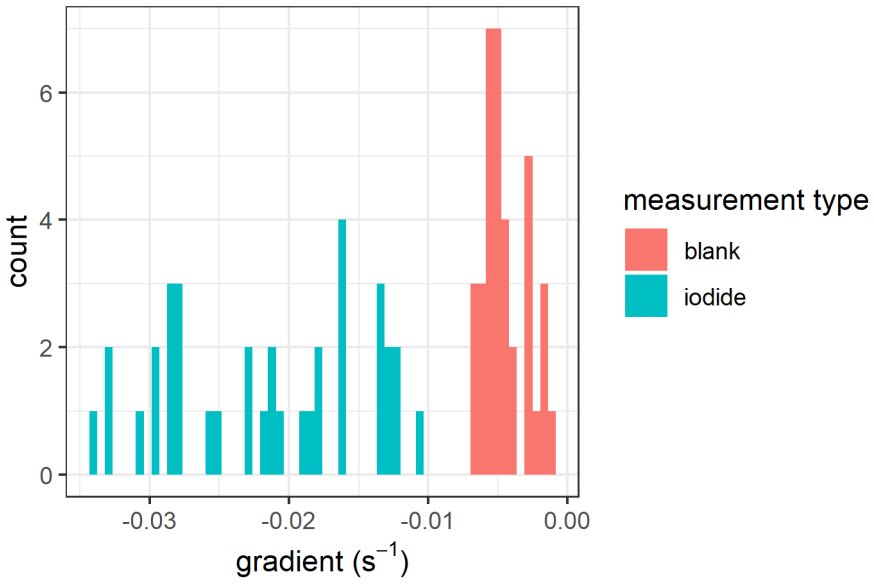

Figure 19: Histogram of gradients of ln[O_3] against reaction time for blank measurements over phosphate buffer (pink) and iodide-containing measurements (turquoise), for work reported in Chapter 3.

2.3.7 Characterisation of Aerodynamic Resistance

It was intended to use the flow reactors to quantify uptake due to chemical reactions in or on the liquid, therefore gas-phase resistances, r_{diff}, were measured for subtraction. In the environment, there is variation in r_{diff}, mostly controlled by wind speed, however in the controlled environment of the flow reactor, these resistances are constant. r_{diff} can therefore be measured and subtracted from r_{tot}, allowing isolation of the chemically-driven uptake for each sample. By measuring ozone uptake over a solution which is very reactive to ozone (*e.g.* 0.02 M iodide), the conductance due to chemical reactions (r_c in Eq. 4) becomes very high, and $r_{tot} \approx r_{diff}$ (Garland et al., 1980). For such high iodide concentrations, iodide was expected to react on the liquid surface (Moreno et al., 2018). In this instance, r_c was represented by $1/\Gamma_{surf}$. Subtraction of r_{diff} from measured r_{tot}, as the inverse of the measured deposition velocity, allows isolation of the resistance to chemically-driven uptake. r_{diff} was calculated separately for both flow reactor sizes.

2.3.7.1 Large Flow Reactor

For [I^-] = 0.02 M, it was confirmed that r_{tot} ($\approx r_{diff}$) was not dependant on ozone concentration. r_{tot} was measured over 6 ozone concentrations, using the larger flow reactor, and experimental measurements are displayed in Fig. 20.

Calculated r_{tot} values are displayed in Fig. 21. There was no statistically significant trend in r_{tot} with applied ozone, it was therefore concluded that r_{diff} is not dependent on ozone concentration. Due to the high uptake over such a high concentration iodide solution, 80 ppb was the lowest applied ozone mixing ratio which gave measurable residual ozone concentrations. The assumption was made that this trend was still valid when extrapolated to the lower ozone mixing ratios used for many of the measurements described in this work (down to 40 ppb).

Similarly, to ensure the contribution from liquid phase reactions were negligible, the same measurement was also repeated over increasing concentrations of iodide, on the understanding that if r_c was truly negligible, increasing the iodide

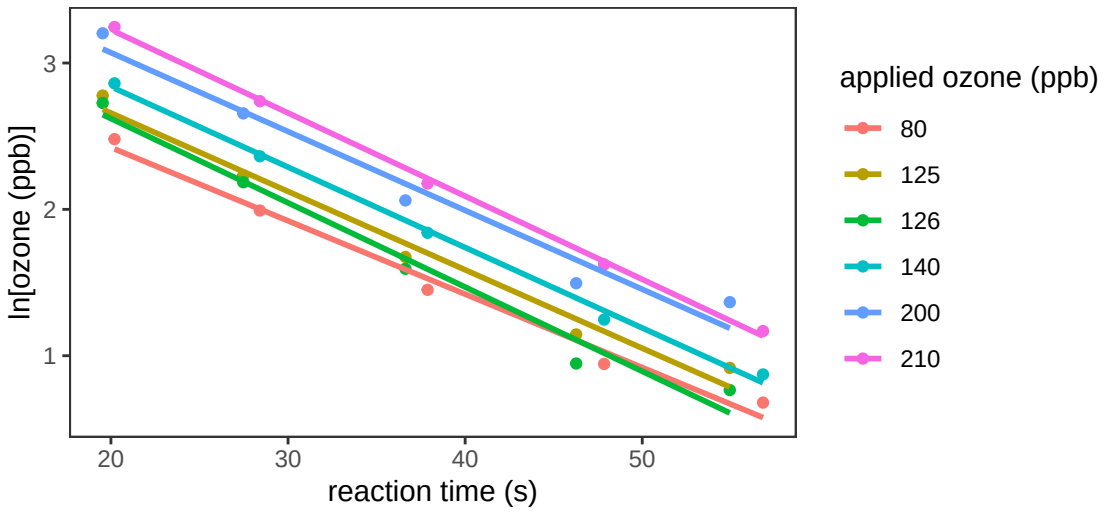

Figure 20: Measured residual ln[ozone] against reaction times for various applied ozone concentrations. [I^-] = 0.02 M, using the large flow reactor.

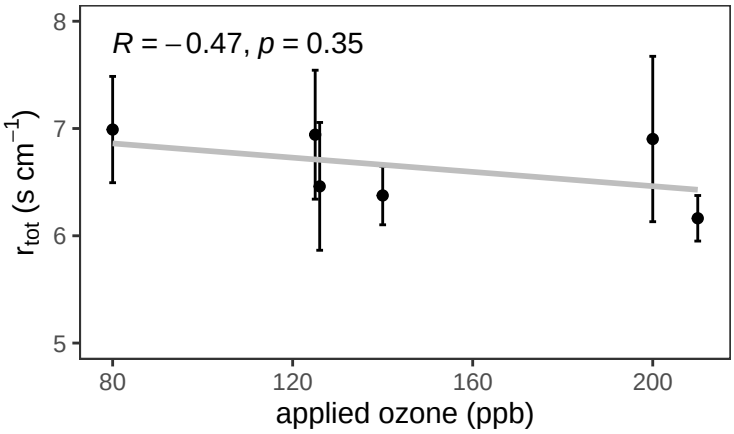

Figure 21: Variation in measured r_{tot} with applied ozone. [I^-] = 0.02 M, large flow reactor.

concentration should not influence r_{tot}. These experiments were carried out with the larger flow reactor, using the movable injector method. Results are displayed in Table 5 and Fig. 22, and do not show a significant trend of decreasing r_{diff} with increasing iodide, indicating that the iodide concentration is sufficiently high at 0.02 M. Values obtained in the iodide concentration study (Table 5) were not included in the average r_{diff} reported below on account of the different methodology used. It is believed that the trend, or lack thereof, is applicable across methodologies.

r_{diff} for the larger flow reactor (used for kinetic studies, Chapter 3) was 6.6 $\pm$ 0.14 s cm^{-1}. This was the mean value obtained in the ozone-dependence series

(Fig. 21), and the reported error is the standard error of the mean.

Table 5: Change in r_{diff} with increasing iodide concentration, at room temperature.

KI (M)	ozone (ppb)	r_{diff} (s cm^{-1})
0.02	173	3.81 $\pm$ 0.44
0.05	449	3.63 $\pm$ 0.35
0.10	446	3.16 $\pm$ 0.36
0.25	472	3.58 $\pm$ 0.29
0.50	466	3.10 $\pm$ 0.44

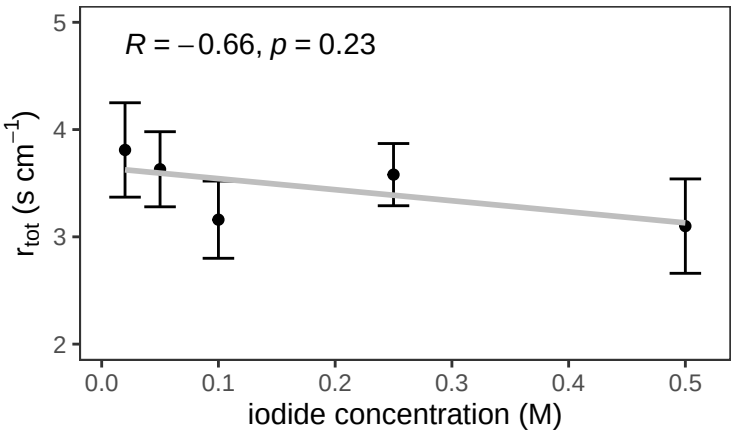

Figure 22: Variation in measured r_{tot} with applied iodide concentration. $[O_3]_0$ outlined in Table 5, experiments carried out in the large flow reactor.

2.3.7.2 Small Flow Reactor

The same measurement was performed for the smaller seawater flow reactor. Over 0.02 M iodide at room temperature, with 430 ppb ozone, three measurements were performed, giving r_{tot} = 4.54, 4.47 and 4.64 s cm^{-1}, with an average of 4.55 $\pm$ 0.05 s cm^{-1}.

2.3.7.3 Estimating Diffusive Resistance from Gas Diffusion

Another method for estimation of r_{diff} in the flow reactor was investigated, accounting for the physical effects of gas diffusion across the laminar flow (Knopf et al., 2015). These corrections account for reductions in the mixing ratio of analyte gas in the bulk gas phase, $[O_3]_g$, at the reactive surface, leading to a near

surface mixing ratio $[O_3]_{gs}$, where $[O_3]_{gs} < [O_3]_g$.

Eq. 19 describes the correction factor, C_{g,O_3}, which is the ratio of near-surface ozone concentrations to bulk ozone concentrations, as well as relating the effective (measured) uptake, γ_{eff,O_3} to the true uptake, γ_{O_3}. γ_{eff,O_3} and associated error are calculated by Eqs. 20 and 21, from the measured deposition velocity, and ω_{O_3}, the thermal velocity of ozone in air, calculated using Eq. 22, where k_B is the Boltzmann constant, *T* is the temperature in Kelvin and *m* is the mass of an ozone molecule.

To calculate γ_{O_3} from γ_{eff,O_3}, Eq. 23 is applied, which uses the Knudsen number, $K_{n_{O_3}}$, and effective Sherwood number N_{Shw}^{eff} to account for effects of gas phase diffusion limitations. Systematic errors in N_{Shw}^{eff} and $K_{n_{O_3}}$ were determined to be negligible, allowing $3/2 N_{Shw}^{eff} \times K_{n_{O_3}}$ to be considered a constant in error analysis, denoted *a* in Eq. 24, from which error in γ_{O_3} was calculated.

The Sherwood number describes the ratio of convective mass transfer to the rate of diffusive mass transport. The effective Sherwood number, N_{Shw}^{eff}, can be approximated by Eq. 25, where A = 0.0978, B = 0.0154 and l* is the dimensionless axial distance calculated by Eq. 26, normalising the axial distance, l (= tube length) using the ratio of D_{g,O_3} to volumetric flow rate, Q. As N_{Shw}^{eff} is dependent on Q, which varies throughout the experiment, it was investigated whether the varying flow rates used in these experiments would require separate treatment in gas phase diffusion corrections. For experimental flow rates of between 1600 – 4500 SCCM, N_{Shw}^{eff} was calculated as 3.73 – 3.86. Due to the small variation in N_{Shw}^{eff}, it was decided to apply the mean value (N_{Shw}^{eff} = 3.78) in all instances to simplify calculations. Error in N_{Shw}^{eff} is reported as half of the range of the 5 possible values corresponding to each experimental flow rate, $\sigma_{N_{Shw}^{eff}}$ = 0.06.

The Knudsen number ($K_{n_{O_3}}$), Eq. 27, is a unitless dimension describing the ratio of the mean free path of a molecule compared to the hydraulic diameter of the flow tube (Eq. 28). The mean free path of an ozone molecule λ_{O_3} was calculated using Eq. 29, where D_{g,O_3} is the gas phase diffusion coefficient. $K_{n_{O_3}}$ for this system was calculated as $\approx$ 6.5 x 10^{-6} ± 1.7 × 10^{-7} (reported error is standard

deviation across all measurement days). $K_{n_{O_3}} << 1$ can indicate the flow could be considered as a continuum, except in situations where the uptake coefficient is low and is of a similar magnitude as $K_{n_{O_3}}$. For all experiments reported herein, γ_{O_3} is of the same order of magnitude as $K_{n_{O_3}}$, therefore gas phase diffusion corrections must be carried out, using Eq. 23.

$$C_{g,O_3} = \frac{[O_3]_{gs}}{[O_3]_g} = \frac{\gamma_{eff,O_3}}{\gamma_{O_3}} \tag{19}$$

$$\gamma_{eff,O_3} = \frac{4v_d}{\omega_{O_3}} \tag{20}$$

$$\sigma_{\gamma_{eff,O_3}} = \frac{4}{\omega_{O_3}} \sqrt{\sigma_{vd}{}^2} \tag{21}$$

$$\omega_{O_3} = \sqrt{\frac{3k_B T}{m}} \tag{22}$$

$$\gamma_{O_3} = \frac{\gamma_{eff,O_3}}{1 - \gamma_{eff,O_3}(\frac{3}{2 \cdot N_{Shw}^{eff} \cdot K_{n_{O_3}}})} \tag{23}$$

$$\sigma_{\gamma_{O_3}} = \sqrt{(\frac{\gamma_{eff,O_3}{}^{-2}}{(\gamma_{eff,O_3}{}^{-1} - a)^2} \cdot \sigma_{\gamma_{eff,O_3}})^2} \tag{24}$$

$$N_{Shw}^{eff} = 3.6568 + \frac{A}{l* + B} \tag{25}$$

$$l* = \frac{\pi D_{g,O_3} l}{2Q} \tag{26}$$

$$K_{n_{O_3}} = \frac{2\lambda_{O_3}}{hydraulic\ diameter} \tag{27}$$

$$hydraulic\ diameter = 4 \times r_h \tag{28}$$

$$\lambda_{O_3} = \frac{3D_{g,O_3}}{\omega_{O_3}} \tag{29}$$

This method was compared against the r_{diff} obtained by direct measurement. For a series of measurements of ozone uptake to iodide solution (experiments described in Chapter 3, which used the large flow reactor), the r_{diff} obtained using the Knopf et al. (2015) method was investigated.

The corrected uptake (γ_{O_3}) was converted to v_d using Eq. 20, and subsequently to a diffusion-corrected r_{tot}. This was subtracted from the measured r_{tot} to obtain the

r_{diff} introduced by this method. The average r_{diff} calculated by this method was 6.25 $\pm$ 1.1 s cm^{-1}, showing good comparability to the air resistance measured for the large flow reactor (6.6 $\pm$ 0.14 s cm^{-1}).

The good comparability between methods granted confidence in the measured r_{diff}, however, there is error introduced due to this method being designed for a perfectly cylindrical flow reactor, when the true headspace is not. This was accounted for by the calculation of the hydraulic diameter, however uncertainly remains.

For simplicity in data processing, and due to the benefit of having a direct r_{diff} measurement, it was decided to proceed with the measured r_{diff} for analysis of iodide kinetics described in Chapter 3, and ozone uptake to seawater in Chapter 4.

2.4 Chapter Conclusion

A flow reactor was developed for measurement of ozone uptake to solution. Based on the movable injector method, the variable flows method was developed whereby the linear flow rate of ozone was changed in a series of steps, allowing a range of reaction times between gas phase ozone and the liquid surface. Functionality was included to allow temperature control and replenishment of the liquid phase. Two different sizes of flow reactor were designed and produced which allow measurement of the kinetics of the reaction between ozone and iodide, and of ozone uptake to seawater. Both methods were characterised in terms of their diffusive resistances and relevant background measurements, allowing isolation of the impact of chemical reaction on ozone uptake.

The variable flows method shall be used throughout this work, with the large flow reactor being used in Chapter 3 for measurement of the kinetics of the reaction between ozone and iodide, and the smaller flow reactor being used for measurement of ozone uptake to seawater samples in Chapter 4.

3 Negligible Temperature Dependence of the Ozone-Iodide Reaction and Implications for Oceanic Emissions of Iodine

3.1 Statement of Authorship

This chapter was published in Atmospheric Chemistry and Physics (Brown et al., 2024). It is presented here with additional clarification at points, and minor alterations to some terminology and symbols, for consistency with other thesis chapters. Contributions from co-authors were as follows;

- Lucy V. Brown carried out laboratory work, analysis of experimental and model output and prepared the paper.
- Ryan J. Pound developed and ran the SML model.
- Lyndsay S. Ives assisted with laboratory work as part of flow reactor training.
- Matthew R. Jones carried out iodide quantification.
- Stephen J. Andrews assisted with development of the laboratory method.
- Lucy J. Carpenter oversaw laboratory and modelling work, and paper preparation.

3.2 Abstract

The reaction between ozone and iodide is one of the main drivers of tropospheric ozone deposition to the ocean, due to the ubiquitous presence of iodide in the ocean surface and its rapid reaction with ozone. Despite the importance of this sea surface reaction for tropospheric ozone deposition, and also as the major source of atmospheric iodine, there is uncertainty in its rate and dependence on aqueous phase temperature. In this work, the kinetics of the heterogeneous second order reaction between ozone and iodide were investigated using conditions

applicable to coupled ocean-atmosphere systems (1×10^{-7} – 1×10^{-5} M [iodide], 40 ppb ozone, 288 – 303 K, 15.0 psi).

Measurement at room temperature (298 K) yielded a second order rate constant of k = 3.8 $\pm$ 1.1 $\times 10^{9}$ M^{-1} s^{-1}. The Arrhenius parameters determined of A = 5.4 ± 23.0 $\times 10^{10}$ M^{-1} s^{-1} and E_a = 7.0 ± 10.5 kJ mol^{-1} show that the reaction has a negligible positive temperature dependence, which could be weakly negative within errors. This is in contrast to a previous study that found a strong positive activation energy and a pre-exponential factor many orders of magnitude greater than determined here.

The re-measured kinetics of ozone and iodide were used to constrain a state-of-the-art sea surface microlayer (SML) model. The model replicated results from a previous laboratory study of the temperature dependence of hypoiodous acid (HOI) and molecular iodine (I_2) emissions from an ozone-oxidised iodide solution. This work has significance for global modelling of dry deposition of ozone to the ocean and the subsequent emissions of iodine-containing species, thus improving understanding of the feedbacks between natural halogens, air quality, and climate change.

3.3 Introduction

As discussed in Chapter 1, oceanic dry deposition is influential in global atmospheric models due to the significant coverage of the Earth by oceans. Despite some varied measurements of the magnitude of of the deposition velocity to the ocean (Table 1), a lack of strong mechanistic understanding and accurate parameterisation methods means global ozone models typically apply a single global deposition velocity of 0.05 cm s^{-1}.

For oceanic dry deposition of ozone, gas transfer is fast but the solubility of ozone is low, therefore deposition is thought to be largely driven by chemical reactions. One of the most significant reactions governing oceanic ozone deposition is its reaction with iodide (R17). This reaction has been hypothesised to proceed via the unstable intermediate $[OOOI]^-$, decaying to products IO^- and O_2. The complex $[OOOI]^-$ is proposed to be short lived, and theoretically could also decompose back to the reactants, however the backwards path is thermodynamically unfavourable, and decomposition to IO^- and O_2 is expected to be the dominant pathway (von Sonntag and von Gunten, 2015; Sakamoto et al., 2009). Several studies have demonstrated that oceanic concentrations of iodide enhance the deposition velocity of ozone (bo Oh et al., 2008; Ganzeveld et al., 2009; Coleman et al., 2010; Sarwar et al., 2016). Sarwar et al. (2016) quantified the effect of iodide in seawater as a 0.023 cm s^{-1} enhancement in ozone deposition velocity (v_d), or an increase in median modelled oceanic v_d over the Northern Hemisphere from 0.007 cm s^{-1} with no explicit chemical effect applied, to 0.030 cm s^{-1} when ozone-iodide interactions are included. Iodide concentrations at the sea surface are positively correlated with temperature (Chance et al., 2014; MacDonald et al., 2014; Sherwen et al., 2019). It should however be noted that at higher temperatures, deposition may become limited by reduced ozone solubility in water, thereby minimising the impact of iodide in tropical and sub-tropical regions (Ganzeveld et al., 2009).

$$O_3 + I^- \rightleftharpoons [OOOI]^- \longrightarrow IO^- + O_2 \qquad \text{(R17)}$$

The mechanism of the ozone-iodide reaction depends upon the surrounding conditions, specifically the concentrations of iodide and ozone, thus experimental studies can potentially differ in their conclusions depending on their choice of these parameters (Moreno et al., 2018). At iodide concentrations below $\sim 10^{-5}$ M, as found in oceanic systems (Chance et al., 2019), the reaction with ozone is thought to occur in the bulk aqueous phase, where ozone is dissolved into solution before reacting. The alternative is surface reactivity following Langmuir-Hinshelwood kinetics, which occurs at higher concentrations of iodide (Moreno et al., 2018; Moreno and Baeza-Romero, 2019). Further, it is known that many other ocean-relevant species, particularly organic compounds, react with ozone via a Langmuir-Hinshelwood mechanism, e.g. chlorophyll-a, polyunsaturated fatty acids such as linoleic acid and oleic acid, and polycyclic aromatic hydrocarbons (PAHs) such as naphthalene, anthracene and pyrene (Mmereki and Donaldson, 2003; Mmereki et al., 2004; Donaldson et al., 2005a; Raja and Valsaraj, 2005; Clifford et al., 2008; Zhou et al., 2014).

To quantify the impact of the ozone-iodide reaction on oceanic dry deposition of ozone, the concentration of iodide [I^-] and second order rate constant for the ozone-iodide reaction, $k_{I^- - O_3}$, must be known. Iodide concentrations in the surface ocean have been measured by several authors, and are typically within the range of 20-200 nM (Souza and Gupta, 1984; Campos et al., 1996, 1999; Chance et al., 2014), with Chance et al. (2014) reporting a median of 74 nM and interquartile range of 27 to 135 nM at the sea surface.

The second order rate constant for the reaction between ozone and iodide, $k_{I^- - O_3}$, has been measured in the past, under a range of conditions (Garland et al., 1980; Hu et al., 1995; Magi et al., 1997; Liu et al., 2001; Rouvière et al., 2010; Shaw and Carpenter, 2013). Published $k_{I^- - O_3}$ values, measured at room temperature, range between $1 - 4 \times 10^9$ M^{-1} s^{-1}. Only one previous study has investigated the temperature dependence of this reaction, obtaining a strong positive dependence with temperature (A = 1.4 × 10^{22} M^{-1} s^{-1} and Ea = 73.08 kJ mol^{-1}, with an estimated error of 40% (Magi et al., 1997)), although this study was carried out under

conditions which could promote surface reactivity. It is important to determine the temperature dependence of this reaction under conditions which favour the bulk reaction. Accurate measurement of the temperature dependence of the ozone-iodide reaction will allow better understanding and prediction of global ozone deposition and iodine-containing emissions.

The reaction between ozone and iodide leads to emissions of hypoiodous acid (HOI) and I_2 according to reactions R18 - R22. Emissions of gaseous iodine have significant impacts on tropospheric ozone. Photolysis of gaseous iodine species produces atomic iodine (I) which is rapidly oxidised to IO by ozone. IO is lost by reaction with HO_2 to re-form HOI. Photocycling of iodine-containing species therefore leads to efficient destruction of ozone in the troposphere (Read et al., 2008; Saiz-Lopez and Glasow, 2012), as well as halogen monoxides directly affecting OH and HO_2 concentrations in the troposphere (Simpson et al., 2007). Furthermore, recent measurements have revealed the presence of iodine in the lower stratosphere, contributing to stratospheric ozone loss, primarily via heterogeneous chemistry occurring on particles (Koenig et al., 2020). Understanding the temperature dependence of the reaction between ozone and iodide is therefore also important for understanding ozone loss in the low temperatures of the stratosphere.

$$\mathrm{IO^- + H^+ \rightleftharpoons HOI} \tag{R18}$$

$$\mathrm{HOI + I^- \longrightarrow HOI_2^-} \tag{R19}$$

$$\mathrm{HOI_2^- + H^+ \longrightarrow I_2 + H_2O} \tag{R20}$$

$$\mathrm{HOI_{(aq)} \rightleftharpoons HOI_{(g)}} \tag{R21}$$

$$\mathrm{I_{2(aq)} \rightleftharpoons I_{2(g)}} \tag{R22}$$

It is clear that knowledge of the kinetics of the reactions of ozone with iodide is essential for understanding reactivity at the sea surface and, in particular, required for accurate modelling of ozone dry deposition to the ocean and subsequent emis-

sions of iodine-containing species. In this chapter, the second order rate constant of the reaction between ozone with iodide and its associated temperature dependence were measured. Our study employed conditions which emulated oceanic reactivity of iodide, i.e. low concentrations of iodide and ozone, to target bulk reactivity. We then use this kinetic knowledge to explore previous lab studies of iodine-containing emissions using a recently developed coupled-chemistry ocean atmosphere exchange model.

3.4 Methods

3.4.1 Experimental Method

Ozone uptake was measured following the method development described in Chapter 2. The large flow reactor was used, with the variable flows technique.

3.4.1.1 Sample Preparation

Ozone was generated by a Pen-Ray ultra-stable ozone generator (97-0067-02, UVP), and the concentration adjusted by moving the lamp jacket. The flow was then diluted by dried, hydrocarbon scrubbed compressed air (lab generated). The ozone concentrations introduced into the flow reactor were measured by bypassing the flow reactor, with detection by a commercial UV photometric ozone analyser (model 49i, Thermo) (Table 2). The primary experimental media was 10 mM phosphoric acid (H_2PO_4 ; Sigma-Aldridge, 98.5 – 101%) in pure water (HPLC grade, Fisher Chemical) at pH 8, attained through small volume additions of 20% NaOH. The primary media was then ozonized to remove ozone-reactive contaminants. After ozonisation and blank measurement, the primary solutions were spiked with an iodide standard (5 mM) to the desired concentration. Potassium iodide (KI; 99% purity, Fluorochem) standards were gravimetrically prepared in, and subsequently diluted by, ultra-pure deionised water (18.2 mΩ).

3.4.1.2 Gas Flow Control

The temperature-controlled kinetic heterogeneous flow reactor outlined in Fig. 13 was used, using variable flow rates of ozone, and hence variable exposure times, over iodide solutions, as described in Section 2.3.4. Hydrocarbon-filtered dry air was separated into three flows; ozonized air controlled by mass flow controller 1 (MFC 1, Alicat, MC-10SLPM-D/CM, CIN), a diluent flow (MFC 2, Alicat, MCP-50SLPM-D/5M) and a third flow diverted to a Nafion dryer (MFC 3, Aalborg, GFC17). The combination of flows from MFC1 and MFC2 enabled the generation of a large total flow of ozone-enriched air with a constant ozone concentration. This ozone enriched air was passed either through the flow reactor or a bypass

line (MFC 4, Alicat, pc-30PSIA-D-PCV65/5P); any excess was removed through a back pressure regulator (BPR 1, Alicat, PCP-100PSIG-D/5P). Downstream of the flow tube the gas was dehumidified using a Nafion dryer (Perma Pure, MD-110-12F-4) and analysed by the ozone monitor ($\sim$ 1.4 SLPM). Gas surplus to the analytical requirement was removed from the system by BPR 2 (15.0 psi), which was a modified MFC (Alicat, MCP-10SLPM-D/CM). This was modified by using absolute pressure as the process variable, and moving the valve downstream of the pressure sensor. The valve action was then inverted, meaning an increase of pressure in the flow reactor would cause an opening of the valve, allowing constant pressure to be maintained. All ozone-containing gas was passed through a charcoal scrubber prior to venting. The ozone monitor was logged using DAQFactory, and all Alicat MFCs and BPRs were controlled and logged with DAQFactory (Azeotech).

3.4.1.3 Temperature and Fluid Control

The flow reactor was temperature controlled by a water jacket, supplied by a recirculating water bath chiller (TX150 and R3, Grant Instruments). The iodide or blank solutions were held within the reservoir of this water bath to equilibrate their temperature. In order to minimise any depletion of iodide from the solution during exposure to ozone, it was continuously pumped into the flow reactor using a peristaltic pump (100 series, Watson Marlow) via chemically resistant flexible tubing (Marprene, Watson Marlow). Once passed through the flow tube, the iodide solution drained into a sealed, pressure equilibrated waste bottle.

To estimate the iodide depletion during the course of the experiment with no replenishment, the rate of loss of iodide, $-d[I-]/dt$, was calculated from the second order rate constant for ozone and iodide and the molar concentrations of iodide and ozone in the reacto-diffusive layer of ozone (Eq. 30). In these calculations $k_{I^- - O_3}$= 1.2 × 10^9 M^{-1} s^{-1} was used (Liu et al., 2001). The reacto-diffusive depth of ozone, δ, is the thickness of the layer in which the ozone-iodide reaction can occur (Davidovits et al., 2006), calculated by Eq. 31. D_{aq} is the molecular diffusivity of ozone in water (1.90 × 10^{-9} M^{-1} s^{-1} at 298 K), calculated using the

temperature-dependent relationship Eq. 32, where T is the temperature in Kelvin (Johnson and Davis, 1996). The reacto-diffusive depth multiplied by the surface area of the liquid gives the liquid volume in the flow reactor in which ozone is available for reaction, V_δ (Eq. 33). Loss of iodide in the reacto-diffusive depth (I^-_{loss}), in moles per second, was calculated by Eq. 34, and total loss of iodide during the total experiment time was calculated by Eq. 35. The potential percent loss of iodide was therefore calculated, relative to the starting iodide concentration ($I^-_{applied}$) by Eq. 36. Where the expected loss of iodide was greater than 10% the solution was pumped through the flow reactor sufficiently fast to give a residence time (Eq. 37) which, when applied in Eqs. 35 and 36 gave a I^- percentage loss of $< 10\%$. Pump rates therefore varied with iodide concentration, however it was verified experimentally that pump rate did not affect deposition velocity within the flow tube.

$$\frac{d[I^-]}{dt} = -k_{I^- - O_3}[O_3][I^-] \tag{30}$$

$$\delta = \sqrt{\frac{D_{aq}}{k_{I^- - O_3}[I^-]}} \tag{31}$$

$$D_{aq} = 1.10 \times 10^{-6} exp(\frac{-1896}{T}) \tag{32}$$

$$V_\delta = \delta \times SA \tag{33}$$

$$I^-_{loss} = \frac{-d[I^-]}{dt} \times V_\delta \tag{34}$$

$$I^-_{loss}\,(absolute) = I^-_{loss} \times total\ experiment\ time \tag{35}$$

$$\%\ loss\ I^- = \frac{I^-\ loss\,(absolute)}{I^-_{applied}} \times 100 \tag{36}$$

$$residence\ time = \frac{liquid\ volume}{pump\ rate} \tag{37}$$

3.4.2 Determining Aqueous Resistance and Ozone Uptake

To measure r_{aq}, ozone-containing gas ($[O_3]_0$ = 40 ppb) was passed over the buffered blank solution or iodide solutions, that were pumped through the reactor

at liquid flow rates of between 9 – 35 ml min^{-1}. Gaseous flow rates were set at 1600, 1900, 2400, 3200 and 4500 SCCM, giving possible ozone-solution reaction times ranging from 20 – 66 s (Eq. 38).

$$reaction\,time = \frac{headspace\,volume}{flow\,rate} \tag{38}$$

The buffered phosphate solution was pre-ozonised by passing a high concentration of ozone (approx. 200 ppb) over the solution in the flow reactor. The total volume of buffer solution required for the experiment was circulated through the reservoir and flow reactor during this time to ensure the entire solution was pre-ozonised. This was continued until a stable ozone concentration was obtained, which typically took around an hour. At this point the glass, tubing, fittings and buffer were considered ”conditioned”. The ozone concentration was lowered to the desired experimental concentration, measured while flowing through the bypass line, which had also been pre-conditioned with ozone. The blank measurement was then carried out over the buffer solution, which was pumping through the flow reactor. Blanks were performed in duplicate or triplicate. Directly following the blank measurement, the solution was spiked with iodide into the reservoir, and the solution mixed and circulated through the flow reactor for approximately 10 minutes to ensure homogeneity. During mixing the ozone was passed through the bypass line to avoid reaction. The iodide measurement was performed directly after mixing, in triplicate. An example experiment output is shown in Fig. 23.

Residual ozone was measured after each reaction time; and a mean ozone concentration for each reaction time was obtained ($[O_3]$). A plot of $\ln[O_3]$ against reaction time (Fig. 24) yielded a linear trend, the gradient of which was calculated for each repeat of both the blank (m_{blank}), and the iodide-containing samples (m_{sample}), which were each averaged. A blank corrected gradient ($m_{corrected}$, Eq. 39) was used to calculate v_d by Eq. 40, where V is the headspace volume and SA is the liquid surface area. (values for all physical constants and meta data provided in Appendix 6.2.1 and calculations described in Appendix 6.2.2). Errors in

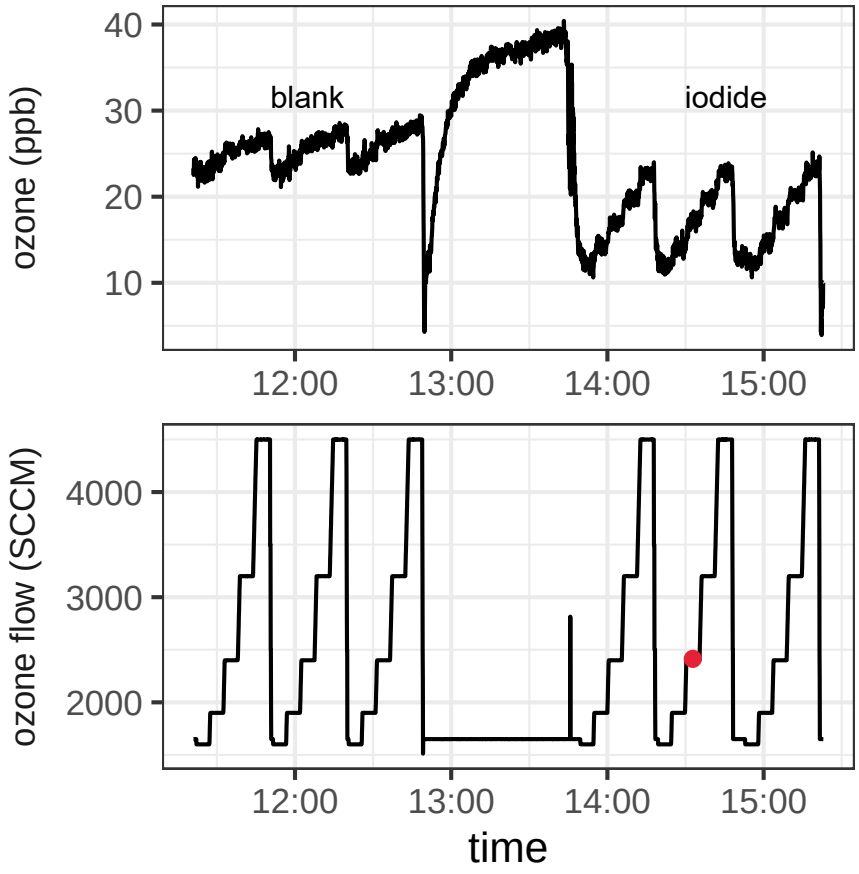

Figure 23: Experimental output for a typical measurement, including residual ozone measured downstream of the flow tube and the concurrent flow rate of ozone over the solution. A blank measurement and the measurement following iodide spiking are shown. The red filled circle indicates the timing of the collection of the iodide "midpoint" sample from the waste stream. Experimental conditions: T = 303 K, [I^-] = 633 nM, phosphate buffer (10 mM, pH = 8), $[O_3]_{starting}$ = 40 ppb.

v_d were propagated from uncertainty in V and SA, as described in Appendix 6.2.2, and from the standard errors of the respective gradients (in this case, m_{sample} and m_{blank}.

Total resistance, r_{tot}, is the inverse of gas-phase corrected v_d, from which r_{aq} can be calculated (Eq. 4). r_{diff} is variable in the environment, but constant in the controlled environment of the flow reactor. Measured over a high iodide concentration (0.02 M), it is assumed that there is negligible liquid-phase resistance, therefore $1/r_{tot} \approx 1/r_{diff}$ (Galbally and Roy, 1980). When measured for this flow reactor, an r_{diff} of 6.6 ± 0.14 s cm^{-1} was obtained (Section 2.3.7). This value was subtracted from total resistance measured for each sample.

$$m_{corrected} = m_{sample} - m_{blank} \tag{39}$$

$$v_d = \frac{-m_{corrected} V}{SA} \tag{40}$$

The relationship between the second order rate constant, $k_{I^- - O_3}$, and r_{aq} was defined by Eq. 9, where H is the temperature-dependent dimensionless Henry's law coefficient of ozone ($H_{gas/aqueous}$ = 3.63 at 298 K), calculated using Eq. 41 (Kosak-Channing and Helz, 1983), T is the solution temperature (K) and μ is the molar ionic strength ($\approx$ molar concentration, at the concentrations used in this work). To apply Eq. 9 to our measurements, for each temperature applied, a plot of $1/r_{aq}$ against $\sqrt{[I-]}$ gave a linear relationship (see Section 3.5.1, Fig. 26), from which the gradient, m, was used to calculate $k_{I^- - O_3}$, according to Eq. 42.

$$lnK_h = -2297T^{-1} + 2.659\mu - 688.0\mu T^{-1} + 12.19 \tag{41}$$

$$k_{I^- - O_3} = \frac{(mH)^2}{D_{aq}} \tag{42}$$

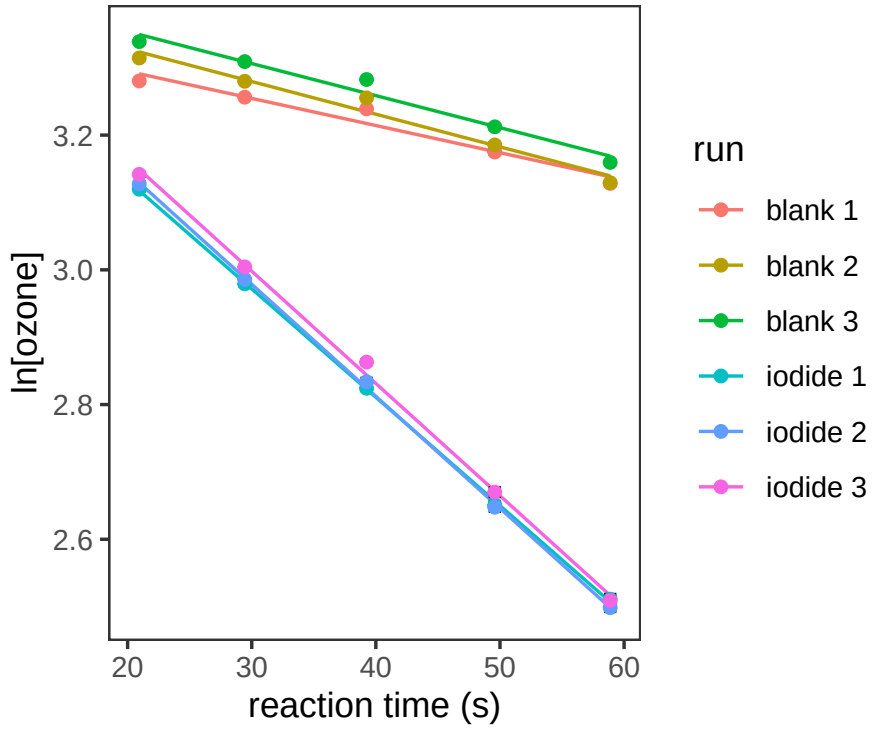

Figure 24: ln[O_3] against reaction time for experimental conditions: T = 303 K, [I^-] = 633 nM, phosphate buffer (10 mM, pH = 8), $[O_3]_0$ = 40 ppb.

3.5 Results and Discussion

3.5.1 Kinetics and temperature dependence of the ozone-iodide reaction

Conditions within the flow reactor were chosen to emulate the remote marine surface ocean and atmospheric boundary layer. The mixing ratio of ozone in air was not expected to affect ozone uptake to iodide solution, as under these conditions a bulk aqueous reaction between ozone and iodide is anticipated, for which a lack of ozone dependence is characteristic. Dependence of uptake on the mixing ratio of ozone would be expected if the reaction proceeded via a surface-mediated Langmuir-Hinshelwood reaction. This is due to surface saturation of ozone at higher mixing ratios limiting potential reactivity on the surface. Therefore, a greater ozone uptake would be expected at lower ozone mixing ratios. Under the conditions of our experiments, there was no significant dependence of deposition velocity on ozone mixing ratio (Fig. 25, p = 0.74), confirming the reaction occurs in the bulk phase under the conditions employed. Despite the lack of dependence of ozone mixing ratio on reactivity, consistent conditions of 40 ppb

ozone were used in each experiment to mimic a typical mixing ratio of ozone in the troposphere (Betancourt et al., 2022). Similarly, although there is evidence that pH has no impact on ozone deposition to iodide solutions (Schneider et al., 2022), the solutions were buffered to pH 8 to mimic typical oceanic alkalinity.

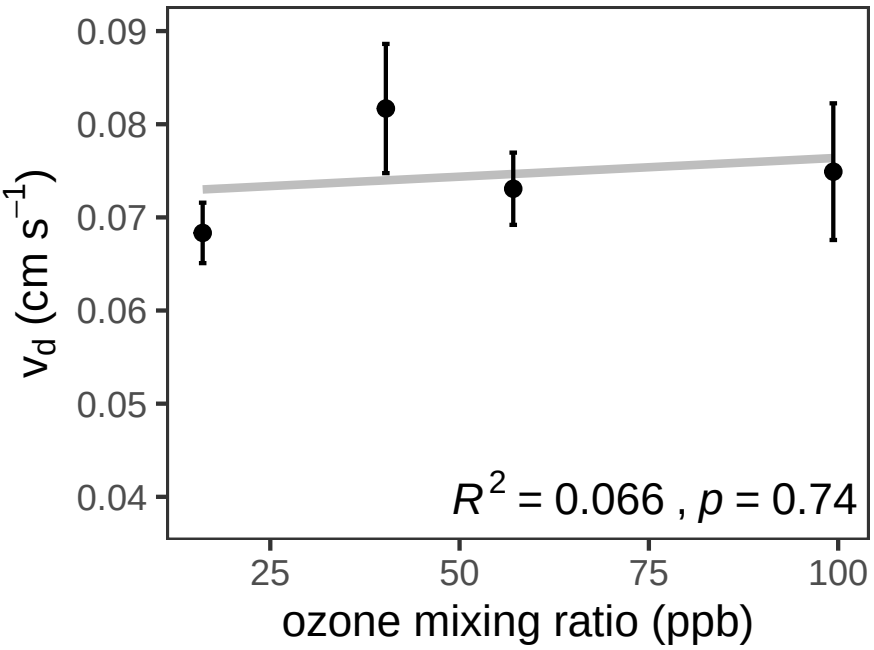

Figure 25: Deposition velocity as a function of ozone mixing ratio over iodide in phosphate buffer (10 mM, pH = 8). Mean [I^-] = 1.79 μM (1.70, 1.73. 1.93, 1.79 μM, from lowest to highest ozone mixing ratio), T = 298 K.

Iodide was the reagent in excess in the pseudo-first order conditions sought for kinetic analysis. At the low iodide concentrations required to emulate marine conditions, iodide was expected to be depleted during the $\sim$90-minute experiment time (Schneider et al., 2020), therefore the liquid phase in the flow reactor was continuously replenished from a reservoir, passing through the flow reactor and out to waste. To verify that the chosen pump rate was sufficient to keep iodide depletion below 10% during the residence time of the liquid in the reactor, liquid samples were collected before and after being exposed to ozone in the flow reactor. The sample after the flow reactor was taken at the mid-point of the experiment (ozone flow rate 3 of 5, during run 2 of 3, indicated by the red diamond on Fig. 23). For all reported experiments, the iodide concentration after the experiment was verified by liquid chromatography. It was confirmed that the concentration during the mid-point of the experiment, taken to represent average iodide loss across all

ozone exposure times, was $<10\%$ different from the starting concentration (Appendix 6.2.3). For all further analysis, the iodide concentrations reported are the mid-point values, rather than the starting values, to best represent the average conditions of the experiments.

The second order rate constant for ozone with iodide was measured for iodide concentrations between 102 nM and 9.88 nM, and water temperatures between 288 and 303 K (Fig. 26). Results were compiled to an Arrhenius plot (Fig. 27), leading to a calculated pre-exponential factor A = 5.4 ± 23.0 × 10^{11} M^{-1} s^{-1} and activation energy, E_a of 7.0 ± 10.5 kJ mol^{-1}. The Pearson correlation coefficient of the Arrhenius plot indicated that the trend was not statistically significant (p = 0.53), therefore the null hypothesis cannot be rejected, i.e. we cannot conclude that the reaction between ozone and iodide is dependent on temperature.

The blank measurement was subtracted from the iodide-containing measurement (Eq. 39), to account for ozone loss to the phosphate buffer, as well as to the glass walls and fittings. It should be noted that if ozone loss during the blank measurement were to be occurring due to reactions outside the iodide-containing reacto-diffusive length, this could cause our measurements to be an under-estimation of the true reaction rate.

Several studies have measured the second order rate constant at around room temperature, as compiled in Table 6. The rate constants obtained from these studies are plotted as a function of temperature in Fig. 28. Based on experimental conditions, and relevance to marine environments, the studies which are most comparable to ours are those which employ iodide concentrations below 10^{-4} M (Moreno et al., 2018); these are Garland et al. (1980); Liu et al. (2001); Shaw and Carpenter (2013). The study by Liu et al. (2001) was carried out with iodide concentrations approaching the upper limit of where aqueous reactivity dominates, but ozone was applied in solution, removing the possibility of surface reactivity. The results of Garland et al. (1980); Liu et al. (2001); Shaw and Carpenter (2013) report a comparable, but slightly lower $k_{I^- - O_3}$ than this work. A possibility for this could be the lack of replenishment of iodide in their studies. Iodide depletion

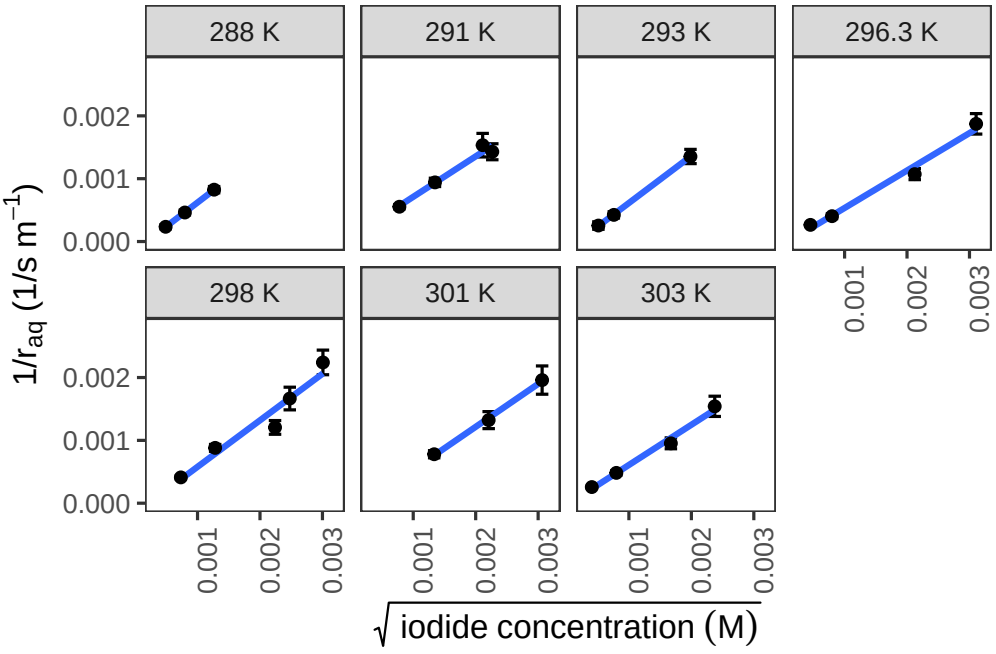

Figure 26: Inverse of r_{aq} calculated for various iodide concentrations (102 nM - 9.88 μM), at temperatures between 288 and 303 K. Measurements were performed in triplicate and error bars were propagated from the r_{diff} error, the standard error in linear fit from experimental output, and the errors in measurements of liquid volume and flow tube dimensions.

could occur within the timeframe of their experiments, which would have resulted in a rate of ozone loss lower than anticipated for their expected iodide concentration. Iodide was not explicitly measured in those studies so any depletion would not be known. For all other reported rate constants, the conditions employed could promote surface reactivity, therefore the measurements are not comparable to the results reported in this work. Additionally, droplet studies (Magi et al., 1997; Hu et al., 1995; Rouvière et al., 2010) have limitations in terms of environmental applicability, for example the diameter of a droplet could be less than the reacto-diffusive length of ozone, and there could be concentration effects of ions on the surface of the droplets (Thomas et al., 2015). For accurate determination of ozone-iodide kinetics with relevance to seawater reactions, experiments with a bulk liquid (Garland et al., 1980; Shaw and Carpenter, 2013) are more appropriate.

There are a range of ionic strengths used in previous literature. High ionic strengths can alter kinetics due to each ion being surrounded by an extended solvation shell, which can screen electrostatic interactions between oppositely charged

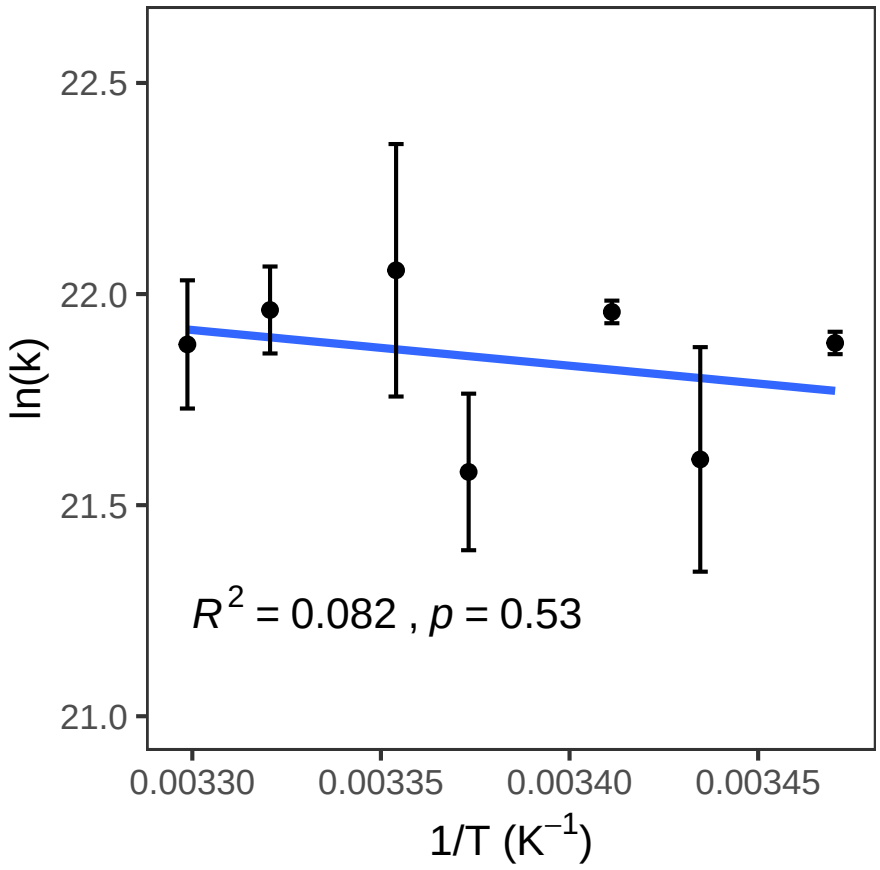

Figure 27: Arrhenius plot for reaction between ozone and iodide, the linear correlation has a p = 0.53 and R^2 = 0.082. Error bars represent the standard error of the linear fit of $1/r_{aq}$ vs [I^-] for each temperature.

species, and increase the reaction rate between equally charged species. For example, in one study, high ionic strengths were found to increase the rate of the of the forward reaction $I^{\cdot} + I^{-} \rightleftharpoons I_2^{\cdot -}$ (Liu et al., 2003). In the same study, the reverse reaction was not strongly influenced by the ionic strength, because it was already at the diffusion-controlled limit. In a study by Schneider et al. (2022), it was determined that ozone loss to KI solutions was not altered by varying pH (between pH 5 and 8, which encompasses all previous literature reports), nor by ionic strength. Experiments were performed in phosphate buffer (0.1 M) with and without NaCl (0.55 M). The increase in ionic strength with NaCl introduced also did not alter ozone loss, therefore it appears the influence of pH and ionic strength cannot explain the discrepancies between literature results.

As demonstrated in the study by Schneider et al. (2022), the high chloride content of seawater appeared not to influence the reaction between ozone and iodide, when it occurs in the liquid bulk, as for seawater. Chloride has however been demonstrated to act as a catalyst for surface-based reactions between halogens and ozone (Moreno and Baeza-Romero, 2019). Supporting the results of Schneider et al. (2022), in real world samples, discussed in detail in Chapter 4, varying salinities were encountered (between 33 and 37 psu, outlined in 68), and no significant trend was observed between ozone uptake and salinity, indicating that the presence of chloride has minimal impact on ozone uptake.

Phosphate buffer is commonly used to control pH in ozone-iodide experiments (in this work, as well as Schneider et al. (2022); Liu et al. (2001); Shaw and Carpenter (2013)). It is however possible that the phosphate buffer reacted with ozone to form hydrogen peroxide (Ferre-Aracil et al., 2015). To investigate whether this potential reactivity altered ozone uptake, experiments should be carried out with different buffer systems, e.g. carbonate, to check whether this alters results. To test for significant reactivity of ozone with the phosphate, the pH could be checked before and after the conditioning step, as well as in the inlet and outlet of the flow reactor, with a change in pH indicating some additional reactivity.

No buffer was used by Magi et al. (1997); Garland et al. (1980); Hu et al. (1995);

Rouvière et al. (2010). The rate constants reported in these studies were in some instances higher (in the study by Hu et al. (1995)), and in some instances lower (in the studies by Magi et al. (1997); Garland et al. (1980); Rouvière et al. (2010)) than the reaction rates presented in this chapter, therefore no clear relationship between absence/presence of buffer and reaction kinetics can be obtained. A future laboratory study could confirm whether buffer effects were influential in the reaction between ozone and iodide.

Table 6: Results and conditions of previous kinetic studies on the reaction between ozone and iodide. "-" denotes condition not reported.

$k_{I^- - O_3}$ ($\times 10^9$ M^{-1} s^{-1})	Conditions T (K)	pH	[I^-]	O_3	Method	Reference
2	298	5.4	0.67 - 6.7 μM	100 ppb	Stopped flow	(Garland et al., 1980)
4	277	-	0.5 - 3 M	7 - 478 ppm*	Droplet train	(Hu et al., 1995)
0.32 - 2.4	275 - 293	-	0.5 - 3 M	-	Droplet train	(Magi et al., 1997)
1.2 ± 0.1	298	6.7	33.4 - 557 μM	27.4 - 40.7 $\mu M_{(aq)}$	Pulse accelerated flow	(Liu et al., 2001)
1.0 ± 0.3	293	-	7.3 M	70 - 300 ppb	Aerosol flow tube	(Rouvière et al., 2010)
1.4 ± 0.2	293	8	10 μM	70 ppb	Heterogeneous flow reactor	(Shaw and Carpenter, 2013)
2.9 – 3.4	288 - 303	8.0	0.1 - 9.88 μM	40 ppb	Heterogeneous flow reactor	This work

*$5 \times 10^{12} - 1 \times 10^{14}$ cm^{-3} ozone reported – converted to ppm (6 – 20 Torr, 277 K)

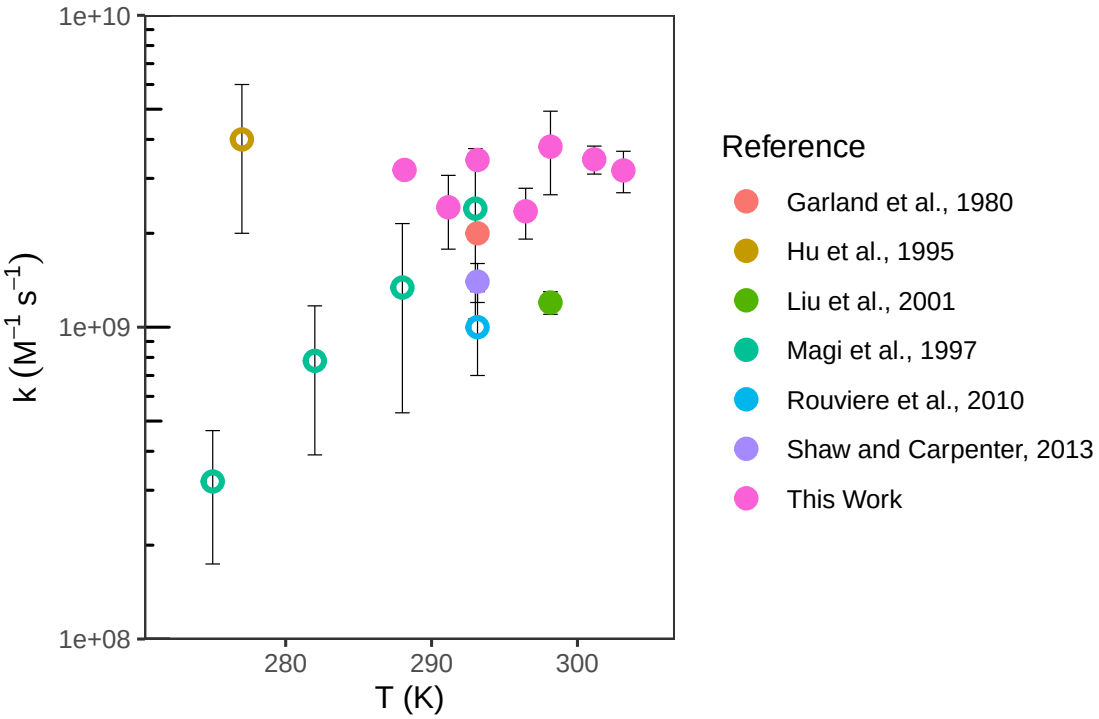

Figure 28: Compilation of literature reported second order rate constants between ozone and iodide as a function of temperature. For Hu et al. (1995), errors were not reported - error bars shown are a lower limit estimate based on statements made in the text. Filled circles indicate experiments performed with environmentally relevant conditions. Empty circles indicate experiments which are not environmentally applicable.

There are reasonably high uncertainties in the measurements reported in this work. Typically the largest uncertainties arose in calculation of $m_{corrected}$, as for the low iodide concentrations used, the gradient of the blank could be as high as 45% (mean 21%) of the gradient of the iodide-containing sample. To ensure environmental applicability, low ozone and iodide concentrations were required for this work, which naturally had higher uncertainty than measurements with higher chemical concentrations. While it was attempted to reduce the blank measurement as much as possible with thorough conditioning and using HPLC-grade water, future work would benefit from finding ways to reduce the blank measurement, i.e. by having less surface area for background ozone deposition.

High uncertainties in calculation of ozone uptake to iodide solutions are not unique to this work. While the errors in the rate constants at each applied temperature in this study compare well to other experiments (as seen in Fig. 28), the errors in the Arrhenius parameters are large - this is due to the trend with temperature having

significant deviations from the line of best fit. It was therefore investigated whether different fitting methods provided different results. In the work presented here, standard linear regression was used, and errors in the fits propagated through calculations. A York regression (York et al., 2004) was tested, which calculates the linear fit with consideration of the exact errors in the x and y values. This was applied to the regressions displayed in Figures 24, 26 and 27, where error in the x-variables were quantified. When the York regression was applied in the analysis, the Arrhenius parameters obtained had a similar magnitudes, but higher uncertainties (A = 7.2 ± 45 × 10^{11} M^{-1} s^{-1} and activation energy, E_a of 2.5 ± 19.1 kJ mol^{-1}) therefore it was decided to use a standard linear regression in analysis. The best way to reduce these errors would be to perform more experiments at each temperature, and to expand the temperature range studied. It was not possible to perform more experiments at each temperature in this work due to time constraints on the equipment, especially regarding it being required for field work. This would constitute valuable future work. The temperature range studied encompassed the sea surface temperatures encountered during the field work performed in this project, however it would be useful to perform these measurements at colder temperatures, especially as this would be useful for ozone uptake analysis in polar and mid latitudes. Issues were encountered in this work at colder temperatures as condensation on the glass walls of the flow reactor proved to be unavoidable, which meant the liquid surface area was unknown. While colder temperature measurements would be useful to reduce the error in the trend and confirm the temperature dependence at low temperatures, the flow reactor setup used in this work is not well suited.

The errors mean that the activation energy obtained in this work could be positive or negative, therefore future work to reduce the uncertainty in the Arrhenius parameters would be useful. However, this work is still valuable for understanding of ozone uptake to seawater as the previously published activation energy is unphysically large at high temperatures, and has been unable to explain trends in emissions (MacDonald et al., 2014). The work presented here demonstrates that

the strong positive activation energy previously obtained could not be reproduced in the current work, and is likely, even within errors, much less strongly positive than previously thought.

Theoretical studies of this reaction have previously been performed. One study simulating the aqueous phase concluded a strong positive activation energy of around 20 kcal mol^{-1}, which corresponds to approx. 84 kJ mol^{-1}, for the formation of intermediate complex $[OOOI]^-$, acting as the rate limiting step (Óscar Gálvez et al., 2016). This was obtained from two solvation models; the polarizable continuum model (PCM, 21.35 kcal mol^{-1}) and the COnductor-like Screening MOdel (COSMO, 20.74 kcal mol^{-1}). A subsequent gas-phase simulation concluded a weaker, but still positive activation energy of 7.5 kcal mol^{-1}, or approx. 32 kJ mol^{-1}, for the same adduct formation (Teiwes et al., 2018). These values are in contradiction with the results of this experimental study, and if the energetic barrier to this reaction is indeed adduct formation, our results indicate this barrier is overestimated by computational studies. Therefore, we propose further work is required to reconcile mechanistic theory with observation.

3.5.2 Application to Previous Laboratory Measurements of Iodine Emissions

A previous laboratory study of inorganic iodine (HOI and I_2) emissions from ozonised iodide solutions (0.1 – 5 μM iodide, 222 – 3600 ppb ozone, temperature 276 – 298 K) yielded effective activation energies of 17 ± 50 kJ mol^{-1} for HOI emission and -7 ± 18 kJ mol^{-1} for I_2 emissions (MacDonald et al., 2014). The emissions of HOI and I_2 depend on several chemical reactions, each with individual dependencies on temperature, and several physical factors including the solubility and diffusivity of ozone. Thus, the temperature dependence can be negative or positive depending on the combination of these factors. The MacDonald et al. (2014) study was carried out in conditions favouring bulk phase reactions between ozone and iodide, making their results experimentally comparable to our work.

When MacDonald et al. (2014) modelled the emissions of HOI and I_2 they demon-

strated that their results could only be accurately replicated when assuming $E_a \sim 0$ kJ mol^{-1} for the ozone-iodide reaction, and not when using the Magi et al. (1997) temperature dependence. The model employed by MacDonald et al. (2014), was the sea surface microlayer (SML) model described by Carpenter et al. (2013) except with the inclusion of temperature-dependent processes. The model with temperature dependence did not account for iodine depletion following its fast reaction with ozone and did not account for iodide replenishment from the waters below (Schneider et al., 2020). To evaluate whether the rate coefficient obtained in our experimental work is consistent with the measured temperature-dependence of fluxes of gaseous iodine compounds from iodide solution under ozone, we applied our data to an updated SML model (Pound et al., 2023). The updated SML model (details in Appendix 6.2.4) includes the mixing of iodide between the SML and underlying water and simulates surface iodide depletion, especially at low wind speeds/reduced turbulence. The depth of the SML in this model is defined as the reacto-diffusive length of ozone, which is unique to each combination of conditions.

The SML model was constrained to the range of conditions reported by MacDonald et al. (2014). The effective activation energy was calculated ($E_a = -gradient \times R$) from an Arrhenius type plot of the natural log of the calculated emissions of HOI and I_2 (in units of molecules cm^{-2} s^{-1}) against the inverse of the temperature (in K). It was not possible to accurately calculate an equivalent wind speed for the MacDonald laboratory experiments, therefore two low wind speeds (0.005 and 0.03 m s^{-1}) were assumed. When assessing the impact of different wind speeds, we applied conditions of 1500 ppb ozone and 2.5 μM iodide.

The HOI and I_2 emissions obtained from the updated SML model are displayed as an effective Arrhenius plot in Fig. 29. The modelled emissions indicate there is a dependence of the effective activation energy on the "wind speed" of the experiments for I_2 emissions. At the higher wind speed, the model overestimates the activation energy, outside the error range of the experimental measurements. The lower wind speed predicts an E_a within the experimental error range. For HOI

emissions, a slightly negative E_a is predicted by the model, which lies within the experimental error range quoted by MacDonald et al. (2014), and does not show a dependence on wind speed.

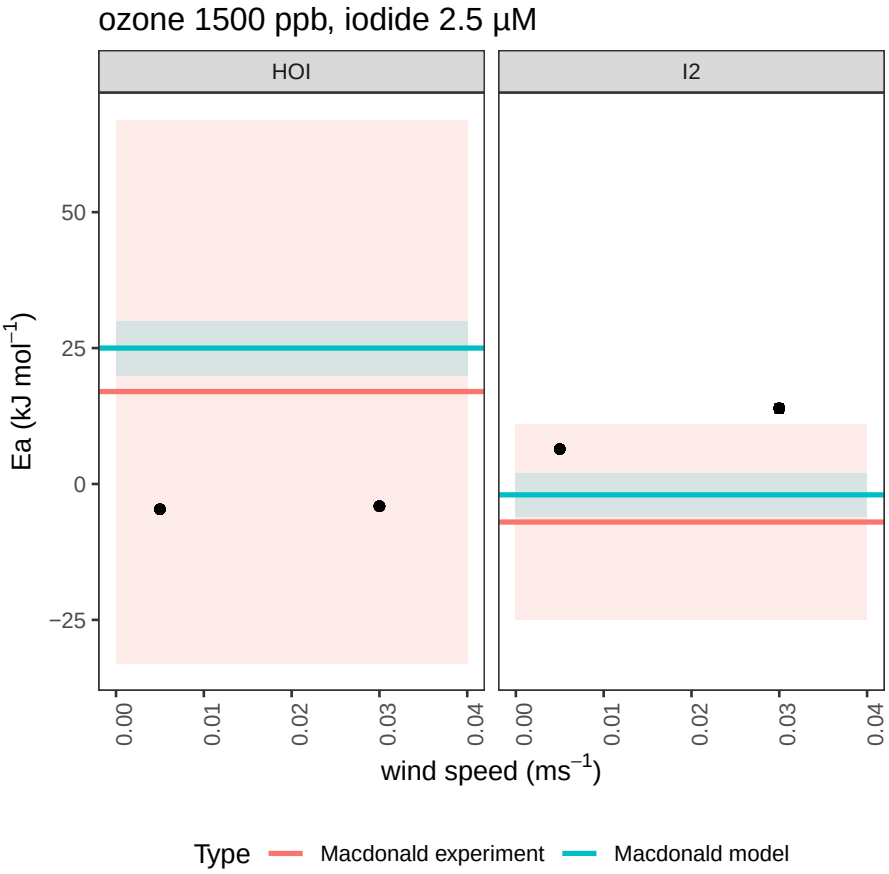

Figure 29: Effective activation energies for emissions of HOI and I_2 from ozone oxidation (1500 ppb) of iodide solution (2.5 μM) as a function of wind speed. Points show modelled emissions using the SML model (Pound et al., 2023)) while red and blue horizontal lines show experimental and modelled emissions respectively, from MacDonald et al. (2014). Errors are shown by shaded areas, and reflect standard error in the linear fit from modelled output.

Knowing that there is negligible temperature dependence on the reaction between iodine and ozone, the relative changes in each step of the production and emission of HOI and I_2 in the Pound et al. (2023) SML model were interrogated to explain the predicted activation energies. Iodide in the surface layer is depleted if the replenishment from the bulk solution occurs at a slower rate than the reaction of iodide with ozone. Iodide depletion was modelled over the range of ozone, iodide and temperature reported by MacDonald et al. (2014), and depletion was predicted to increase with increasing ozone concentration, wind speed

and with decreasing iodide concentration, and slightly decrease with temperature (Fig. 30). The SML model shows that iodide depletion increases with increasing ozone concentration and with decreasing iodide concentrations due to chemical consumption of the available iodide. A greater depletion is seen at the higher wind speed because of the increase in ozone deposition as aerodynamic resistance (r_a) is reduced with higher airside turbulence ($v_d \approx 0.0013$ cm s^{-1}at 0.03 m s^{-1} and $v_d \approx 0.0003$ cm s^{-1} at 0.005 m s^{-1}). Waterside transfer velocity, k_w, which replenishes iodide from the bulk to the SML is still low at these wind speeds and does not offset the increase in ozone-iodide reactivity, therefore iodide is seen to be more depleted at 0.03 m s^{-1} compared to 0.005 m s^{-1}. This is the opposite to what we expect in the environment, where greater wind speeds would be associated with a greater degree of mixing from the bulk, and less iodide depletion. This is discussed in detail in Pound et al. (2023). The trend with wind speed we describe in the current work is specific to low "wind speed" laboratory conditions. This should therefore be considered in future experimental design, if environmentally-applicable emission data is sought.

The SML model predicted iodide depletion to slightly decrease with temperature, i.e. we predict a higher iodide concentration in the SML at higher temperature, given equal wind speed and ozone concentration. This is due to the small positive temperature dependence in the ozone-iodide reaction being offset by the increase in k_w with temperature, which increases mixing of iodide from the bulk to the SML. The effect of temperature is more pronounced at higher wind speed because, though small, k_w is higher at greater wind speed, therefore has greater impact at 0.03 m s^{-1} compared to 0.005 m s^{-1}. This impact is minor compared to the effects of ozone, iodide and wind speed. In light of this discussion, it should be noted that there are very few observations of iodide concentrations at or proximal to the surface layer (Stolle et al., 2020), and it is this iodide which is available for reaction with ozone. Concentrations of iodide at or proximal to the surface may frequently be different from the reported bulk concentration.

For both wind speeds investigated, ozone deposition velocity was effectively con-

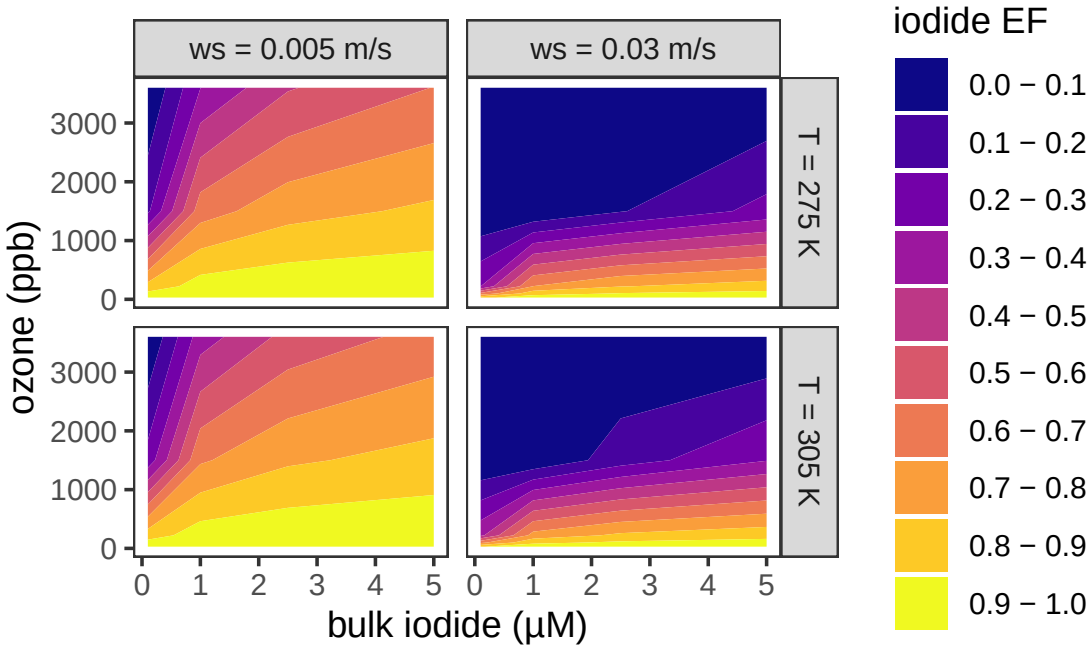

Figure 30: Modelled iodide depletion for ozone-oxidised iodide solution, under conditions 0.1 – 5 μM [iodide], 222 – 3600 ppb ozone, T = 276 – 298 K. Iodide enrichment factor (EF) = $[iodide]_{SML}/[iodide]_{bulk}$.

stant over the modelled temperature range (Fig. 31). This is because at low wind speeds, the deposition of ozone is limited by air-side resistance, r_a, which has no temperature dependence. Therefore, factors which decrease r_{aq}, e.g. changes in ozone solubility, aqueous diffusivity of ozone and reaction rate between ozone and iodide with temperature do not influence deposition significantly. Hence, the availability of ozone in solution was constant over the prescribed temperature range. Temperature trends in HOI emissions are therefore controlled by drivers in mixing to the bulk, or drivers in R21, which could include airside transfer velocity, k_a, and solubility of HOI, expressed as the dimensionless Henry's law coefficient, H_{HOI}, calculated using equations in Johnson (2010) and using physical constants from Thompson and Zafiriou (1983). The relative changes in selected chemical and physical drivers across the temperature range is displayed in Fig. 31. Flux to the air, F_a, is controlled by Eq. 43, where C_{SML} and C_a are concentrations of the species in question in the SML and in the air, respectively. In this model, C_a is assumed to be zero. Across this temperature range, we expect a small decrease in the product of $H_{HOI} \times k_{a(HOI)}$, resulting in lower flux of HOI to the atmosphere as T increases, hence the slight negative E_a for HOI emissions.

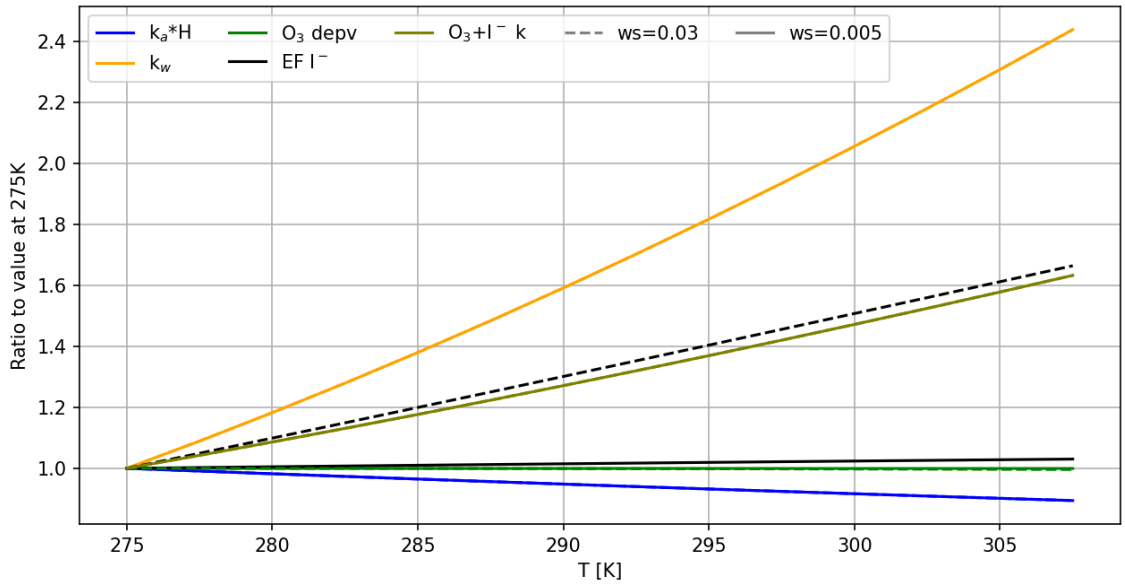

Figure 31: Relative change in selected variables with respect to the lowest modelled temperature. Variables selected are those with the greatest impact on emissions of HOI. Model conditions: ozone mixing ratio = 1500 ppb, [iodide] = 2.5 μM. k_a, k_w and H calculated for HOI. Dashed lines correspond to ws = 0.03 m s^{-1} and the solid lines refer to ws = 0.005 m s^{-1}. Where the dashed line is not visible, this is because it is identical to the solid line.

Due to its high solubility, the majority of HOI produced in the SML is mixed into the bulk liquid phase, F_b, Eq.44, rather than being emitted. Here, k_w is the waterside transfer velocity, and C_b is the bulk concentration, set to zero in this model. Chemical production of HOI is the only source of HOI in the SML, and the second order rate constant of chemical formation of HOI, $k_{I^- - O_3}$, increases with temperature. At 0.03 m s^{-1} wind speed, this is augmented by the reduced iodide depletion with higher temperature, leading to more HOI production. At 0.005 m s^{-1} wind speed, this effect is reduced by the effectively unchanging iodide depletion across the temperature range. In both instances, increased HOI production with T counteracts some of the increased loss to the bulk, more so at 0.03 m s^{-1} wind speed. This results in a slightly higher [HOI] in the SML at the higher temperature range which increases the E_a slightly at the higher wind speed (from -4.65 kJ mol^{-1} at 0.005 m s^{-1} compared to -4.08 kJ mol^{-1} at 0.03 m s^{-1}).

$$F_a = k_a(H \times C_{SML} - C_a) \tag{43}$$

$$F_b = k_w(C_b - C_{SML}) \tag{44}$$

For I_2, emissions are largely controlled by its low solubility. Temperature impacts on chemical and physical drivers are displayed in Fig. 32. We calculate a strong increase in $k_{a(I_2)} \times H_{I_2}$, leading to a higher F_a at greater temperatures, and a positive E_a at both wind speeds. While the rate constant of mixing to the bulk, k_b, also increases with temperature, its effect is counteracted by increased chemical production of I_2 with increased temperature, driven by increased $k_{I^- - O_3}$ and decreased iodide depletion. This results in a more positive E_a at the higher wind speed.

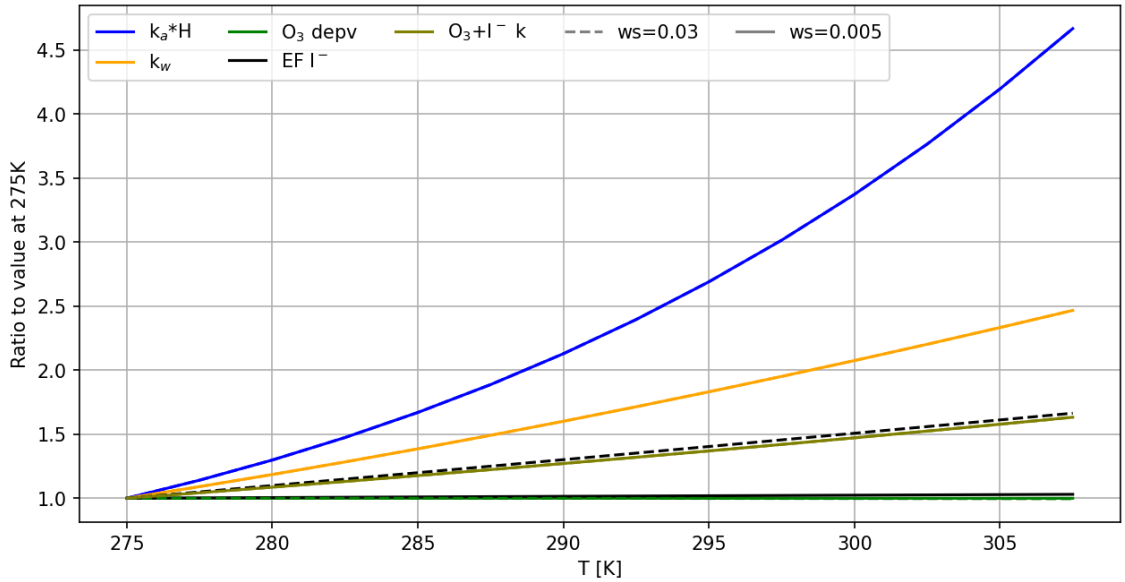

Figure 32: Relative change in each variable with respect to the lowest modelled temperature. Variables selected are those with the greatest impact on emissions of I_2. Model conditions: ozone mixing ratio = 1500 ppb, [iodide] = 2.5 μM. k_a, k_w and H calculated for I_2. Dashed lines correspond to ws = 0.03 m s^{-1} and the solid lines refer to ws = 0.005 m s^{-1}. Where the dashed line is not visible, this is because it is identical to the solid line.

The effects of varying iodide concentrations on HOI and I_2emissions was also investigated, at a wind speed of 0.005 m s^{-1}, due to the model's better comparability to experimental results at this wind speed. The calculated activation energies are displayed in Fig. 33. For the range of iodide concentrations used in MacDonald et al., (2014), we calculate that the E_a of HOI emissions has no dependence on iodide, and remains slightly negative for all modelled conditions (driven by increased mixing to the bulk at higher temperature, as above). For I_2 emissions, the modelled E_a was more strongly positive at the lowest iodide concentration, due to

greater iodide depletion in the SML. The iodide limitation is counteracted at higher temperatures by increased mixing from the bulk. In Fig. 34, it can be observed that for 100 nM iodide, the iodide enrichment factor increases with temperature, which is not observed for the other iodide concentrations. This results in a more strongly positive E_a at the lowest modelled iodide concentration of 100 nM, which is comparable to conditions found in the environment. We therefore believe that the activation energy of I_2 emissions reported in MacDonald et al., (2014) may underestimate the temperature dependence of oceanic I_2 emissions.

The model was also used to test for ozone sensitivity, however across the range studied here, ozone mixing ratio was not determined to influence activation energy for HOI or I_2 emissions.

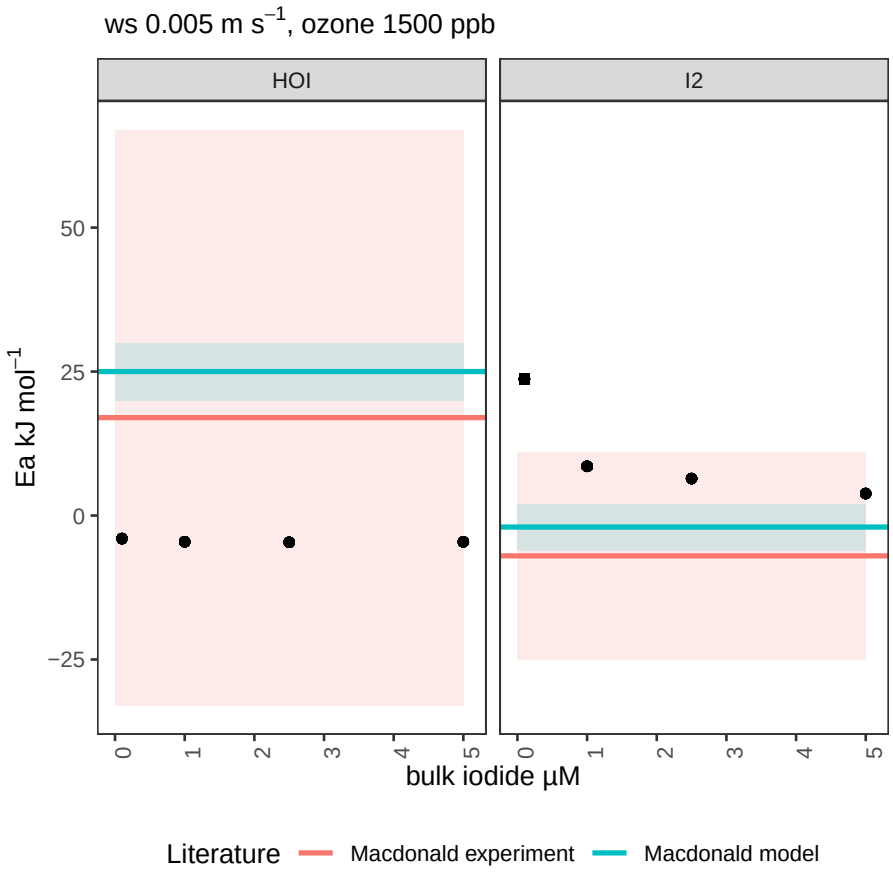

Figure 33: Effective activation energies for emissions of HOI and I_2 from ozone oxidation (1500 ppb, wind speed 0.005 m s^{-1}) of iodide solution, as a function of bulk iodide concentration. Points show modelled emissions using the SML model (Pound et al., 2023), while red and blue horizontal lines show experimental and previously modelled emissions respectively, from MacDonald et al. (2014). Errors are shown by shaded areas, and reflect standard error in the linear fit from modelled output.

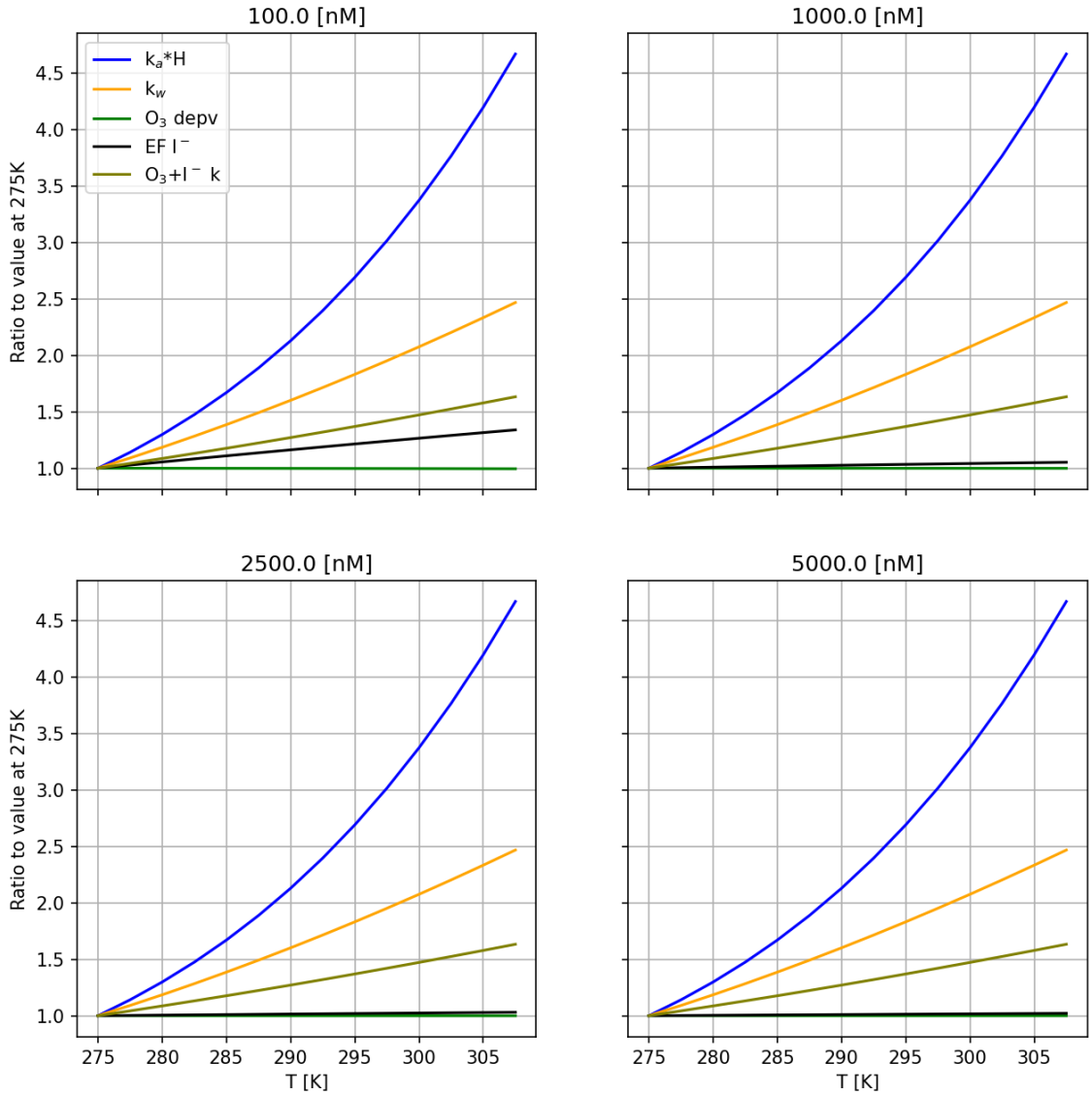

Figure 34: Relative change in selected variables with respect to the lowest modelled temperature for each modelled bulk iodide concentration. Variables selected with significance for emission of I_2. Model conditions: ozone mixing ratio = 1500 ppb, wind speed = 0.005 m s^{-1}. k_a, k_w and H calculated for I_2.

3.6 Chapter Conclusion

A thorough understanding of the kinetics of the reaction between ozone and iodide in oceanic systems is important for predicting and understanding tropospheric ozone concentrations in remote ocean regions. The second order rate constant of the reaction between ozone and iodide and its temperature dependence were measured in this work using a variable flow methodology, under conditions which emulate the bulk kinetics expected in the surface ocean. A negligible, non-statistically significant temperature dependence was obtained, contradicting a previous study. We therefore conclude that the temperature dependence of this reaction in the ocean has previously been over-estimated.

Though a lack of temperature dependence has previously been implied by comparison between studies, and by back-calculating from emissions, this is the first study, to our knowledge, to show this by direct measurement. The temperature dependence obtained was used to replicate and explore results produced from a previous laboratory study of HOI and I_2 emissions from an iodide solution exposed to ozone. This result has implications for oceanic ozone deposition, and emissions of gaseous iodine species to the troposphere (Carpenter et al., 2013). Despite being outside of the temperature range studied here, this work has potential further implications for halogen emissions to the stratosphere (Koenig et al., 2020). In related work, we have incorporated these kinetics into a global transport model (GEOS-Chem), to improve our understanding of ozone in the troposphere. This work also demonstrates that the laboratory-measured temperature dependence of I_2 and HOI emissions, which are a result of complex interactions between physical and chemical parameters, are highly dependent on experimental conditions (including both iodide concentration and wind speed), therefore cannot easily be translated into ambient emissions. It is noteworthy that the “wind speeds” applied in our and other authors’ experiments are not comparable to those found in the environment. In particular, the very low or negligible water turbulence accessible in laboratory experiments is far lower than those typically found in the ocean. The result of this is that while we simulate increasing iodide

depletion in the surface layer with "wind speed" at very low wind speeds, this is not typically expected in the environment where we predict that iodide depletion decreases with increasing wind speed (Pound et al., 2023). The latter is a result of greater wind-induced turbulence increasing the rate of iodide replenishment from the bulk to the surface layer. We also find that such iodide depletion in the SML, as expected under ambient conditions, can impact the temperature dependence of I_2 emissions. Therefore caution should be applied in extrapolating laboratory results to the environment, and the various factors which impact iodine-containing emissions from seawater should be considered in experimental design when planning future laboratory work. Despite this, the good comparability between the modelled results and experimental measurements found in this study validates both the kinetic results and the model recently developed by Pound et al. (2023).

4 Ozone Uptake to Seawater and its Chemical Drivers

4.1 Abstract

Currently in global ozone models, dry deposition to the ocean is either not parameterised, or parameterised based on iodide concentrations alone, however previous studies have determined that ozone uptake to seawater is driven by a combination of reactions between iodide and organic matter. These studies were performed on limited samples, either collected from coastal UK locations, or made artificially from riverine organic matter.

In this work, it was sought to assess the biogeochemistry and ozone uptake of SML and underlying water (ULW) samples from a range of oceanographic sources. The aim was to assess the contributions of bulk phase iodide reactions to ozone uptake, and hence quantify the contribution of missing reactivity sources, specifically surface-mediated reactions with DOC components. This was achieved by measuring ozone uptake over authentic seawater samples, including underlying water and SML, using a heterogeneous flow reactor. In addition to ozone uptake, a suite of complementary measurements were obtained, including iodine speciation, DOC and fatty acid concentrations, and surface tension, providing a powerful array of measurements to determine the driving forces of ozone uptake to seawater.

Key findings Ozone uptake for the CONNECT cruise ranged from 2.97 to 6.32 $\times 10^{-6}$, while for the PML campaign ranged 0.87 to 4.00 $\times 10^{-6}$. Bulk-phase iodide kinetics accounted for 25.0 to 66.3 $\%$ of ozone uptake during the CONNECT campaign, and 36.0 to 148.2 $\%$ of ozone uptake to PML samples. Due to suspected sample alterations by filtering and freezing the PML samples, the CONNECT samples were analysed for surface reactivity. It was determined that unsaturated fatty acids were a potential driver of surface-based reactions, and it was attempted to model ozone uptake with reactions of ozone with iodide and unsaturated fatty acids only. The uncertainties which remain regarding surface-mediated reactions were discussed.

An improved quantification of the impact of iodide on ozone uptake to real-world samples will allow improved modelling of ozone deposition to the ocean, impacting expected emissions of iodine-containing compounds. This work also demonstrated the potential importance of unsaturated fatty acids for ozone uptake, but highlighted further research required for accurate estimation of their contribution to ocean uptake to the sea surface.

4.2 Introduction

4.2.1 Background and Motivation

As early as 1980, ozone deposition to seawater was determined to be driven partly by iodide, but with a missing contribution, from an unidentified source.

By measurement of ozone uptake to seawater using a box-decay technique, the aqueous reactivity ($\lambda = k \times c$, where k is the second order rate constant of ozone with the species in question, and c is the species' concentration) of the seawater was measured as approximately 1000 s^{-1}. Applying a measured $k_{I^-O_3}$ of 2 $\times 10^9$ M^{-1} s^{-1} and assuming an iodide concentration of 100 nM, Garland et al. (1980) approximated an iodide-driven reactivity of 200 s^{-1}, leading to the conclusion that 20 $\%$ of ozone depositing to the sea surface reacted with iodide. Organic surfactants were proposed as a probable additional driver of ozone deposition enhancement.

Later, experiments were performed to investigate the relative effects of iodide and organic matter, the contribution of iodide and Suwannee River natural organic matter were determined experimentally to be approximately equal when measured separately, however when ozone uptake was measured over a mixed solution, the deposition velocity was approximately 80 $\%$ of their combined values, demonstrating further uncertainty in the mechanisn of ozone deposition to seawater (Martino et al., 2012).

Finally, a study analysed ozone deposition measurements performed over coastal seawater, and inferred a reactivity for coastal marine DOC that was 2-5 times higher than that which could be attributed to iodide (Shaw and Carpenter, 2013).

In the work by Shaw and Carpenter (2013), ozone uptake experiments performed over DOC collected by solid phase extraction of dissolved organic matter (SPE-DOM) calculated a DOC ozone reactivity of $\lambda = 1820 \pm 560$ s^{-1}. Because a reactivity due to marine DOM of only 100 - 500 s^{-1} was inferred by ozone deposition measurements over coastal seawater, the large reactivity of the extracted DOM was attributed to over-extraction of the more reactive compounds during SPE-DOM. Nevertheless, this study clearly demonstrated that ozone uptake to seawater was augmented by organic matter.

All of these studies considered the reaction with organic material as an aqueous-phase process, however it is now known that organic material reacts with ozone via a different mechanism; a surface-mediated Langmuir-Hinshelwood process. Furthermore, limited knowledge of the chemical makeup of seawater samples hindered identification of organic drivers to ozone deposition. Additionally, these studies were performed with a liquid phase which was not replenished, therefore chemical depletion of seawater constituents could have altered the results. The aims of this study were therefore to perform ozone uptake measurements to a large range of authentic seawater samples, with a suite of complementary biogeochemical measurements to aid analysis. An updated model for analysis of simultaneous aqueous-phase and surface-phase reactions was used to deconvolute the process of deposition. With improved knowledge of the rate of reaction of ozone with iodide, the contribution of iodide to ozone uptake was assessed, and from this baseline, the ”missing” reactivity quantified. The surface-phase contribution to ozone uptake was investigated, and the possible components of DOC responsible for enhanced ozone uptake identified.

4.2.2 Iodide at the Sea Surface

As discussed in Chapter 3, the reaction between ozone and iodide in seawater occurs rapidly in the liquid phase. For ozone uptake to the ocean, this is relevant due to the ubiquitous presence of iodide in surface seawater.

Iodine species are present in the ocean at a constant level of around 450 - 500

nM, however the speciation between ozone reactive iodide and ozone refractory iodate varies significantly. Concentrations of iodide in the iodine pool are typically in the range of approximately 50 - 250 nM, but can vary from essentially zero (below LOD), and have been measured as high as 450 nM. A summary of some available measurements is available in Table 7. Global surface iodide concentrations were modelled by Sherwen et al. (2019) and displayed in Fig. 35, demonstrating that iodide is predicted to be present globally, with concentrations greater in warmer water.

Table 7: Approximate ranges and locations of some near-surface iodide measurements.

iodide (nM)	Location	Reference
10 - 150	Sea of Japan	Tsunogai and Henmi (1971)
200 - 400	Hawaii	Campos et al. (1996)
100 - 120	Bermuda	Campos et al. (1996)
20 - 100	Weddell Sea to 25 °S	Campos et al. (1999)
20 - 250	Indian and Southern oceans	Chance et al. (2020)

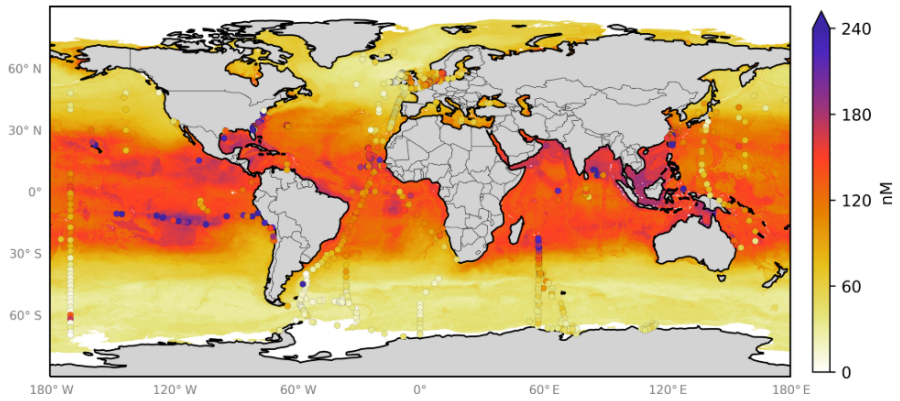

Figure 35: Annual average predicted surface iodide concentrations. Image reproduced from Sherwen et al. (2019).

Almost every reported value for iodide concentration in the sea surface has been collected from the underlying water. It is however important to consider whether this is representative of iodide in the SML, as the SML is the site of mass exchange between the ocean and atmosphere. Past literature is conflicted regarding whether the SML is enriched, depleted or equal in iodide to the underlying water. Few previous studies have quantified iodide in the SML and underlying water simultaneously, and those which have are limited to coastal regions of the

North Sea.

During the MILAN (Sea Surface Microlayer at Night) campaign, iodide in the SML and ULW were measured in the Wadden Sea (In the North Sea, off the coast of North-East Germany) across different times of day (Stolle et al., 2020). Iodide was potentially enriched in the SML, however this trend was not certain (SML depth was not given, while underlying water was collected from a CTD (conductivity, temperature and density sampler) at 1.2 - 2 m). A further study collected SML from a depth of 300 μm, and an ULW depth of 15 cm (Chapman and Liss, 1981). There is a large variation in enrichment factor reported from 21 samples, across five sampling events in two locations (Yarmouth and the Solent), with a maximum enrichment factor (EF) of 3.10 and a minimum EF of 0.13. The minimum and maximum EF values were obtained from samples collected on the same day and location. The mean EF and standard deviation were 1.13 $\pm$ 0.70, which was not a statistically significant difference between the SML and the ULW.

Recently, laboratory and modelling studies have given evidence for iodide depletion in the SML, across the reacto-diffusive depth of ozone (on the order of a few μm). One study measured the effect of depleted iodide in the surface layer of an artificial seawater solution in the form of reduced ozone uptake (Schneider et al., 2020). A further study later demonstrated that under environmental conditions, iodide could be expected to be depleted across the reacto-diffusive depth of ozone (Pound et al., 2023). The mechanism for this depletion was that iodide lost via fast reaction with ozone could not be fully replenished by mixing from the bulk.

The broad range of conclusions obtained from measurements, lab studies and theoretical studies warrants further investigation of iodide depletion and/or enrichment in the SML, and further measurements are desirable. A depletion or enrichment of iodide in the SML would significantly alter our understanding of ozone deposition to the ocean.

4.2.3 Reactions between Ozone and Organic Compounds

Organic matter is present in the ocean in various forms, from zooplankton to dissolved organic carbon (DOC). DOC constitutes the largest reservoir of organic carbon in the ocean, at 2 $\times 10^{17}$ g, compared to phytoplankton (4 $\times 10^{15}$ g), zooplankton (1 $\times 10^{14}$ g) and bacteria (1 $\times 10^{14}$ g) (Cauwet, 1977). DOC is mostly produced in the ocean by photosynthetic plankton in the surface ocean, which then sinks to greater depths, resulting in the highest DOC concentrations observed at the ocean surface (Hansell et al., 2009).

The presence of DOC at the ocean surface leads to potential interaction with atmospheric gases, including ozone. In the ocean, ozone reacts with organic compounds on the water surface, following a Langmuir-Hinshelwood mechanism. This has been demonstrated for several compounds, including chlorophyll (Clifford et al., 2008), unsaturated fatty acids e.g. oleic and linoleic acid (Zhou et al., 2014; McNeill et al., 2007; González-Labrada et al., 2007; King et al., 2009, 2020), and polycyclic aromatic hydrocarbons (PAHs), e.g. napthalene, anthracene and pyrene (Mmereki and Donaldson, 2003; Mmereki et al., 2004; Donaldson et al., 2005b; Raja and Valsaraj, 2005).

The Langmuir-Hinshelwood reaction pathway proceeds as follows. A site is an available point on the liquid surface where an ozone molecule can adsorb, and an adsorbed molecule of ozone is termed $O_{3(surf)}$. Adsorbed ozone can then react with an interstitial DOC compound ($DOC_{(int)}$), to form an ozone adduct. Ozone has been determined by several authors to adsorb to liquid surfaces by a Langmuir isotherm, therefore the concentration of adsorbed ozone can be described by Eq 12.

$$O_{3(gs)} + \text{site} \rightleftharpoons O_{3(surf)} \tag{R23}$$

$$O_{3(surf)} + DOC_{(int)} \rightleftharpoons DOC{-}OOO^{-}_{(int)} \tag{R24}$$

Within the DOC pool, reactivity towards ozone is highly variable. Aromatic compounds can be highly reactive to ozone, dependant on the ring substituents. The rate of reaction with ozone can vary by up to 10 orders of magnitude, for example

a highly deactivated aromatic compound, e.g. nitrobenzene, has a second order rate constant of 9 $\times 10^{-2}$ M^{-1} s^{-1}, while the phenolate ion has a rate constant of 1.4 $\times 10^{9}$ M^{-1} s^{-1} (von Sonntag and von Gunten, 2015). Aromatic compounds typically found in seawater are polycyclic aromatic hydrocarbons (PAHs), which are mostly introduced via anthropogenic pollution, and have a second order rate constant with ozone on the order of 10^3 to 10^4 M^{-1} s^{-1}, depending on their identity (Trapido et al., 1995). Other compounds which are ozone-reactive include amines and DMS (von Sonntag and von Gunten, 2015). The contribution of DMS to ozone uptake was negligible, except for exceptionally high concentrations which may be found in algal blooms (Chang et al., 2004).

On carbon chains, the site of ozone reaction is the carbon-carbon double bond, therefore aliphatic compounds are ozone refractory (von Sonntag and von Gunten, 2015). For unsaturated compounds, e.g. unsaturated fatty acids, ozone reacts with the double bond via addition, forming an unstable primary ozonide (Fig. 36). For unsaturated fatty acids, this breaks down to carbonyl containing compounds, either aldehydes or carboxylic acids, and an unstable Criegee intermediate (Criegee, 1975; Vesna et al., 2009). The Criegee intermediate can go on to rearrange to the corresponding acid, or react further, e.g. with water, carbonyl groups, carboxylic acid groups or other Criegee intermediates. This is an important class of ozone-reactive DOM due to the ubiquitous presence of fatty acids, both saturated and unsaturated, in the surface ocean. Their presence in the ocean is attributed to microbial production (Gašparović et al., 2007).

Fatty acids (FA) have a hydrophilic head and hydrophobic tail, therefore are surface-active compounds. This, combined with the ozone reactivity of unsaturated fatty acids (detailed in Section 4.7.3), makes them relevant to discussion of DOC-mediated ozone uptake enhancement, however, SML measurements of fatty acids are sparse. The available literature is outlined in Table 8, which demonstrates that coastal areas tend to be higher in fatty acid concentration than the open ocean, as well warmer waters (the Gulf of Mexico and North Mediterranean) promoting higher concentrations than cold waters (the English Channel). In very cold wa-

ters, e.g. the Norwegian Fjords, higher fatty acid concentrations were attributed to high lipid content of phytoplankton (Gašparović et al., 2007).

Table 8: Previously reported mean concentration of fatty acids in SML samples.

Location	Type	Mean Conc. (μg L^{-1})	Reference
coastal			
Norwegain Fjords	Saturated	84.6	Gašparović et al. (2007)
	Unsaturated	24.4	Gašparović et al. (2007)
Gulf of Mexico	Saturated	112.5	Slowey et al. (1961)
	Unsaturated	37.5	Slowey et al. (1961)
North Mediterranean	Saturated	147.62	Daumas et al. (1976)
	Unsaturated	132.53	Daumas et al. (1976)
English Channel	Saturated	20	Weddell (2023)
	Unsaturated	15.3	Weddell (2023)
open ocean			
NE Tropical Atlantic	Saturated	6.95	Marty et al. (1979)
	Unsaturated	1.6	Marty et al. (1979)
Trans-Atlantic and	Saturated	14.4	Weddell (2023)
Equatorial Pacific	Unsaturated	0.8	Weddell (2023)

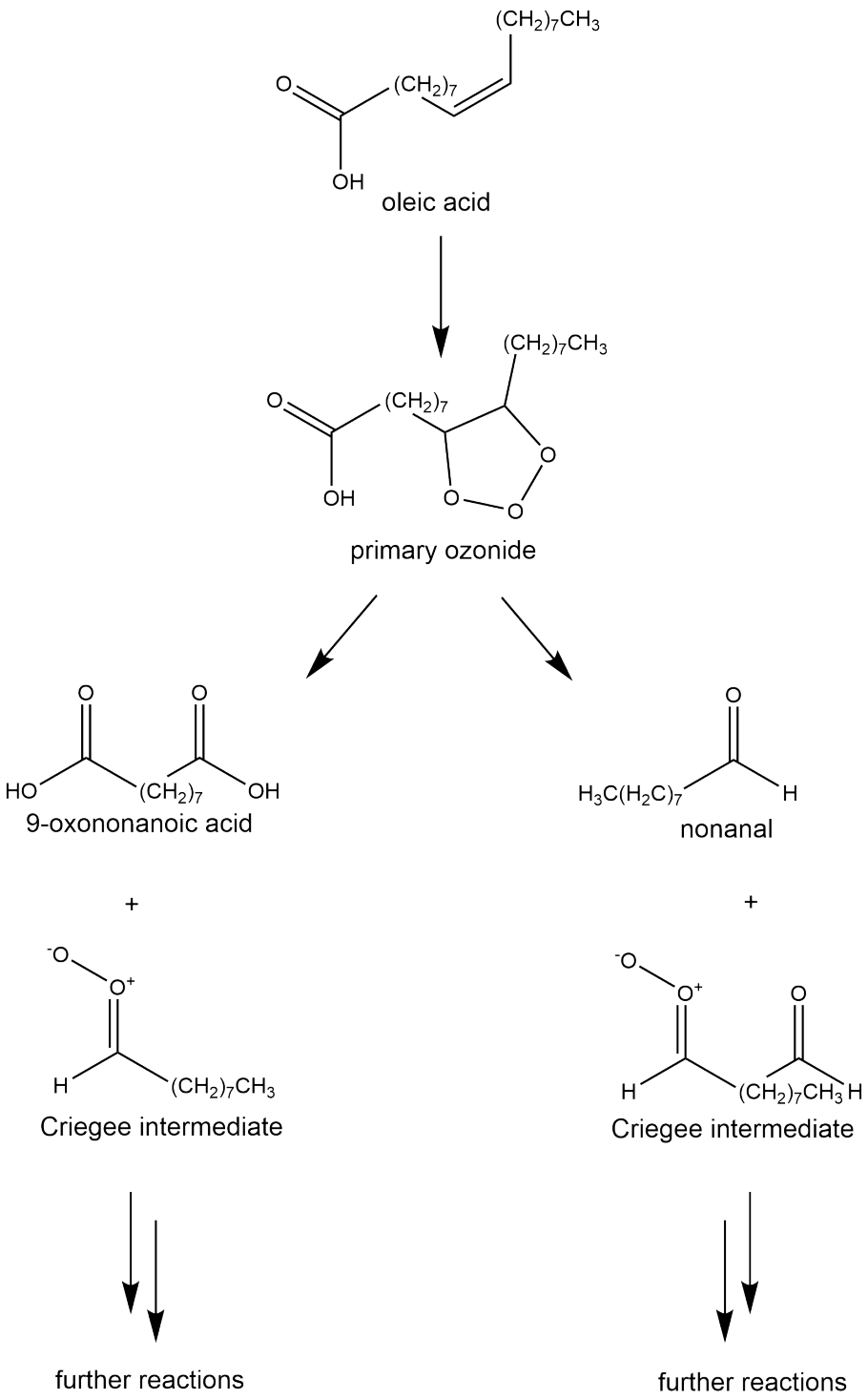

Figure 36: Mechanism of ozonolysis of oleic acid.

During the CONNECT and PML campaigns (described in Section 4.3.1) the available literature on SML fatty acid concentrations was extended (Weddell, 2023), which demonstrated that open ocean water was indeed lower in concentration than coastal water, particularly in terms of unsaturated fatty acids. The measurements of fatty acids made during these campaigns coincided with a suite of other measurements, including ozone uptake measurements, allowing their contribution to ozone uptake to be assessed.

A further impact of the presence of surface active compounds is alteration to the surface tension of seawater. The ampiphilic nature of surfactants acts to reduce the hydrogen bonds in the water surface, reducing the surface tension. The impact of surfactants has been demonstrated to reduce air-sea exchange of gases such as carbon dioxide and oxygen by reducing turbulence and diffusion at the sea surface (Schmidt and Schneider, 2011; Salter et al., 2011). For a reactive gas such as ozone, the relationship with surface tension is not well defined, as it could be altered by the presence of ozone-reactive surfactants, e.g. unsaturated fatty acids. This work allowed comparison of ozone uptake to surface tension measurements.

4.2.4 Chapter Aims

The goal of this chapter was to perform ozone uptake measurements to a wide range of seawater samples, to include open ocean samples, which have been under-represented in previous ozone uptake studies. Powerful datasets are available to complement these measurements, including a wide range of physical and biogeochemical factors, which were utilised to investigate combined driving forces of ozone uptake to the ocean.

4.3 Methods

4.3.1 Seawater Sample Collection

Relative locations of all seawater samples discussed in this chapter are displayed in Figure 37.

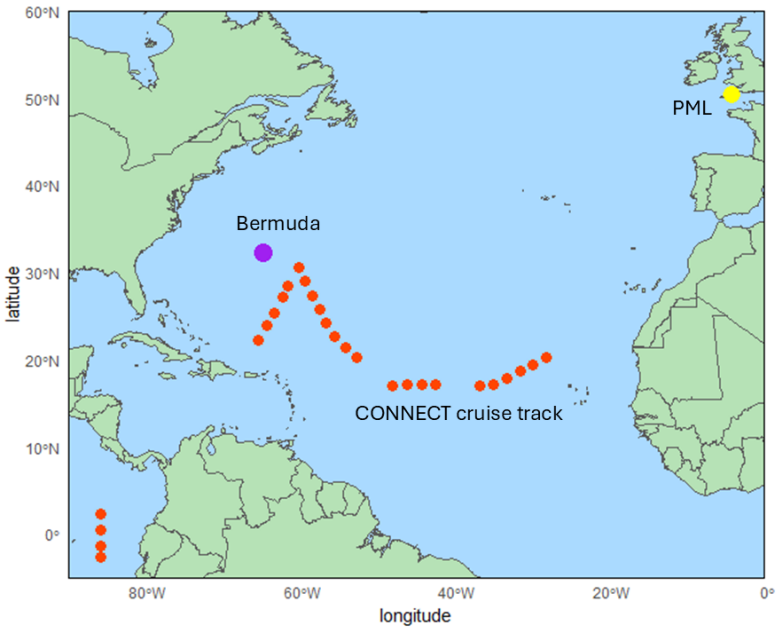

Figure 37: Sampling locations for all seawater measurements described in this chapter. PML is displayed in yellow, the CONNECT cruise track in red and Bermuda is displayed in purple.

4.3.1.1 Sampling times and locations

PML The Plymouth Marine Laboratory is a marine research organisation, situated on the South-East coast of England, and who have collaborated extensively with us on work into ozone uptake to seawater. During this joint campaign, samples were collected weekly off the coast of Plymouth, between 11th November 2019 and 13th September 2021. The sampling location was approximately 0.5 km offshore of Rame Head, Cornwall, in the English Channel. Several locations were sampled from (Fig. 38), including the long-term measurement site, L4, of the Western Channel Observatory (WCO) (Mcevoy et al., 2023).

CONNECT (Pan-Atlantic Connectivity of Marine Biogeochemical Processes / Impact of Anthropogenic Pressures) was a research cruise from Gran Canaria to

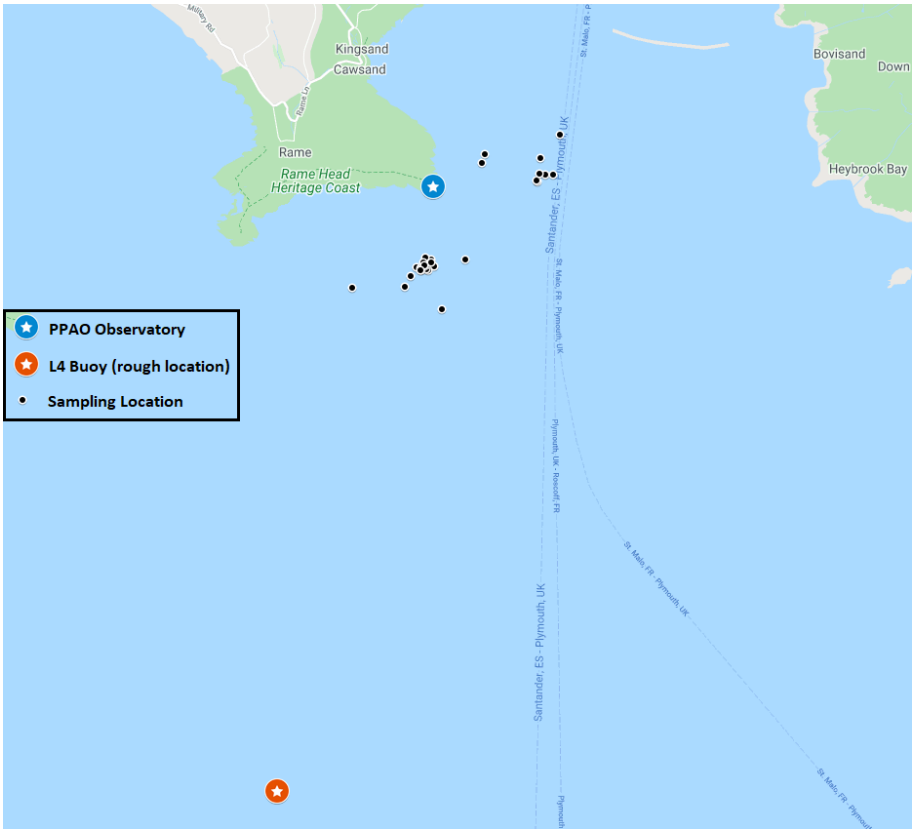

Figure 38: Sampling locations for PML campaign.

Guayaquil, Ecuador, from the 11th December 2021 to 11th January 2022. This cruise sampled locations across the Atlantic Ocean, through the Caribbean Sea and into the Equatorial Pacific. The stations along the cruise track are shown in Figure 39.

BLEACH (Bermuda Boundary Layer Experiment on the Atmospheric Chemistry of Halogens) samples were collected in two locations (fig. 40). During the summer campaign, in June and July 2022, samples were collected off the coast of Tudor Hill, on the south-west tip of Bermuda. During the winter campaign, in January and February 2023, samples were collected on or near the Bermuda Atlantic Time Series (BATS) site (Karl et al., 2001).

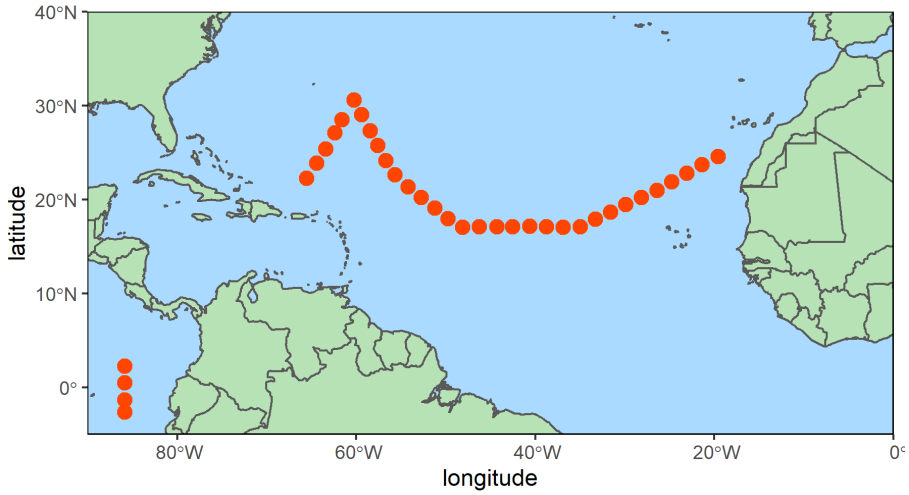

Figure 39: Station locations for the CONNECT cruise.

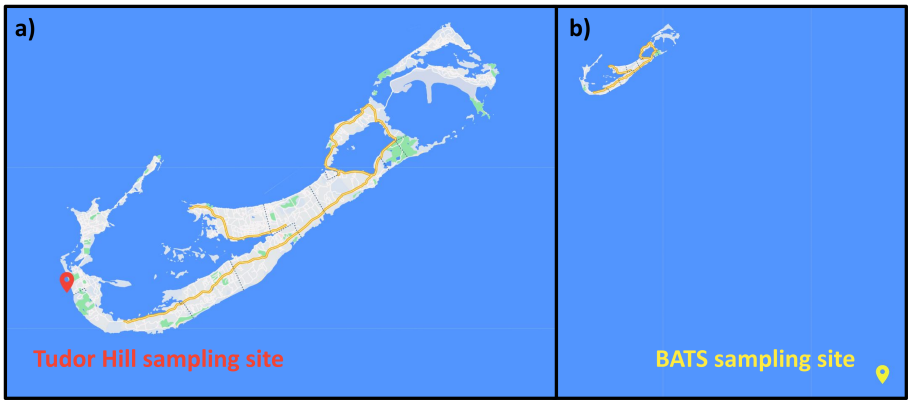

Figure 40: a) Map of Bermuda showing the Tudor Hill sampling site, highlighted by the red marker. b) map of near-Bermuda Atlantic ocean, highlighting the BATS sampling site in yellow. Maps produced by snazzymaps.com, images courtesy of Google Maps.

4.3.2 Sampling methods

SML Collection SML was collected using an aluminium mesh Garrett screen (details in Table 9, and Fig. 41a). Garrett screens feature a metal mesh enclosed in a frame, and use the surface tension of the water to retain the uppermost layer within its mesh (Cunliffe and Wurl, 2014). To collect SML, the screen was lowered below the surface of the water and slowly drawn up parallel to the water surface. The SML, held within the mesh, was collected by tilting the screen vertically, allowing the sample to drip through a funnel into a bottle. Bottles were conditioned with SML by vigorously shaking, and discarding the first collected dip. Details on

the collected SML are available in Table 10.

The choice of Garrett screen in this work was necessitated by a trade-off between sample thickness and sample volume; to perform the required suite of measurements on each sample, up to 12 L of SML were collected in each sampling trip. This would not have been practical with a sampling method with a thinner SML sample, e.g. a glass plate.

Table 9: Garrett screen details

	PML	CONNECT and BLEACH
screen length (cm)	78.3	102
screen width (cm)	52.5	74
screen area (cm^2)	4111	7548
wire outer diameter (mm)	0.35	0.35
mesh count (wires per inch)	16	20
void space (%)	60.8	52

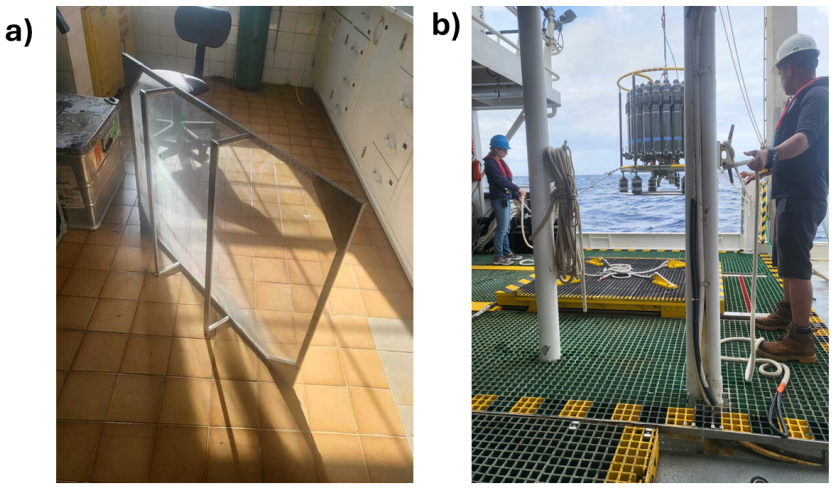

Figure 41: Picture of a) the Garrett screen used for SML sampling and b) the CTD rosette being lowered into the water aboard the RV Atlantic Explorer.

The screen was rinsed with milli-Q water prior to use, and dipped into the seawater at least three times, without sample collection, to condition the mesh. Additional cleaning with methanol, subsequent to milli-Q cleaning, was carried out during the BLEACH campaign.

On the PML campaign, SML was collected by the crew at PML, from the bow of the research vessel (RV) Plymouth Quest. On the CONNECT cruise, SML was collected from the side of a small rubber inflatable zodiac boat, approximately 100

m further upwind of the RV Sonne, when weather conditions allowed. Otherwise, SML was collected using a crane from the aft-deck of the RV Sonne, approximately 1 m from the wall of the ship, and lowered approximately 6 m to the sea surface. On the summer BLEACH campaign, SML was collected from the side of a Twin Vee boat, and in the winter campaign, collected using a winch from the side of the RV Atlantic explorer, where the deck was approximately 0.5 m from the water surface. On many occasions on both CONNECT and BLEACH, weather conditions did not allow SML sampling by any method.

To calculate the thickness of the collected SML, the volume of liquid collected per dip is considered along with the geometry of the screen (given in Table 9). The sampling area is calculated from the area of the screen, minus the area occupied by mesh wires. The void space (quoted from the supplier) is the proportion of the area which is empty, therefore is used to calculate sampling area according to Eq. 45. The volume of sample collected is then used to calculate the depth of the theoretical cuboid, using the sampling area, according to Eq. 46. The average volume per dip and resulting SML thickness during each campaign are outlined in Table 10. SML details for CONNECT and BLEACH samples are given for the average volume collected during sampling from the zodiac or Twin Vee, and not crane collections. This is assumed to be the best representation of the true sample volume and thickness, due to windy conditions on crane sampling days causing some sample loss during transfer from the ocean surface to the deck. Inclusion of this data would cause us to conclude an artificially thinner SML (580 μm for BLEACH and 471 μm for CONNECT, when both crane and small boat samples are included in the average).

$$sampling\ area = screen\ area \times (void\ space\ percentage/100) \tag{45}$$

$$SML\ thickness = sample\ volume/sampling\ area \tag{46}$$

ULW Collection Underlying water (ULW) was collected by various methods from below the water surface. On the PML campaign, this was collected from an inlet pipe on the hull of the RV Plymouth Quest, at approximately 3 m depth. The

Table 10: SML sampling details

	PML	CONNECT	BLEACH
Average volume per dip (ml)	163	233	300
SML thickness (μm)	653	593	764

SML details for CONNECT and BLEACH samples are given for average volume collected during sampling from the zodiac or Twin Vee, and not crane collections.

water is pumped to a hose on deck for collection. On the CONNECT cruise, seawater was collected from both a CTD rosette deployed from the RV Sonne, at approximately 6 m depth, and from the ship's continuous underway pump, also at approximately 6 m depth. A CTD rosette is a rig which holds sampling bottles, which can be automatically closed at set depths (Figure 41b). There are also sensors, including those for conductivity, temperature and density, which give the rig its name. On the summer BLEACH campaign, ULW was collected using a handheld bilge pump from the bow of the Twin Vee boat, at approximately 0.5 - 1 m depth. On the winter BLEACH campaign, ULW was collected from a CTD rosette, at approximately 6 m depth.

Cleaning and Storage Samples were collected into plastic bottles which were acid washed between uses. The cleaning procedure involved rinsing with hot tap water, rinsing with or soaking in dilute HCl, and rinsing 3 times with milli-Q water. All samples were stored in insulated dark boxes for storage and transport to the lab.

4.3.3 Chemical Analyses

Iodine Speciation

Iodide was directly quantified using UV-vis spectrophotometry at 226 nm following ion exchange chromatography (IC) (Jones et al., 2023) using an Agilent 1100 HPLC and 1260 series detector. The IC used a Dionex IonPac AS23 guard and analytical column (4 x 50 mm and 4 x 250 mm, respectively), with a mobile phase eluent of 0.4 M NaCl flowing at 0.64 ml min^{-1}. The sample injection volume was 400 μl, run time 16.1 minutes, and iodide was detected at 11.8 minutes.

Iodate analysis was preceeded by offline addition of NH_2OH-HCl to a final concentration of 7 mM. This addition converted all iodate to iodide, which was subsequently quantified as above to give a measurement of total inorganic iodine. Subtraction of the previously quantified iodide fraction from the total inorganic iodine allowed quantification of iodate.

Dissolved organic iodine was quantified following analysis of total dissolved iodine. Total dissolved iodine was quantified following a three-step offline procedure: $Ca(ClO)_2$ was added to a final concentration of 189 μM, and left for approximately one hour. Na_2SO_3 was then added to a final concentration of 380 μM, to neutralise ClO^-. Finally, NH_2OH-HCl was added to convert all iodate to iodide, quantified as above. Subtraction of total inorganic iodine from the total dissolved iodine fraction yields the concentration of dissolved organic iodine.

All iodine speciation measurements were carried out by Dr Matthew Jones.

Dissolved Organic Carbon 9 ml of sample was transferred to an acid-washed glass vial (12 ml), and acidified with 10% HCl to purge inorganic carbon. DOC was quantified using an Elementar Vario TOC cube instrument. Samples were quantified in reference to standards prepared using a commercial TOC standard (50 mg L-1, 76319 - 250 ml - F, Supelco) which was diluted with milli-Q water.

All DOC measurements were carried out by Katherine Weddell.

Fatty Acids Fatty acids were quantified following solid phase extraction (SPE) of seawater samples. The sample was filtered through an inline 0.7 μm GFF filter and either frozen at -20 °C (BLEACH, PML) or directly processed (CONNECT).

If frozen, samples were defrosted and acidified to pH 2 using HCl (37%, ACS grade). SPE cartridges (Agilent Bond Elut, PPL 500 mg, 6 mL) were conditioned with 3 headspaces of methanol (Fisher, Optima LC/MS grade), and the acidified seawater slowly pulled through under vacuum (no faster than 10 ml/min). When the whole seawater sample had passed through the cartridge, the cartridges were rinsed with 3 headspaces of HCl (0.01 M), dried for 5 minutes, and the extract eluted with 8 mL of methanol (Fisher, Optima LC/MS grade), which was collected in ashed glass vials. Eluted samples were capped and sealed with parafilm, and stored at -20 °C. For the second BLEACH campaign, it was not possible to elute the extract, therefore the cartridge was dried for 5 minutes under vacuum, and the dry cartridge stored at -20 °C, for elution at a later date according to the same procedure.

Following extraction, the fatty acids were analysed by GC-MS. The samples were first derivatised by esterification. 50 μl of an internal standard solution (methyl nonadecanoate, 0.1 mg/ml, analytical standard, 98% GC, Sigma-Aldrich) was added to each methanol extract, along with 0.103 ml sulfuric acid (puriss., 95 - 97%, Sigma-Aldrich). 4 ml of hexane was added to each sample ($\geq$95% HPLC grade, Fisher Chemical) and the headspace flushed with nitrogen. The vials were sealed and gently heated until the solvent refluxed off the sides of the vials for 2 hours, completing derivatisation. The acidity of the sample was reduced by addition of 1 ml of hexane to each vial along with 2 ml of distilled water, and samples manually shaken for 5 seconds, before removal of the aqueous layer by pipette. This step was carried out three times. Following Vertex centrifugation, the hexane layer was collected and reduced to dryness under nitrogen, before redissolution in 100 μl of hexane.

This sample was analysed by GC-MS (Agilent Technologies 6850 GC and 5975C inert XL EI/CI MSD with Triple-Axis Detector), with injection volume 1 μl, split ratio of 5:1 and inlet temperature 250 °C. With a flow fate of helium through the column of 1 ml/min, the oven temperature was held at 50°C for 2 minutes, ramped to 140 °C at 10 °C /min, then to 220 °C at 3 °C /min, and finally to 260 °C at 30 °C /min,

where it was held for 6 minutes. Each sample was run with a full mass scan from *m/z* 50 to 500, followed by three runs using single ion mode, switching between *m/z* of 55, 67 69, 74, 79, 81, 87 and 93, with a dwell time at each *m/z* of 50 ms. Data was processed using Agilent MassHunter and the NIST Mass Spectral Library. External calibration was carried out using commercially available standards where available.

Seawater extractions were carried out by Katherine Weddell on PML and CONNECT samples, and by Lucy Brown for BLEACH samples. Fatty acid derivatisation and quantification by GC-MS was carried out by Katherine Weddell on all samples. Further details of the development of this method are available in Weddell (2023).

Surface Tension Surface tension samples were stored in 60 ml polypropylene bottles. For the CONNECT and BLEACH campaigns, samples were initially frozen at -80°C before transferring to -20°C for long-term storage (Yousif Assiri, *pers. comm.*). PML samples were initially frozen at -20°C. Surface tension of the samples was measured using a Kibron EZ-pi+ with a Wilhelmy plate and thermocouple probe. Prior to measurement the thermocouple probe was rinsed with milli-Q and the plate was rinsed with milli-Q and flamed until red-hot. The plate was then inserted perpendicular to the liquid surface and allowed to equilibrate until a stable surface tension measurement was obtained for a duration of at least 5 minutes. Measurements were performed in duplicate, by Yousif Assiri (PML, CONNECT) or Lucy Brown (BLEACH).

Salinity During the PML campaign, salinity was measured for discrete SML and ULW samples using a handheld Greisinger GLF 100 Temperature-Salinity probe. During the CONNECT campaign, salinity was measured by a SBE 4 conductivity sensor, mounted on the CTD rosette.

4.3.4 Flow Reactor Method

The variable flows method (Chapter 2) was used for all seawater samples, with flow rates applied of 400, 480, 600, 800 and 1200 SCCM, and an applied ozone

concentration of 60 ppb. The small flow reactor was used, which gave reaction times between ozone and the seawater surface of approx. 19 - 74 seconds. To make up the total flow required for analysis by the ozone monitor (Thermo 49i, $\approx$ 1.4 SLPM), a dilution flow of compressed air was applied directly after the flow reactor (1000 SCCM). During the CONNECT campaign, uptake was measured to seawater at the in-situ temperature (controlled by Grant Optima R3/TX150 re-circulating water bath). For PML samples, all samples were measured at 20 °C. Background uptake was measured as a blank to the glass surface, as described in Section 2.3.6.2. Deposition velocity was calculated using the same analytical method as in Chapter 3.

A picture of the flow reactor set-up on the ship is included in Fig. 42.

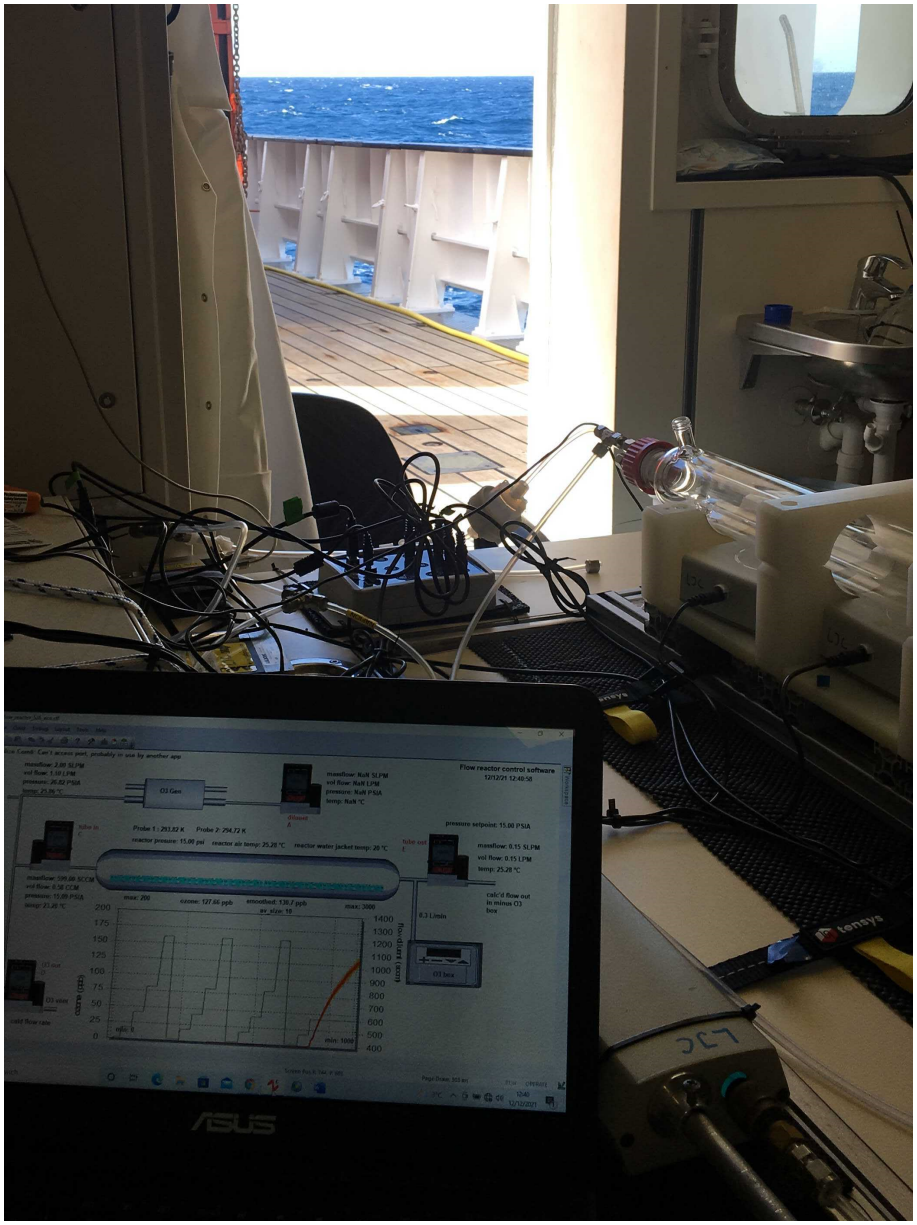

Figure 42: Picture of the small flow reactor set up on the RV Sonne during the CONNECT campaign, demonstrating the proximity of the sampling and ozone uptake measurements.

4.3.5 Sample Treatment and Storage

The goal of this work was to measure ozone uptake over authentic seawater samples to attempt to gauge the true chemically driven ozone uptake. To avoid chemically altering the sample, storage and processing were kept to a minimum prior to measurement, however were sometimes necessary due to time and location restraints. A summary of sample treatment and storage is provided in Table 11.

For the PML campaign, it was necessary to freeze the samples prior to measure-

ment, due to the distance between sample collection and laboratory measurement. All samples collected were filtered prior to being frozen, and stored frozen for up to 3 years prior to ozone uptake measurement.

On the CONNECT campaign, it was possible to perform ozone uptake measurements on the ship, directly after sample collection, within approximately 2 hours for SML samples and 6 hours for ULW samples. These were therefore not frozen, and were also unfiltered. These uptake measurements are therefore the most likely to be a true representation of the ozone-reactivity of the SML and underlying water.

In terms of comparative measurements, surface tension samples were frozen unfiltered, however flash frozen at -80 °C, which was determined to be the most effective way of preserving the true surface tension of a frozen sample (Yousif Assiri - *pers. comm.*). It was however not possible to perform all analyses on unfiltered samples. Iodine speciation and fatty acid analysis must be performed on filtered samples to avoid blocking the solid phase components of the analytical instruments. A previous study demonstrated that for 13 of 16 measured fatty acids, filtering did not impact recovery. There was however some loss of three specific fatty acids during this sample preparation step; octanoic acid, nonanoic acid and octadecanoid acid (Weddell, 2023). For octanoic acid and nonanoic acid it was suggested that the higher polarity compounds had a greater affinity for the filters, however no route of loss was determined for octadecanoic acid. In seawater, to the authors knowledge there is not literature available on the impact of freezing on fatty acid concentrations, however it is known in food science that freezing reduced fatty acid concentrations in meat (Zymon et al., 2007). Filtration was necessary for quantification of DOC, to separate particulate organic carbon (POC) prior to measurement. Quantification of organic carbon without filtering would measure total organic carbon (TOC). Filtering and freezing is standard practise for many biogeochemical species, including DOC (Dickson et al., 2007), however to our knowledge no studies exist to show the impact of freezing filtered seawater on subsequent fatty acid measurements.

On the BLEACH campaign, samples were collected for analysis of iodine speciation, DOC concentration, and surface tension. Ozone uptake experiments were attempted on this campaign, however instrument issues meant that no viable measurements were made.

Table 11: Summary of sample storage and treatment across campaigns.

Campaign	Parameter	Filtered?	Frozen?
PML	Ozone uptake	yes	yes
	Iodine speciation	yes	yes
	DOC	yes	yes
	Surface tension	yes	yes∅
	Fatty acids	yes	yes
CONNECT	Ozone uptake	no	no
	Iodine speciation	yes	yes
	DOC	yes	yes
	Surface tension	no	yes
	Fatty acids	yes	yes
BLEACH	Iodine speciation	yes	yes
	DOC	yes	yes
	Surface tension	no	yes

∅ indicates samples were frozen at -20°C, rather than the preferred -80°C.

Sample logs for the CONNECT cruise are available in Appendix 6.3.1. Sampling locations and station-specific sampling information, including SML thicknesses, are also available in Appendix 6.3.2 for the CONNECT cruise.

4.4 Results and Discussion

4.4.1 Biogeochemistry of the SML and ULW

For meaningful examination of the drivers of ozone uptake to seawater, the chemical makeup of the sample must be understood. Four key characteristics were explored; DOC concentration, fatty acid concentration, surface tension and iodide concentration (fatty acid concentrations were not measured on the BLEACH campaign, and at the time of writing, DOC measurements for the BLEACH campaign are not available). Summary statistics of each measurement in the SML and ULW for each campaign are outlined in Appendix 6.4.1 (Table 21), and explored in the subsequent discussions.

Samples of the SML and ULW were collected at the same location, and at roughly the same time. This allowed measurement of ozone uptake to paired seawater samples, to assess the differences in ozone reactivity of the SML compared to the bulk water. To support this analysis, the biogeochemical differences between the SML and ULW samples were explored. Where applicable, the enrichment factor (EF) of a species or characteristics was calculated to quantify the difference between the SML and ULW. The EF of characteristic X is the ratio of X in the SML compared to the ULW, per Eq. 47. X in the following discussion refers to the concentration of DOC, fatty acids or iodide, measured for each sample.

$$EF_X = \frac{X_{SML}}{X_{ULW}} \tag{47}$$

Dissolved Organic Carbon DOC was measured for all samples during the PML and CONNECT campaigns. A timeseries of DOC concentrations throughout the PML campaign is displayed in Fig 43. A map of DOC concentrations across the CONNECT cruise track is shown in Figure 44. The mean concentrations of DOC in the SML and ULW during the PML campaign were 1.6 $\pm$ 0.5 and 1.5 $\pm$ 0.5 mg C L^{-1}, respectively, where the error is given as one standard deviation. DOC was higher during the CONNECT campaign, with mean values of 2.7 $\pm$ 2.2 and 1.9 $\pm$ 0.4 mg C L^{-1} for SML and ULW, respectively. The average DOC concentration

during the CONNECT campaign was likely higher because of the warmer water temperatures increasing biological activity and hence DOC production, compared to those in the English Channel. Additionally, samples were collected near some high productivity areas, for example the Mauritiana upwelling off the west coast of Africa. Upwelling regions experience a flux of nutrients from the deep ocean, therefore experience high primary productivity (Hansell and Orellana, 2021).

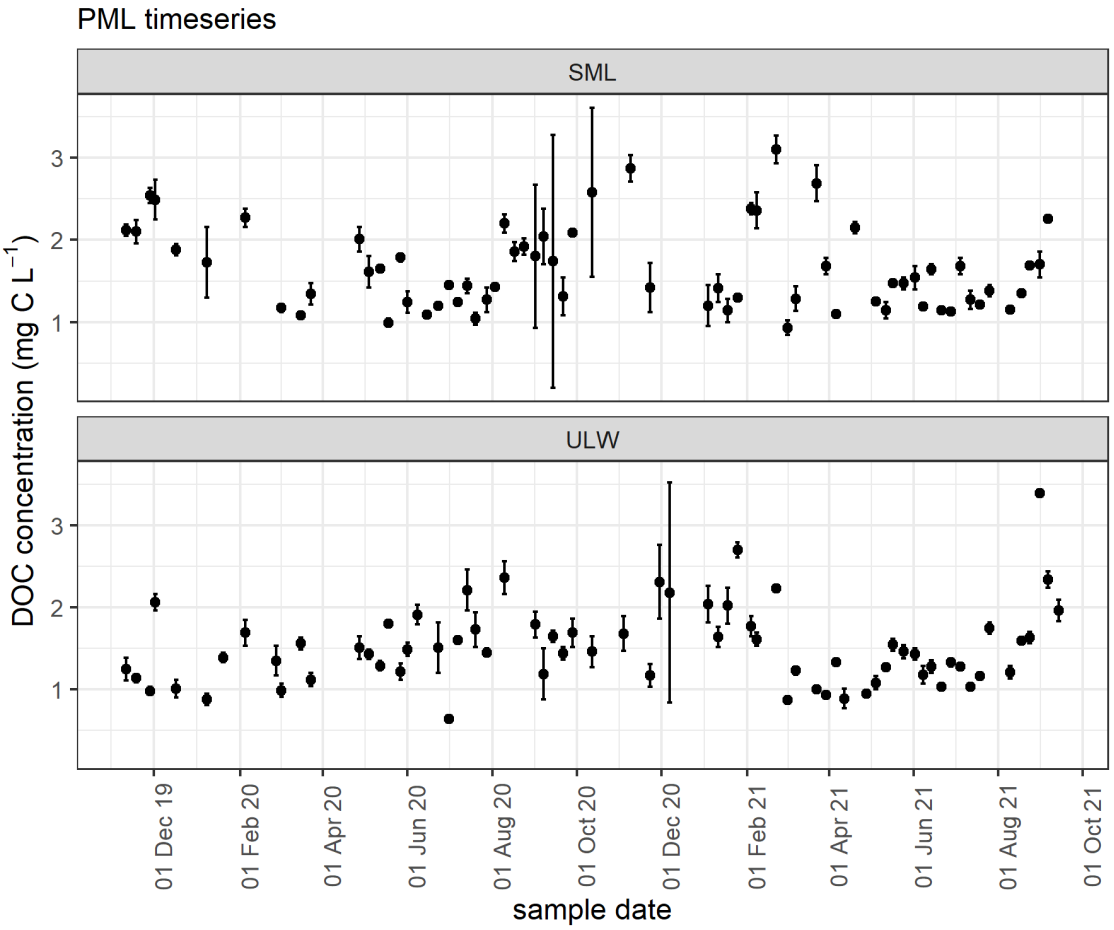

Figure 43: Timeseries of DOC concentrations during the PML campaign, in the SML and ULW.

Previous measurements of DOC concentrations in the SML were reported as 2.7 $\pm$ 2.1 mg C l^{-1} (225 $\pm$ 175 μmol L^{-1}) from 79 samples, and 1.9 $\pm$ 1.6 mg C l^{-1} (161 $\pm$ 139 μmol L^{-1}) in ULW, from 78 samples (Pinxteren et al., 2017). These values were collated from several locations in the Atlantic Ocean, including south-north transects from Punta Arenas, Chile to Bremerhaven, Germany and from South Africa to Bremerhaven. Values were also reported for samples collected from the Cape Verde Atmospheric Observatory (CVAO), and from the

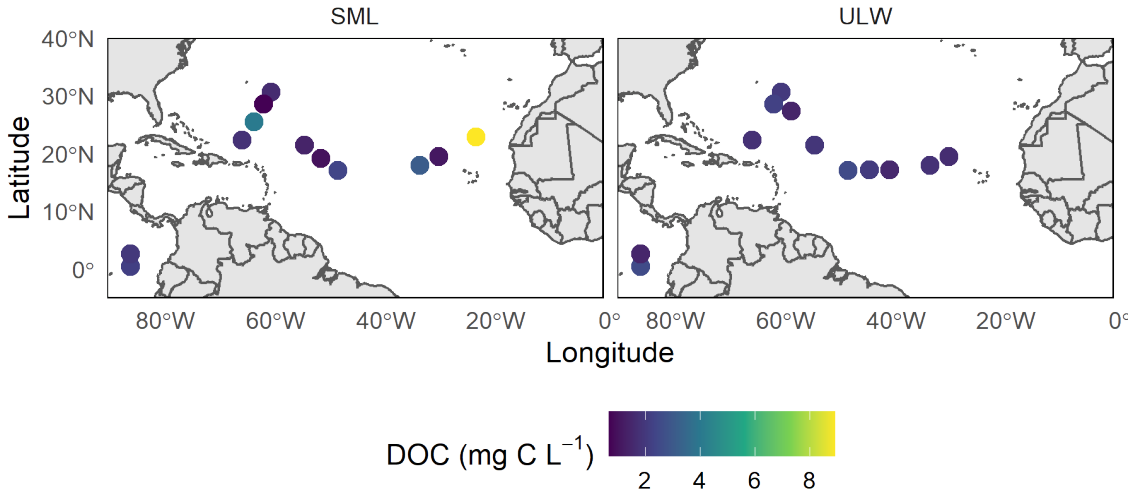

Figure 44: Map of DOC concentrations during the CONNECT cruise, in the SML and ULW.

Raune Fjord in Bremen, Norway.

To probe whether the SML was measurably different in DOC concentration compared to the ULW, the enrichment factors of DOC (EF_{DOC}) were calculated for this work (fig. 45). There is not a clear trend between the campaigns, nor within individual campaigns. The errors are noticeably higher in samples from the PML campaign; this was due to higher variability between repeat samples. These EFs were compared to previous reported values, focusing on studies that have sampled in the same approximate areas as this work (Table 12). In this work, samples from the PML campaign were overall enriched in DOC compared to the underlying water (EF_{DOC} = 1.5). During the CONNECT campaign, two measurements of EF_{DOC} were made during the Pacific leg of the cruise, with one sample showing depletion (EF_{DOC} = 0.86) and the other showing enrichment (EF_{DOC} = 1.36). During the Atlantic Ocean phase, on average samples were depleted in DOC in the SML (median EF_{DOC} = 0.9), however again a range of enrichment and depletion was observed (Table 12).

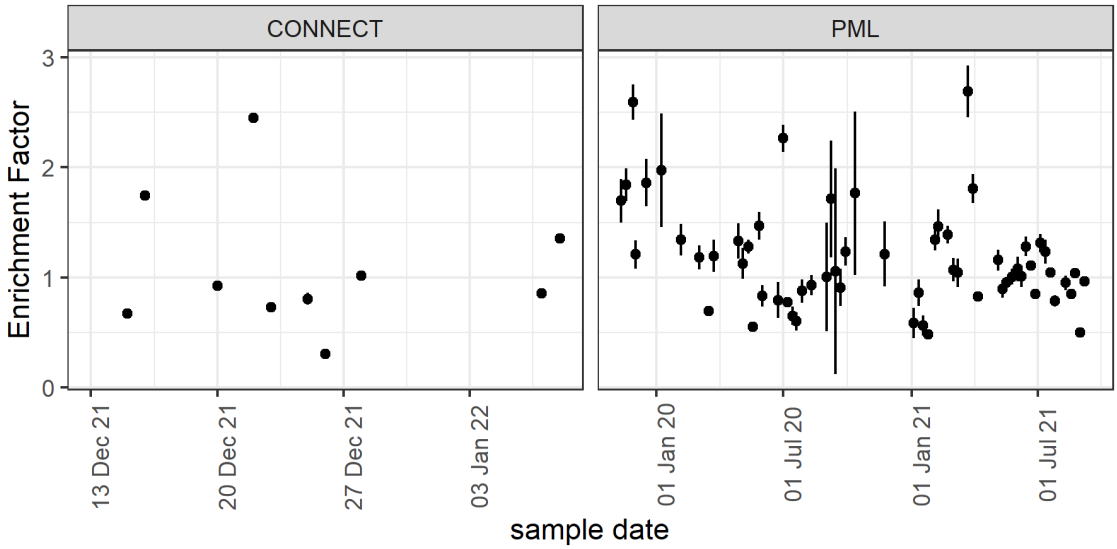

Figure 45: Timeseries of DOC EF during the CONNECT and PML campaigns.

Table 12: Literature values for enrichment factors of DOC in the SML.

EF_{DOC} min - max	median	SML thickness (μm)	Location	coastal or open ocean	Reference
0.2 - 9.1	1.1	50 - 243	Atlantic Ocean - Cape Verde	coastal	Pinxteren et al. (2017)
1.1 - 2.3	1.4	40 - 80	Atlantic Ocean - subtropical	open ocean	Reinthaler et al. (2008)
1.2 - 1.9	1.6	150	Atlantic Ocean - North	open ocean	Sieburth et al. (1976)
0.7 - 3.8	1.3	50 - 243	Atlantic Ocean - Cape Verde	open ocean	Pinxteren et al. (2017)
0.7 - 2.8	1.4	50 - 243	Atlantic Ocean - transect	open ocean	Pinxteren et al. (2017)
0.8 - 5.3	1.7	50 - 243	Atlantic Ocean - transect	open ocean	Pinxteren et al. (2017)
0.30 - 2.45	0.9	593	Atlantic Ocean - transect	open ocean	This Work
0.9 - 2		45 - 60	Equatorial Pacific	mixed	Engel and Galgani (2016)
1.0 - 1.5		41.3	Equatorial Pacific	mixed	Zäncker et al. (2017)
0.86 - 1.36	1.1	593	Equatorial Pacific	open ocean	This Work
0.97 - 1.05		-	North Sea	coastal	Stolle et al. (2020)
0.8 - 5.3	1.4	50 - 243	North Sea - Bergen	coastal	Pinxteren et al. (2017)
0.48- 2.69	1.5	653	English Channel	coastal	This Work

”-” denotes value not reported.

For previously reported values, the most extensive study by Pinxteren et al. (2017) reported EF_{DOC} for several locations throughout the Atlantic Ocean (Table 12). This study reported EF_{DOC} values which ranged from 0.20 to 9.09, demonstrating the wide range in enrichment factors that can be encountered.

One study determined that in the Equatorial Pacific, the greatest enrichment in DOC was measured for open ocean samples, compared to coastal samples (Zäncker et al., 2017). In this work, coastal samples (PML) were slightly more enriched in DOC compared to the open ocean samples obtained during the CONNECT cruise, in contrast to the findings of Zäncker et al. (2017), however our samples were collected in different regions and during different time periods.

These measurements demonstrate that for the DOC pool as a whole, there is not a large or consistent difference between the SML and the ULW, so is unlikely to predict or explain any differences in ozone uptake to the SML and ULW. The concentration of DOC is a measure of the organic content of a water sample, however does not tell us anything of the chemical makeup of the organic pool. Due to the chemical selectivity of ozone as an oxidant, analysis of individual compounds within the DOC pool are required for detailed understanding of acceleration of ozone uptake due to organic compounds.

Fatty Acids Targeted analysis of fatty acids in the DOC was performed for samples collected during the CONNECT and PML campaigns, and quantified by GC-MS, as described in detail in Weddell (2023). Concentrations of fatty acids are displayed in Figure 46 for the CONNECT cruise, and Figure 47 for the PML campaign. Summary statistics are described in Appendix 6.4.1.

Samples collected during the CONNECT campaign had mean concentrations of total, saturated and unsaturated fatty acids of 15.1, 14.4 and 0.8 μg L^{-1} in the SML, and 8.4, 8.1 and 0.4 μg L^{-1} in the ULW, respectively. For the PML campaign, the mean total, saturated and unsaturated fatty acid concentrations were 35.2, 20.0 and 15.3 μg L^{-1} in the SML and 64.6, 11.8 and 52.8 μg L^{-1} in the ULW. Samples collected during the PML campaign were therefore higher in concentration in fatty acids than those collected during the CONNECT campaign. The

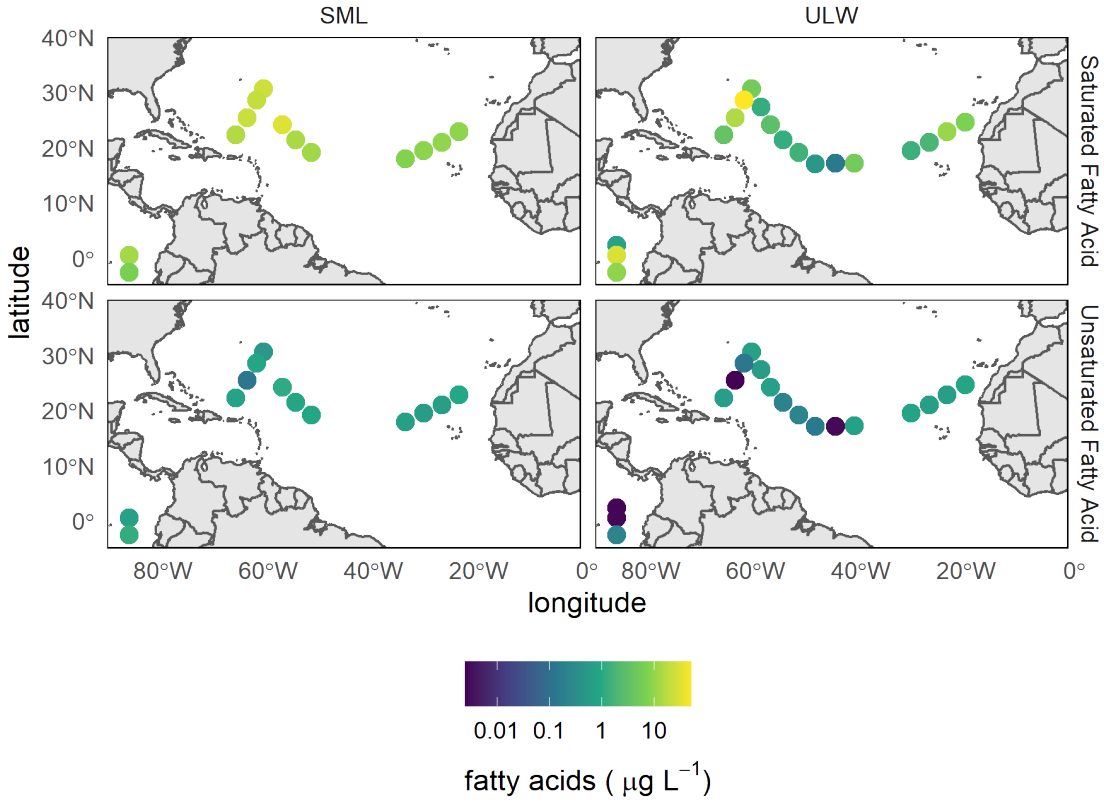

Figure 46: Concentrations of fatty acids in the ULW and SML across the CONNECT cruise track.

unsaturated fatty acid concentrations during the CONNECT campaign were particularly low, which was attributed to lower biological activity in open ocean water compared to coastal water, as well as indicating more aged seawater (Weddell, 2023).

The CONNECT samples can be compared to the results of Marty et al. (1979), which described open ocean measurements of fatty acids, and which were similarly low in concentration (mean concentration of 6.95 μg L^{-1} saturated fatty acids and 1.6 μg L^{-1} unsaturated fatty acids in the SML). The low concentrations measured by this work and by Marty et al. (1979) are indicative of the generally oligotrophic conditions of the open ocean.

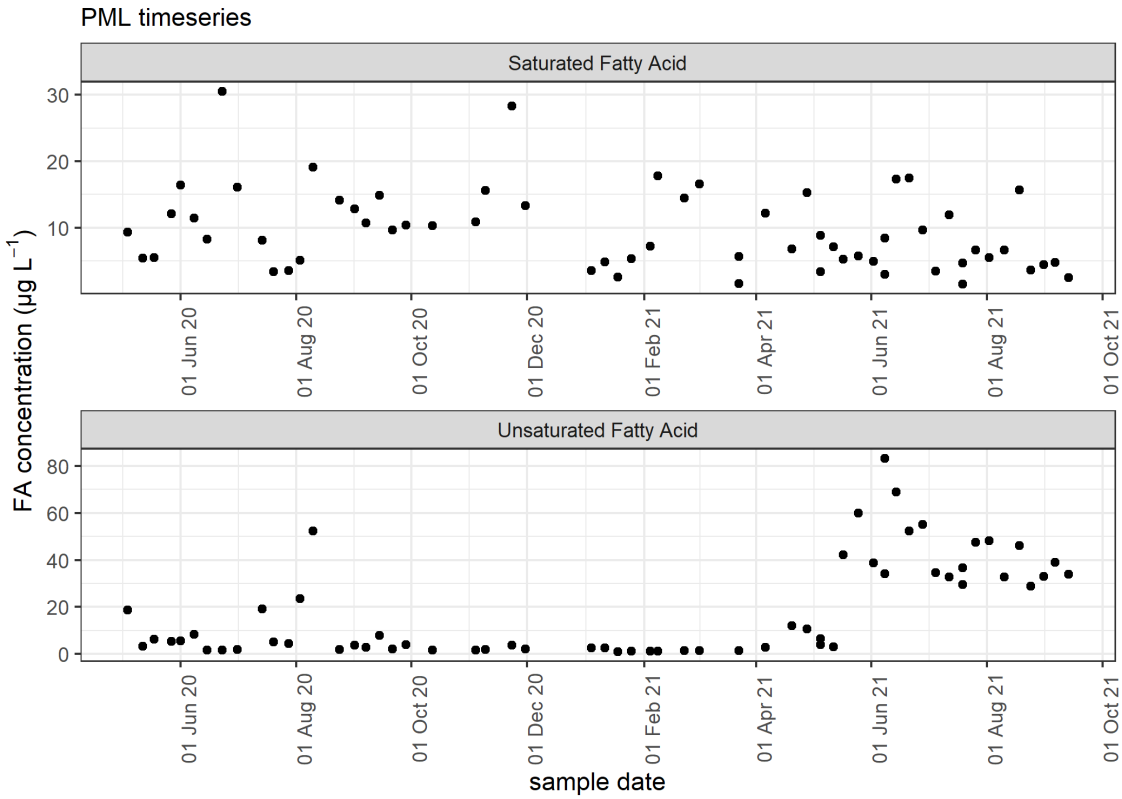

Figure 47: Concentrations of saturated and unsaturated fatty acids in the ULW and SML during the PML campaign.

The studies performed by Gašparović et al. (2007); Slowey et al. (1961); Daumas et al. (1976) sampled coastal water, and are therefore more comparable to the measurements obtained from the PML campaign. In all cases, the concentrations of fatty acids obtained (Table 8) were higher than the measurements described in the work of Weddell (2023); this could be due to the higher temperature waters sampled by Slowey et al. (1961) and Daumas et al. (1976) increasing biological productivity, or by the higher lipid content of cold water phytoplankton described by Gašparović et al. (2007).

Fatty acids are naturally surface active, due to their hydrophilic head and hydrophobic tail. To investigate whether this resulted in a fatty-acid rich SML, the enrichment factors of fatty acid concentrations across the CONNECT and PML campaigns were calculated and are shown in Fig 48.

Mean and median enrichment of unsaturated fatty acids during the PML campaign were 1.2 and 1.0, compared to 28.3 and 2.7 for the CONNECT cruise. The mean values during the CONNECT cruise were heavily influenced by two sam-

ples which were highly enriched in unsaturated fatty acids, however this was due to extremely low concentrations of unsaturated fatty acids in the ULW (0.003 μg L^{-1} for EF = 263 and 0.002 μg L^{-1} for EF = 49), rather than high SML concentrations. Excluding these two points, the highest EF for unsaturated fatty acids during this campaign was 7.1. SML collected during the CONNECT campaign was therefore more enriched in unsaturated fatty acids compared to PML, however with far lower relative concentrations.

The enrichment of fatty acids in the SML is variable, but can represent a substantial difference between bulk-phase fatty acids, and those which are available for reaction with ozone. This demonstrates the importance of separate consideration of the ULW and the SML for ozone uptake. Due to the small amount of data previously available for fatty acids in the SML, this dataset of fatty acid concentrations is a powerful complement to ozone uptake measurements, allowing analysis of their potential contribution to enhanced ozone uptake in seawater.

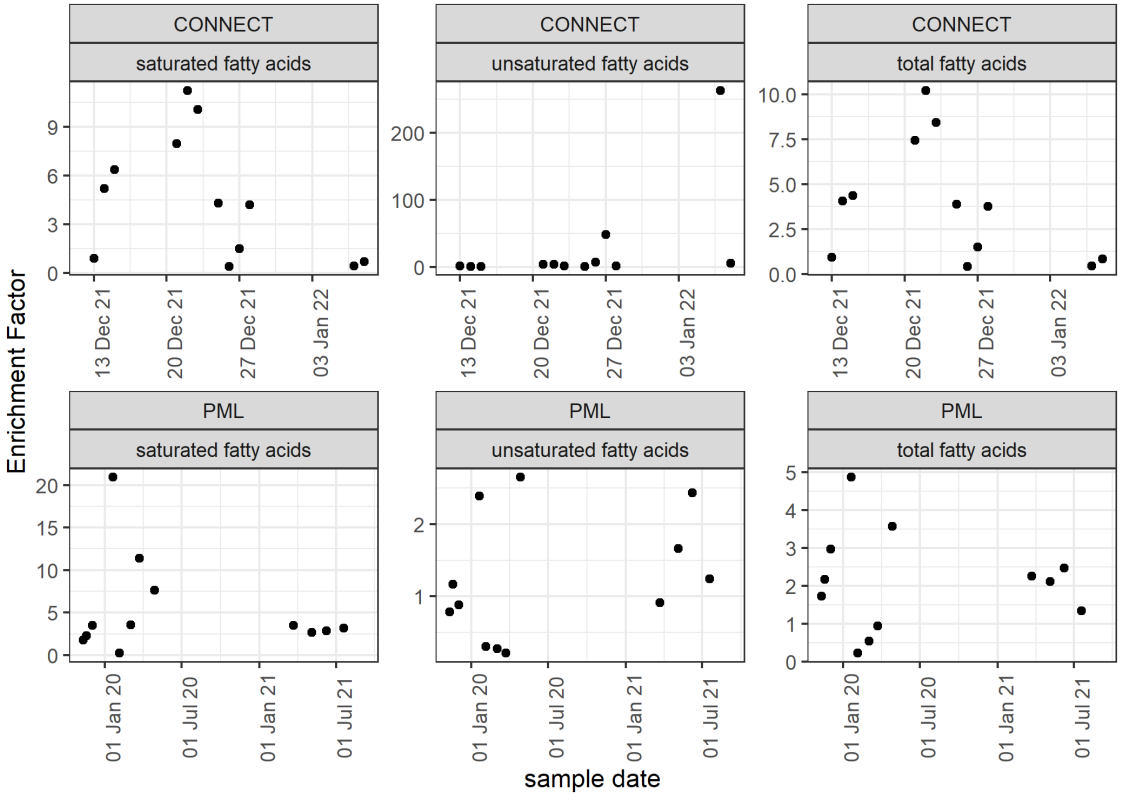

Figure 48: Enrichment factors of fatty acid concentration in the SML compared to the ULW for CONNECT and PML campaigns.

Surface Tension An enrichment in surface active substances (SAS) in the SML would lead to a lower surface tension of the SML compared to the ULW. It was demonstrated that the most effective way of storing samples for surface tension measurement was flash freezing unfiltered samples at -80 °C (Yousif Assiri, *pers. comm.*). This procedure was not known prior to PML sample collection, therefore these samples were frozen at -20 °C, and their surface active properties likely altered. Surface tension measurements from PML are therefore not displayed in this section. Measurements from the CONNECT and BLEACH campaigns are displayed in Figure 49. The measurements obtained during the BLEACH campaign have large errors due to inconsistency between repeat measurements. This is possibly because it is desirable to perform these measurements on an anti-vibration surface, e.g. a large stone block, which was not available during this campaign.

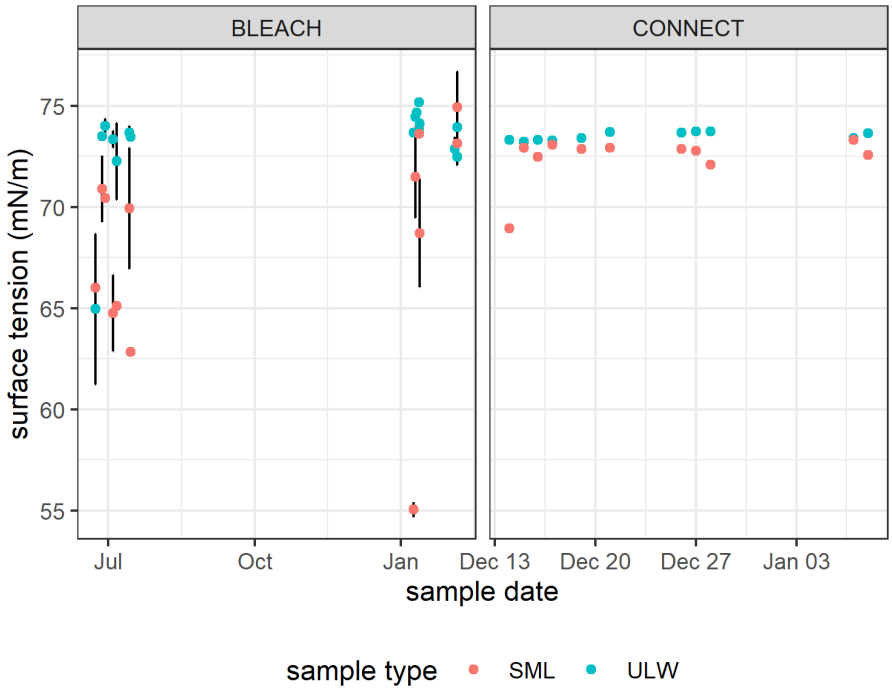

Figure 49: Surface tension measurements in the SML and ULW during CONNECT and BLEACH campaigns. Error bars show standard deviation of replicate measurements, which were very low for the CONNECT campaign.

For the CONNECT campaign, the surface tension of the SML was slightly depressed. The mean and median EF_{ST} during the CONNECT campaign were both 0.99 with an IQR of 0.01. The summer portion of the BLEACH campaign had a

mean and median EF_{ST} of 0.93 and 0.94. These surface tension measurements are the only results presented here which were not frozen prior to measurement. The winter portion has mean and median of 0.94 and 0.98, with the mean skewed low by one extremely low EF_{ST}, which was driven by an SML surface tension measurement of 55 mN/m; an unusually low value.

From the small amount of data available, it therefore appears the lowest enrichment factors of surface tension were obtained from fresh, unfrozen samples, indicating that the process of freezing may impact the surface activity of seawater samples.

The impact of surfactants on surface tension was quantified as film pressure, $\Delta\sigma$, and estimated by two methods. Firstly, the ULW was assumed to be surfactant free, therefore depression of surface tension in the corresponding SML sample was due to surfactants in the SML. $\Delta\sigma$ was quantified as the surface tension of the SML subtracted from the surface tension of the corresponding ULW. The second method uses a calculated reference surface tension at a given temperature (T, in $^{\circ}$C) for pure water, σ_w (Eq. 48), which is adjusted for salinity (S, in g/kg) to give σ_{sw} (Eq. 49), which is the reference surface tension at a given salinity and temperature, with no impact from surfactants.The measured SML surface tension is subtracted from this, giving $\Delta\sigma$ (Nayar et al., 2014). In the original literature source, σ_w and σ_{sw} were labelled γ_w and γ_{sw}; they were relabelled in this work to avoid confusion with uptake coefficients.

$$\sigma_w = 235.8 \times \left(1 - \frac{t + 273.15}{647.096}\right)^{1.256} \times \left(1 - 0.625\left(\frac{t + 273.15}{647.096}\right)\right) \tag{48}$$

$$\sigma_{sw} = \sigma_w \left(1 + 3.766 \times 10^{-4} S + 2.347 \times 10^{-6} St\right) \tag{49}$$

The impact of surfactancts on the surface tension of the SML collected during the CONNECT campaign, calculated using these two methods, are displayed in Figure 50. Using the ULW-SML difference, the surface tension of samples is consistently depressed, demonstrated by the positive $\Delta\sigma$ value. Using the method

described by Nayar et al. (2014), there are instances where the surface tension is similar to that predicted with no influence from surfactants.

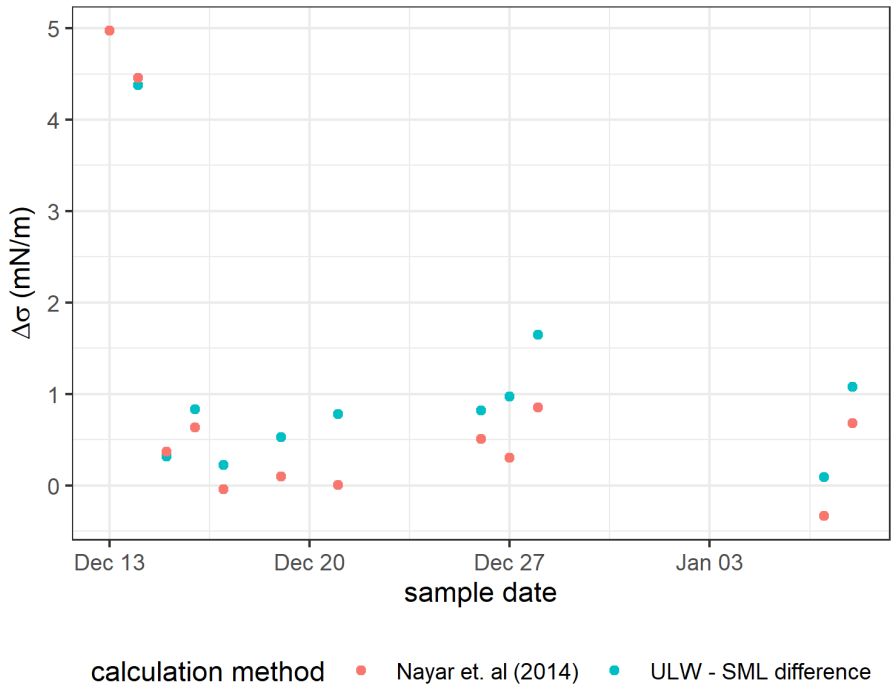

Figure 50: Depression of surface tension by surfactants in the CONNECT samples, calculated by the difference in measured ST for ULW and SML samples, and using the method described in Nayar et al. (2014).

For comparison, surface tension in SML and ULW samples were measured in the Delaware Bay (Burdette et al., 2022), with surface tensions of 69.65 to 70.82 mN m^{-1} for SML and 70.12 to 70.60 mN m^{-1} for ULW. These corresponded to surface tension depression by SASs of 3.36 to 4.11 mN m^{-1} for the SML.

Iodide Iodide measured throughout the PML campaign is displayed in Figure 51. Iodide measured during the CONNECT campaign is displayed in Figure 52. Across all campaigns, iodide in the underlying water ranged from 58 - 172 nM. In the SML, iodide was generally lower, ranging from 32 - 135 nM. The lowest average iodide in the SML was collected during the CONNECT campaign, which also had the lowest variation (considering IQR as a percentage of the median value).

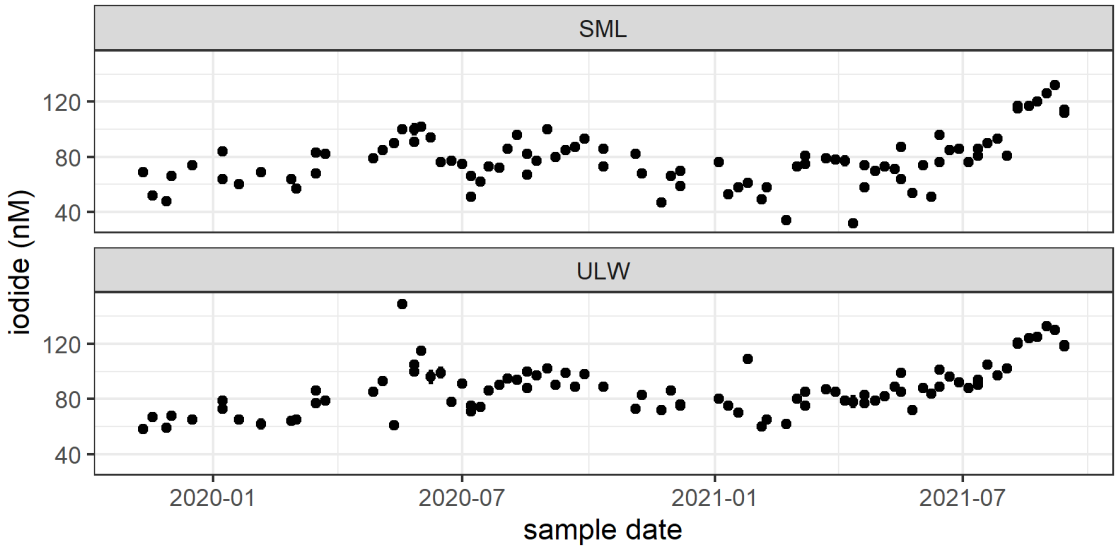

Figure 51: Concentration of iodide throughout the PML time series campaign. Error bars are not visible, but show the standard deviation of duplicate measurements.

Iodide has been measured reasonably extensively in surface waters, with most samples collected between 40°N and 40°S (Sherwen et al., 2019), and the most recent dataset of surface ($<$ 20 m depth) iodide measurements containing 1342 observations (Chance et al., 2019). Utilising the large number of observations, models have been developed for iodide prediction in surface waters (Chance et al., 2014; Sherwen et al., 2019; MacDonald et al., 2014). Surface waters in the context of these publications refers to the near-surface underlying water, not the sea surface microlayer. The first parameterisation was put forward by MacDonald et al. (2014), which parameterised iodide concentration as a function of sea-surface temperature (SST, measured in Kelvin), according to Eq. 50. No other variables were tested for co-dependency, and the iodide concentration predicted by this equation has an estimated uncertainty of approximately 50%, compared

to measured values.

$$[I^-_{(aq)}] = 1.46 \times 10^6 \times exp(\frac{-9134}{SST}) \tag{50}$$

A further study tested several variables as predictors for iodide concentrations (SST, latitude, nitrate, chlorophyll-a, salinity, mixed layer depth), and found SST (squared) to be the strongest predictor, with nitrate concentration proving the second-strongest (Chance et al., 2014). Iodide concentration can therefore be predicted from the single variable Equation 51, where SST is measured in °C. This fit of this equation, compared to the measurement data, had an R^2 of 0.61. The predicting power was improved by inclusion of a combination of variables, with Eq. 52 improving the fit, resulting in R^2 of 0.676. This model gives an improved estimate of iodide concentration, and despite relying on more variables, it is based on parameters which are commonly measured during seawater sampling.

$$[I^-_{(aq)}] = 0.225 \times SST^2 + 19 \tag{51}$$

$$\begin{aligned}[I^-_{(aq)}] = {} & 0.28 \times SST^2 + 1.7 \times latitude + 0.9 \times nitrate \\ & -0.020 \times mixed\ layer\ depth + 7 \times salinity - 309\end{aligned} \tag{52}$$

These two models disagree in predicted iodide concentration by 2 - 4 times (with the MacDonald et al. (2014) parameterisation predicting consistently lower concentrations, Fig. 52). The disagreement could be due to the smaller number of measurements used in the MacDonald et al. (2014) work, and the fact that the Chance et al. (2014) work included coastal measurements, which are generally higher than open-ocean iodide concentrations.

The current state-of-the-art for prediction of surface ocean iodide concentrations is a machine-learning based parameterisation developed by Sherwen et al. (2019). The Sherwen et al. (2019) parameterisation addresses previous issues by inclusion of a larger set of iodide concentrations (including coastal and open ocean observations), with the database being updated as new observations are made.

This model provides monthly predictions for iodide concentrations in a 12.5 x 12.5 km grid. In this work, several variables were tested for co-dependency (temperature, nitrate, phosphate, salinity, shortwave radiation, topographic depth, mixed layer depth and chlorophyll-a); it was determined once more that temperature was the strongest predictor for iodide concentration. The predicted annual surface iodide concentrations are displayed in Figure 35. Predictions fall within 0 - 240 nM iodide, with the highest concentrations in tropical and sub-tropical regions, consistent with the higher temperatures. It should however be noted that at higher temperatures, while iodide concentrations are expected to be higher, deposition may become limited by reduced ozone solubility in water, which would dampen the impact of iodide in tropical and sub-tropical regions (Ganzeveld et al., 2009).

To put our measurements in context, the results of the CONNECT cruise were compared to the available models (Fig. 52). The Chance et al. (2014) and Sherwen et al. (2019) models compared favourably to the ULW measurements. The MacDonald et al. (2014) model typically predicts iodide concentrations lower than the Chance et al. (2014) and Sherwen et al. (2019) schemes, and this is observed here. The MacDonald et al. (2014) scheme compared quite favourably to the depleted iodide in the SML observations, despite being developed to predict iodide in the underlying surface water.

The Sherwen et al. (2019) model was built on the largest database of iodide measurements, which continues to grow due to it following a ”living data” model. This means it is continually updated as new observations are made. This therefore represents a good indicator of the status-quo of iodide measurements, especially as the CONNECT cruise traversed a well-sampled region of the ocean. For a comparison of model performance compared to observations across different latitudes, see Fig. 7 in Sherwen et al. (2019). The good comparison between our ULW iodide measurements and the Sherwen et al. (2019) model grant confidence in both the model and in the oceanographic representativeness of our measurements.

In the context of ozone deposition to the ocean, the iodide in the SML is more

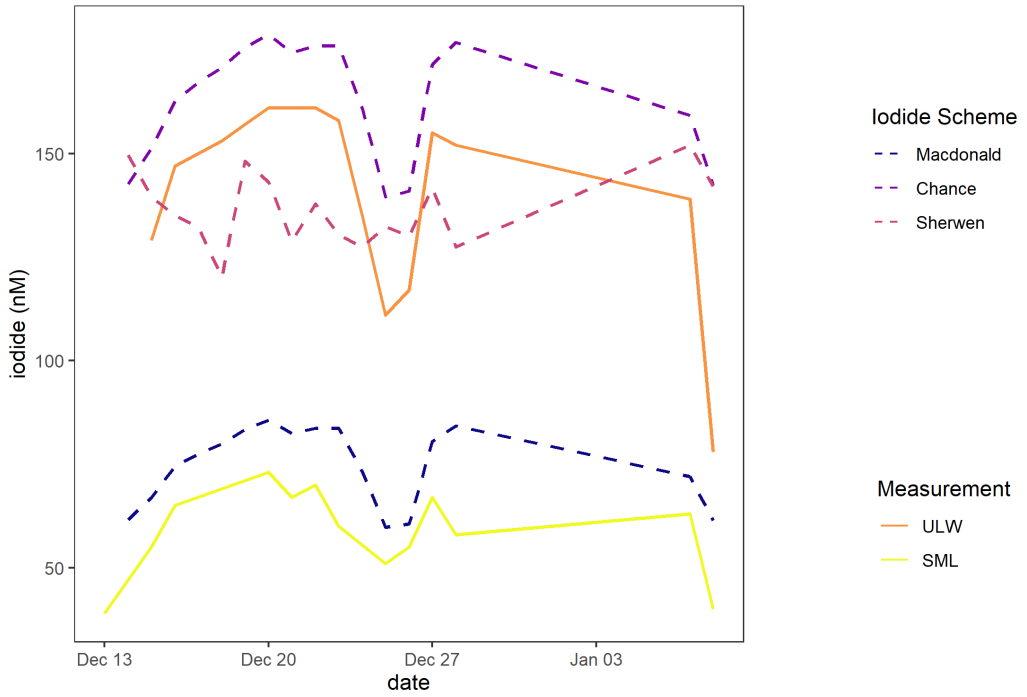

Figure 52: Measured iodide concentrations (solid lines) collected during the CONNECT cruise, for ULW and SML samples. Reported iodide concentrations were measured from samples collected before flow reactor experiments. Concentrations predicted by models are shown in dashed lines (Chance et al., 2014; Sherwen et al., 2019; MacDonald et al., 2014).

relevant than the iodide in the bulk water. While the Chance et al. (2014) and Sherwen et al. (2019) models predict ULW iodide quite well, an adaptation to the models would need to be developed to predict SML concentrations, however this would require a greater number of samples to be taken, to increase the temporal and geographical range of iodide SML observations.

A range of iodide concentrations were encountered across both SML and ULW samples. Given that temperature has consistently been found to be the strongest predictor of iodide concentration in the surface ocean, its correlation with iodide was tested for these samples. Temperature was a very strong predictor of iodide concentration during the CONNECT cruise, both in the SML and in the ULW. Despite only an approximately 3.5 °C range, R^2 values of 0.7 and 0.87 for SML and ULW respectively were obtained for the correlation between iodide and water temperature, consistent with the previous literature for underlying water (Chance et al., 2014; MacDonald et al., 2014). To our knowledge this has not previously been shown to be true for the SML, and could be a powerful tool for SML iodide

prediction.

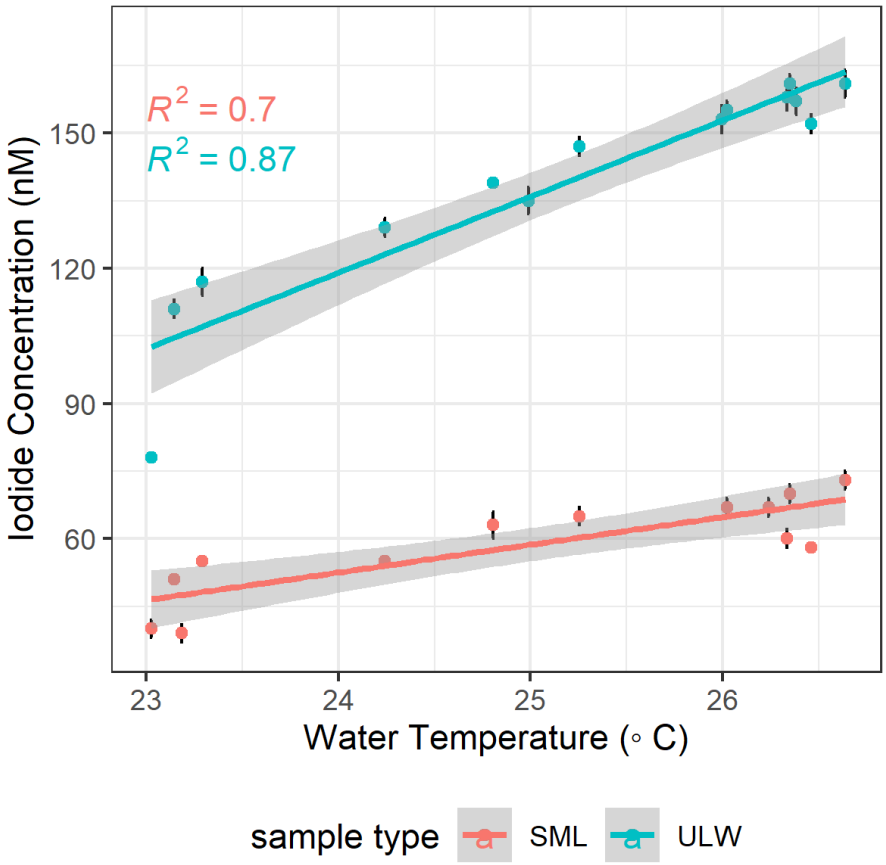

Figure 53: Correlation of measured iodide with water temperature during the CONNECT cruise.

To demonstrate the difference in iodide in the SML and ULW, enrichment factors were calculated, and displayed in Figure 54. The median EF_{iodide} for the PML campaign was 0.89, with a IQR of 0.14. The median EF_{iodide} for the CONNECT campaign was 0.43 with an IQR of 0.05, and for the BLEACH campaign, the median was 0.89 with IQR of 0.10. All campaigns demonstrate depletion of iodide in the SML, with this effect most noticeable in the CONNECT campaign, resulting from the low SML iodide.

The depletion of iodide was markedly greater in the CONNECT campaign, compared to the BLEACH and PML samples, which displayed similar depletion levels. For all three campaigns, samples for iodine speciation measurements were treated in the same way; filtered and frozen prior to storage. Previous work has shown freezing to be the most suitable method of preserving iodine speciation in seawater samples, however some random losses of iodide were observed (Cam-

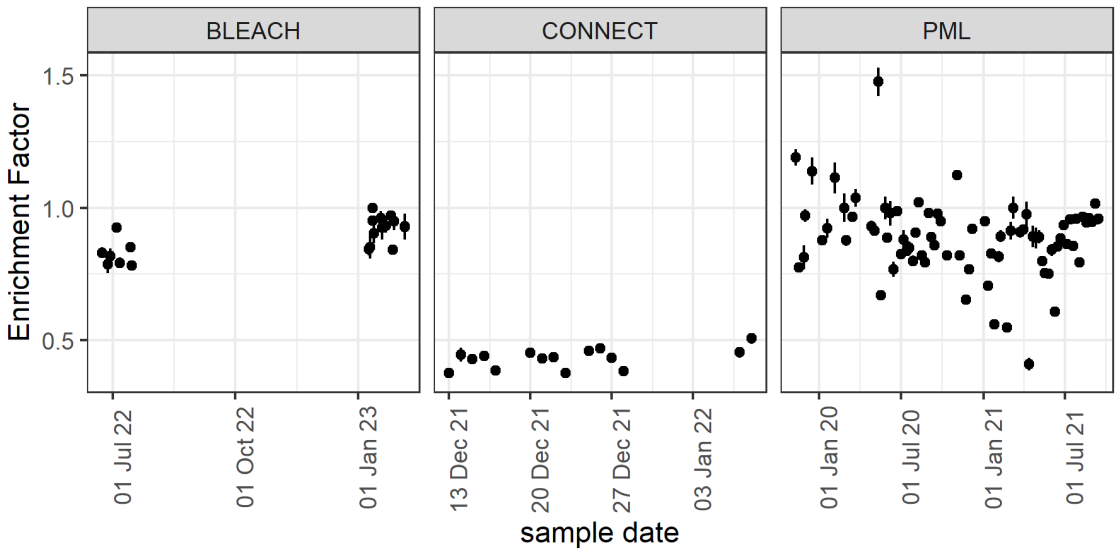

Figure 54: Enrichment factor of iodide in the SML compared to the ULW.

pos, 1997). The consistency of depletion in the CONNECT samples, demonstrated by the low IQR, indicated that random losses were likely not responsible for the high degree of depletion observed.

It was investigated whether iodide was being lost to the Garrett screen mesh, or from oxidation by atmospheric ozone. Tests were carried out whereby an iodide solution was exposed to mesh from the Garrett screen, and the iodide concentration measured as a function of mesh exposure time. A further experiment was carried out which measured iodide as a function of Garrett screen draining time (Appendix 6.4.2). No trend was observed between mesh or screen exposure time and measured iodide concentration, indicating this is not a sampling bias (Jones 2024, *in prep*).

Iodide depletion in the SML was described across a smaller depth in the SML by Pound et al. (2023), whereby ozone was anticipated to be depleted across the reacto-diffusive depth of ozone (Pound et al., 2023), on the order of a few microns. For a bulk iodide concentration of 100 nM, at 30 ppb atmospheric ozone and a sea surface temperature of 285 K, an iodide depletion in the reacto-diffusive depth of ozone of between 2 to 17.5 % was predicted between wind speeds of 0.1 and 9.5 m s^{-1}, with the greatest depletion at low wind speeds. Similarly, iodide depletion in the SML is consistent with the work of Schneider et al. (2020), where reduced ozone uptake was measured over artificial seawater over time, which

was attributed to iodide depletion in the surface layer. Applying their model to the environment, a depletion of iodide of only 0.3 % was modelled in the ocean. In both modelling studies, the mechanism for iodide depletion was iodide reaction with ozone occurring faster than replenishment from the bulk water into the SML. Both authors concluded that variations in turbulence have a strong impact on the extent of iodide depletion, due to changes in mixing from the bulk.

The depth of depletion studied in these publications are far smaller than the SML sampled in this work, therefore this cannot fully explain the observed depletion. It is postulated that there are several sub-layers which make up the upper boundary of the ocean, described as the nanolayer, microlayer, millilayer and centilayer (Hardy, 1997). Due to the thick SML collected in this work, there could be an influence from these distinct layers, and the complex interactions between them.

As discussed in Section 4.2.2, previous measurements on iodide enrichment and/or depletion in the SML have not found a statistically significant difference between the SML and ULW, however our measurements suggest a consistent depletion of iodide in the sea surface in both coastal and remote ocean areas. This could be a result of improved analytical capabilities; during the MILAN campaign iodide concentrations were measured using square wave voltammetry, a technique which is known to have issues with reproducibility (Jones et al., 2023). In the study by Chapman and Liss (1981), iodide was quantified by the difference in total iodine and iodate, quantified by colourimetry. Measurements quantified by difference have an inherently larger error than measurements made by a single quantification. The analytical accuracy of these methods may not have been great enough to capture the nanomolar differences in iodide in the SML and the ULW.

4.4.2 Alterations to Iodine Speciation Following Ozone Exposure

If ozone uptake to seawater were occurring solely due to reaction with iodide, it would be possible to predict iodide loss over time, using the kinetics calculated in Chapter 3. An experiment was carried out to measure the change in iodide

concentration after prolonged ozone exposure, and calculations were performed to attempt to model the change in iodide throughout the experiment.

100 ml of sample was placed in the flow reactor, and stirred without pumping, and ozone (60 ppb) was flowed over the solution at a continuous flow rate of 500 sccm. Aliquots of the liquid phase were removed at intervals, from 1 minute up to 45 minutes of ozone exposure. Once removed from the flow reactor, the samples were filtered and frozen, and iodide quantified subsequently by IC.

This experiment was carried out twice during the CONNECT cruise; once on underlying water, and once on SML, both of which were unfiltered and unfrozen at the time of the experiment. Sample details are described in Table 13.

Table 13: Samples used in ozone exposure experiments

	D1	D2
sample type	underlying	SML
sample date	02/01/2022	07/01/2022
approximate location	Caribbean	Equatorial Pacific
initial iodide (nM)	157	63
DOC (mg L^{-1})	1.82	2.18
saturated fatty acids (nM)	below LOQ	62
unsaturated fatty acids (nM)	below LOQ	3
surface tension (mN m^{-1})	not available	73.3

The measurements of iodide during these experiments are displayed in Figure 55, by the round points. For underlying water, there was a strong decrease in aqueous iodide with increasing ozone exposure. This was consistent with expectations, whereby iodide depletion occurs due to reaction with ozone.

Conversely, for D2, the SML sample, there was very little change in iodide concentration over the course of the experiment. In this experiment, it appears reaction with iodide was being ”blocked”.

A calculation was carried out to contextualise these measurements according to the expected loss. An approximation of iodide lost over the course of the experiment was made using the method described in Section 3.4.1.3. The time between each aliquot removal was treated as a time step. The iodide concentration prior to ozone exposure was used as the starting condition. The rate of iodide loss was calculated from the aqueous ozone and iodide concentrations, and the rate

coefficient calculated in Chapter 3, according to Eq. 30. The total iodide available to ozone was calculated for the volume determined by the reacto-diffusive length of ozone (Eqs. 31 to 34), and the iodide loss during each time step calculated by the rate of loss multiplied by the time step length (Eq. 35). The same calculations were carried out for each time step, with the final predicted iodide concentration from the previous time step used as the starting condition for the next. The reacto-diffusive volume during each time step was different due to aliquot removal and lowering iodide concentrations.

The ozone concentration varied through the length of the flow reactor, between the applied concentration (60 ppb) and the minimum residual ozone concentration (34.5 ppb for D1 and 28.5 ppb for D2). Iodide loss according to both of these upper and lower ozone concentrations was calculated, and displayed as the ribbon traces on Figure 55.

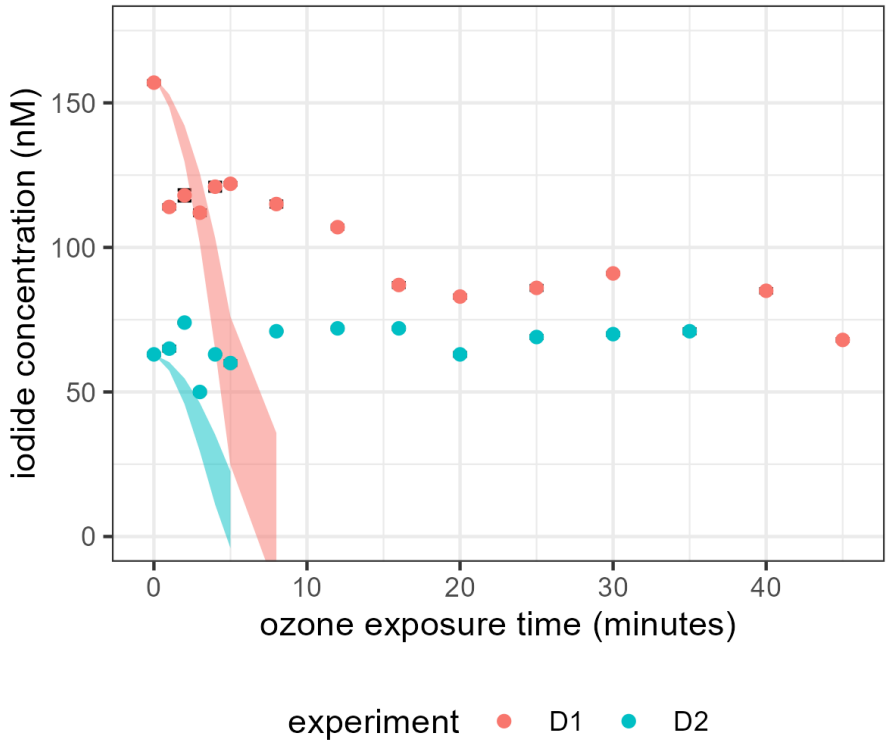

Figure 55: Change in aqueous iodide concentration as a function of ozone exposure, for D1; underlying water, and D2; SML. Ribbon traces show the predicted iodide concentrations, calculated using bulk-phase reaction kinetics. The top boundary of the traces was calculated using the minimum (residual) ozone concentrations, while the bottom boundary was calculated using the maximum (applied) ozone concentration of 60 ppb.

For both samples, iodide was expected to be depleted within minutes (as low as 5 minutes for the SML D2 and as low as 8 minutes for the ULW D1). In both experiments, iodide remained in the bulk solution for the duration of the experiment, potentially indicating that ozone-iodide reactivity was blocked in the seawater, and is consistent with the large disagreement between predicted and measured reactivity for seawater samples discussed later in this work. It is clear that ozone was consumed by the solution, as the residual ozone was significantly lower than the applied concentration, therefore this is an indication that while species in the seawater were reacting with ozone, reaction with bulk iodide was minimal. During the experiment, some iodide loss in the ULW was observed, but less than was predicted kinetically. For the SML this effect was the most pronounced, with little variation in bulk iodide throughout the whole experiment.

In terms of differences between the two samples, their overall DOC concentration was similar, however the SML samples contained measurable concentrations of fatty acids, in particular unsaturated fatty acids. These surface-active species could have been more efficiently reacting with ozone, and/or the large concentration of saturated fatty acids could be blocking the transfer of ozone to the aqueous phase, thus blocking the ozone-iodide reaction.

For these samples, full iodide speciation was measured, however for experiment D1, a complete mass balance was not conserved (total iodine concentration dropped from approx. 410 nM to 250 nM over the 45 minutes of ozone exposure, Appendix 6.4.3). This could be due to loss of iodine-containing species to the gas phase, e.g. as HOI and I_2, or by partitioning to species not measurable by this IC method. The full speciation over the course of the experiment is available in Appendix 6.4.3.

For routine flow reactor experiments, samples were pumped through the flow reactor to avoid depletion of iodide during the experiment time, resulting in a residence time of seawater in the flow reactor of less than 2 minutes. By analysis of the iodine speciation before entering the flow reactor, and from the sample taken at the midpoint of the experiment, it was sought to verify that iodide was

not being depleted. Unexpectedly, and in particular during the CONNECT campaign, iodide concentrations were often observed to increase during this period, concurrent with a decrease in concentration of DOI. This led to the conclusion that iodide was being released from organic compounds following ozone exposure. This trend was not as strongly observed during the PML campaign, with increases and decreases seen in both iodide and DOI. An increase in iodide was not observed in measurements of iodide in phosphate buffer following ozone exposure (Appendix 6.2.3), indicating this was not a systematic error.

An increase in DOI is possible via a mechanism of reactive iodine species, e.g. HOI, reacting with organic matter. For example, HOI was determined to react with phenolic compounds with second order rate constants of up to $\approx 10^7$ M^{-1} s^{-1} at pH 8, depending on the functional groups (Zhao et al., 2017b). This study demonstrated a high degree of iodine incorporation into the organic model compounds following reaction; greater than 95 $\%$ halogen incorporation was recorded for the reaction between HOI and phenol at pH 8, 23 $^{\circ}$C.

Conversely, loss of DOI following ozone exposure could be due to hydroxyl radical reactions liberating iodide from DOI. A study, which generated hydroxyl radicals by application of hydrogen peroxide and Cu(II), measured complete recovery of iodide from iodine containing organic x-ray tracers at pH 8 (Fono and Sedlak, 2007). Hydroxyl radicals could be present in these samples as they could be released following ozone reaction with DOM with electron-withdrawing components (von Sonntag and von Gunten, 2015). Other hydroxyl radical formation routes were considered, including the UV-induced reaction of O_3 with H_2O to form O_2 and peroxide. The peroxide ion (HO_2^-) can go on to react with ozone to form the hydroxyl radical (von Sonntag and von Gunten, 2015). UV radiation was not expected, as both experiments were carried out indoors, and at night-time. Additionally, it is expected that if any UV were present, it would be attenuated by the glass of the flow reactor, and the $\approx$ 1 cm thick water jacket.

To reconcile the fact that DOI was sometimes lost and sometimes gained, it is proposed that two pathways could be occurring concurrently. The reaction with

DOM to form hydroxyl radicals could be occurring in all samples, leading to an initial DOI loss and iodide gain. Reactions of ozone with iodide, which form reactive iodine species such as HOI could then also occur, integrating iodide into DOI. Whether there is a net loss or gain of DOI would depend on the dominant pathway occurring, with more iodide-ozone reactions leading to a greater increase in DOI.

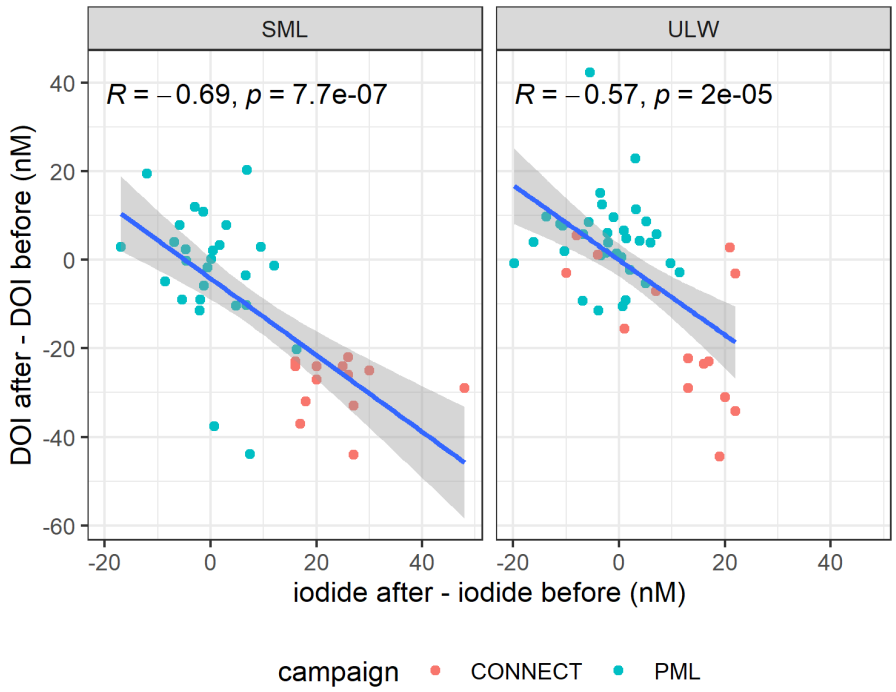

Figure 56: Change in aqueous iodide and DOI concentrations following ozone exposure during flow reactor experiments.

For experiment D2 above, it was investigated whether the lack of iodide loss following ozone exposure was a result of partitioning from DOI to iodide, however the measured DOI concentrations throughout the experiment showed the same trend as iodide; very little change throughout the experiment (Appendix 6.4.3). This supports the conclusion of negligible formation of reactive iodine-containing compounds, due to few ozone-iodide reactions occuring. For experiment D1, there was an increase in DOI concentration from zero to 13 nM, which plateaued after 8 minutes, potentially after all possible iodine incorporation was complete. Previously, formation of volatile organo-iodine compounds was observed following ozone exposure to DOM and iodide-containing North Sea seawater, demonstrating the propensity for HOI and I_2 to react with marine DOM (Martino et al., 2009).

Conversely, a buffered solution of iodide and marine-origin DOC showed reduced emission of I_2 compared to a buffered iodide-only solution, however this was attributed to reduced physical transfer of I_2 from the liquid phase to the gas phase (Shaw and Carpenter, 2013). Similarly, reduction of iodine-containing emissions from ozone-oxidised SML samples was observed, but attributed to increased solubility of I_2 in the organic rich SML (Tinel et al., 2020).

Measurement of gaseous iodine-containing compounds from ozone-oxidised SML would advance this finding, however these results are an indication that the presence and identity of organic compounds has the ability to alter emissions of halogens from seawater following oxidation. This is also an indication that ozone reactions with SML water cannot be modelled by simple ozone-iodide kinetics alone.

This finding formed the basis for using the ”after” sample in calculation of the contribution of iodide to ozone uptake. Because the ”after” sample was collected during the middle reaction time between ozone and the seawater, this is the best representation of the average biogeochemical state of the water in the flow reactor, whether iodide was lost or gained during the experiment.

4.5 Ozone Uptake to Seawater; Differences Between SML and ULW

As highlighted in previous sections, the SML is a region of the ocean which is chemically distinct from the underlying water, likely to interact differently with ozone. Because the SML is the site of mass and energy transfer between the ocean and the atmosphere, it is important to understand ozone uptake to the SML, specifically.

Ozone uptake is presented here as a corrected uptake. This was calculated by Equations 53 and 54; it is the uptake which has had the effects of gas phase diffusion removed. Removal of gas phase diffusion resistance means $\gamma_{corr} > \gamma$. In this work, the mean ratio across CONNECT and PML ozone uptake measurements of γ_{corr} to γ was 1.12, with a range of 1.04 to 1.28.

$$v_{d_{corr}} = \frac{1}{r_{tot} - r_{diff}} \tag{53}$$

$$\gamma_{corr} = \frac{4v_{d_{corr}}}{\omega} \tag{54}$$

Measured γ_{corr} for the PML and CONNECT campaigns are displayed in Figure 57, with a comparison to uncorrected uptake, γ. It is observed that the samples with the highest γ_{corr}, and consequently highest ozone reactivity were collected during the CONNECT campaign. The mean and standard deviation of γ_{corr} on the CONNECT campaign was 4.34 $\pm$ 0.7 $\times 10^{-6}$ for ULW samples and 4.86 $\pm$ 0.7 $\times 10^{-6}$ for SML samples. The mean γ_{corr} on the PML campaign was 2.01 $\pm$ 0.4 $\times 10^{-6}$ for ULW samples and 1.94 $\pm$ 0.6 $\times 10^{-6}$ for SML samples. The measurements during the CONNECT campaign were higher in uptake, therefore more impacted by gas-phase diffusion. This means there is greater difference between γ_{corr} and γ during CONNECT, compared to PML.

Sources of errors in γ_{corr} include uncertainty in tube dimensions (Table 3), and error propagated from standard errors in regressions of ln(O_3) against reaction time, as discussed in Section 3.5.1. The uncertainties in measurements of ozone uptake to seawater are lower, relatively, compared to measurements over iodide solution, as the blank measured to the glass surface was lower than the blank measured to the phosphate buffer solution (Fig. 18).

The distribution of γ_{corr} within both SML and ULW groups was tested for normality, using the Shapiro-Wilk's method (Yazici and Yolacan, 2007). For both SML and ULW on CONNECT the distribution of data were not significantly different from the normal distribution (p = 0.32 and 0.78, respectively, where H_0 = the sample distribution is normal), therefore parametric statistical analysis was performed. The paired t-test was used to determine if the two groups were distinct from each other, and it was determined that γ_{corr} was different between the SML and the ULW to the 95% significance level (p = 0.004). The SML collected during the CONNECT cruise therefore appears to be more reactive to ozone than the underlying water.

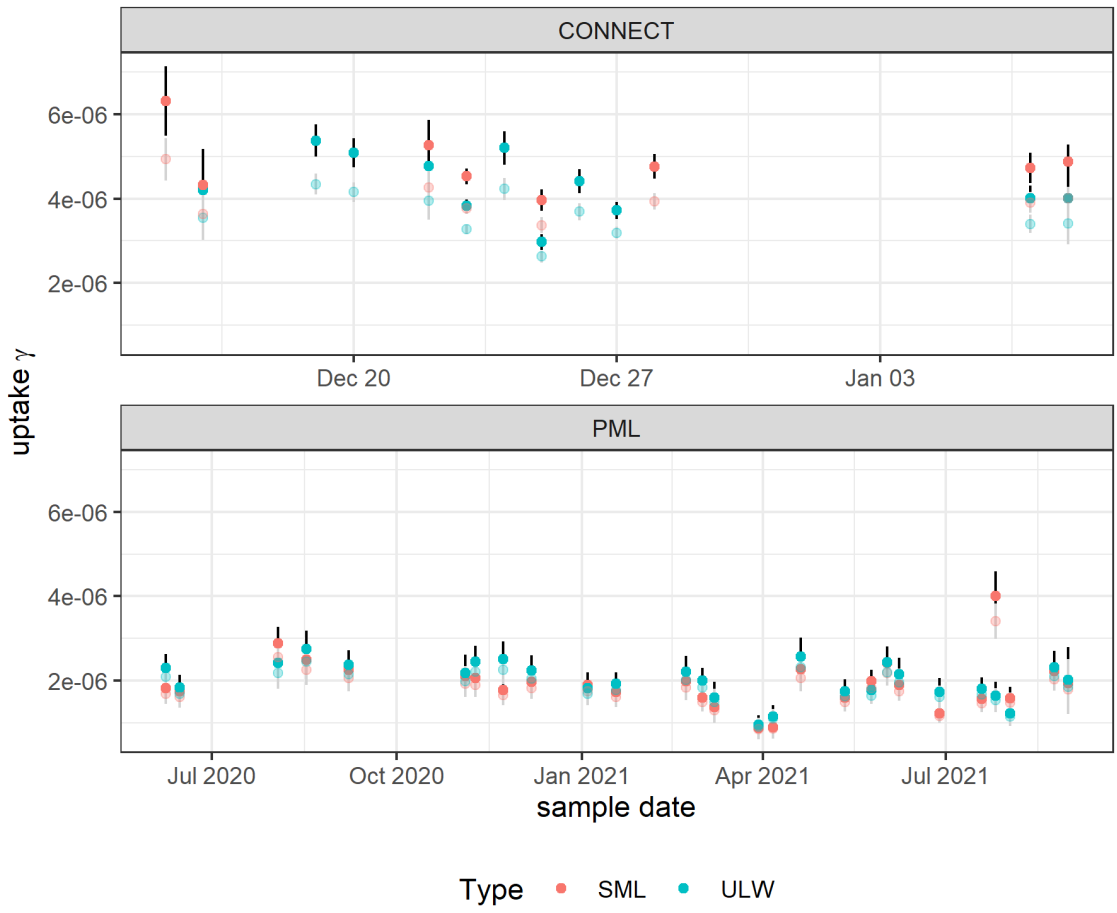

Figure 57: Time series of measured uptake for CONNECT and PML campaigns. γ_{corr} is displayed in solid points, uptake not corrected for gas-phase diffusion, γ, in transparent points.

For the PML series, γ_{corr} of the ULW samples were normally distributed (p = 0.28, Shapiro-Wilk's test), however the SML samples were significantly different from a normal distribution (p = 0.01), therefore a paired t-test was not performed.

Ratios of $\gamma_{corr\,SML}$:$\gamma_{corr\,ULW}$ are displayed in Fig. 58. Enhanced ozone uptake is observed in the CONNECT SML, with a mean ratio and standard deviation of $\gamma_{corr\,SML}$:$\gamma_{corr\,ULW}$ of 1.17 ± 0.1. For the PML samples the mean ratio obtained was 0.97 ± 0.3, leading to the conclusion that SML samples collected during the PML campaign did not have consistently greater ozone uptake than the corresponding underlying water.

The greater ozone-reactivity of the SML compared to the ULW on the CONNECT cruise contradicts the depleted iodide in the SML. If iodide-reactivity was the sole driver of ozone uptake, a less reactive SML would be expected, compared to the ULW. This is therefore a strong indication that there is a significant influence of

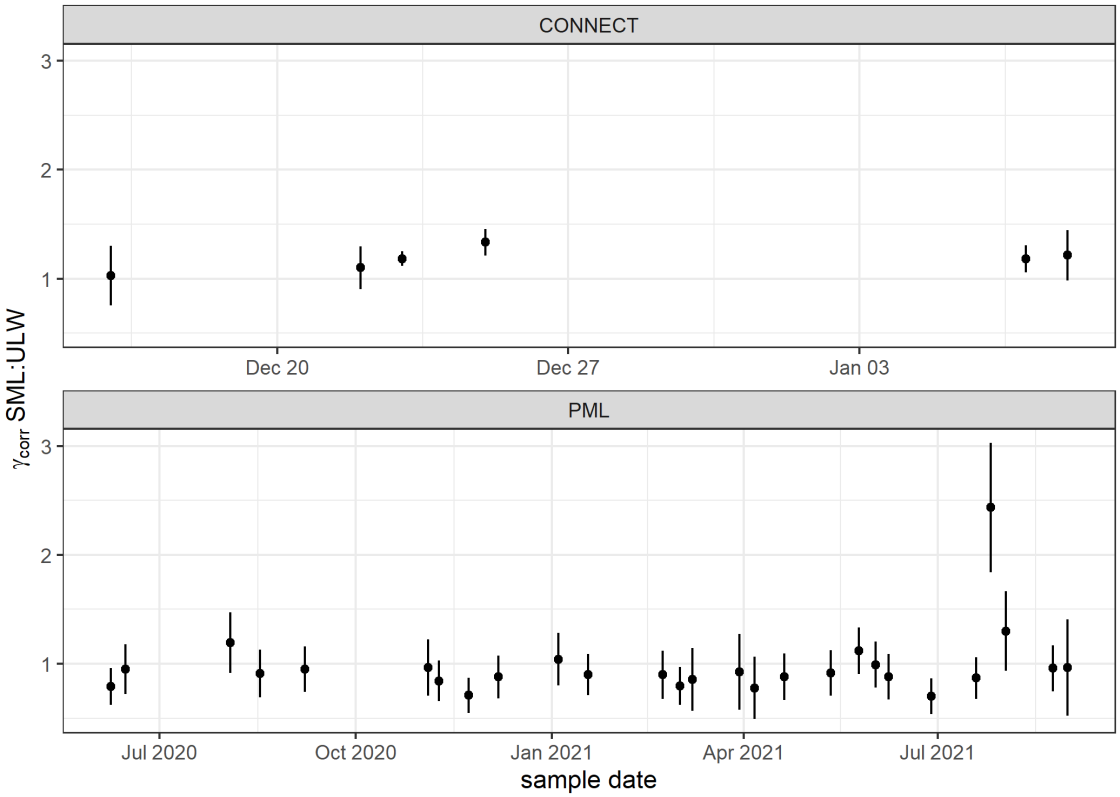

Figure 58: Ratio of γ_{corr} of SML compared to ULW samples for CONNECT and PML campaigns, where paired samples are available.

ozone reactions with other compounds.

To investigate whether differences in DOC or surface tension were predictors of differences in γ_{corr} for SML and ULW samples, $\Delta\sigma$ (calculated by the ULW-SML difference) and EF_{DOC} values were tested against the ratio of γ_{corr}SML:γ_{corr}ULW. There was no clear correlation for either, possibly because many surfactants and components of DOC are not reactive to ozone. It was therefore concluded that ozone uptake could not be parameterised based on the DOC pool as a whole.

The surface tension of the PML samples reported here were measured on filtered frozen samples, to be consistent with the filtered and frozen ozone uptake experiments. It is therefore not likely to be a true representation of the *in-situ* surface tension of the SML in the English Channel.

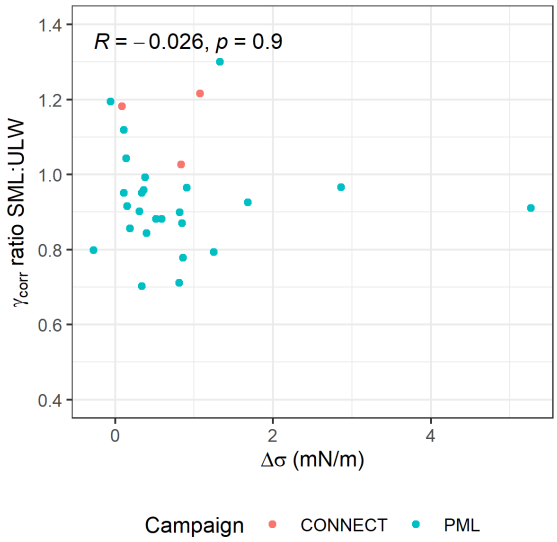

Figure 59: Ratio of corrected ozone uptake for SML:ULW samples, compared to $\Delta\sigma$, calculated by the ULW - SML ST difference, for CONNECT and PML campaigns.

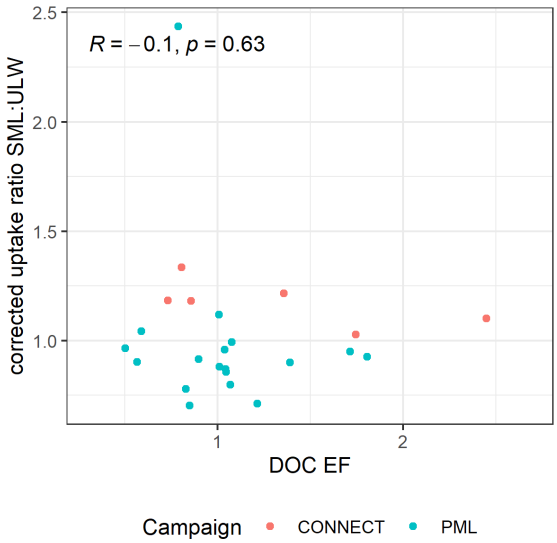

Figure 60: Ratio of corrected ozone uptake for SML:ULW samples, compared to EF_{DOC} for CONNECT and PML campaigns

4.6 Contribution of Iodide to Ozone Uptake

It was sought to understand how much of the measured ozone uptake could be explained by the reaction of ozone and iodide alone. In this section, γ_{aq} was calculated according to Eq. 8 and 9, using the measured iodide concentrations in the seawater samples and the kinetics measured in Chapter 3.

An assumption was made that all bulk-phase reactivity was due to the reaction between ozone and iodide. The relative contribution of aqueous ozone-iodide reactions to overall reactivity is displayed in Figure 61, with the percent uptake due to iodide calculated according to Eq. 55.

$$\%\ uptake\ due\ to\ iodide = \frac{\gamma_{aq}}{\gamma_{corr}} \times 100 \tag{55}$$

Temperature and salinity dependent Henrys law coefficients and D_{aq} were calculated according to the method described by Johnson (2010), using the salinity measurements in Appendix 6.4. For the CONNECT samples, the salinity of the SML was not measured, therefore the salinity of the corresponding ULW was applied. The mean and median ratio of salinity of the corresponding SML and ULW samples during the PML campaign were both 1.00, with a standard deviation of 0.05, therefore this assumption was deemed acceptable to apply to CONNECT samples.

For inclusion in Eq. 8, it was attempted to estimate α_{aq} using results described in Chapter 3. From Equation 8, a graph of γ_{corr} against $\sqrt{iodide\ concentration}$ yields information on $1/\alpha_{aq}$ (Appendix 6.4.4). Intercepts were scattered above and below zero, therefore accurate determination of α_{aq} was not possible. A mean value of -6.5×10^{-5} was obtained (range of -1.4×10^{-5} to $+2 \times 10^{-4}$), which, as well as being negative, was lower than the accommodation coefficient for ozone over water ($\alpha_{aq} > 10^{-3}$) (Ammann et al., 2013). It was therefore determined that this value was not appropriate to use, and the assumptions for α_{aq} and α_{surf} described in Moreno et al. (2018) were used. These were based on measurements made by Magi et al. (1997); the higher uptake coefficients measured in their work would

have a greater contribution of α_{aq}, making their measurements more suitable for its determination. At the uptake coefficients described here, the model is not sensitive to the values of α_{aq} and α_{surf}, therefore their contributions could not be assessed, but are also not of importance.

The iodide concentration used for these calculations was the ”after” flowtube sample, which was taken at the mid-point of the measurement (the same procedure as was used in Chapter 3). This is due to the change in iodide speciation observed following ozone application, as discussed in Section 4.4.2. This measurement was deemed the most representative of the average iodine speciation, and hence iodide concentration, during the course of the experiment. To capture the range of iodide concentrations possible during the experiment, an error in iodide concentration of 2 times the before-after difference was applied.

Errors in estimation of γ_{aq} were also considered from three other sources; uncertainty in the ozone-iodide rate coefficient, in the Henry's law coefficient for ozone solubility in seawater, and uncertainty in the aqueous diffusivity of ozone in seawater. Uncertainties in H and D_{aq} were estimated as 10% and 25%, respectively, by Johnson (2010). Uncertainty in the rate coefficient was taken as the average percentage error in the rate coefficients determined for each temperature in Chapter 3; this was 15.1 %.

For the CONNECT campaign, uptake due to iodide under-estimates measured reactivity, in both the SML and the ULW. Percent uptake due to iodide ranged between 25.0 and 38.5 % for SML samples, while for the ULW ranged from 39.2 to 66.3 %. For the PML campaign, iodide contributed 52.2 to 137.7 % in the ULW and 36.0 to 148.2 % in the SML. Like for the CONNECT campaign, there were situations where γ_{aq} under-predicted γ_{corr}, indicating the presence of other reactive species. However, there were also instances where γ_{aq} over-predicted the measured reactivity, suggesting the influence of a blocking, or dampening effect.

Few previous laboratory studies regarding this matter have been carried out. From ozone uptake measurements over North-Sea seawater, DOC was determined to be responsible for 2.5 - 5 times as much reactivity as iodide (Shaw and

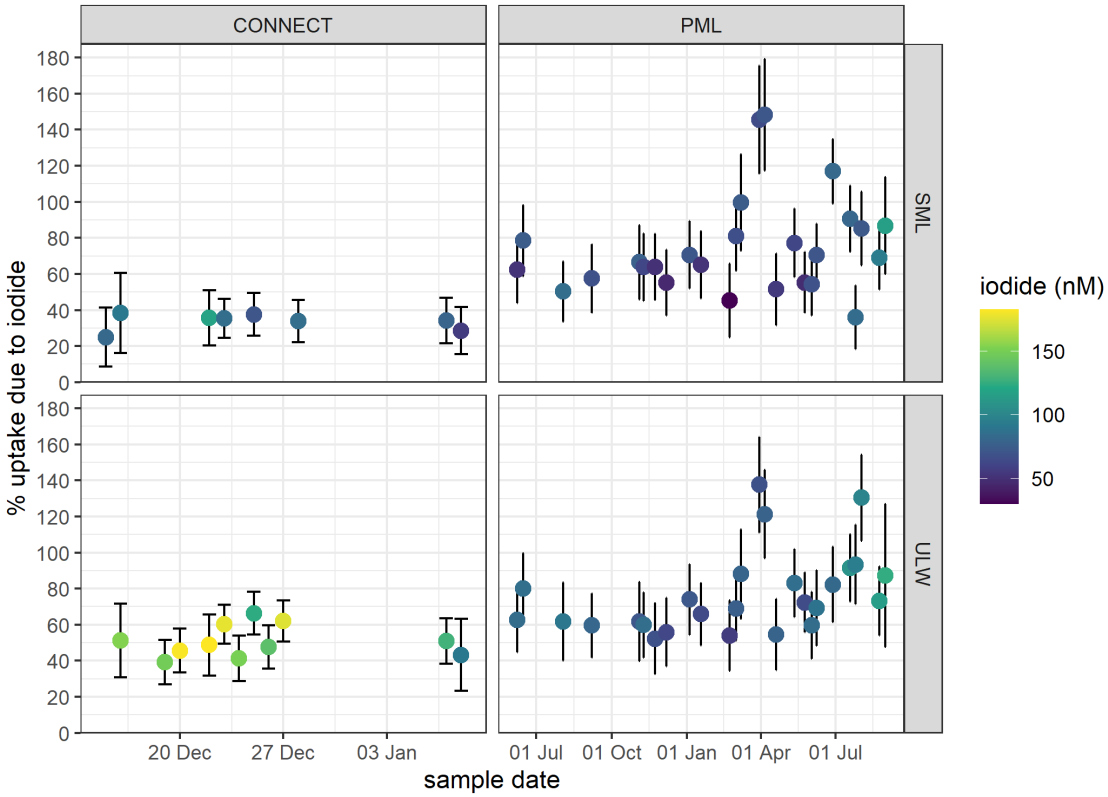

Figure 61: Percent contribution of iodide to measured uptake. Error bars are propagated from uncertainty in γ_{corr}, H, D_{aq}, the concentration of iodide and rate coefficient between ozone and iodide.

Carpenter, 2013). Over an artificial solution of buffered (pH 8) iodide and DOM (Suwannee River NOM), similar contributions to ozone uptake enhancement were observed for iodide and DOM (Martino et al., 2012). One other field study has been carried out, where ozone uptake was measured across an Atlantic cruise following a South-North transect. Ozone uptake was measured to fresh, unfiltered ULW samples, and the iodide contribution to uptake subtracted from the total ozone uptake. It was determined that iodide could explain on average 2/3 of measured ozone uptake (Ming-Xi Yang, *in prep*).

The possible dampening effect acting on PML samples could be due to a layer of non-reactive surfactants on the surface of the seawater. Previous work has shown chemical enhancement of ozone deposition to be equal for separate solutions of marine DOM and iodide, however was only 80% of their summed values when iodide and DOM were combined in solution (Martino et al., 2012). This dampening effect could be happening via a similar mechanism to that observed in the PML samples.

The higher percentage of uptake attributable to iodide in the PML sample also supports the finding that the increase in DOI following ozone reaction was greater for PML samples than for CONNECT samples. A greater number of reactions between ozone and iodide would have led to more reactive iodine species in the liquid phase, leading to integration of iodide into organic matter.

A reduction in the number of ozone-iodide reactions expected for a given deposition velocity of ozone to the ocean has implications for understanding of emissions of iodine-containing species to the atmosphere. There remains discrepancies between modelled and measured reactive iodine species, e.g IO, as described in Pound et al. (2023). The findings in the current work demonstrate that in a halogen-only chemical regime for ozone deposition to the ocean, iodine-containing emissions could be over-estimated by current models.

4.7 Surface Contribution to Ozone Uptake

4.7.1 Sample Selection

Based on the high degree of missing reactivity in the CONNECT samples, and the lack of iodide consumption in the SML observed during the ozone exposure experiment, it is clear that there are species other than iodide which are contributing to ozone reactivity. It has previously been hypothesised that components of DOC are a significant factor in ozone uptake.

In our analysis of surface reactivity, it was decided to focus on the CONNECT samples, and exclude the PML samples from this analysis. This is due to uncertainty in preservation of surface-active materials and reactivity during filtering and prolonged frozen storage. Several arguments were considered in making this decision, based on the work described in this thesis;

- The lower ozone uptake to PML samples compared to CONNECT samples, despite higher fatty acid concentrations.
- The lack of difference in ozone uptake to SML compared to ULW, despite enriched fatty acids in the PML SML samples.

- Previous studies have demonstrated that freezing at -20 °C does not preserve the depressed surface tension of SML samples, hence demonstrating an alteration of the surface-active substances in the sample (Yousif Assiri, *pers. comm.*).

Experiments carried out subsequent to this work have supported this conclusion. Ozone uptake to English Channel SML and ULW samples was reduced by filtering, and by prolonged storage ($>$ 48 hours) of unfiltered samples (Charlotte Stapleton, *pers. comm.*). For this type of analysis, it was therefore concluded that ozone uptake should only be measured to fresh, unfrozen seawater samples. Testing this hypothesis on future campaigns would be highly desirable. Despite not being able to use PML samples for surface uptake analysis, the alteration of ozone uptake by filtering and freezing does give us valuable information that this type of sample treatment reduces ozone uptake. Whatever changes occur in a seawater sample during filtration and/or freezing have an impact on ozone uptake, therefore the sources of these changes hold information on some of the drivers of ozone uptake, and warrant further study.

4.7.2 Quantification of Surface-Driven Uptake

It has previously been demonstrated that there is a surface component of ozone uptake to seawater. Several experiments were performed where ozone uptake to North Sea seawater samples were measured over a range of ozone concentrations in the work of Saint (2019). With ozone concentrations ranging from approximately 10 - 200 ppb, for all seawater samples measured, the deposition velocity increased with decreasing ozone concentration, which is characteristic of Langmuir-Hinshelwood surface reactions.

Some authors have previously reported a second-order rate constant for the reaction between ozone and the entire oceanic DOC pool (Sarwar et al., 2016; Shaw and Carpenter, 2013). This has been done assuming an additive relationship in reactivity, and also assuming that DOC reacts in the bulk phase. However, as discussed extensively, it is clear that in ozone uptake to seawater, reactions occur

both in the bulk phase and on the surface of the water. The surface reaction must be considered as a decoupled process, happening in parallel to the bulk-phase ozone-iodide reaction. The mixed surface and bulk framework was used to assess the surface contribution in this work.

To quantify the surface contribution, Eq. 14 was used. The measured diffusive resistance (Section 2.3.7) was used in these calculations, as well as γ_{aq} described in Section 4.6.

Estimations of $\alpha_{surf} = 0.3$ and $\alpha_{aq} = 0.1$, were used as described in Moreno et al. (2018), and all residual reactivity was attributed to Γ_{surf}. Resistance due to surface reactions, $1/\Gamma_{surf}$ was calculated for the whole DOC pool, with the awareness that the composition of the DOC pool changes spatially and temporally. "DOC" in this section was used to represent any species reacting on the surface. Following this method, the calculated γ_{surf} values for CONNECT samples ranged from 1.1 $\times 10^{-6}$ to 5.2 $\times 10^{-6}$.

Several measurements were tested for correlation with surface uptake, including unsaturated fatty acids, CDOM, Chl-a, DMS, NO_2, NO_3, PO_4, SiO_2, surface tension and water temperature. For all species except unsaturated fatty acids, no strong correlations with surface driven uptake were found (displayed in Appendix 6.4.5).

4.7.3 Unsaturated Fatty Acids as a Driver of Surface Uptake

A strong candidate for surface reactivity in seawater is unsaturated fatty acids. These compounds are reactive towards ozone and are commonly found on the ocean surface. Concentrations of unsaturated fatty acids across the cruise track were described in Section 4.4.1. To test if these compounds influence ozone uptake to seawater, calculated γ_{surf} was compared to the measured unsaturated fatty acid concentration of the samples (Fig. 62). A trend was observed whereby increasing unsaturated fatty acid concentration correlated to an increase in γ_{surf}. The trend was not significant to the 95 % confidence level, however this trend was judged to be reasonably strong for such a small dataset, with several competing

physical processes. A few potential outliers are observed (two ULW samples, and one SML sample), therefore more data would be desirable to confirm this relationship. The relationship between γ_{surf} and unsaturated fatty acid concentration was the stronglest relationship of all those tested (Appendix 6.4.5).

A caveat to this analysis is that filtering the seawater was required prior to extraction of fatty acids into methanol, which was stored at -20 °C, and fatty acids quantified by GC at a later date. Due to methodological constraints, it would not be possible to quantify fatty acids using gas chromatography without filtering. It was concluded that uptake was affected by filtering and freezing, however the cause of this alteration has not yet been determined. It cannot therefore be ruled out that the fatty acids measured and described in Weddell (2023) were altered, compared to those present during the flow reactor uptake measurements. Weddell (2023) demonstrated that for most fatty acids studied, filtering did not impact the recovered concentration, however to our knowledge no studies exist showing the impact of freezing on dissolved fatty acid quantification.

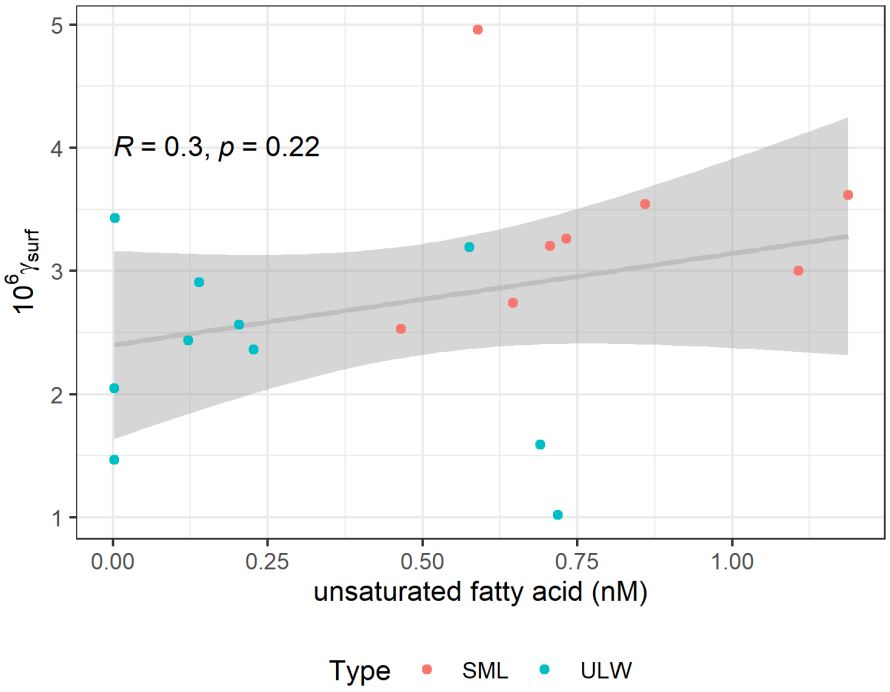

Figure 62: Relationship between γ_{surf} and bulk concentration of unsaturated fatty acids.

To determine whether combined knowledge of iodide and unsaturated fatty acid concentrations could be used to predict ozone uptake, the kinetics of the reac-

tion between ozone and unsaturated fatty acids were investigated. Unsaturated fatty acids were treated as a grouped concentration, however in reality this is a complex mix of several individual species, not all of which have been quantified in terms of ozone reactivity. Analysis was therefore based on a model compound; oleic acid. Oleic acid is a mono-unsaturated fatty acid, with formula $C_{18}H_{34}O_2$ (Figure 36). It is the most extensively studied fatty acid in terms of ozone reactivity, therefore forms the baseline of our understanding of ozone deposition to surfaces containing unsaturated fatty acids.

Measured second order rate constants for the reaction between ozone and oleic acid are displayed in Table 14. $k_{O_3-oleic\,acid}$ values were reported on the order of 10^{-11} cm^2 molecule s^{-1} by González-Labrada et al. (2007), King et al. (2009), King et al. (2020) and Kleber et al. (2013). These were all measured to a monolayer of oleic acid over a liquid surface.

Based on their obtained second order rate coefficients, authors have predicted ozone uptake due to a monolayer of oleic acid. $\gamma \approx 2-5\times10^{-6}$ were calculated by King et al. (2009), González-Labrada et al. (2007)and Kleber et al. (2013). While they compare quite well to the γ_{surf} values displayed in Figure 62, they have been calculated using a different method, therefore may not be directly applicable. The ozone concentration used in calculations is the concentration which has dissolved into an organic layer. In this work, calculations were carried out on the assumption that no solvation term for ozone is required for Langmuir-Hinshelwood surface reactions. Due to the presence of a solvation term, the uptake coefficients reported in the previous literature may be an under-estimation.

The cross sectional area of oleic acid is 3.5 $\times10^{-15}$ cm^2 molecule^{-1} (Kleber et al., 2013), therefore the theoretical maximum surface coverage of oleic acid is 2.9×10^{14} molecules cm^{-2}; this concentration constitutes a monolayer. All of the authors reported in Table 14 worked with monolayers of oleic acid around this concentration. Above this concentration, a plateau in γ_{surf} would be expected due to saturation of reactive surface sites. The concentrations of total unsaturated fatty acids measured in the CONNECT SML samples were much lower

(discussed in upcoming sections), therefore the increase in γ_{surf} with unsaturated fatty acid concentration could reflect the increase in reactive surface sites.

Table 14: Reported values for $k_{O_3-oleic\ acid}$ and ozone uptake due to oleic acid.

$k_{O_3-oleic\ acid}$ (cm^2 molecule s^{-1})	Uptake Coefficient (dimensionless)	FA surface coverage	Ozone (molecules cm^{-3})	Reference
4.9 $\times 10^{-11}$	$(2.6 \pm 0.1) \times 10^{-6}$	monolayer	7 - 615 $\times 10^{12}$	González-Labrada et al. (2007)
7.3 $\pm$ 0.9 $\times 10^{-11}$	4×10^{-6}	monolayer	4 - 16 $\times 10^{12}$	King et al. (2009)
7.8 $\pm$ 0.7 $\times 10^{-11}$	not calculated	monolayer	1.2 - 29.2 $\times 10^{12}$	King et al. (2020)
7.1 $\pm$ 2.8 $\times 10^{-11}$	4.7 $\pm$ 1.8 $\times 10^{-6}$	monolayer	2 - 17 $\times 10^{12}$	Kleber et al. (2013)

4.8 Application of Bulk and Surface Reactions to Predict Ozone Uptake

It was sought to estimate ozone uptake due to the combined impact of iodide and unsaturated fatty acids, for comparison to the measured ozone uptake to CONNECT seawater samples. In calculation of surface resistance (Eq. 13), and hence overall uptake (Eq. 14), several factors require assumption, or have wide reported ranges, therefore the impact of these ranges was investigated. Firstly, $[O_3]_{gs}$ was calculated using the method described in Section 2.3.7.3 (Eq. 19).

Because all unsaturated fatty acids were assumed to react with ozone on the liquid surface, the measured bulk phase concentrations, in moles per litre, were converted to a surface-based concentration, in molecules per cm^{-2}. To perform this conversion, initially an assumption was made that in the flow reactor the fatty acids were well mixed throughout the sample, and there was no surface enhancement, due to the pumping and stirring. Concentration per unit area was calculated by multiplying the volumetric concentration by the length of an oleic acid molecule, estimated as 1.90 nm (González-Labrada et al., 2007). There is uncertainty in this assumption because this depends on the orientation of oleic acid molecules. The median surface concentration in the SML experiments using this method was 3.0 $\times 10^5$ molecules cm^{-2} (range 5.3 $\times 10^4$ to 4.9 $\times 10^5$ molecules cm^{-2}). For the ULW experiments, the median surface concentration was 9.1 $\times 10^4$ molecules cm^{-2} (range 1.1 $\times 10^3$ to 3.1 $\times 10^5$ molecules cm^{-2}). Surface concentrations assuming no enrichment are termed ”homogenous” concentrations herein.

Oleic acid has a strong affinity for surfaces, therefore there was likely some surface enhancement of unsaturated fatty acids in the flow reactor. The exact amount of surface enrichment cannot be quantified, given the pumping and stirring throughout the experiment. To estimate the maximum surface concentration possible, the total number of molecules in the flow reactor was calculated from the bulk concentration of unsaturated fatty acids and the known volume of liquid in the flow reactor. This was divided by the liquid surface area to obtain the

maximum surface concentration. The median surface concentration in the SML using this method was 4.5 $\times 10^{11}$ molecules cm^{-2} (range 8.1 $\times 10^{10}$ to 9.7 $\times 10^{11}$ molecules cm^{-2}). In the ULW, the median surface concentration was 1.2 $\times 10^{11}$ molecules cm^{-2} (range 1.6 $\times 10^{9}$ to 6.9 $\times 10^{11}$ molecules cm^{-2}), assuming complete bulk/surface partitioning.

The concentrations calculated using both methods are below the surface concentration which would constitute a monolayer. The large range of possible surface concentrations of unsaturated fatty acids adds a great deal of uncertainty to these calculations, and warrants consideration in future experiments. It is unlikely that the surface concentration lies at either of these extremes, as while some surface enrichment is to be expected from a surface-active compound, complete surface-bulk partitioning is unlikely.

Assumptions were also made regarding the second order rate constant of ozone with unsaturated fatty acids. The second order rate constant for each measured unsaturated fatty acid was estimated by $k_{O_3-oleic\ acid}$, scaled according to the number of double bonds present. It has been demonstrated that the rate of reaction towards ozone of dienes with non-conjugated double bonds was accurately predicted by multiplication of the rate of reaction of the corresponding monoalkene by the number of double bonds, n_{FA} (King et al., 1999).

This scaled second order rate coefficient was used in conjunction with the surface concentration of each fatty acid to estimate its first order rate of loss. The contribution of each unsaturated fatty acid was summed to estimate the total first order rate of loss of ozone due to unsaturated fatty acids (Eq. 56). Application of this assumption raised the first order rate constant for enriched fatty acid concentrations from a mean rate of 22.2 s^{-1} with no scaling, to 27.7 s^{-1} with scaling, representing an average 24.8 % increase.

$$first\ order\ rate\ constant = \sum k_{O_3-oleic\ acid} \times n_{FA} \times [FA]_{surf} \tag{56}$$

The ozone adsorption coefficient, K_{O_3}, also varies depending on the liquid surface, with some previous measurements summarised in Table 15. Our predicted

uptake coefficients were also tested for sensitivity to this parameter, with calculations performed for the mean value, with consideration of the the minimum and maximum values, i.e. over water and over chlorophyll, as errors.

Table 15: Reported values for K_{O_3} over pure water, aqueous organic solutions and organic films.

$10^{16}\ K_{O_3}$ (cm^3 molecule^{-1})	Condition	Reference
4.67	water	Mmereki and Donaldson (2003)
5.20	stearic acid film	Mmereki et al. (2004)
8.47	hexanoic acid (aq)	Mmereki et al. (2004)
14.7	octanoic acid (aq)	Mmereki et al. (2004)
19.7	1-octanol (aq)	Mmereki and Donaldson (2003)
25	chlorophyll	Clifford et al. (2008)

Ozone uptake due to iodide and unsaturated fatty acids was predicted, assuming iodide reacts in the bulk phase, and that unsaturated fatty acids react following a Langmuir-Hinshelwood reaction, on the surface. For bulk-phase iodide concentrations, γ_{aq} was calculated according to Eq. 8 and 9, using the measured iodide concentrations in the seawater samples and the kinetics measured in Chapter 3, as described in Section 4.6.

The contribution from surface reactions was calculated according to Eq. 13. An average literature value of $k_{O_3-oleic\ acid}$ was applied of 6.8 $\times 10^{-11}$ cm^2 molecule s^{-1}, calculated from the values given in Table 14. This was applied along with the possible range of unsaturated fatty acid surface concentrations to calculate the conductance due to surface reactions.

Predicted ozone uptake coefficients due to iodide and unsaturated fatty acids were calculated by Eq. 14. Predicted ozone uptake coefficients for homogeneous and well mixed fatty acids, in parallel with bulk-phase iodide, are displayed in Figure 63, and compared to the measured γ_{corr}. The measured values fall within the predicted values given by the homogeneous and surface enriched calculations of surface fatty acid concentration.

For homogeneous fatty acid concentrations, Γ_{surf} is low, therefore $\gamma_{corr} \approx \gamma_{aq}$ (the mean difference was 0.02 %). If ozone uptake is indeed partly driven by unsat-

urated fatty acids, this therefore indicates that there must be a degree of surface enhancement, to facilitate uptake which is competitive with the bulk-phase pathway.

At the opposite end of the range, if total bulk/surface partitioning is assumed, ozone uptake is vastly over-estimated in most cases, relative to the measured γ_{corr}. Good agreement is seen in ULW samples collected on 19/12/2021, 27/12/2021 and 01/07/2022, however the unsaturated fatty acid concentrations in these samples were extremely low (0.003, 0.002 and 0.003 μg L^{-1}, respectively).

The uptake coefficients predicted from the surface enhanced concentrations of unsaturated fatty acids are greater than those calculated in previous literature regarding oleic acid oxidation (King et al., 2009; González-Labrada et al., 2007; Kleber et al., 2013). The reason for this is that in the current work, the ozone concentration available for reaction was calculated according to the Langmuir isotherm. In the previous works, the ozone concentration was taken as that which has dissolved into an organic monolayer, therefore is limited by the low solubility of ozone. This is due to the expectation that in an unsaturated organic monolayer, the double bond could be considered to be contained within an organic medium, as shown by molecular dynamic simulations (Vieceli et al., 2004). It is expected that there is not an organic monolayer on the surface of the seawater samples in this work. A monolayer of oleic acid was characterised by a film pressure, $\Delta\sigma$, of 20 mN/m (González-Labrada et al., 2007), while the CONNECT SML samples had far lower $\Delta\sigma$ values of typically $\approx$ 0 to 1 mN/m, with two samples displaying $\Delta\sigma$ values of 4.5 to 5 mN/m. Furthermore, due to the demonstration of Langmuir-Hinshelwood behaviour of ozone uptake to seawater samples, characterised by the increase in ozone uptake at lower ozone concentrations (Saint, 2019), it was decided to calculate ozone concentration by the Langmuir isotherm (Eq. 12), and hence surface conductance by Eq. 13.

Study of the rate of reaction between ozone and oleic acid when it is not present as a monolayer would be desirable to clarify whether this difference in approach is appropriate. Clearly there are large discrepancies in ozone reactivity which cen-

tre around the accessibility of the double bond, therefore more knowledge on the specific interfacial properties of seawater are desirable for future study. If unsaturated fatty acids do indeed react via a Langmuir-Hinshelwood mechanism, they have a potential for large contributions to ozone uptake, and the ozone uptake coefficients calculated by King et al. (2009); González-Labrada et al. (2007) and Kleber et al. (2013) may not be appropriate to apply to seawater.

The overestimation of ozone uptake under the assumption of complete surface enhancement was not surprising. Complete partitioning of fatty acids in the flow reactor would not be expected, due to the stirring of the sample in the flow reactor, and continuous pumping in and out of the flow reactor disrupting the surface. An upper estimate for the surface concentration of fatty acid was used in lieu of accurate measurements of surface concentrations. To know the true surface enrichment in the flow reactor, additional equipment would be required, for example neutron reflection used in conjunction with deuterated fatty acid samples, as used by King et al. (2020). Alternatively, an alteration could be made to the flow reactor which would allow simultaneous measurement of ozone uptake and surface tension. Difficulties in combining surface tension and uptake measurements arise due to the requirement for a sealed vessel in the variable flows uptake method; this makes the inclusion of the hanging Wilhelmy plate difficult. The large range in possible surface concentrations calculated in this work is the largest source of error in these estimations, therefore thorough understanding of the interfacial properties of seawater, both in the flow reactor and in the environment, are recommended as an important future study.

It would be expected that the predicted ozone uptake due to iodide and unsaturated fatty acids would under-estimate γ_{corr}. This is because there are other organic species known to react with ozone on the surface of seawater, for example chlorophyll (Clifford et al., 2008) and PAHs (Kwamena et al., 2004).

To assess whether our choice of K_{O_3} impacted our predictions significantly, the range of reported values described in Table 15 were also tested. Bars on figure 63 used a mean K_{O_3}, calculated from K_{O_3} measured over water (4.67 $\times 10^{16}$)

and K_{O_3} measured over chlorophyll (25 $\times 10^{15}$). Mean K_{O_3} was therefore 1.48 $\times 10^{15}$. Error bars on this graph show the results of the same calculations, using the minimum (water) and maximum (chlorophyll) K_{O_3} values. Some variation in predictions is observed when enriched surface concentrations of unsaturated fatty acids were used, however the uncertainty range is small compared to those introduced by the possible range of surface concentrations.

This set-up was not initially designed for accurate quantification of surface kinetics, therefore the purpose of this section is not to recommend which physical parameters should be used for estimation of ozone uptake to seawater. This work has provided a demonstration of the potential for a combined bulk and surface ozone uptake framework for seawater, as well as discussion of the limitations of the current technique. With better estimations of the surface concentrations of unsaturated fatty acids, it is believed that this framework has potential to more accurately predict ozone uptake to seawater.

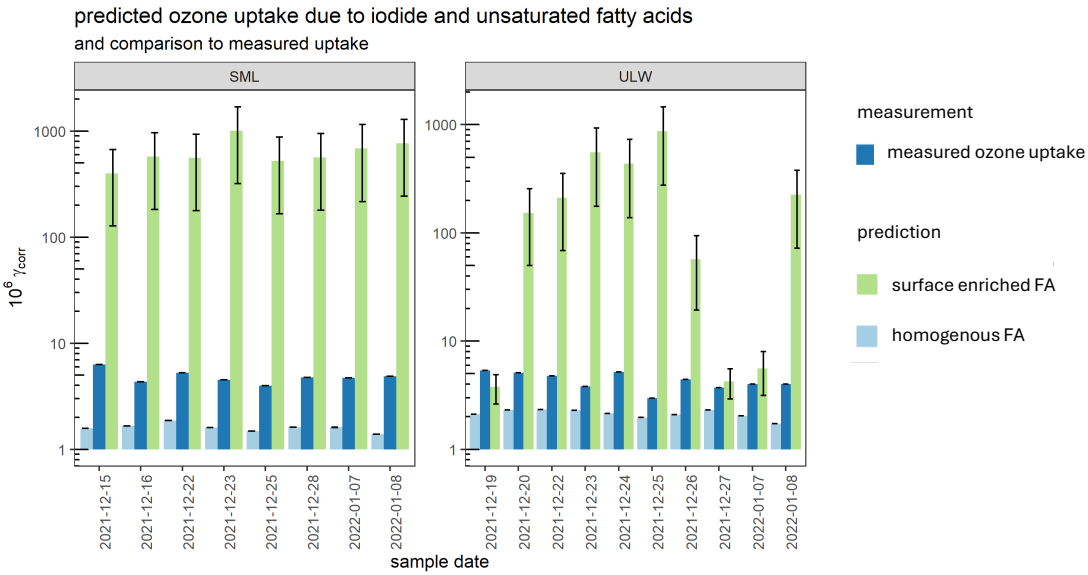

Figure 63: Measurements of ozone uptake to SML samples collected during the CONNECT cruise, compared to predicted values, calculated using an average value of $k_{O_3-oleic\ acid}$ = 6.8 $\times 10^{-11}$ cm^2 molecules s^{-1}, where $k_{O_3-oleic\ acid}$ was scaled according to the number of double bonds in each measured unsaturated fatty acid. ”homogenous” refers to the fatty acid concentration calculated assuming no surface enhancement, while ”surface enriched” refers to the surface concentration assuming total surface-bulk partitioning. Mean K_{O_3} used = 1.48 $\times 10^{15}$, error bars show the results when minimum (Mmereki and Donaldson, 2003) and maximum (Clifford et al., 2008) K_{O_3} values were applied.

Further study of surface reactions on seawater would be a desirable next step to understand ozone uptake to seawater. A first recommendation for further study on ozone uptake to unsaturated fatty acids would be re-measurement of the second order rate constant between ozone and oleic acid. This should ideally be done over environmental concentrations of unsaturated fatty acids. Ozone-oleic acid kinetic measurements are typically performed on a monolayer of oleic acid to allow pseudo-first order kinetic experiments to be performed (King et al., 2009, 2020; González-Labrada et al., 2007; Kleber et al., 2013). In a monolayer, oleic acid molecules are more ordered, with the double bond contained within an organic layer (Vieceli et al., 2004) however below the monolayer-forming concentration the molecules are more disperse and typically less ordered. This could mean the ozone-reactive unsaturated tail could be either more or less accessible to ozone, which would also impact ozone uptake.

This leads into the second recommendation, which involves better characterisation of the surface concentrations of unsaturated fatty acids in the ocean and in the flow reactor. The flow reactor method used in this work was not optimised for surface-reactivity, therefore very large uncertainties exists regarding the impact of pumping and stirring on the surface-bulk partitioning of fatty acids.

If a significant portion of ozone uptake to seawater can be attributed to reactions with organic matter, this could be a source of oxidised VOCs (OVOCs) to remote marine environments, which would alter our understanding of the chemistry of the marine boundary layer.

4.9 Chapter Conclusion

Ozone uptake to genuine seawater samples was measured, along with complementary biogeochemical measurements, to explore the drivers of ozone uptake to the ocean. The differences between the SML and ULW were demonstrated, with enrichment/depletion of iodide and fatty acids of particular importance. By analysis of the relative concentrations of selected species in the SML and ULW, it was shown that for ozone uptake to the ocean, the SML must be sampled or modelled. This is because the SML is chemically distinct from the bulk water, both in terms of biogeochemistry and ozone uptake.

Historically considered one of the main drivers of ozone uptake to the ocean, iodide was determined to only contribute 25-66 % of ozone uptake over fresh seawater and 36 - 148 % of uptake over filtered and frozen samples. Measurement of the bulk-phase iodide concentration of seawater samples during prolonged ozone exposure showed that for the ULW sample, with a low DOC content and no measurable fatty acids, iodide was depleted from the water, but the rate of depletion was lower than anticipated, based on expectations of bulk-phase ozone-iodide reactivity measured in Chapter 3. In the same experiment performed over SML, there was very little depletion of bulk-phase iodide over the period of ozone exposure. Both experiments indicated that there were competing ozone sinks, which were more pronounced in the SML, and suggested that reaction with iodide might

not be the sole driver of ozone deposition to the ocean. A candidate for the remaining ozone uptake was identified as unsaturated fatty acids, the bulk concentration of which correlated reasonably well with the ”missing” reactivity, which was attributed to surface reactions.

The samples from the CONNECT cruise were determined to be the best representation of true SML, due to ozone uptake being measured over unfiltered and unfrozen samples. Despite the strong depletion of iodide in the SML in these samples, the ozone uptake was greater to SML than to ULW. This demonstrated the importance of surface reactions, in particular of unsaturated fatty acids, which were enriched in the SML of the CONNECT samples.

To further study the surface reactions of ozone with seawater, some alterations to the experimental set up would have to be made, including investigation of the impact of stirring the solution on surface-bulk partitioning. Following alterations to the method, investigation into the rate of reaction between unsaturated fatty acids and ozone would be required for more detailed analysis of their contribution to ozone deposition. Ideally, this would be carried out under conditions which more accurately represent the sea surface. This would allow further analysis of the impact of additional surface active compounds, e.g. bromide, and other components of the DOC pool. Despite this, a combination of knowledge of iodide and unsaturated fatty acids was demonstrated to have potential to give an estimation of the water-side drivers of ozone uptake to seawater.

The comparable contributions of iodide and organic materials will have implications for emissions from seawater following reaction with ozone. For the same measured or predicted ozone deposition, the findings reported in this work would indicate less emissions of iodine-containing species, e.g. HOI and I_2, and a greater emission of OVOCs. While this mechanism of emissions of OVOCs from seawater would be small compared to land based sources, in remote ocean areas this could prove a significant source of OVOCs to the pristine atmosphere.

5 Conclusions

This work began with an investigation into a fundamental chemical process expected to be occurring in the sea surface. Disagreements in the literature were addressed by re-measuring the temperature dependence of ozone-iodide kinetics. The only previous measure of the temperature dependence of this rate coefficient provided an unrealistic rate at high temperatures (Magi et al., 1997). To the author's knowledge, the investigation described in the current work was the first comprehensive study of this rate coefficient at varied temperatures, which used conditions applicable to the marine environment. Therefore, this work contributes improved understanding of ozone-iodide interactions at the sea surface.

With improved knowledge of the ozone-iodide reaction, the contribution of iodide to ozone deposition to the sea surface was quantified. It was demonstrated in this work that, especially in the sea-surface microlayer, the process of ozone deposition is a complex process, that does not appear to be driven by iodide alone. Reactions of ozone with organic compounds, notably unsaturated fatty acids, were shown to have an equal or larger contribution to ozone uptake as iodide. This has implications for predictions of ozone deposition to the ocean, and for emissions of oxidation products from the ocean surface to the atmosphere.

It has proven difficult to replicate the sea surface in a flow reactor, and this is something which should be considered in future experimental design. While it was possible to use flow reactor measurements (of the ozone-iodide second order rate constant) to replicate and model emissions of HOI and I_2 from a previous flow reactor experiment (MacDonald et al., 2014), differences in turbulence and mixing within the liquid phase in the flow reactor mean these are likely not directly comparable to the environment. Even the low "wind speeds" accessible within a flow reactor introduce differences from the environment, as was discussed in the context of iodide depletion in the SML (Pound et al., 2023). During this project it was not possible to investigate the fate of surface active substances in the flow reactor - assumptions were made regarding their surface enhancement, or lack

thereof, however for future study into surface mediated reactions, this should be more accurately quantified.

Despite this, evidence was presented that the influence of iodide on ozone uptake to seawater may have been over-estimated in the past. The complex series of reactions occurring at the sea surface are not currently captured in models of ozone deposition to the ocean. For example, in the commonly used Luhar et al. (2018) model, only iodide reactions are used to estimate oceanic deposition velocity, due to the uncertainty in further organic reactivity.

5.1 Future Work

It would be desirable to perform measurements on a thinner SML sample, perhaps collected using a glass plate, and to develop a method which can measure a more ”instantaneous”, in-situ ozone uptake, which would minimise the impact of ozone-related chemical loss throughout the experiment. Additionally, applying higher wind speeds and turbulence to the seawater samples would better mimic environmental conditions, important for studying emissions following oxidation.

Measurement of the oxidation products following ozone deposition would also give valuable insight into the dominant reactions, whether iodide-based or otherwise. Concentrations of HOI and I_2 by chemical ionisation mass spectrometry (CIMS) would be an excellent next step, as well as organic emisisons (OVOCs) by selected ion flow tube mass spectrometry (SIFT-MS).

For measurement of surface reactions, an improved understanding of the chemical makeup of the air-water interface is necessary. Additionally, for experimental work alterations to the flow reactor would be required to have a better characterised surface phase for measurements.

Finally, more in-situ measurements of ozone uptake to seawater would expand the dataset started with the CONNECT measurements, and allow investigation of why filtering and/or freezing appeared to have a dramatic impact on ozone uptake. All of this would be a crucial next step in accurately identifying the ”missing”, non-iodide sources of ozone reactivity in seawater.

6 Appendix

6.1 Chapter 2 Appendices

6.1.1 Detailed Experimental Method

This experimental method was used for kinetic studies of the ozone and iodide reaction.

Condition the Flow Tube and Gas Lines

- Turn on ozone to high concentration (few hundred ppb) and flow through flow tube
- Measure required volume of liquid required for experiment (buffer solution with no iodide added) and put in large bottle in a water bath, if the experiment is to be temperature controlled
- Pump blank through the flow reactor and out into the same bottle, exposing to ozone until the measured ozone concentration is stable - at least 1 hour

Set Experimental Ozone Concentration

- Switch gas flow to bypass and turn off water pumps
- Leave until ozone concentration stabilises, indicating the bypass line is conditioned (this should be slightly higher than the stable concentration over the blank, and never lower)
- Push in the cover on the ozone generator until desired concentration is reached, and measure for a few minutes to obtain a measure of the applied ozone concentration

Blank Measurement

- Switch gas flow to flow tube
- Turn on water pumps, and adjust pump rate to experimental setting. The blank will still be draining into the same bottle

- Leave 5-10 minutes until ozone concentration stabilises
- Check experimental parameters on DAQFactory:
  Steps: 1600, 1900, 2400, 3200 and 4500 SCCM
  Volume increment: 10 SCCM
  Time increment: 2 s
- Press “Run Step and Ramp Experiment” and let run 3 times

Spike with Iodide

- Switch gas flow to bypass and turn off water pumps
- Pipette required volume of iodide stock solution into reservoir bottle, while stirring
- Turn on water pump, adjust to 200 RPM and let it pump through the flow tube for at least 10 minutes to mix the reservoir with the solution remaining in the flow tube

Iodide Measurement

- Adjust down the pump RPM to chosen experimental rate
- Put liquid waste line into a waste bottle
- Switch the gas flow to the flow tube
- Wait for ozone concentration to stabilise - 5-10 minutes
- Press “Run Step and Ramp Experiment” and let run 3 times
- Take a “before” sample for iodide from the reservoir bottle (can do this at any point from now on) using a glass pipette, filling the vial to approximately 4.5 ml
- During the experiment, take an “after” sample by collecting the waste stream into a vial during the third step of the second run i.e. the middle point of the experiment. Can take more samples during other steps if useful

Clean Up

- Turn off ozone generator and switch gas flow to bypass
- Turn off both peristaltic pumps simultaneously
- Measure the liquid volume in the flow tube. Drain the contents of the flow tube into a large vessel by adjusting the angle of the flow tube (tilting the flow tube to get all the liquid), then measure the volume collected
- Remove the gas inlets and outlets and replace the ends with bottle caps. Leave stirrer bars in
- Fill and empty with hot tap water if organics are in the liquid phase
- Acid wash by pumping in 10% HCl at 200 RPM, and letting it drain into the same bottle. Adjust the angle of the flow tube so the ports are at the top, allowing the whole tube to fill with acid, leave it for some time (at least 15 minutes, longer if possible)
- Rotate flow tube to drain the acid out into its original bottle. Remove the cap from the opposite gas port to allow it to drain, and replace fitting on glass port
- Fill and empty 3 times with milliQ
- Reposition the stirrer bars using a stick, and set them stirring
- Reattach the gas inlet and outlet, switch gas flow to flow tube and use compressed air to dry the flow tube overnight. Take off one of the plastic fittings on the flow reactor to avoid over/under pressurising in case of failure at any point in the system

For field studies, a similar method was used with some adaptations

- the blank measurement was performed in an empty flow tube, therefore the conditioning and blank measurement steps had no liquid
- no iodide spike was performed

- the flow rates for the smaller tube were 400, 480, 600, 900, 1200 SCCM
- a 1000 SCCM dilution was added directly after the flow tube to ensure the gas flow met the requirements of the ozone monitor (which was approximately 1400 SCCM)
- multiple measurements were performed each day, therefore after cleaning, the tube was dried with ozone-enriched air, therefore combining the drying and conditioning steps to save time

6.2 Chapter 3 Appendices

6.2.1 Physical Constants

All physical constants and the values used are outlined in Table 16

Table 16: Physical constants used in calculations.

Constant	Symbol	Value	Unit	Reference
Boltzmann constant	k_B	1.380649 × 10^{-23}	m^2 kg s^{-2} K^{-1}	
Universal gas constant	R	8.3145	J mol^{-1} K^{-1}	
Gaseous diffusivity of ozone in air	D_{g,O_3}	0.15 ± 0.01	cm^2 s^{-1}	(Langenberg et al., 2020)
Temperature	T	298	K	
Tube length	l	149.4 ± 0.1	cm	
Tube radius	r	2.02 ± 0.0203	cm	
Liquid volume*	liquid volume	333 ± 1	cm^3	
Liquid height *	h	0.92	cm	

* Liquid volume in the flow reactor varied day to day, average values for liquid volume and resulting liquid height are provided here for illustrative purposes, however the measured daily volumes were used in calculations.

6.2.2 Geometric Equations and Error Calculation

Errors were propagated using the exact formula for the propagation of error (Eq. 57)

$$\sigma_x^2 = (\frac{\delta_x}{\delta_a})^2\sigma_a^2 + (\frac{\delta_x}{\delta_b})^2\sigma_b^2 + (\frac{\delta_x}{\delta_c})^2\sigma_c^2 + ... + (\frac{\delta_x}{\delta_n})^2\sigma_n^2 \tag{57}$$

For Eqs. 58 to 63, definitions and values for physical constants can be found in Table 16. Flow tube volume, V_{FT} (Eq. 58), and associated error (Eq. 59).

$$V_{FT} = \pi r^2 l \tag{58}$$

$$\sigma_{V_{FT}} = \sqrt{(2\pi rl \cdot \sigma_r)^2 + (\pi r^2 \cdot \sigma_l)^2} \tag{59}$$

Headspace volume, V_H (Eq. 60), and associated error (Eq. 61).

$$V_H = V_{FT} - liquid\ volume \tag{60}$$

$$\sigma_{V_H} = \sqrt{{\sigma_{V_{FT}}}^2 + {\sigma_{liquid\ volume}}^2} \tag{61}$$

Surface area of liquid, SA (Eq. 62), and associated error (Eq. 63).

$$SA = 2l\sqrt{2rh - h^2} \tag{62}$$

$$\sigma_{SA} = \sqrt{(2\sqrt{2rh-h^2} \cdot \sigma_l)^2 + (\frac{2lh}{\sqrt{2rh-h^2}} \cdot \sigma_r)^2 + (\frac{2l(2r-2h)}{2\sqrt{2rh-h^2}} \cdot \sigma_h)^2} \tag{63}$$

6.2.3 Iodide concentrations measured by IC

Iodide concentrations before and after passing through the flow tube are outlined in Table 17, as well as calculated r_s at each iodide concentration and temperature.

Table 17: Iodide concentrations before and after passing through the flow reactor, and associated r_{aq} measurements. "-" denotes measurement not available.

T (K)	$[I^-]$ before (M)	$[I^-]$ after (M)	% change	r_{aq} (s cm^{-1})	r_{aq} error (s cm^{-1})
288.15	1.73×10^{-6}	1.60×10^{-6}	-7.4	12.05	0.45
288.15	6.14×10^{-7}	6.35×10^{-7}	3.4	21.69	1.36
288.15	2.37×10^{-7}	2.39×10^{-7}	0.7	42.81	4.99
291.15	5.29×10^{-6}	5.14×10^{-6}	-3.0	6.82	0.31
291.15	4.48×10^{-6}	4.46×10^{-6}	-0.5	6.36	0.39
291.15	1.92×10^{-6}	1.82×10^{-6}	-5.1	10.15	0.44
291.15	6.64×10^{-7}	6.06×10^{-7}	-8.7	17.58	0.76
293.15	5.81×10^{-7}	5.76×10^{-7}	-0.8	23.47	2.19
293.15	2.82×10^{-7}	2.62×10^{-7}	-7.2	39.30	7.93
293.15	4.13×10^{-6}	3.94×10^{-6}	-4.5	7.24	0.31
296.45	9.62×10^{-6}	9.65×10^{-6}	0.3	5.29	0.19
296.45	4.55×10^{-6}	4.51×10^{-6}	-0.9	9.16	0.43
296.45	6.34×10^{-7}	6.38×10^{-7}	0.5	24.57	1.89
296.45	2.27×10^{-7}	2.05×10^{-7}	-9.5	37.90	2.36
298.15	-	5.02×10^{-6}		8.39	0.41
298.15	6.53×10^{-6}	6.13×10^{-6}	-6.0	5.70	0.29
298.15	1.73×10^{-6}	1.64×10^{-6}	-5.0	11.32	0.42
298.15	5.46×10^{-7}	5.37×10^{-7}	-1.6	24.36	1.13
298.15	8.98×10^{-6}	9.05×10^{-6}	0.7	4.38	0.14
301.15	9.88×10^{-6}	9.39×10^{-6}	-5.0	5.05	0.25
301.15	5.19×10^{-6}	4.88×10^{-6}	-6.0	7.51	0.41
301.15	1.90×10^{-6}	1.78×10^{-6}	-5.9	12.73	0.60
301.15	6.74×10^{-7}	-		21.38	1.17
303.15	5.75×10^{-6}	5.64×10^{-6}	-2.0	6.32	0.33
303.15	6.33×10^{-7}	6.38×10^{-7}	0.7	20.70	1.07
303.15	1.82×10^{-7}	1.65×10^{-7}	-9.3	38.98	2.53
303.15	2.97×10^{-6}	2.80×10^{-6}	-5.9	10.03	0.56

6.2.4 Model Description

This model was developed for prediction of ozone deposition to the SML and calculation of subsequent emission of halogenated species. It was designed for environmental conditions, however has been adapted and applied to lab experiments over iodide solutions for the purpose of this work. This model was developed in Python using Cantera as the chemistry solver (Goodwin et al., 2022). The model presented here also uses functions from SciPy (Virtanen et al., 2020), Pandas (pandas development team, 2020), and NumPy (Harris et al., 2020). A summary of the model is included below, but for a complete description and characterisation of the model, see Pound et al. (2023).

In the model, ozone dry deposition velocity (v_d) is calculated using the resistance-in-series scheme (Wesely and Hicks, 1977), which calculates the flux of ozone into the ocean surface microlayer. Airside resistances that represent turbulent transport to the surface and transport through the quasilaminar sub-layer, which is the air directly in contact with the surface microlayer are calculated from wind speed, friction velocity, and the Schmidt number of ozone in air (Chang et al., 2004). The aqueous resistance (r_{aq}) is calculated using the two-layer method of (Luhar et al., 2018), from the dimensionless solubility, the chemical reactivity, the diffusivity in water, the water-side friction velocity, the thickness of the reaction-diffusion layer of the sea-surface microlayer, and modified Bessel functions of the second kind with order zero and one respectively. v_d is coupled to the SML chemistry via I^- concentration and is recalculated as the model advances towards equilibrium.

This model focuses on the aqueous inorganic halogen chemistry in the SML, applying an extended set of inorganic iodine chemistry compared to that described by Carpenter et al. (2013). The rate constant used for the reaction between ozone and iodide is that which was calculated in this work. The net flux of $I_2$and HOI into the atmosphere is calculated from the concentration in the liquid surface and the concentration in the atmosphere, along with the dimensionless Henry's law coefficient for each species, the friction velocity, drag coefficient, Schmidt number

and von Karman constant.

This model accounts for mixing from the surface into underlying solution and follows the form of approach used by Cen-Lin and Tzung-May (2013). The first of these (molecular transfer) is calculated from the waterside transfer velocity and the bulk and surface concentrations of the species in question. In this model there is the facility to account for the effects of surfactants, however we expect no surfactant effect in this work, so this was turned off. The second process, mixing from surface renewal, is a significantly slower process than the mixing described above and is typically on the order of several minutes, but has been included for completeness.

Conditions were chosen to mimic the experiments described by MacDonald et al. (2014). The model is “buffered” to pH 8 by manually resetting H^+ and OH^- at each time-step to maintain a constant pH.

6.3 Chapter 4 Appendices

6.3.1 Sample Logs for CONNECT, PML and BLEACH Campaigns

Table 18 shows instances of sample collection and successful measurement from the CONNECT campaign. Samples were collected jointly between Lucy Brown, David Loades and Katherine Weddell. Iodine measurements were performed by Matthew Jones, DOC and fatty acids were analysed by Katherine Weddell, surface tension was measured by Yousif Assiri, and ozone uptake was measured by Lucy Brown.

Table 18: Summary of measurements made during the CONNECT campaign.

Date	Iodine	DOC	Fatty Acids	Surface Tension	Ozone Uptake
12/12/2021	SML	-	CTD	-	-
13/12/2021	CTD, SML, UW	SML, UW	CTD, SML, UW	SML	-
14/12/2021	CTD, SML	-	CTD, SML, UW	CTD, SML	-
15/12/2021	CTD, SML, UW	CTD, SML, UW	CTD, SML, UW	CTD, SML, UW	SML
16/12/2021	CTD, SML	CTD, SML	SML, UW	CTD, SML, UW	CTD, SML
17/12/2021	CTD, SML, UW	UW	-	CTD, SML, UW	UW
18/12/2021	CTD	CTD	CTD, UW	CTD, UW	-
19/12/2021	CTD, SML, UW	CTD, UW	CTD, UW	CTD, SML, UW	CTD, UW
20/12/2021	CTD, SML, UW	CTD, SML, UW	CTD	CTD	CTD, SML, UW
21/12/2021	CTD, SML, UW	SML, UW	CTD, SML, UW	CTD, SML, UW	-
22/12/2021	CTD, SML	CTD, SML	CTD, SML, UW	CTD	CTD, SML
23/12/2021	CTD, SML, UW	CTD, SML	CTD, SML, UW	CTD, UW	SML, UW
24/12/2021	CTD, UW	CTD, UW	CTD, UW	CTD	CTD, UW
25/12/2021	CTD, SML, UW	CTD, SML	CTD, SML, UW	CTD, UW	CTD, SML
26/12/2021	CTD, SML	CTD, SML	CTD, SML, UW	CTD, SML, UW	CTD
27/12/2021	CTD, SML, UW	SML, UW	CTD, SML, UW	CTD, SML, UW	CTD, UW
28/12/2021	CTD, SML	CTD, SML	CTD, SML, UW	CTD, SML, UW	CTD*, SML
29/12/2021	UW	UW	UW	UW	UW
30/12/2021	UW	UW	UW	UW	-
31/12/2021	UW	-	UW	-	UW
01/01/2022	UW	UW	-	UW	UW
02/01/2022	UW	UW	UW	-	UW
03/01/2022	-	-	-	-	-
04/01/2022	-	-	-	-	-
05/01/2022	UW	UW	UW	UW	UW
06/01/2022	UW	UW	UW	UW	UW
07/01/2022	CTD*, SML, UW	CTD, SML	CTD, SML, UW	CTD, SML, UW	CTD, SML
08/01/2022	CTD, SML, UW	CTD, SML	CTD, SML, UW	CTD, SML, UW	CTD*, SML

* indicates day and night-time samples measured

6.3.2 Station Locations and SML Sampling information for CONNECT and PML and BLEACH Campaigns

Table 19: Station locations for CTD and SML samples, and summary of SML samples collected during the CONNECT campaign.

Date	Time	Lat (°N)	Long (°W)	method	volume (L)	no. of dips	volume per dip (L)	SML thickness (μm)
12/12/2021	Noon	24.5541	-19.56939	crane	6.1	42	0.145	369
13/12/2021	Noon	22.79538	-23.07246	crane	10.4	68	0.153	390
14/12/2021	Noon	20.95516	-26.3984	crane	7.4	42	0.176	448
15/12/2021	Noon	19.4451	-29.87004	crane	10.4	63	0.165	420
16/12/2021	Noon	17.89442	-33.28376	zodiac	11.6	52	0.223	568
17/12/2021	Noon	17.05818	-36.86342	zodiac	13.0	64	0.203	517
18/12/2021	Noon	17.12922	-40.62066	crane	1.0	6	0.167	425
19/12/2021	Noon	17.0972	-44.26722	-	-	-	-	-
20/12/2021	Noon	17.03036	-48.11434	crane	7.2	32	0.225	573
21/12/2021	Noon	19.10153	-51.20516	crane	5.1	NR	NR	NR
22/12/2021	Noon	21.3496	-54.21262	zodiac	11.6	NR	NR	NR
23/12/2021	Noon	24.15224	-56.66914	zodiac	10.4	NR	NR	NR
24/12/2021	Noon	27.33658	-58.45326	-	-	-	-	-
25/12/2021	Noon	30.5839	-60.25848	crane	11.9	58	0.205	522
26/12/2021	Noon	28.51868	-61.60638	crane	7.7	37	0.208	529
27/12/2021	Noon	25.3884	-63.38476	crane	10.5	64	0.164	418
28/12/2021	Midnight	23.8728	-64.4046	-	-	-	-	-
28/12/2021	Noon	22.24332	-65.54	zodiac	NR	NR	NR	NR
07/01/2022	Midnight	2.26398	-85.83312	-	-	-	-	-
07/01/2022	Noon	0.45354	-85.83284	zodiac	10.4	NR	NR	NR
08/01/2022	Noon	-2.66638	-85.83156	zodiac	9.9	NR	NR	NR

NR denotes not recorded. - denotes SML sample not collected.

6.4 Salinity Measurements

Table 20: Salinity measurements across CONNECT and PML campaigns.

Sample Date	Salinity (psu)	Type	Campaign
2021-12-12	36.9	ULW	CONNECT
2021-12-13	37.1	ULW	CONNECT
2021-12-14	36.9	ULW	CONNECT
2021-12-15	37.1	ULW	CONNECT
2021-12-16	36.8	ULW	CONNECT
2021-12-17	36.7	ULW	CONNECT
2021-12-18	36.9	ULW	CONNECT
2021-12-19	37.1	ULW	CONNECT
2021-12-20	37.0	ULW	CONNECT
2021-12-21	37.4	ULW	CONNECT
2021-12-22	37.2	ULW	CONNECT
2021-12-23	36.9	ULW	CONNECT
2021-12-24	37.1	ULW	CONNECT
2021-12-25	36.9	ULW	CONNECT
2021-12-26	36.8	ULW	CONNECT
2021-12-27	37.0	ULW	CONNECT
2021-12-28	36.5	ULW	CONNECT
2022-01-07	33.4	ULW	CONNECT
2022-01-08	33.9	ULW	CONNECT
2019-11-11	25.1	ULW	PML

Continued on next page

Table 20: Salinity measurements across CONNECT and PML campaigns. (Continued)

Sample Date	Salinity (psu)	Type	Campaign
2019-11-11	30.6	SML	PML
2019-11-18	-	ULW	PML
2019-11-18	28.2	SML	PML
2019-11-28	26.8	ULW	PML
2019-11-28	30.1	SML	PML
2019-12-02	32.2	ULW	PML
2019-12-02	32.6	SML	PML
2019-12-17	32.4	ULW	PML
2019-12-17	31.9	SML	PML
2020-01-08	32.4	ULW	PML
2020-01-08	32.1	SML	PML
2020-01-20	32.2	ULW	PML
2020-01-20	31.8	SML	PML
2020-02-05	32.4	ULW	PML
2020-02-05	33.3	SML	PML
2020-02-27	33.1	ULW	PML
2020-02-27	32.8	SML	PML
2020-03-02	33.2	ULW	PML
2020-03-02	32.2	SML	PML
2020-03-16	32.4	ULW	PML
2020-03-16	30.7	SML	PML
2020-03-23	32.8	ULW	PML

Continued on next page

Table 20: Salinity measurements across CONNECT and PML campaigns. (Continued)

Sample Date	Salinity (psu)	Type	Campaign
2020-03-23	33.4	SML	PML
2020-04-27	33.8	ULW	PML
2020-04-27	34.3	SML	PML
2020-05-04	33.7	ULW	PML
2020-05-04	34.6	SML	PML
2020-05-12	34.7	ULW	PML
2020-05-12	34.7	SML	PML
2020-05-18	34.6	ULW	PML
2020-05-18	34.4	SML	PML
2020-05-27	34.4	ULW	PML
2020-05-27	33.8	SML	PML
2020-06-01	34.5	ULW	PML
2020-06-01	34.4	SML	PML
2020-06-08	35.0	ULW	PML
2020-06-08	34.1	SML	PML
2020-06-15	34.5	ULW	PML
2020-06-15	34.2	SML	PML
2020-06-23	34.6	ULW	PML
2020-06-23	34.0	SML	PML
2020-07-01	29.5	ULW	PML
2020-07-01	34.3	SML	PML
2020-07-07	34.0	ULW	PML

Continued on next page

Table 20: Salinity measurements across CONNECT and PML campaigns. (Continued)

Sample Date	Salinity (psu)	Type	Campaign
2020-07-07	33.6	SML	PML
2020-07-14	31.3	ULW	PML
2020-07-14	34.0	SML	PML
2020-07-20	34.4	ULW	PML
2020-07-20	34.9	SML	PML
2020-07-28	34.8	ULW	PML
2020-07-28	34.9	SML	PML
2020-08-03	34.6	ULW	PML
2020-08-03	34.8	SML	PML
2020-08-10	34.9	ULW	PML
2020-08-10	34.6	SML	PML
2020-08-17	34.5	ULW	PML
2020-08-17	33.9	SML	PML
2020-08-24	34.4	ULW	PML
2020-08-24	34.6	SML	PML
2020-09-01	34.2	ULW	PML
2020-09-01	34.1	SML	PML
2020-09-07	34.7	ULW	PML
2020-09-07	34.8	SML	PML
2020-09-14	34.5	ULW	PML
2020-09-14	34.5	SML	PML
2020-09-21	34.7	ULW	PML

Continued on next page

Table 20: Salinity measurements across CONNECT and PML campaigns. (Continued)

Sample Date	Salinity (psu)	Type	Campaign
2020-09-21	34.9	SML	PML
2020-09-28	34.4	ULW	PML
2020-09-28	34.6	SML	PML
2020-10-12	34.4	ULW	PML
2020-10-12	32.4	SML	PML
2020-11-04	33.3	ULW	PML
2020-11-04	33.2	SML	PML
2020-11-09	33.3	ULW	PML
2020-11-09	25.5	SML	PML
2020-11-23	33.3	ULW	PML
2020-11-23	31.8	SML	PML
2020-11-30	33.7	ULW	PML
2020-11-30	33.3	SML	PML
2020-12-07	33.4	ULW	PML
2020-12-07	31.7	SML	PML
2021-01-04	33.7	ULW	PML
2021-01-04	33.9	SML	PML
2021-01-11	33.6	ULW	PML
2021-01-11	33.5	SML	PML
2021-01-18	34.4	ULW	PML
2021-01-18	34.5	SML	PML
2021-01-25	33.0	ULW	PML

Continued on next page

Table 20: Salinity measurements across CONNECT and PML campaigns. (Continued)

Sample Date	Salinity (psu)	Type	Campaign
2021-01-25	33.3	SML	PML
2021-02-04	32.9	ULW	PML
2021-02-04	32.6	SML	PML
2021-02-08	33.1	ULW	PML
2021-02-08	33.4	SML	PML
2021-02-22	32.7	ULW	PML
2021-02-22	27.9	SML	PML
2021-03-02	34.4	ULW	PML
2021-03-02	34.1	SML	PML
2021-03-08	33.9	ULW	PML
2021-03-08	34.0	SML	PML
2021-03-23	34.0	ULW	PML
2021-03-23	33.7	SML	PML
2021-03-30	34.4	ULW	PML
2021-03-30	34.6	SML	PML
2021-04-06	34.4	ULW	PML
2021-04-06	34.7	SML	PML
2021-04-12	34.6	ULW	PML
2021-04-12	35.0	SML	PML
2021-04-20	34.5	ULW	PML
2021-04-20	34.8	SML	PML
2021-04-28	34.9	ULW	PML

Continued on next page

Table 20: Salinity measurements across CONNECT and PML campaigns. (Continued)

Sample Date	Salinity (psu)	Type	Campaign
2021-04-28	34.9	SML	PML
2021-05-05	34.9	ULW	PML
2021-05-05	35.1	SML	PML
2021-05-12	34.9	ULW	PML
2021-05-12	34.8	SML	PML
2021-05-17	34.9	ULW	PML
2021-05-17	33.3	SML	PML
2021-05-25	33.1	ULW	PML
2021-05-25	33.1	SML	PML
2021-06-02	34.1	ULW	PML
2021-06-02	33.8	SML	PML
2021-06-08	33.7	ULW	PML
2021-06-08	34.0	SML	PML
2021-06-14	34.3	ULW	PML
2021-06-14	34.5	SML	PML
2021-06-21	34.7	ULW	PML
2021-06-21	34.6	SML	PML
2021-06-28	34.9	ULW	PML
2021-06-28	34.9	SML	PML
2021-07-05	33.4	ULW	PML
2021-07-05	33.3	SML	PML
2021-07-12	34.3	ULW	PML

Continued on next page

Table 20: Salinity measurements across CONNECT and PML campaigns. (Continued)

Sample Date	Salinity (psu)	Type	Campaign
2021-07-12	34.5	SML	PML
2021-07-19	34.0	ULW	PML
2021-07-19	34.5	SML	PML
2021-07-26	34.4	ULW	PML
2021-07-26	34.5	SML	PML
2021-08-02	33.5	ULW	PML
2021-08-02	34.4	SML	PML
2021-08-10	34.2	ULW	PML
2021-08-10	34.5	SML	PML
2021-08-18	33.6	ULW	PML
2021-08-18	34.1	SML	PML
2021-08-24	34.0	ULW	PML
2021-08-24	34.5	SML	PML
2021-08-31	34.4	ULW	PML
2021-08-31	34.8	SML	PML
2021-09-06	34.5	ULW	PML
2021-09-06	34.8	SML	PML
2021-09-13	34.6	ULW	PML
2021-09-13	34.6	SML	PML

6.4.1 Summary of Biogeochemical Measurements Across Campaigns

Table 21: Summary of DOC, fatty acid, surface tension and iodide measurements made during all campaigns.

Campaign	Measurement	Type	Unit	Minimum	Maximum	Mean	Median	IQR
PML	DOC	SML	mg C l^{-1}	0.9	3.1	1.6	1.5	0.7
		ULW	mg C l^{-1}	0.6	3.4	1.5	1.5	0.6
	Total Fatty Acids	SML	μg l^{-1}	2.9	207	35.2	19.4	31.0
		ULW	μg l^{-1}	3.1*	431	64.6	20.2	45.4
	Unsaturated Fatty Acids	SML	μg l^{-1}	1.0	83.2	15.3	5.6	20.8
		ULW	μg l^{-1}	1.5*	34.2	11.8	6.7	8.5
	Saturated Fatty Acids	SML	μg l^{-1}	1.5	199	20.0	9.5	10.1
		ULW	μg l^{-1}	0.4*	401	52.8	2.4	39.9
	Surface Tension	SML	mN m^{-1}	65.5	74.8	72.6	73.1	1.2
		ULW	mN m^{-1}	71.3	75.5	73.7	73.6	0.5
	Iodide	SML	nM	32	132	78	76	20

Continued on next page

Table 21: Summary of DOC, fatty acid, surface tension and iodide measurements made during all campaigns. (Continued)

Campaign	Measurement	Type	Unit	Minimum	Maximum	Mean	Median	IQR
		ULW	nM	58	149	86	88	22
CONNECT	DOC	SML	mg C l^{-1}	0.7	8.9	2.7	2.0	1.7
		ULW	mg C l^{-1}	1.4	2.6	1.9	1.9	0.4
	Total Fatty Acids	SML	μg l^{-1}	7.6*	30.1	15.1	12.7	10.9
		ULW	μg l^{-1}	0.1*	50.7	8.4	3.8	7.1
	Unsaturated Fatty Acids	SML	μg l^{-1}	0.1*	1.2	0.8	0.7	0.2
		ULW	μg l^{-1}	0.0* †	0.9	0.4	0.4	0.55
	Saturated Fatty Acids	SML	μg l^{-1}	6.4*	29.0	14.4	12.0	10.8
		ULW	μg l^{-1}	0.1*	50.6	8.1	3.2	7.2
	Surface Tension	SML	mN m^{-1}	68.9	73.3	72.4	72.9	0.4
		ULW	mN m^{-1}	73.2	73.7	73.5	73.4	0.4
	Iodide	SML	nM	39	73	59	60	13

Continued on next page

Table 21: Summary of DOC, fatty acid, surface tension and iodide measurements made during all campaigns. (Continued)

Campaign	Measurement	Type	Unit	Minimum	Maximum	Mean	Median	IQR
		ULW	nM	78	172	139	149	36
BLEACH	Surface Tension	SML	mN m^{-1}	55.0	74.9	68.6	70.2	7.4
		ULW	mN m^{-1}	65.0	75.2	73.1	73.7	0.8
	Iodide	SML	nM	50	135	99	109	65
		ULW	nM	64	150	115	126	43

* denotes some samples were below the LOQ of the analytical method, and these samples are not included in the statistical summary.

† denotes sample quantified, but rounded to 0.0 μg l^{-1}.

6.4.2 Iodide Concentration as a Function of Garrett Screen Mesh Exposure

This mesh exposure test was carried out by Dr Matthew Jones.

Steel mesh from the Garrett screens was cut into 2 cm x 2 cm squares, and approximately 60 g of mesh added to 300 ml unfiltered seawater. Aliquots were taken at regular intervals up to 20 minutes, and filtered prior to analysis by ion chromatography. The T_0 sample was collected prior to mesh addition.

No trend of diminishing iodide concentration was seen as a function of mesh exposure time (Fig. 64. A typical contact time between seawater and the Garrett screen was approximately 1-2 minutes. This experiment granted confidence that the stainless steel mesh did not alter iodide speciation (Matthew Jones, *in prep.*).

A further experiment was carried out in which seawater was collected by Garrett screen from a large container, and samples collected at various points during the draining process (Fig. 65). Again, iodide depletion was not observed as a function of time spent on the Garrett screen, indicating that the sample collection method did not bias the results.

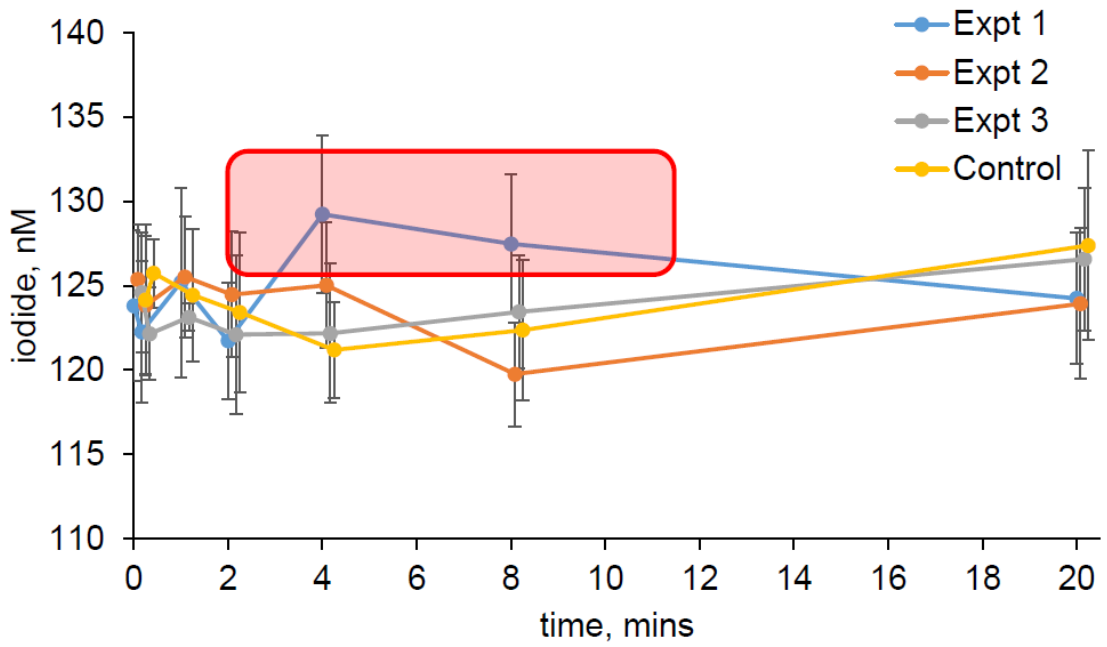

Figure 64: Change in iodide concentration as a function of stainless steel mesh exposure. Experiments 1, 2 and 3 are repeats, the control experiment had no mesh exposure. Error bars represent standard deviation of analytical replicates. The red box highlights samples that might have been unfiltered, due to human error.

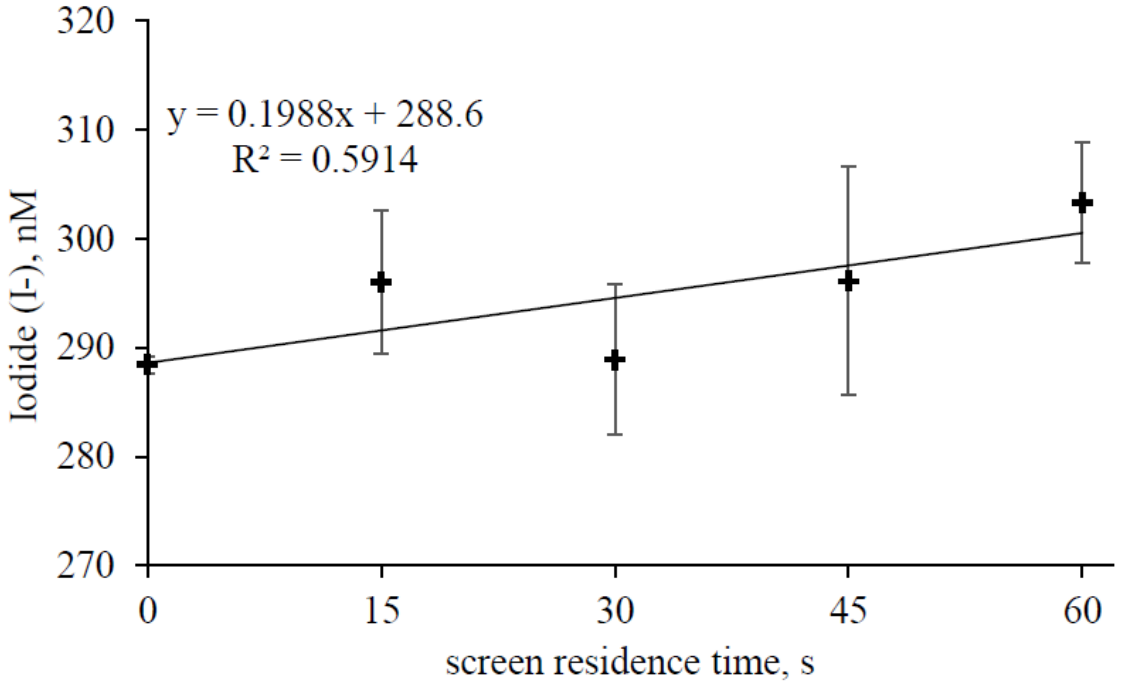

Figure 65: Change in iodide concentration as a function of draining time from the Garrett screen. Error bars represent standard deviation of analytical replicates.

6.4.3 Iodine Speciation During Ozone Exposure

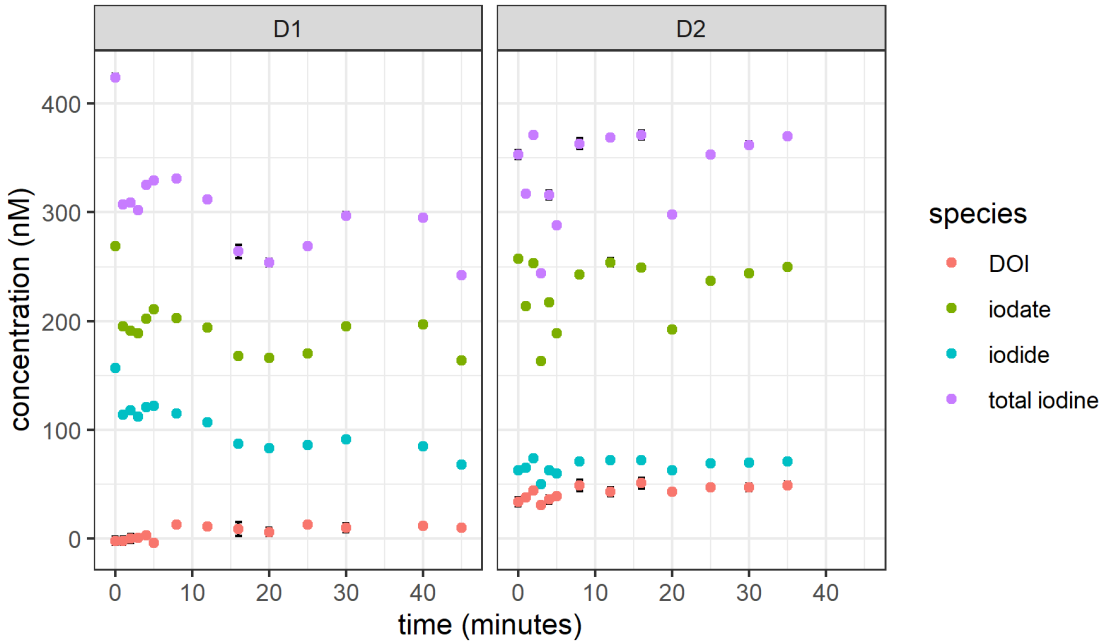

Figure 66: Change in full iodine speciation during ozone exposure experiments.

6.4.4 Calculation of Bulk Accommodation Coefficient

Using Eq. 8, information on the bulk accommodation coefficient, α_{aq} can be obtained. α_{aq} was calculated for this work by investigating the intercept of the relationship between γ_{corr} (corrected for gas diffusion using r_{diff}, described in Section 2.3.7.3) and $\sqrt{iodide}$ (Fig. 67). The y-intercepts obtained for each temperature are displayed in Table 22. The intercepts, and hence α_{aq} are scattered around zero, however the mean value is $\alpha_{aq} = -6.5 \times 10^{-5}$.

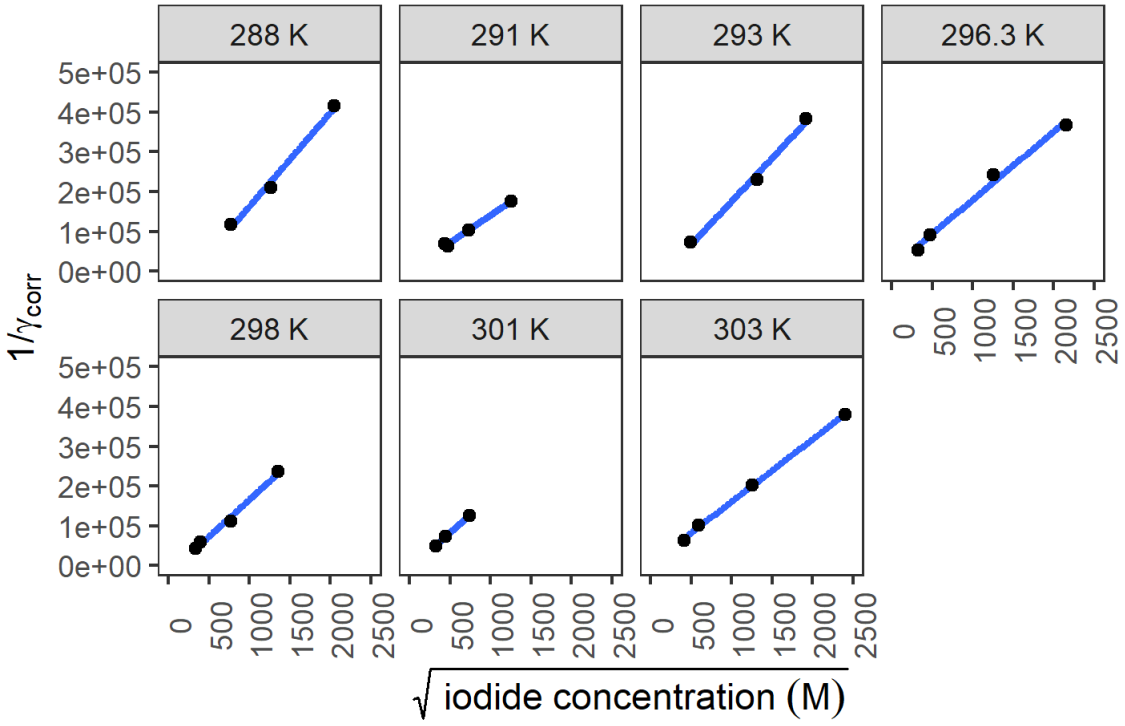

Figure 67: Relationship between corrected uptake and $\sqrt{iodide}$.

Table 22: Intercept details for calculation of the bulk accommodation coefficient.

Temperature (K)	Intercept	α_{aq}
288	-70747	-1.4×10^{-5}
291	7626	$+1.3 \times 10^{-4}$
293	-39464	-2.5×10^{-5}
296.3	10620	$+9.4 \times 10^{-5}$
298	-18323	-5.4×10^{-5}
301	-3056	-3.3×10^{-4}
303	5019	$+2.0 \times 10^{-4}$

6.4.5 Correlations of Supplementary Measured Parameters with Surface Uptake

Several factors were tested for correlation with the missing surface reactivity, as displayed in Figure 68.

Mounted on the CTD rosette, CDOM was measured by a Wet Labs ECO-FLCDTRD CDOM Sensor (data reproduced with permission of Anja Engel, GEOMAR), Chl-a was measured by fluorescence (Wet Labs ECO-AFL/FL), and salinity by SBE 4C, and water temperature was measured by a SBE 3plus (Rosa et al., 2024).

From discrete CTD samples, nitrite, nitrate, phosphate and silicate were measured by SEAL Quattro autoanalyser (data reporduced with permission of Birgit Quack, GEOMAR, PI of the CONNECT cruise). DMS was measured by GC-FPD (reproduced with permission of Christa Marandino, GEOMAR). Surface tension was measured by an EZ-pi tensiometer by Yousif Assiri.

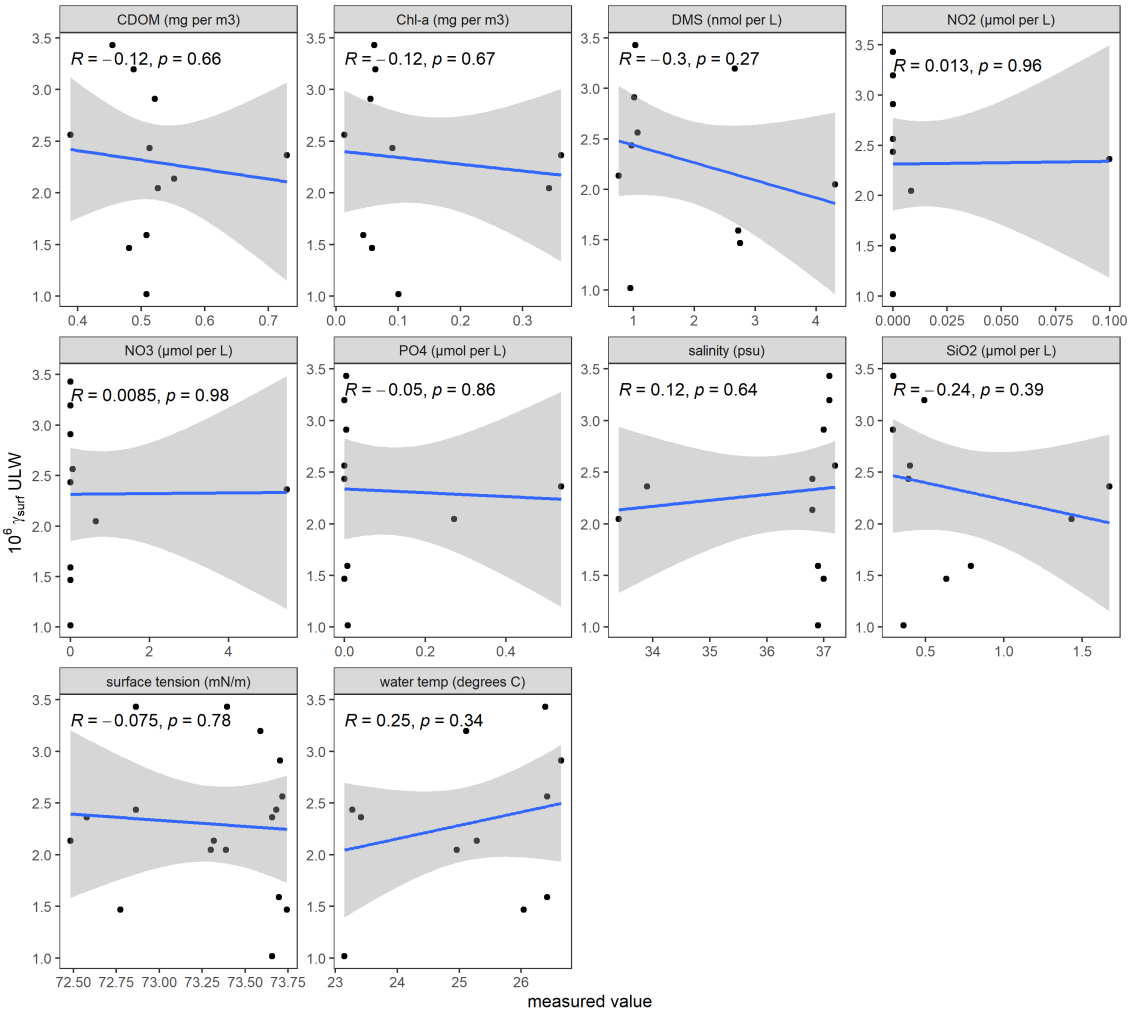

Figure 68: Correlations of tested factors against surface uptake.

References

Ainsworth, E. A., Yendrek, C. R., Sitch, S., Collins, W. J., and Emberson, L. D.: The effects of tropospheric ozone on net primary productivity and implications for climate change, Annual Review of Plant Biology, 63, 637–661, https://doi.org/10.1146/annurev-arplant-042110-103829, 2012.

Ammann, M., Cox, R. A., Crowley, J. N., Jenkin, M. E., Mellouki, A., Rossi, M. J., Troe, J., and Wallington, T. J.: Evaluated kinetic and photochemical data for atmospheric chemistry: Volume VI - Heterogeneous reactions with liquid substrates, Atmospheric Chemistry and Physics, 13, 8045–8228, https://doi.org/10.5194/acp-13-8045-2013, 2013.

Archer, C. L. and Jacobson, M. Z.: Evaluation of global wind power, Journal of Geophysical Research D: Atmospheres, 110, 1–20, https://doi.org/10.1029/2004JD005462, 2005.

Atkinson, R. W., Butland, B. K., Dimitroulopoulou, C., Heal, M. R., Stedman, J. R., Carslaw, N., Jarvis, D., Heaviside, C., Vardoulakis, S., Walton, H., and Anderson, H. R.: Long-term exposure to ambient ozone and mortality: A quantitative systematic review and meta-analysis of evidence from cohort studies, BMJ Open, 6, 1–10, https://doi.org/10.1136/bmjopen-2015-009493, 2016.

Benavent, N., Mahajan, A. S., Li, Q., Cuevas, C. A., Schmale, J., Angot, H., Jokinen, T., Quéléver, L. L., Blechschmidt, A. M., Zilker, B., Richter, A., Serna, J. A., Garcia-Nieto, D., Fernandez, R. P., Skov, H., Dumitrascu, A., Pereira, P. S., Abrahamsson, K., Bucci, S., Duetsch, M., Stohl, A., Beck, I., Laurila, T., Blomquist, B., Howard, D., Archer, S. D., Bariteau, L., Helmig, D., Hueber, J., Jacobi, H. W., Posman, K., Dada, L., Daellenbach, K. R., and Saiz-Lopez, A.: Substantial contribution of iodine to Arctic ozone destruction, Nature Geoscience, 15, 770–773, https://doi.org/10.1038/s41561-022-01018-w, 2022.

Betancourt, C., Stomberg, T. T., Edrich, A. K., Patnala, A., Schultz, M. G., Roscher, R., Kowalski, J., and Stadtler, S.: Global, high-resolution map-

ping of tropospheric ozone-explainable machine learning and impact of uncertainties, Geoscientific Model Development, 15, 4331–4354, https://doi.org/10.5194/gmd-15-4331-2022, 2022.

bo Oh, I., Byun, D. W., cheol Kim, H., Kim, S., and Cameron, B.: Modeling the effect of iodide distribution on ozone deposition to seawater surface, Atmospheric Environment, 42, 4453–4466, https://doi.org/10.1016/j.atmosenv.2008.02.022, 2008.

Brown, L. V., Pound, R. J., Ives, L. S., Jones, M. R., Andrews, S. J., and Carpenter, L. J.: Negligible temperature dependence of the ozone-iodide reaction and implications for oceanic emissions of iodine, Atmospheric Chemistry and Physics, 24, 3905–3923, https://doi.org/10.5194/acp-24-3905-2024, 2024.

Burba, G.: Eddy Covariance Method for Scientific, Industrial, Agricultural and Regulatory Applications, LI-COR Biosciences, 2013.

Burdette, T. C., Bramblett, R. L., Deegan, A. M., Coffey, N. R., Wozniak, A. S., and Frossard, A. A.: Organic Signatures of Surfactants and Organic Molecules in Surface Microlayer and Subsurface Water of Delaware Bay, ACS Earth and Space Chemistry, 6, 2929–2943, https://doi.org/10.1021/acsearthspacechem.2c00220, 2022.

Campos, M. L. A.: New approach to evaluating dissolved iodine speciation in natural waters using cathodic stripping voltammetry and a storage study for preserving iodine species, Marine Chemistry, 57, 107–117, https://doi.org/10.1016/S0304-4203(96)00093-X, 1997.

Campos, M. L. A., Farrenkopf, A. M., Jickells, T. D., and Luther, G. W.: A comparison of dissolved iodine cycling at the Bermuda Atlantic Time-series station and Hawaii Ocean Time-series station, Deep-Sea Research Part II: Topical Studies in Oceanography, 43, 455–466, https://doi.org/10.1016/0967-0645(95)00100-x, 1996.

Campos, M. L. A., Sanders, R., and Jickells, T. D.: The dissolved iodate and iodide distribution in the South Atlantic from the Weddell Sea to Brazil, Marine Chemistry, 65, 167–175, https://doi.org/10.1016/S0304-4203(98)00094-2, 1999.

Carpenter, L. J., MacDonald, S. M., Shaw, M. D., Kumar, R., Saunders, R. W., Parthipan, R., Wilson, J., and Plane, J. M.: Atmospheric iodine levels influenced by sea surface emissions of inorganic iodine, Nature Geoscience, 6, 108–111, https://doi.org/10.1038/ngeo1687, URL http://dx.doi.org/10.1038/ngeo1687, 2013.

Cauwet, G.: Organic chemistry of seawater particulates - concepts and developments, Marine Chemistry, 5, 551–552, https://doi.org/10.1016/0304-4203(77)90040-8, 1977.

Cen-Lin, H. and Tzung-May, F.: Air-Sea Exchange of Volatile Organic Compounds: A New Model with Microlayer Effects, Atmospheric and Oceanic Science Letters, 6, 97–102, https://doi.org/10.1080/16742834.2013.11447063, 2013.

Chance, R. J., Baker, A. R., Carpenter, L. J., and Jickells, T. D.: The distribution of iodide at the sea surface, Environmental Sciences: Processes and Impacts, 16, 1841–1859, https://doi.org/10.1039/c4em00139g, 2014.

Chance, R. J., Tinel, L., Sherwen, T., Baker, A. R., Bell, T., Brindle, J., Campos, M. L. A., Croot, P., Ducklow, H., Peng, H., Hopkins, F., Hoogakker, B., Hughes, C., Jickells, T. D., Loades, D. C., Macaya, D. A. R., Mahajan, A. S., Malin, G., Phillips, D., Roberts, I., Roy, R., Sarkar, A., Sinha, A. K., Song, X., Winkelbauer, H., Wuttig, K., Yang, M., Peng, Z., and Carpenter, L. J.: Global sea-surface iodide observations, 1967–2018, Scientific Data, 6, 1–8, https://doi.org/10.1038/s41597-019-0288-y, 2019.

Chance, R. J., Tinel, L., Sarkar, A., Sinha, A. K., Mahajan, A. S., Chacko, R., Sabu, P., Roy, R., Jickells, T. D., Stevens, D. P., Wadley, M., and Carpenter, L. J.: Surface Inorganic Iodine Speciation in the Indian and Southern Oceans

From 12°N to 70°S, Frontiers in Marine Science, 7, 1–16, https://doi.org/10.3389/fmars.2020.00621, 2020.

Chang, W., Heikies, B. G., and Lee, M.: Ozone deposition to the sea surface: chemical enhancement and wind speed dependence, Atmospheric Environment, 38, 1053–1059, 2004.

Chapman, P. and Liss, P. S.: The sea surface microlayer : Measurements of dissolved iodine species and nutrients in coastal waters, 26, 1981.

Clifford, D., Donaldson, D. J., Brigante, M., D'Anna, B., and George, C.: Reactive uptake of ozone by chlorophyll at aqueous surfaces, Environmental Science and Technology, 42, 1138–1143, https://doi.org/10.1021/es0718220, 2008.

Coleman, L., Varghese, S., Tripathi, O. P., Jennings, S. G., and O'Dowd, C. D.: Regional-Scale Ozone Deposition to North-East Atlantic Waters, Advances in Meteorology, 2010, 1–16, https://doi.org/10.1155/2010/243701, 2010.

Criegee, R.: Mechanism of Ozonolysis, Angewandte Chemie International Edition in English, 14, 745–752, https://doi.org/10.1002/anie.197507451, 1975.

Cunliffe, M. and Wurl, O.: Guide to best practices to study the ocean's surface, Occasional Publications of the Marine Biological Association of the United Kingdom, 2014.

Cunliffe, M., Engel, A., Frka, S., Ženka Gašparović, B., Guitart, C., Murrell, J. C., Salter, M., Stolle, C., Upstill-Goddard, R., and Wurl, O.: Sea surface microlayers: A unified physicochemical and biological perspective of the air-ocean interface, Progress in Oceanography, 109, 104–116, https://doi.org/10.1016/j.pocean.2012.08.004, 2013.

Daumas, R. A., Laborde, T. L., Marty, J. C., and Saliot, A.: Influence of sampling method on the chemical composition of water surface film, Limnology and Oceanography, 21, 319–326, https://doi.org/10.4319/lo.1976.21.2.0319, 1976.

Davidovits, P., Kolb, C. E., Williams, L. R., Jayne, J. T., and Worsnop, D. R.: Mass accommodation and chemical reactions at gas-liquid interfaces, Chemical Reviews, 106, 1323–1354, https://doi.org/10.1021/cr040366k, 2006.

Dickson, A. G., Sabine, C. L., and Christian, J. R.: Guide to best practices for ocean CO¡sub¿2¡/sub¿ measurements, PICES Special Publication 3, 3, 191, URL http://aquacomm.fcla.edu/1443/, 2007.

Dingenen, R. V., Dentener, F. J., Raes, F., Krol, M. C., Emberson, L., and Cofala, J.: The global impact of ozone on agricultural crop yields under current and future air quality legislation, Atmospheric Environment, 43, 604–618, https://doi.org/10.1016/j.atmosenv.2008.10.033, URL http://dx.doi.org/10.1016/j.atmosenv.2008.10.033, 2009.

Donaldson, D. J., Mmereki, B. T., Chaudhuri, S. R., Handley, S., and Oh, M.: Uptake and reaction of atmospheric organic vapours on organic films, Faraday Discussions, 130, 227–239, https://doi.org/10.1039/b418859d, 2005a.

Donaldson, D. J., Mmereki, B. T., Chaudhuri, S. R., Handley, S., and Oh, M.: Uptake and reaction of atmospheric organic vapours on organic films, Faraday Discussions, 130, 227–239, https://doi.org/10.1039/b418859d, 2005b.

Drysdale, W. S., Loades, D. C., Stapleton, C. G., Lee, J. D., Peters, A., Alexander, B., and Carpenter, L. J.: Measurements of Oceanic Ozone Deposition at Two Coastal Sites, in: American Geophysical Union, 2023.

Engel, A. and Galgani, L.: The organic sea-surface microlayer in the upwelling region off the coast of Peru and potential implications for air-sea exchange processes, Biogeosciences, 13, 989–1007, https://doi.org/10.5194/bg-13-989-2016, 2016.

Ferre-Aracil, J., Cardona, S. C., and Navarro-Laboulais, J.: Kinetic study of ozone decay in homogeneous phosphate-buffered medium, Ozone: Science and Engineering, 37, 330–342, https://doi.org/10.1080/01919512.2014.998756, URL http://dx.doi.org/10.1080/01919512.2014.998756, 2015.

Fono, L. J. and Sedlak, D. L.: A simple method for the measurement of organic iodine in wastewater and surface water, 41, 1580–1586, https://doi.org/10.1016/j.watres.2006.12.032, 2007.

Forster, P., Ramaswamy, V., Artaxo, P., Berntsen, T., Betts, R., Fahey, D., Haywood, J., Lean, J., Lowe, D., Myhre, G., Nganga, J., Prinn, R., Raga, G., Schulz, M., and Dorland, R. V.: Changes in Atmospheric Constituents and in Radiative Forcing. In: Climate Change 2007: The Physical Science Basis. Contribution of Working Group I to the Fourth Assessment Report of the Intergovernmental Panel on Climate Change, Cambridge University Press, https://doi.org/10.20892/j.issn.2095-3941.2017.0150, 2007.

Frka, S., Kozarac, Z., and Ćosović, B.: Characterization and seasonal variations of surface active substances in the natural sea surface micro-layers of the coastal Middle Adriatic stations, Estuarine, Coastal and Shelf Science, 85, 555–564, https://doi.org/10.1016/j.ecss.2009.09.023, 2009.

Galbally, I. E. and Roy, C. R.: Destruction of ozone at the earth's surface, Quarterly Journal of the Royal Meteorological Society, 106, 599–620, 1980.

Gallagher, M. W., Beswick, K. M., and Coe, H.: Ozone deposition to coastal waters, Quarterly Journal of the Royal Meteorological Society, 127, 539–558, 2001.

Ganzeveld, L., Helmig, D., Fairall, C., Hare, J. E., and Pozzer, A.: Atmosphere-ocean ozone exchange: A global modeling study of biogeochemical, atmospheric, and waterside turbulence dependencies, Global Biogeochemical Cycles, 23, 1–16, https://doi.org/10.1029/2008GB003301, 2009.

Garland, J. A., Elzerman, A. W., and Penkett, S.: The Mechanism for Dry Deposition of Ozone to Seawater Surfaces, Journal of Geophysical Research, 85, 7488–7492, 1980.

Gašparović, B., Plavšić, M., Ćosović, B., and Saliot, A.: Organic matter characterization in the sea surface microlayers in the subarctic Norwegian fjords region,

Marine Chemistry, 105, 1–14, https://doi.org/10.1016/j.marchem.2006.12.010, 2007.

González-Labrada, E., Schmidt, R., and DeWolf, C. E.: Kinetic analysis of the ozone processing of an unsaturated organic monolayer as a model of an aerosol surface, Physical Chemistry Chemical Physics, 9, 5814–5821, https://doi.org/10.1039/b707890k, 2007.

Goodwin, D. G., Moffat, H. K., Schoegl, I., Speth, R. L., and Weber, B. W.: Cantera: An Object-oriented Software Toolkit for Chemical Kinetics, Thermodynamics, and Transport Processes, URL https://www.cantera.org, 2022.

Gorham, E.: Acid deposition and its ecological effects : a brief history of research, Environmental Science Policy, 1, 1998.

Gusten, H. and Heinrich, G.: ON-LINE MEASUREMENTS OF OZONE SURFACE FLUXES: PART I. METHODOLOGY AND INSTRUMENTATION, 1996.

Hansell, D. A. and Orellana, M. V.: Dissolved organic matter in the global ocean: A primer, Gels, 7, https://doi.org/10.3390/gels7030128, 2021.

Hansell, D. A., Carlson, C. A., Repeta, D. J., and Schlitzer, R.: Dissolved Organic Matter in the Ocean: A Controversy Stimulates New Insights, The O, 22, 2009.

Hardacre, C., Wild, O., and Emberson, L.: An evaluation of ozone dry deposition in global scale chemistry climate models, Atmospheric Chemistry and Physics, 15, 6419–6436, https://doi.org/10.5194/acp-15-6419-2015, 2015.

Hardy, J. T.: Biological effects of chemicals in the sea-surface microlayer, pp. 339–370, Cambridge University Press, 1997.

Harris, C. R., Millman, K. J., van der Walt, S. J., Gommers, R., Virtanen, P., Cournapeau, D., Wieser, E., Taylor, J., Berg, S., Smith, N. J., Kern, R., Picus, M., Hoyer, S., van Kerkwijk, M. H., Brett, M., Haldane, A., del Río, J. F., Wiebe, M., Peterson, P., Gérard-Marchant, P., Sheppard, K., Reddy, T., Weckesser, W., Abbasi, H., Gohlke, C., and Oliphant, T. E.: Array programming with NumPy,

Nature, 585, 357–362, https://doi.org/10.1038/s41586-020-2649-2, URL http://dx.doi.org/10.1038/s41586-020-2649-2, 2020.

Helmig, D., Boylan, P., Johnson, B., Oltmans, S., Fairall, C., Staebler, R., Weinheimer, A., Orlando, J., Knapp, D. J., Montzka, D. D., Flocke, F., Frieó, U., Sihler, H., and Shepson, P. B.: Ozone dynamics and snow-atmosphere exchanges during ozone depletion events at Barrow, Alaska, Journal of Geophysical Research Atmospheres, 117, 1–15, https://doi.org/10.1029/2012JD017531, 2012.

Hu, J. H., Shi, Q., Davidovits, P., Worsnop, D. R., Zahniser, M. S., and Kolb, C. E.: Reactive uptake of Cl2(g) and Br2(g) by aqueous surfaces as a function of Br- and I- ion concentration. The effect of chemical reaction at the interface, Journal of physical chemistry, 99, 8768–8776, https://doi.org/10.1021/j100021a050, 1995.

Jerrett, M., Burnett, R. T., Pope, C. A., Ito, K., Thurston, G., Krewski, D., Shi, Y., Calle, E., and Thun, M.: Long-Term Ozone Exposure and Mortality, New England Journal of Medicine, 360, 1085–1095, https://doi.org/10.1056/nejmoa0803894, 2009.

Johnson, M. T.: A numerical scheme to calculate temperature and salinity dependent air-water transfer velocities for any gas, Ocean Science, 6, 913–932, https://doi.org/10.5194/os-6-913-2010, 2010.

Johnson, P. N. and Davis, R. A.: Diffusivity of ozone in water, Journal of Chemical and Engineering Data, 41, 1485–1487, https://doi.org/10.1021/je9602125, 1996.

Jones, A. E. and Shanklin, J. D.: Continued decline of total ozone over Halley, Antarctica, since 1985, Nature, 376, 409–411, https://doi.org/10.1038/376409a0, 1995.

Jones, M. R., Chance, R. J., Dadic, R., Hannula, H. R., May, R., Ward, M., and Carpenter, L. J.: Environmental iodine speciation quantification in seawater and snow using ion exchange chromatography and UV spectrophotometric detec-

tion, Analytica Chimica Acta, 1239, 340 700, https://doi.org/10.1016/j.aca.2022.340700, URL https://doi.org/10.1016/j.aca.2022.340700, 2023.

Karl, D. M., Dore, J. E., Lukas, R., Michaels, A. F., Bates, N. R., and Knap, A.: Building the Long-term Picture : The U.S. JGOFS Time-series Programs, The Oceanography Society, 14, 6–17, 2001.

Kawa, S. R. and Jr., R. P.: Ozone Budgets From the Dynamics and Chemistry of Marine Stratocumulus Experiment, Journal of Geophysical Research, 94, 9809–9817, 1989.

King, M. D., Canosa-Mas, C. E., and Wayne, R. P.: A structure-activity relationship (SAR) for predicting rate constants for the reaction of NO3, OH and O3 with monoalkenes and conjugated dienes, Physical Chemistry Chemical Physics, 1, 2239–2246, https://doi.org/10.1039/a901193e, 1999.

King, M. D., Rennie, A. R., Thompson, K. C., Fisher, F. N., Dong, C. C., Thomas, R. K., Pfrang, C., and Hughes, A. V.: Oxidation of oleic acid at the air-water interface and its potential effects on cloud critical supersaturations, Physical Chemistry Chemical Physics, 11, 7699–7707, https://doi.org/10.1039/b906517b, 2009.

King, M. D., Jones, S. H., Lucas, C. O., Thompson, K. C., Rennie, A. R., Ward, A. D., Marks, A. A., Fisher, F. N., Pfrang, C., Hughes, A. V., and Campbell, R. A.: The reaction of oleic acid monolayers with gas-phase ozone at the air water interface: The effect of sub-phase viscosity, and inert secondary components, Physical Chemistry Chemical Physics, 22, 28 032–28 044, https://doi.org/10.1039/d0cp03934a, 2020.

Kinney, P. L., Thurston, G. D., and Raizenne, M.: The effects of ambient ozone on lung function in children: A reanalysis of six summer camp studies, Environmental Health Perspectives, 104, 170–174, https://doi.org/10.1289/ehp.96104170, 1996.

Kleber, J., Laß, K., and Friedrichs, G.: Quantitative time-resolved vibrational sum frequency generation spectroscopy as a tool for thin film kinetic studies: New insights into oleic acid monolayer oxidation, Journal of Physical Chemistry A, 117, 7863–7875, https://doi.org/10.1021/jp404087s, 2013.

Knopf, D. A., Pöschl, U., and Shiraiwa, M.: Radial Diffusion and Penetration of Gas Molecules and Aerosol Particles through Laminar Flow Reactors, Denuders, and Sampling Tubes, Analytical Chemistry, 87, 3746–3754, https://doi.org/10.1021/ac5042395, 2015.

Koenig, T. K., Baidar, S., Campuzano-Jost, P., Cuevas, C. A., Dix, B., Fernandez, R. P., Guo, H., Hall, S. R., Kinnison, D., Nault, B. A., Ullmann, K., Jimenez, J. L., Saiz-Lopez, A., and Volkamer, R.: Quantitative detection of iodine in the stratosphere, Proceedings of the National Academy of Sciences of the United States of America, 117, 1860–1866, https://doi.org/10.1073/pnas.1916828117, 2020.

Kosak-Channing, L. F. and Helz, G. R.: Solubility of Ozone in Aqueous Solutions of 0-0.6 M Ionic Strength at 5-30 ℃, URL `https://pubs.acs.org/sharingguidelines`, 1983.

Kwamena, N. O. A., Thornton, J. A., and Abbatt, J. P.: Kinetics of surface-bound benzo[a]pyrene and ozone on solid organic and salt aerosols, Journal of Physical Chemistry A, 108, 11 626–11 634, https://doi.org/10.1021/jp046161x, 2004.

Langenberg, S., Carstens, T., Hupperich, D., Schweighoefer, S., and Schweighoefer, S.: Technical note: Determination of binary gas-phase diffusion coefficients of unstable and adsorbing atmospheric trace gases at low temperature - Arrested flow and twin tube method, Atmospheric Chemistry and Physics, 20, 3669–3682, https://doi.org/10.5194/acp-20-3669-2020, 2020.

Lenschow, D. H., Jr., R. P., and Stankov, B. B.: Measurement of Ozone Vertical Flux to Ocean and Forest, Journal of Geophysical Research, 87, 8833–8837, 1982.

Liss, P. S. and Duce, R. A.: Preface, vol. 14, pp. xiii–xv, Cambridge University Press, https://doi.org/10.1111/j.1468-2273.1960.tb01734.x, 1997.

Liu, Q., Schurter, L. M., Muller, C. E., Aloisio, S., Francisco, J. S., and Margerum, D. W.: Kinetics and mechanisms of aqueous ozone reactions with bromide, sulfite, hydrogen sulfite, iodide, and nitrite ions, Inorganic Chemistry, 40, 4436–4442, https://doi.org/10.1021/ic000919j, 2001.

Liu, Y., Sheaffer, R. L., and Barker, J. R.: Effects of temperature and ionic strength on the rate and equilibrium constants for the reaction Iaq• + Iaq- I2•-aq, Journal of Physical Chemistry A, 107, 10 296–10 302, https://doi.org/10.1021/jp036126a, 2003.

Loades, D. C., Yang, M., Bell, T. G., Vaughan, A. R., Pound, R. J., Metzger, S., Lee, J. D., and Carpenter, L. J.: Ozone deposition to a coastal sea: Comparison of eddy covariance observations with reactive air-sea exchange models, Atmospheric Measurement Techniques, 13, 6915–6931, https://doi.org/10.5194/amt-13-6915-2020, 2020.

Luhar, A. K., Woodhouse, M. T., and Galbally, I. E.: A revised global ozone dry deposition estimate based on a new two-layer parameterisation for air-sea exchange and the multi-year MACC composition reanalysis, Atmospheric Chemistry and Physics, 18, 4329–4348, https://doi.org/10.5194/acp-18-4329-2018, 2018.

MacDonald, S. M., Martín, J. C. G., Chance, R. J., Warriner, S., Saiz-Lopez, A., Carpenter, L. J., and Plane, J. M.: A laboratory characterisation of inorganic iodine emissions from the sea surface: Dependence on oceanic variables and parameterisation for global modelling, Atmospheric Chemistry and Physics, 14, 5841–5852, https://doi.org/10.5194/acp-14-5841-2014, 2014.

Magi, L., Schweitzer, F., Pallares, C., Cherif, S., Mirabel, P., and George, C.: Investigation of the uptake rate of ozone and methyl hydroperoxide by water

surfaces, Journal of Physical Chemistry A, 101, 4943–4949, https://doi.org/10.1021/jp970646m, 1997.

Martino, M., Mills, G. P., Woeltjen, J., and Liss, P. S.: A new source of volatile organoiodine compounds in surface seawater, Geophysical Research Letters, 36, 2–6, https://doi.org/10.1029/2008GL036334, 2009.

Martino, M., Lézé, B., Baker, A. R., and Liss, P. S.: Chemical controls on ozone deposition to water, Geophysical Research Letters, 39, 39–43, https://doi.org/10.1029/2011GL050282, 2012.

Marty, J. C., Saliot, A., Buat-Menard, P., Chesselet, R., and Hunter, K. A.: Relationship between the lipid compositions of marine aerosols, the sea surface microlayer, and subsurface water, Journal of Geophysical Research: Oceans, 84, 5707–5716, https://doi.org/https://doi.org/10.1029/JC084iC09p05707, 1979.

Mcevoy, A. J., Atkinson, A., Airs, R. L., Brittain, R., Brown, I., Fileman, E. S., Findlay, H. S., Mcneill, C. L., Ostle, C., Smyth, T. J., Somerfield, P. J., Tait, K., Tarran, G. A., Thomas, S., Widdicombe, C. E., Woodward, E. M. S., Beesley, A., Conway, D. V., Fishwick, J., Haines, H., Harris, C., Harris, R., Hélaouët, P., Johns, D., Lindeque, P. K., Mesher, T., Mcquatters-Gollop, A., Nunes, J., Perry, F., Queiros, A. M., Rees, A., Rühl, S., Sims, D., Torres, R., and Widdicombe, S.: The Western Channel Observatory: a century of physical, chemical and biological data compiled from pelagic and benthic habitats in the western English Channel, Earth System Science Data, 15, 5701–5737, https://doi.org/10.5194/essd-15-5701-2023, 2023.

McKay, W. A., Stephens, B. A., and Dollard, G. J.: Laboratory measurements of ozone deposition to sea water and other saline solutions, Atmospheric Environment Part A, General Topics, 26, 3105–3110, https://doi.org/10.1016/0960-1686(92)90467-Y, 1992.

McNeill, V. F., Wolfe, G. M., and Thornton, J. A.: The oxidation of oleate in submi-

cron aqueous salt aerosols: Evidence of a surface process, Journal of Physical Chemistry A, 111, 1073–1083, https://doi.org/10.1021/jp066233f, 2007.

McVeigh, P., O'Dowd, C., and Berresheim, H.: Eddy Correlation Measurements of Ozone Fluxes over Coastal Waters West of Ireland, Advances in Meteorology, 2010, 1–7, https://doi.org/10.1155/2010/754941, 2010.

Mmereki, B. T. and Donaldson, D. J.: Direct Observation of the Kinetics of an Atmospherically Important Reaction at the Air-Aqueous Interface, Journal of Physical Chemistry A, 107, 11 038–11 042, https://doi.org/10.1021/jp036119m, 2003.

Mmereki, B. T., Donaldson, D. J., Gilman, J. B., Eliason, T. L., and Vaida, V.: Kinetics and products of the reaction of gas-phase ozone with anthracene adsorbed at the air-aqueous interface, Atmospheric Environment, 38, 6091–6103, https://doi.org/10.1016/j.atmosenv.2004.08.014, 2004.

Moreno, C. G. and Baeza-Romero, M. T.: A kinetic model for ozone uptake by solutions and aqueous particles containing I- and Br-, including seawater and sea-salt aerosol, Physical Chemistry Chemical Physics, 21, 19 835–19 856, https://doi.org/10.1039/c9cp03430g, 2019.

Moreno, C. G., Gálvez, O., Moreno, V. L.-A., Espildora-García, E. M., and Baeza-Romero, M. T.: A revisit of the interaction of gaseous ozone with aqueous iodide. Estimating the contributions of the surface and bulk reactions, Physical Chemistry Chemical Physics, 20, 27 571–27 584, https://doi.org/10.1039/c8cp04394a, 2018.

Myhre, G., Shindell, D., Bréon, F.-M., Collins, W., Fuglestvedt, J., Huang, J., Koch, D., Lamarque, J.-F., Lee, D., Mendoza, B., Nakajima, T., Robock, A., Stephens, G., Takemura, T., and Zhang, H.: Anthropogenic and Natural Radiative Forcing. In: Climate Change 2013: The Physical Science Basis. Contribution of Working Group I to the Fifth Assessment Report of the Intergovernmental Panel on

Climate Change, vol. 9781107057, Cambridge University Press, https://doi.org/10.1017/CBO9781107415324.018, 2013.

Nayar, K. G., Panchanathan, D., McKinley, G. H., and Lienhard, J. H.: Surface Tension of Seawater, Journal of Physical and Chemical Reference Data, 43, https://doi.org/10.1063/1.4899037, URL http://dx.doi.org/10.1063/1.4899037, 2014.

Nuvolone, D., Petri, D., and Voller, F.: The effects of ozone on human health, Environmental Science and Pollution Research, 25, 8074–8088, https://doi.org/10.1007/s11356-017-9239-3, 2018.

Pinxteren, M. V., Barthel, S., Fomba, K. W., Müller, K., Tümpling, W. V., and Herrmann, H.: The influence of environmental drivers on the enrichment of organic carbon in the sea surface microlayer and in submicron aerosol particles – measurements from the Atlantic Ocean, Elementa, 5, https://doi.org/10.1525/elementa.225, 2017.

Pound, R. J., Brown, L. V., Evans, M. J., and Carpenter, L. J.: An improved estimate of inorganic iodine emissions from the ocean using a coupled surface microlayer box model, Atmospheric Chemistry and Physics Discussions, Preprint, 1–40, https://doi.org/10.5194/egusphere-2023-2447, 2023.

Pöschl, U., Canagaratna, M., Jayne, J. T., Molina, L. T., Worsnop, D. R., Kolb, C. E., and Molina, M. J.: Mass accommodation coefficient of H2SO4 vapor on aqueous sulfuric acid surfaces and gaseous diffusion coefficient of H2SO4 in N2/H2O, Journal of Physical Chemistry A, 102, 10 082–10 089, https://doi.org/10.1021/jp982809s, 1998.

Rai, R. and Agrawal, M.: Impact of tropospheric ozone on crop plants, Proceedings of the National Academy of Sciences India Section B - Biological Sciences, 82, 241–257, https://doi.org/10.1007/s40011-012-0032-2, 2012.

Raja, S. and Valsaraj, K. T.: Heterogeneous oxidation by ozone of naphthalene adsorbed at the air-water interface of micron-size water droplets, Journal of

the Air and Waste Management Association, 55, 1345–1355, https://doi.org/10.1080/10473289.2005.10464732, 2005.

Ramaswamy, V., Boucher, O., Haigh, J., Hauglustaine, D., Haywood, J., Myhre, G., Nakajima, T., Shi, G., and Solomon, S.: Radiative forcing of climate change. In: Climate Change 2001: The Scientific Basis. Contribution of Working Group I to the Third Assessment Report of the Intergovernmental Panel on Climate Change, vol. 94, Cambridge University Press, https://doi.org/10.1023/A:1026752230256, 2001.

Read, K. A., Mahajan, A. S., Carpenter, L. J., Evans, M. J., Faria, B. V., Heard, D. E., Hopkins, J. R., Lee, J. D., Moller, S. J., Lewis, A. C., Mendes, L., McQuaid, J. B., Oetjen, H., Saiz-Lopez, A., Pilling, M. J., and Plane, J. M.: Extensive halogen-mediated ozone destruction over the tropical Atlantic Ocean, Nature, 453, 1232–1235, https://doi.org/10.1038/nature07035, 2008.

Reinthaler, T., Sintes, E., and Herndl, G. J.: Dissolved organic matter and bacterial production and respiration in the sea-surface microlayer of the open Atlantic and the western Mediterranean Sea, Limnology and Oceanography, 53, 122–136, https://doi.org/10.4319/lo.2008.53.1.0122, 2008.

Rosa, A., Cardoso, C., Reis, J., Azevedo, C., and Rui Faria, Ricardo, C.: CONNECT (SO287) Oceanographic Campaign - RV SONNE Oceanographic and Meteorological Final Report, 2024.

Rouvière, A., Sosedova, Y., and Ammann, M.: Uptake of ozone to deliquesced KI and mixed KI/NaCl aerosol particles, Journal of Physical Chemistry A, 114, 7085–7093, https://doi.org/10.1021/jp103257d, 2010.

Saint, A.: Atmospheric chemistry at the ocean surface: investigating ozonolysis in the sea surface microlayer, p. X, URL http://etheses.whiterose.ac.uk/26204/, 2019.

Saiz-Lopez, A. and Glasow, R. V.: Reactive halogen chemistry in the troposphere,

Chemical Society Reviews, 41, 6448–6472, https://doi.org/10.1039/c2cs35208g, 2012.

Sakamoto, Y., Yabushita, A., Kawasaki, M., and Enami, S.: Direct emission of I 2 molecule and IO radical from the heterogeneous reactions of gaseous ozone with aqueous potassium iodide solution, Journal of Physical Chemistry A, 113, 7707–7713, https://doi.org/10.1021/jp903486u, 2009.

Salter, M., Upstill-Goddard, R. C., Nightingale, P. D., Archer, S. D., Blomquist, B., Ho, D. T., Huebert, B., Schlosser, P., and Yang, M.: Impact of an artificial surfactant release on air-sea gas fluxes during Deep Ocean Gas Exchange Experiment II, Journal of Geophysical Research: Oceans, 116, 1–9, https://doi.org/10.1029/2011JC007023, 2011.

Sarwar, G., Kang, D., Foley, K., Schwede, D., Gantt, B., and Mathur, R.: Technical note: Examining ozone deposition over seawater, Atmospheric Environment, 141, 255–262, https://doi.org/10.1016/j.atmosenv.2016.06.072, URL http://dx.doi.org/10.1016/j.atmosenv.2016.06.072, 2016.

Schmidt, R. and Schneider, B.: The effect of surface films on the air-sea gas exchange in the Baltic Sea, Marine Chemistry, 126, 56–62, https://doi.org/10.1016/j.marchem.2011.03.007, 2011.

Schneider, S. R., Lakey, P. S. J., Shiraiwa, M., and Abbatt, J. P.: Reactive Uptake of Ozone to Simulated Seawater: Evidence for Iodide Depletion, Journal of Physical Chemistry A, https://doi.org/10.1021/acs.jpca.0c08917, 2020.

Schneider, S. R., Lakey, P. S., Shiraiwa, M., and Abbatt, J. P.: Iodine emission from the reactive uptake of ozone to simulated seawater, Environmental Science: Processes and Impacts, https://doi.org/10.1039/d2em00111j, 2022.

Scientific, T.: Model 49i Instruction Manual, URL www.thermo.com/WEEERoHS., 2007.

Shaw, M. D. and Carpenter, L. J.: Modification of ozone deposition and I2 emissions at the air-aqueous interface by dissolved organic carbon of marine ori-

gin, Environmental Science and Technology, 47, 10 947–10 954, https://doi.org/10.1021/es4011459, 2013.

Sherwen, T., Chance, R. J., Tinel, L., Ellis, D., Evans, M. J., and Carpenter, L. J.: A machine-learning-based global sea-surface iodide distribution, Earth System Science Data, 11, 1239–1262, 2019.

Shiraiwa, M., Pfrang, C., and Pöschl, U.: Kinetic multi-layer model of aerosol surface and bulk chemistry (KM-SUB): The influence of interfacial transport and bulk diffusion on the oxidation of oleic acid by ozone, Atmospheric Chemistry and Physics, 10, 3673–3691, https://doi.org/10.5194/acp-10-3673-2010, 2010.

Sieburth, J. M., Willis, P. J., Johnson, K. M., Burney, C. M., Lavoie, D. M., Hinga, K. R., Caron, D. A., French, F. W., Johnson, P. W., and Davis, P. G.: Dissolved organic matter and heterotrophic microneuston in the surface microlayers of the North Atlantic, Science, 194, 1415–1418, https://doi.org/10.1126/science.194.4272.1415, 1976.

Simpson, W. R., Glasow, R. V., Riedel, K., Anderson, P., Ariya, P., Bottenheim, J., Burrows, J., Carpenter, L. J., Frieß, U., Goodsite, M. E., Heard, D., Hutterli, M., Jacobi, H.-W., Kaleschke, L., Neff, B., Plane, J., Platt, U., Richter, A., Roscoe, H., Sander, R., Shepson, P., Sodeau, J., Steffen, A., Wagner, T., and Wolff, E.: Atmospheric Chemistry and Physics Halogens and their role in polar boundary-layer ozone depletion, URL www.atmos-chem-phys.net/7/4375/2007/, 2007.

Slowey, J. F., Jeffrey, L. M., and Hood, D. W.: The fatty-acid content of ocean water, Geochimica et Cosmochimica Acta, 26, 607–616, https://doi.org/https://doi.org/10.1016/0016-7037(62)90041-8, 1961.

Souza, F. P. D. and Gupta, R. S.: Fluoride, bromide and iodide in the southwestern Indian Ocean sector of the Southern Ocean, Deep Sea Research Part B. Oceanographic Literature Review, 31, 856, https://doi.org/10.1016/0198-0254(84)93266-7, 1984.

Stapleton, C. G., Loades, D. C., Drysdale, W. S., Brooks, I. M., Lee, J. D., Johnson, R. J., Lethaby, P., Edwards, P., and Carpenter, L. J.: Shipborne Eddy Covariance Measurements of Oceanic Ozone Fluxes, in: American Geophysical Union, 2023.

Stevenson, D. S., Dentener, F. J., Schultz, M. G., Ellingsen, K., van Noije, T. P., Wild, O., Zeng, G., Ammann, M., Atherton, C. S., Bell, N., Bergmann, D. J., Bey, I., Butler, T., Cofala, J., Collins, W. J., Derwent, R. G., Doherty, R. M., Drevet, J., Eskes, H. J., Fiore, A. M., Gauss, M., Hauglustaine, D. A., Horowitz, L. W., Isaksen, I. S., Krol, M. C., Lamarque, J. F., Lawrence, M. G., Montanaro, V., Müller, J. F., Pitari, G., Prather, M. J., Pyle, J. A., Rast, S., Rodriquez, J. M., Sanderson, M. G., Savage, N. H., Shindell, D. T., Strahan, S. E., Sudo, K., and Szopa, S.: Multimodel ensemble simulations of present-day and near-future tropospheric ozone, Journal of Geophysical Research Atmospheres, 111, https://doi.org/10.1029/2005JD006338, 2006.

Stolle, C., Ribas-Ribas, M., Badewien, T. H., Barnes, J., Carpenter, L. J., Chance, R. J., Damgaard, L. R., María, A., Quesada, D., Engel, A., Frka, S., Galgani, L., Gašparović, B., Gerriets, M., Ili, N., Mustaffa, H., Herrmann, H., Kallajoki, L., Pereira, R., Radach, F., Revsbech, N. P., Rickard, P., Saint, A., Salter, M., Striebel, M., Triesch, N., Uher, G., Upstill-G, Oddard, R. C., Pinxteren, M. V., Zäncker, B., Zieger, P., and Wurl, O.: The MILAN Campaign: Studying Diel Light Effects on the Air–Sea Interface, Bulletin of the American Meteorological Society, 101, 146–166, 2020.

Team, R. C.: R: A Language and Environment for Statistical Computing, 2021.

Teiwes, R., Elm, J., Handrup, K., Jensen, E. P., Bilde, M., and Pedersen, H. B.: Atmospheric chemistry of iodine anions: Elementary reactions of I-, IO-, and IO2- with ozone studied in the gas-phase at 300 K using an ion trap, Physical Chemistry Chemical Physics, 20, 28 606–28 615, https://doi.org/10.1039/c8cp05721d, 2018.

Thomas, D. A., Wang, L., Goh, B., Kim, E. S., and Beauchamp, J. L.: Mass

Spectrometric Sampling of a Liquid Surface by Nanoliter Droplet Generation from Bursting Bubbles and Focused Acoustic Pulses: Application to Studies of Interfacial Chemistry, Analytical Chemistry, 87, 3336–3344, https://doi.org/10.1021/ac504494t, 2015.

Thompson, A. M. and Zafiriou, O. C.: Air-sea fluxes of transient atmospheric species, Journal of Geophysical Research: Oceans, 88, 6696–6708, 1983.

Tinel, L., Adams, T. J., Hollis, L. D., Bridger, A. J., Chance, R. J., Ward, M. W., Ball, S. M., and Carpenter, L. J.: Influence of the Sea Surface Microlayer on Oceanic Iodine Emissions, Environmental Science and Technology, 54, 13 228–13 237, https://doi.org/10.1021/acs.est.0c02736, 2020.

Trapido, M., Veressinina, Y., and Munter, R.: Ozonation and advanced oxidation processes of polycyclic aromatic hydrocarbons in aqueous solutions - a kinetic study, Environmental Technology (United Kingdom), 16, 729–740, https://doi.org/10.1080/09593331608616312, 1995.

Tsunogai, S. and Henmi, T.: Iodine in the surface water of the ocean, Journal of the Oceanographical Society of Japan, 27, 67–72, https://doi.org/10.1007/BF02109332, 1971.

Vesna, O., Sax, M., Kalberer, M., Gaschen, A., and Ammann, M.: Product study of oleic acid ozonolysis as function of humidity, Atmospheric Environment, 43, 3662–3669, https://doi.org/10.1016/j.atmosenv.2009.04.047, URL http://dx.doi.org/10.1016/j.atmosenv.2009.04.047, 2009.

Vieceli, J., Ma, O. L., and Tobias, D. J.: Uptake and collision dynamics of gas phase ozone at unsaturated organic interfaces, Journal of Physical Chemistry A, 108, 5806–5814, https://doi.org/10.1021/jp0494584, 2004.

Virtanen, P., Gommers, R., Oliphant, T. E., Haberland, M., Reddy, T., Cournapeau, D., Burovski, E., Peterson, P., Weckesser, W., Bright, J., van der Walt, S. J., Brett, M., Wilson, J., Millman, K. J., Mayorov, N., Nelson, A. R., Jones, E., Kern, R., Larson, E., Carey, C. J., Polat, I., Feng, Y., Moore, E. W., VanderPlas,

J., Laxalde, D., Perktold, J., Cimrman, R., Henriksen, I., Quintero, E. A., Harris, C. R., Archibald, A. M., Ribeiro, A. H., Pedregosa, F., van Mulbregt, P., Vijaykumar, A., Bardelli, A. P., Rothberg, A., Hilboll, A., Kloeckner, A., Scopatz, A., Lee, A., Rokem, A., Woods, C. N., Fulton, C., Masson, C., Häggström, C., Fitzgerald, C., Nicholson, D. A., Hagen, D. R., Pasechnik, D. V., Olivetti, E., Martin, E., Wieser, E., Silva, F., Lenders, F., Wilhelm, F., Young, G., Price, G. A., Ingold, G. L., Allen, G. E., Lee, G. R., Audren, H., Probst, I., Dietrich, J. P., Silterra, J., Webber, J. T., Slavič, J., Nothman, J., Buchner, J., Kulick, J., Schönberger, J. L., de Miranda Cardoso, J. V., Reimer, J., Harrington, J., Rodríguez, J. L. C., Nunez-Iglesias, J., Kuczynski, J., Tritz, K., Thoma, M., Newville, M., Kümmerer, M., Bolingbroke, M., Tartre, M., Pak, M., Smith, N. J., Nowaczyk, N., Shebanov, N., Pavlyk, O., Brodtkorb, P. A., Lee, P., McGibbon, R. T., Feldbauer, R., Lewis, S., Tygier, S., Sievert, S., Vigna, S., Peterson, S., More, S., Pudlik, T., Oshima, T., Pingel, T. J., Robitaille, T. P., Spura, T., Jones, T. R., Cera, T., Leslie, T., Zito, T., Krauss, T., Upadhyay, U., Halchenko, Y. O., and Vázquez-Baeza, Y.: SciPy 1.0: fundamental algorithms for scientific computing in Python, Nature Methods, 17, 261–272, https://doi.org/10.1038/s41592-019-0686-2, 2020.

Vogt, R., Sander, R., Glasow, R. V., and Crutzen, P. J.: Iodine Chemistry and its Role in Halogen Activation and Ozone Loss in the Marine Boundary Layer: A Model Study, 1999.

von Sonntag, C. and von Gunten, U.: Chemistry of Ozone in Water and Wastewater Treatment: From Basic Principles to Applications, IWA Publishing, https://doi.org/10.2166/9781780400839, 2015.

Watson, R., Zinyowera, M., Moss, R., Moreno, R. A., Adhikary, S., Adler, M., Agrawala, S., Aguilar, A. G., Al-Khouli, S., Allen-Diaz, B., Ando, M., Andressen, R., Ang, B., Arnell, N., Arquit-Niederberger, A., Baethgen, W., Bates, B., Beniston, M., Bierbaum, R., Bijlsma, L., Boko, M., Bolin, B., Bolton, S., Bravo, E., Brown, S., Bullock, P., Cannell, M., Canziani, O., Carcavallo, R., Cerri, C. C., Chandler, W., Cheghe, F., Liu, C., Cole, V., Cramer, W., Cruz, R., Davidson, O.,

Desa, E., Xu, D., Diaz, S., Dlugoleck, A., Edmonds, J., Everett, J., Fischlin, A., Fitzharris, B., Fox, D., Friaa, J., Gacuhi, A. R., Galinski, W., Gitay, H., Groffman, P., Grubler, A., Gruenspecht, H., Hamburg, S., Hoffman, T., Holten, J., Ishitani, H., Ittekkot, V., Johansson, T., Kaczmarek, Z., Kashiwagi, T., Kirschbaum, M., Komor, P., Krovnin, A., Klein, R., Kulshrestha, S., Lang, S. H., Houerou, L., Leemans, R., Levine, M., Erda, L., Lluch-Belda, D., MacCracken, M., Magnuson, J., Mailu, G., Maitima, J. M., Marland, G., Maskell, K., McLean, R., McMichael, A., Michaelis, L., Miles, E., Moomaw, W., Moreira, R., Mulholland, P., Nakicenovic, N., Nicholls, R., Nishioka, S., Noble, I., Nurse, L., Odongo, R., Ohashi, R., Okemwa, E., Oquist, M., Parry, M., Perdomo, M., Petit, M., Piver, W., Ramakrishnan, P., Ravindranath, N., Reilly, J., Riedacker, A., Rogner, H.-H., Sathaye, J., Sauerbeck, D., Scott, M., Sharma, S., Shriner, D., Sinha, S., Skea, J., Solomon, A., Stakhiv, E., Starosolszky, O., Jilan, S., Suarez, A., Svensson, B., Takakura, H., Taylor, M., L.Tessier, Tirpak, D., Lien, T. V., Troadec, J.-P., Tsukamoto, H., Tsuzaka, I., Vellinga, P., Williams, T., Young, P., Xie, Y., and Fengqi, Z.: IPCC 1995: Second Assessment: Climate Change, URL https://archive.ipcc.ch/pdf/climate-changes-1995/ipcc-2nd-assessment/2nd-assessment-en.pdf%0Ahttps://www.ipcc.ch/site/assets/uploads/2018/05/2nd-assessment-en-1.pdf, 1995.

Weddell, K.: Links Between Oceanic Ozone Uptake and Ocean Biology, pp. 1–92, 2023.

Wesely, M. L. and Hicks, B. B.: Some factors that affect the deposition rates of sulfur dioxide and similar gases on vegetation, Journal of the Air Pollution Control Association, 27, 1110–1116, https://doi.org/10.1080/00022470.1977.10470534, 1977.

Wesely, M. L. and Hicks, B. B.: A review of the current status of knowledge on dry deposition, Atmospheric Chemistry and Physics Discussions, 34, 2261–2282, 2000.

Wesely, M. L., Cook, D. R., and Williams, R. M.: Field Measurement of Small

Ozone Fluxes to Snow, Wet Bare Soil, and Lake Water, Boundary-Layer Meteorology, 20, 459–471, 1981.

Whitehead, J. D., Mcfiggans, G. B., Gallagher, M. W., and Flynn, M. J.: Direct linkage between tidally driven coastal ozone deposition fluxes, particle emission fluxes, and subsequent CCN formation, Geophysical Research Letters, 36, 1–5, https://doi.org/10.1029/2008GL035969, 2009.

WHO: WHO global air quality guidelines. Particulate matter (PM2.5 and PM10), ozone, nitrogen dioxide, sulfur dioxide and carbon monoxide, World Health Organisation, URL https://apps.who.int/iris/bitstream/handle/10665/345329/9789240034228-eng.pdf?sequence=1&isAllowed=y, 2021.

Wurl, O., Miller, L., Röttgers, R., and Vagle, S.: The distribution and fate of surface-active substances in the sea-surface microlayer and water column, Marine Chemistry, 115, 1–9, https://doi.org/10.1016/j.marchem.2009.04.007, URL http://dx.doi.org/10.1016/j.marchem.2009.04.007, 2009.

Wurl, O., Wurl, E., Miller, L., Johnson, K., and Vagle, S.: Formation and global distribution of sea-surface microlayers, Biogeosciences, 8, 121–135, https://doi.org/10.5194/bg-8-121-2011, 2011.

Yazici, B. and Yolacan, S.: A comparison of various tests of normality, Journal of Statistical Computation and Simulation, 77, 175–183, https://doi.org/10.1080/10629360600678310, 2007.

York, D., Evensen, N. N., Martınez, M. L., and Delgado, J. D. B.: Unified equations for the slope, intercept, and standard errors of the best straight line, American Journal of Physics, 72, 367–375, 2004.

Zhang, Z., Liu, L., Liu, C., and Cai, W.: Studies on the sea surface microlayer: II. The layer of sudden change of physical and chemical properties, Journal of Colloid and Interface Science, 264, 148–159, https://doi.org/10.1016/S0021-9797(03)00390-4, 2003.

Zhao, R., Chen, S., Wang, W., Huang, J., Wang, K., Liu, L., and Wei, S.: The impact of short-term exposure to air pollutants on the onset of out-of-hospital cardiac arrest: A systematic review and meta-analysis, International Journal of Cardiology, 226, 110–117, https://doi.org/10.1016/j.ijcard.2016.10.053, URL http://dx.doi.org/10.1016/j.ijcard.2016.10.053, 2017a.

Zhao, X., Ma, J., and von Gunten, U.: Reactions of hypoiodous acid with model compounds and the formation of iodoform in absence/presence of permanganate, Water Research, 119, 126–135, https://doi.org/10.1016/j.watres.2017.04.033, URL http://dx.doi.org/10.1016/j.watres.2017.04.033, 2017b.

Zhou, S., Gonzalez, L., Leithead, A., Finewax, Z., Thalman, R., Vlasenko, A., Vagle, S., Miller, L. A., Li, S. M., Bureekul, S., Furutani, H., Uematsu, M., Volkamer, R., and Abbatt, J.: Formation of gas-phase carbonyls from heterogeneous oxidation of polyunsaturated fatty acids at the air-water interface and of the sea surface microlayer, Atmospheric Chemistry and Physics, 14, 1371–1384, https://doi.org/10.5194/acp-14-1371-2014, 2014.

Zymon, M., Strzetelski, J., Pustkowiak, H., and Sosin, E.: EFFECT OF FREEZING AND FROZEN STORAGE ON FATTY ACID PROFILE OF CALVES' MEAT, polish journal of food and nutrition sciences, 57, 647–650, 2007.

Zäncker, B., Bracher, A., Röttgers, R., and Engel, A.: Variations of the organic matter composition in the sea surface microlayer: A comparison between open ocean, coastal, and upwelling sites off the Peruvian coast, Frontiers in Microbiology, 8, 1–17, https://doi.org/10.3389/fmicb.2017.02369, 2017.

Óscar Gálvez, Baeza-Romero, M. T., Sanz, M., and Pacios, L. F.: A theoretical study on the reaction of ozone with aqueous iodide, Physical Chemistry Chemical Physics, 18, 7651–7660, https://doi.org/10.1039/c5cp06440f, 2016.